UNIVERSITY OF YAOUNDE I

FACULTY OF SCIENCE

POSTGRADUATE SCHOOL OF SCIENCE,TECHNOLOGY AND GEOSCIENCES

RESEARCH AND TRAINING UNIT FOR GEOSCIENCES AND APPLICATION

UNIVERSITE DE YAOUNDE I

FACULTE DES SCIENCES

CENTRE DE RECHERCHE ET DE FORMATION DOCTORALE EN SCIENCES TECHNOLOGIE ET GEOSCIENCES

UNITE DE FORMATION ET DE RECHERCHE DOCTORALE EN SCIENCES TECHNOLOGIE ET GEOSCIENCES

DEPARTMENT OF EARTH SCIENCES
DEPARTEMENT DES SCIENCES DE LA TERRE

Laboratory of Geosciences for Internal Formations and Applications
Laboratoire de Géosciences des Formations Profondes et Applications

QUARTZ-RICH FAULT ROCKS HOSTED WITHIN THE ETAM SHEAR ZONE AS POTENTIAL HIGH PURITY QUARTZ RESOURCE, SW CAMEROON: QUARTZ MATERIAL PROPERTIES AND HOST ROCK PETROLOGY

A thesis submitted in the Partial Fulfilment of the Requirements for the award of the

Degree of Doctor of Philosophy (Doctorat/Ph.D) in Earth Sciences.

Option **Petrology and Structural Geology**

By
SIGUE Cyrille

Register N°: 97R013
Master in Earth Sciences
Public defense on 06/01/2021

Jury:

PRESIDENT:	NDJIGUI Paul Desire, Professor, Univ. Yaounde I.
SUPERVISORS:	CHEO SUH Emmanuel, Professor, Univ. Buea. MOUNDI Amidou, Associate Professor, Univ. Yaounde I.
MEMBERS:	AGYINGI Christopher, Associate Professor, Univ. Buea. TCHOUANKOUE Jean P., Associate Professor, Univ. Yaounde I. OWONA Sebastien, Associate Professor, Univ. Douala.

UNIVERSITE DE YAOUNDE I

FACULTE DES SCIENCES

CENTRE DE RECHERCHE ET DE FORMATION DOCTORALE EN SCIENCES TECHNOLOGIE ET GEOSCIENCES

UNITE DE FORMATION ET DE RECHERCHE DOCTORALE EN SCIENCES TECHNOLOGIE ET GEOSCIENCES

UNIVERSITY OF YAOUNDE I

FACULTY OF SCIENCE

POSTGRADUATE SCHOOL OF SCIENCE, TECHNOLOGY AND GEOSCIENCES

RESEARCH AND TRAINING UNIT FOR GEOSCIENCES AND APPLICATION

Laboratory of Geosciences for Internal Formations and Applications
Laboratoire de Géosciences des Formations Profondes et Applications

ATTESTATION DE CORRECTION DE LA THESE DE DOCTORAT/Ph.D

Spécialité :	Pétrologie et Géologie Structurale
Nom du candidat :	SIGUE Cyrille
Matricule:	97R013
Titre de la thèse:	Quartz-Rich Fault Rocks hosted within the Etam Shear Zone as potential high purity quartz resource, SW Cameroon: quartz material properties and host rock petrology
Date de soutenance :	Mercredi 06 Janvier 2021

Nous membres du jury, après avoir lu le document qui nous a été présenté ce jour, attestons que le candidat a effectué toutes les corrections conformément aux observations formulées lors de la soutenance.

En foi de quoi nous lui délivrons cette **Attestation de correction** pour servir et faire valoir ce que de droit.

Fait à Yaoundé le 29.11.2021

Le Président du Jury

NDJIGUI Paul Désiré
Professeur

L'examinateur

TCHOUANKOUE Jean Pierre
Maître de conférence

DEDICATION

To my father **LIYOUCK Patrice** and my late mother **NGO SACK Agnes.**

ACKNOWLEDGMENT

As we come to the end of this work, I would like to express my sincere gratitude to those who have made this PhD work possible.

My sincere thanks goes to my supervisors: firstly, Professor **Cheo Suh Emmanuel**, author of the title of this thesis and whose role was not only focused on the supervision of the thesis but also in the search of various sources of funding and analytical laboratories. Seccondly, Professor **Moundi Amidou,** who accepted to supervise this work. Dear Professors, your availability, your support and your advice have strengthened in me the scientific and researchspirit. It was a pleasure to learn so much from you, not only scientifically but also in other ways. Please find here the expression of my sincere gratitude.

My gratitude equaly goes to Dr. **Morillo Santos** from the Department of Materials Engineering, Faculty of Mechanical Engineering, Campinas State University, Brazil for performing LA-ICP-MS, Fluid inclusion and fusion over silica analyzes that have raised the scientific dimension of this thesis.

My thanks goes to all the lecturers of the **Department of Earth Sciences of the University of Yaoundé I**, who, each in his specialty helped me to carry this geologist profile.

To all my colleagues at Buea University, first of all "Seniors colleagues": **Prof. Suh,Prof. Ayingi, Prof. Njoh, Prof. Ako A, Dr. Mboudou, Dr. Fozao, Dr. Lordon**. Thank you, for your attention, your advice and support. Secondly the "junior colleagues" as I affectionately call you: **Dr.Ndema**, without you, simply this thesis could never progress normally. You put yourself at my disposal. Remember all these prolonged telephone discussions sometimes late into the night has sought to raise an enigma ... Thank you toall my brother. **Dr. Tiabou,** always able to encourage, to push someone to go forward. Thank you with all my heart. **Dr. Mbowou**, first of all I greet Madame who welcomed me in Douala every time I came to your home. Thank you. I appreciated your encouragement and sense of a multi-dimensional man. I just wanted to reassure you that we will now look for our pozzolan quarry if you want. **Dr. Che,** lovingly called younger sister, always available. By the way, keep what you owe me in the fridge.

I think of you **Jeanne d'Arc Ngo Nken**, who since our first meeting at the University of Yaounde I, bear my innumerable defects, I love you…I love you!

My three children, **Nken Sonia Emilienne**, **Sigue Abdoul-Akim** and **Sigue Liyouck Andy Patrice**, Adorable little ones, I am first tempted to leave you here an advice, but I will not do it. I leave this role to life, which is so hard and can only do that. You have put a new light since your appearance in my life.

I think of my father and my mother. Thank you for everything. I have often been the object of your torment. I would like to be able, now, to participate to give you more joy and happiness where you are.

My brothers and sisters, you who have shared my sufferings, our sufferings, you who shared all with me: for all the past moments, for the moments to come, we will remain united.

I think of M. **Tchadjeu Christophe**. This is a name I will never forget. Thank you for your multifaceted support.

I would like to thank all those who, from near or far and whose names I haven't mentioned, contributed to the realization of this thesis.

TABLE OF CONTENT

LIST OF FIGURES

LIST OF TABLES

LIST OF ANNEXES

LIST OF ABBREVIATIONS OF MINERALS USED (IUGCS, 2007)

Ab : Albite
Amp : Amphibole
Ap : Apatite
Bt : Biotite
Chl : Chlorite
px : pyroxene
Ep : Epidote
Hbl : Hornblend
Kfs **:** K-Feldspars
Ms **:** Muscovite
Pl : Plagioclase
Px : Pyroxene
Py : Pyrite
Pyr : Pyrope
Qtz : Quartz
Ru : Rutile
Sér : Sericite

ABSTRACT

Etam is located in the southwestern sector of the Tombel plain and belongs to the central domain of the Central African Fold Belt in Cameroon. In addition to basaltic rocks, this area is made up of a metamorphic basement (gneisses) intruded by felsic plutons (Granodiorite, Granites). These formations were affected by a major discontinuity: the Etam Shear Zone (ESZ).

Etam granitoids (biotite granite, fine grain granite and granodiorite) are syntectonic S-type granitoids. They are high-k calc-alkaline affinity to shoshonitic, feroanand strongly peraluminous. The high Rb/Sr (0.92 – 1.46) and low Sr/Ba (0.18 – 0.26) ratios coupled with strong negative Eu (Eu/Eu* = 0.37-0.59) anomaly characterized the lower degrees of vapour-absent crustal melting upon their formation. The CaO/NaO_2>3 ratio shows that granitoids from Etam were derived from mostly clay-poor, plagioclase-rich psammitic source material and probably crystallized between 800 and 950 °C, at ~750 kbar.

The Etam shear Zone (ESZ) which is considered here as part of the Central Cameroon Shear Zone (CCSZ) is a NNE-SSE- to NE-SW-trending discontinuity with coexistence of a sinistral ductile shearing mylonitic corridor and brittle zone. The mylonitic zone is evidence of progressive deformation from the wall rock towards the shear zone centre. Primary minerals include Qtz1 + Kfs1 + Pl1 + Bt1. These minerals increasingly and gradually reduce from the wall rock towards the shear zone center. Quartz recrystallization also gradually increases in the same direction. Microstructures observed include: recrystallization, sub-grain boundary, myrmekites and undulose extinction. Mica-chlorite-epidote assemblages define the greenschist assemblage, but the observation of amphibole in the mylonite and the presence of "flame perthite" in feldspar suggest transitional greenschist-amphibolite metamorphic condition in the Etam Shear Zone.

This study focused on the evaluation of the high purity quartz (HPQ) potential of a shear zone-hosted hydrothermal and metamorphic quartz deposit in Etam, southwest-Cameroon. The shear zone quartz-rich rock is monomineralic and consists of both milky and translucent varieties. The combination of ICP-MS and LA-ICP-MS analytical techniques was used to assess the chemical purity of both quartz varieties. These compositional analyses show that all quartz samples have SiO_2 content of 98.46–99.75 wt% with very low concentrations of all the other elements. Translucent quartz when compared to the milky quartz variety show low concentration of most of elements including the following principal impurities: Al (mean 107µg.g^{-1}), Ca (mean 27.85µg.g^{-1}) and Fe (mean 26.05 µg.g^{-1}). Bubble generation in the samples after flame-fusion over a silica plate was assessed to test the suitability of the quartz in industrial uses. The results obtained from the chemical analyses and bubble formation tests indicate that all the samples investigated do not meet the HPQ requirement. However, the translucent quartz shows characteristics of medium purity quartz and can produce silica glass for some industrial manufacturing even without further purification. In this study the fluid inclusions in the samples were examined as this bears information on the economic viability of the deposit and provides clues on the genesis of the quartz vein. Also, tiny mineral inclusions within individual quartz grains were identified by SEM-EDS. The results of these studies show that the deposit is probably of metamorphic origin marked by crystal-plastic deformation in quartz grains. The veins were later modified by hydrothermal fluid input. The results also indicate that the majority of impurities are likely hosted by fluid inclusions and thus the quartz can be upgraded to HPQ after purification by suitable methods as HCl-NH_4Cl and H_2SO_4-NH_4Cl systems.

Key words: Etam shear Zone, hydrothermal quartz, medium purity quartz, High Purity Quartz

RESUME

Etam est situé dans le secteur sud-ouest de la plaine de Tombel et appartient au domaine central de la chaine panafricaine d'Afrique Centrale au Cameroun. En plus des roches basaltiques, cette zone est constituée d'un socle métamorphique (gneissique) et montre un plutonisme felsique (granodiorite, granites). Toutes ces formations ont été affectées par une discontinuité majeure : le cisaillement Etam (ESZ) ou sont observes des gisements de quartz hydrothermales.

Les granitoïdes d'Etam sont syn-tectoniques et de type S. Ils ont une forte affinité calco-alcaline a shoshonitique et sont fortement peralumineux. Les rapports Rb/Sr (0,92 - 1,46) et Sr/Ba (0,18 - 0,26) élevés, associés à une forte anomalie Eu négative (Eu/Eu* = 0,37-0,59), caractérisent des faibles degrés de fusion de la croute en l'absence de liquides lors de leur formation. Le rapport CaO/NaO2>3 montre que les granitoïdes de l'Etam dérivent d'un matériau psammitique principalement pauvre en argile et riche en plagioclases et ont probablement cristallisé entre 800 et 950 °C, à ~750 kbar.

La zone de cisaillement de l'Etam (ESZ) est orientée NNE-SSE à NE-SW avec une coexistence d'un corridor mylonitique et d'une zone fragile. La zone mylonitique montre une déformation progressive de la roche saine vers le centre du cisaillement. Les minéraux (Qtz1 + Kfs1 + Pl1 + Bt1) diminuent de taille progressivement vers le centre de la zone de cisaillement, tandis que la recristallisation du quartz augmente également progressivement dans la même direction. Les microstructures observées sont : la recristallisation, les myrmekites et l'extinction roulante. Les assemblages mica-chlorite-épidote + flamme perthite dans le feldspath suggèrent un métamorphisme transitionnel schist vert-amphibolite dans cette zone

Cette étude fait l'évaluation des gisements de quartz hydrothermal et métamorphique d'Etam comme source potentielle du quartz de haute pureté (HPQ). Ces roches sont monominérales et sont composées de variétés de quartz laiteux et transluciide. La combinaison des techniques d'analyse ICP-MS et LA-ICP-MS a été utilisée pour évaluer la pureté chimique des deux variétés de quartz. Ces analyses montrent que tous les échantillons de quartz ont une teneur en SiO_2 qui varit de 98,46 à 99,75 %. Le quartz translucide, comparé à la variété de quartz laiteux, présente une faible concentration de la plupart des éléments, y compris les principales impuretés suivantes Al (moyenne 107µg.g-1), Ca (moyenne 27,85µg.g-1) et Fe (moyenne 26,05 µg.g-1). La production de bulles de vapeur dans les échantillons après fusion à la flamme sur une plaque de silice a été évaluée et montre que tous les échantillons étudiés ne satisfont pas à l'exigence de QHP. Cependant, le quartz translucide présente les caractéristiques d'un quartz de pureté moyenne et peut produire du verre de silice pour certaines fabrications industrielles, même sans autre purification. Dans cette étude, les inclusions fluides et des analyses SEM-EDS ont été également faites. il en découle de ces etudes que les gisements sont probablement d'origine métamorphique et ont été modifiées par la suite par l'apport de fluide hydrothermals. Les résultats indiquent également que la majorité des impuretés est probablement logee dans des inclusions fluides et donc ce quartz peut être re evaluer en HPQ après purification par des méthodes appropriées telles que les systemes HCl-NH_4Cl et H_2SO_4-NH_4Cl .

Mots clés : Cisaillement d'Etam, quartz hydrothermale, quartz de pureté moyenne,quartz de haute pureté

GENERAL INTRODUCTION

I Context and justification

High-purity quartz (HPQ) defined as quartz with < 50 μg/g content of contaminating substances (Muller et al., 2010), is essentially pure quartz with very low levels of impurities and pigmenting agents such as Ti, V, Ni and Cr. Because the levels of these trace elements in quartz are generally very low, the process of ascertaining the prospectivity of quartz occurrences as potential HPQ deposits requires high quality cathodoluminiscence (CL), scanning electron microscopy (SEM) and laser ablation inductively coupled plasma mass spectrometry (LA-ICP-MS) analysis of the quartz crystals. These analytical techniques provide quantitative data that allow for the comparison of quartz from less studied areas with HPQ from currently producing sites across the world. These data, combined with the composition of mineral inclusions in quartz also permit economic geologists to calculate the temperature of metamorphism/formation, model element diffusion (solid-solid redistribution) between quartz and the mineral inclusion phases as well as the mechanisms by which inclusions in quartz exsolve from the silicate phase with falling temperature and/or pressure. These aspects are of significance to science and are examined in this thesis.

Laser ablation techniques are increasingly being used to determine trace element composition in various mineral phases especially elements whose concentrations are within the parts per billion (ppb) range (e.g. Pasava et al., 2013, Depine et al., 2013, Oberthur, 2013). These studies have increasingly pointed to the fact that the trace element content of mineral phases can be a useful tool for provenance studies of mineral deposits (magmatic, hydrothermal/metamorphic or post depositional enrichment). Although literature has a fair amount of such high-quality data relating to pyrite (e.g. Koglin et al. 2010), same can not be said of HPQ. This study seeks to contribute to this knowledge gap. This is particularly relevant as the demand for HPQ worldwide is increasing and its usefulness for various industrial applications relies on the minor element content in the quartz crystals.

In southwestern Cameroon numerous quartz-rich rocks of metamorphic and fault-related origin have been described (e.g. Njome and Suh, 2005). These rocks lie essentially along a fault trend that is part of the transatlantic shear zone system referred to as the Central African Shear zone that extends from the interior of Africa across the Atlantic into South America (Fig. 1, e.g. Ngako et al., 2008, Kankeu et al., 2012). Although this structure has witnessed numerous structural and economic studies (Mosoh Bambi et al., 2013), no previous studies have focused on these quartz-rich fault rocks whose contribution to the over all

evolution of the shear zone and potential role as HPQ source is of more than local significance.

II Objectives of study

The principal objective of this work was to evaluate the suitability of quartz-rich fault rocks in Etam and environs in southwestern Cameroon as potential HPQ sources.

The specific objectives were:

i. To produce a geological map underling the quartzitic rocks and their metamorphic/igneous associated rocks in the Etam area.
ii. To determine the origin of quartzitic rocks and quartz vein relatively to the host rocks
iii. To Determine trace element concentration in quartz by LA-ICP-MS, bubble formation by fusion of quartz grains over silica plate
iv. To determine the quality of Etam HPQ relative to standart (IOTA) and other HPQ
v. To identify the methods used to upgrade low and medium purity quartz to high purity qurtz

III Thesis outline

The main results of this work are presented in four (04) chapters which previously start by a General Introduction that rise problem relative to HPQ over the world and immediately follow by **Chapter one** whichdeals with natural setting and generalities. **Chapter two** presents thematerials andmethods used, while **Chapter three** gives the results of the study, **Chapter four** deals with the interpretationand discussion. The work ends by a General conclusion and Recommandation.

CHAPTER I

GEOGRAPHYCAL SETTING AND GENERALITIES

I Geographical setting of the study area

I.1 Location

Etam area is located in the Kupe Manenguba Division, South West Region of Cameroon. It has a grid reference location between latitude N04°36’52’’- N04° 48’ 3’’and longitude E 09°28’ 5’’- E09°39’8’’ (Fig. 1).

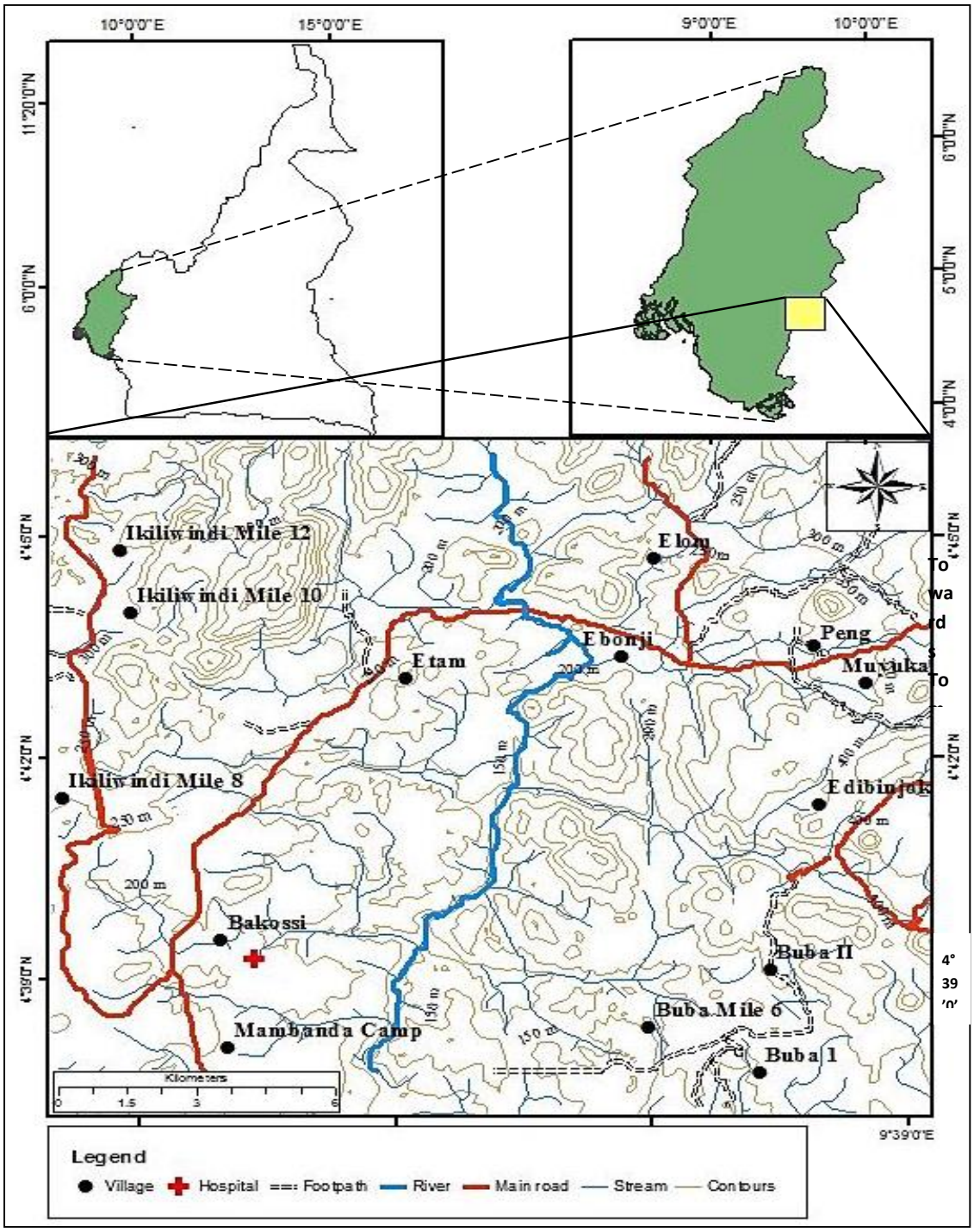

Figure 1: Location of the study area.

I.2 Relief

Basically, Etam is lowland but comprises of a number of hills and valleys. The hills are characterized by steep slopes, while the valleys are narrow and deep. The maximum height noted in the study area is about 590m and the lowest is 300m (Fig. 1).

I.3 Drainage

The drainage pattern in Etam is dendritic (Fig. 2) due to the branching of smaller streams (Jambo, Sambo) into rivers (Kobe) which eventually drain into the River Mungo, which flows from North (Rumpi Mountain) to South. Rivers in this area are mostly interrupted by falls and rapids.

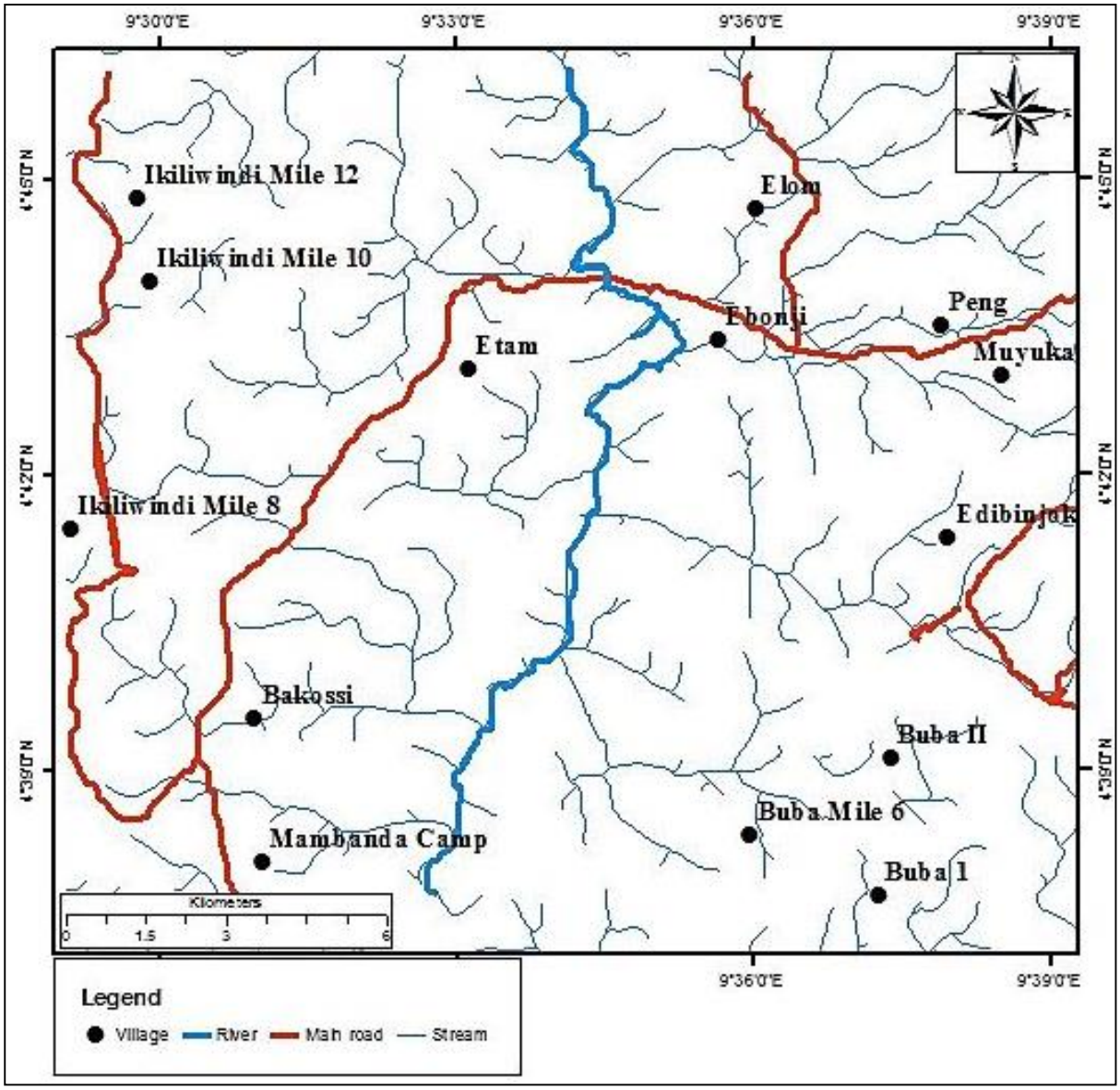

Figure 2: Drainage pattern of the study area.

I.4 Climate

Etam and its environs have a tropical climate. This type of climate has shot slightly dry season. Temperature and precipitation vary during the year (Fig. 3). The total annual average temperature is about 25.9°C while the average precipitation is usually about 2865mm for total annual precipitation (www.besttimetovisit.com.pk, acess on 22 April 2019).

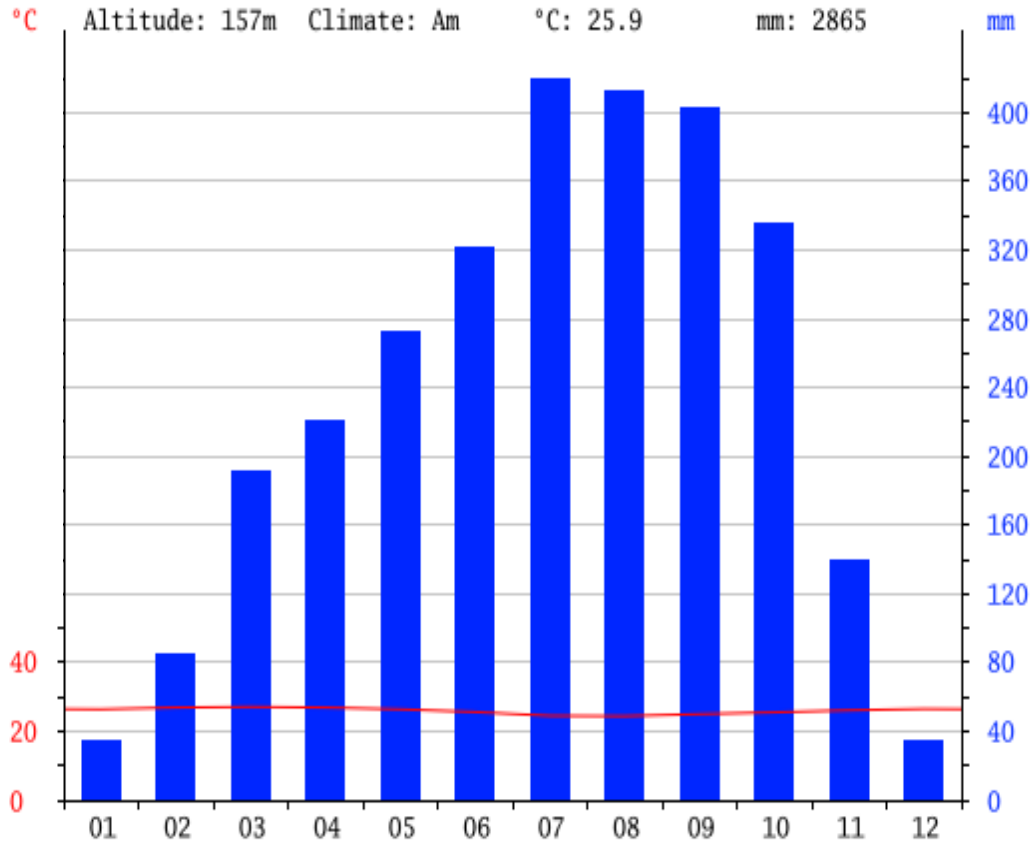

Figure 3: Etam climate: temperature (red line) and precipitation (blue stick). 01, 02, 03…and 12 represent January, February, March… and December respectively.

I.5 Vegetation

The vegetation of the study area falls within the primary, secondary, and tertiary type of vegetation. The tropical rainforest and the equatorial rain forest make up the primary vegetation characterised by a thick canopy which results to scanty undergrowth. The secondary vegetation is made up of a relatively tempered forest; while the tertiary vegetation consists of farmlands and shrubs.Some of the tall evergreen hardwoods found here are mahogany, Iroko, Sapelle, Akan and Boma.

I.6 Soil

Vertisols and lateritic soils are common in the area. Vertisols are dark and clayey while lateritic soils are locally impregnated with iron-rich nodular crust.

I.7 Land use pattern

The major ethnic groups in this area are the Bakossi tribe, which constitute the Bantus (Eyongetah and Brian, 1981) and the Bafaws. People from the Northwest region (Meta) have also settled here for agricultural reasons. Land use is mainly restricted to agriculture. Both small scale and plantation agriculture are practised in the area.

II Geological setting

II.1 Regional geological setting

The study area is located in the south-west region of Cameroon. It is part of the Tombel graben, which is a southwestern segment of the Central African Shear Zone (Njome and Suh, 2005) in Cameroon (Fig. 4a). Etam also belongs to Adamaoua Yade Domain (AYD) of the Central African fold belt in Cameroon (Fig. 4b, Penaye et al., 1993; Toteu et al., 2001; 2004.).

The Central African fold belt in Cameroon is also known as Pan-African North Equatorial Fold Belt (Nzenti et al., 1988; Ngnotue et al., 2000) and it is a part of the Central African orogenic belt (Trompette, 1997), generally trending E-W with 5000 Km in length and over 300Km wide (Fig.4a). It is bordered to the West by Pan-African Trans-Saharian fold belt, to the South by the Congo Craton, and runs into the Northeast of Brazil through the Sergipano Belt, which represents the Brasiliano-Pan-African orogeny (Almeida et al., 1981; Castaing et al., 1994; Brito de Neves et al., 2002). The Brasiliano-Pan-African fold belt resulted from the convergence and collision of large continental blocks involving West Africa, Sao Francisco and Congo Cratons as well as the intermediate domain of Neoproterozoic age that consists of the polycyclic basement domain of Hoggar, Nigeria and Borborema. Moreover, paleomagnetic, geochronologic, geochemical and structural similarities between the Africa and South America suggest that the separate units once formed a continuous unit in the past called the composite megacontinent of Gondwana (Abdelsalam, 2002).

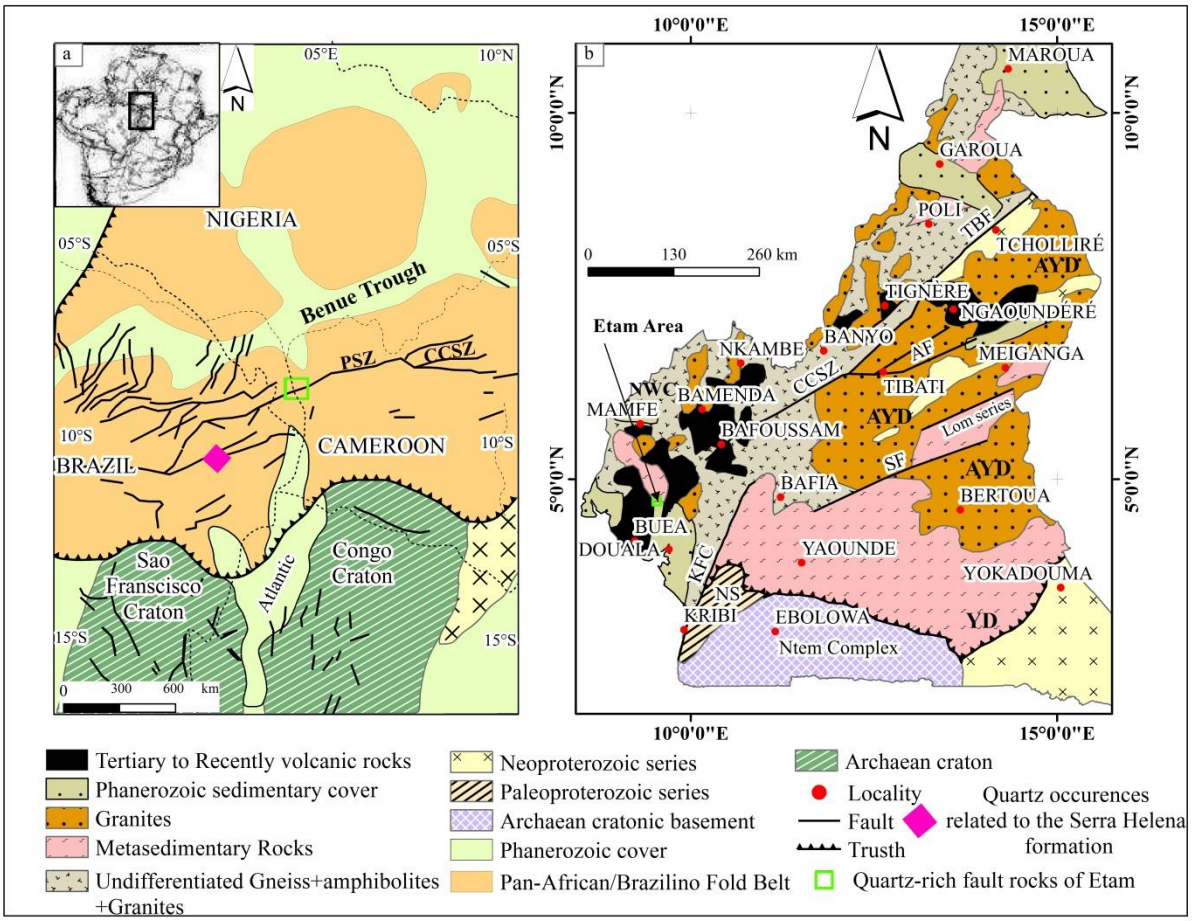

Figure 4: Geological map of Cameroon, showing major lithotectonic units and shear zones: a) Continental structures of Western Gondwana after Pan-African tectonic evolution (modified after Njome & Dewit, 2014). Shear Zones: CCSZ (Central Cameroon Shear Zone); (SF) Sanaga Fault; (TBF)Tchollire-banyo Fault; (Pe) Pernambuco fault; (Pa) Patos Fault. b) Geological map of Cameroon (modified after Toteu et al., 2001). The Central Cameroon Shear Zone is defined by a system of NE trending faults comprising Tchollire-Banyo Fault (TBF), Adamawa Fault (AF), Sanaga Fault (SF), and Kribi-Campo Fault (KCF). NWC, North western Cameroon domain; AYD, Adamawa-Yade Domain; YD, Yaounde Domain.

II.2 Geology of Cameroon

II.2.1 Precambrian geology

It is a period on the geologic timescale older than 600± 50Ma) and consists of rocks of two main age range: the Archaean (>2500Ma) and the Proterozoic (2500Ma- 600Ma, Cahen, 1984).

II.2.1.1 Archaean lithologies in Cameroon

The Archean Ntem Complex defines the north-western border of the Congo Craton. The principal Archean domains found in Cameroon include:

(1) ***The Ntem Unit:*** This is part of the Congo Craton (Fig.5) and represents the oldest lithologic group in Cameroon. It is a set of Palaeoarchaean to Mesoarchaean and Late Archaean charnockites, Mesoarchaean greenstone formations, Late archaean TTG basement, dolerite dykes and high-K granite (Shang et al., 2010; Chombong et al., 2013; Ganno et al., 2015; 2018; Ndime et al., 2018). Archean rocks in the Ntem Complex are dominated by massive and banded plutonic rocks of the charnockite suite and by intrusive tonalites, trondhjemites and granodiorites. Some of these bodies were previously dated at ca. 2.9 Ga (Toteu et al., 1994;, Lasserre and Soba, 1976).Two important reactivation episodes affected the Ntem complex in Eburnean and Pan-African times. Old Rb–Sr whole-rock data from Lasserre and Soba (1976), though seemingly unreliable, suggest recrystallization between 2400 and 1800 Ma. Shang et al., (2004) reported Rb–Sr biotite ages between 2299 and 2064 Ma, confirming Lasserre and Soba (1976), and interpreted this as Eburnean reactivation. Recent reviews of the geochronologic data from the Ntem complexreveals that the charnockites crystallized at ~2.92 Ga; the trondhjemitesand associated amphibolite protoliths, crystallized synchronouslyat 2.87–2.86 Ga (Li et al., 2016).

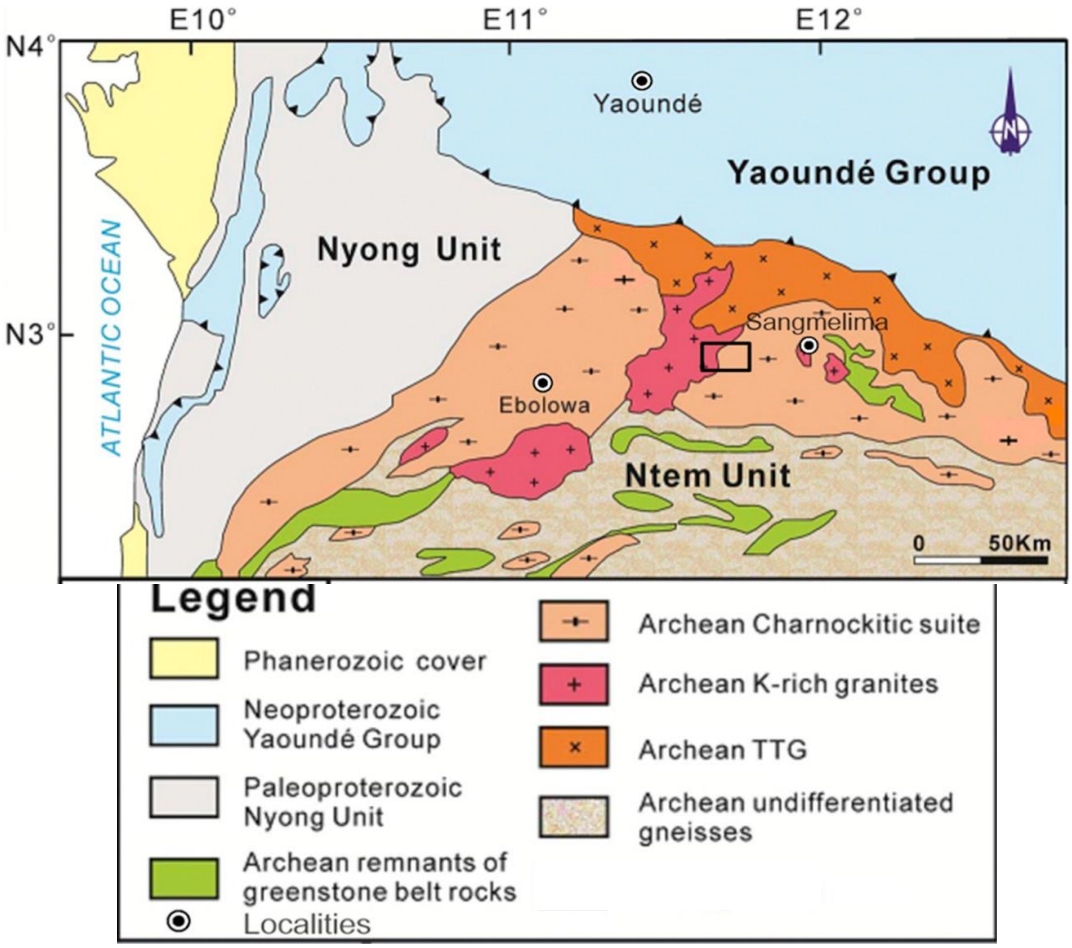

Figure 5: Geological sketch map of southwestern Cameroon (modified after Maurizot et al., 1986; Tchameni et al., 2010)

This complex hosts severalrock units of economic importance which include high grade iron ore and itabirites (Suh et al., 2008; Ilouga et al., 2013; Nforba et al., 2010; Feybesse et al., 1998, Ganno et al., 2017; Ndime et al., 2018) with less prominent ultrabasic rocks containing elevated Ni, Cr and Co contents (Milesi et al., 2006).

(2) ***The Nyong unit:*** The Nyong unit, constitutes the northwestern border of the Ntem Complex (Fig. 5), it is about 240 km long and 160 km wide NNE-SSW trending band of dominantly Paleoproterozoic metasedimentary and metaigneous rocks. Initially interpreted as being part of the Archean Congo craton reactivated during Paleoproterozoic and Pan-African orogenies (Lasserre and Soba, 1976; Maurizot et al., 1986), this unit is now considered as a Paleoproterozoic nappe thrust onto the Congo craton (Penaye et al., 2004; Lerouge et al., 2006), yielding both Archaean and Paleoproterozoic materials associated with various migmatitic gneisses of TTG composition, granitoids, and remnants of greenstone belts commonly made up of pyroxenites, serpentinites, banded iron formations (BIF), mafic and ultramafic metavolcanics and post-tectonic metadoleritic dykes (Ndema Mbongue et al., 2014; Ganno et al. 2017; Soh et al., 2018). More recently, Loose and Schenk (2018), Bouyo Houketchang et al. (2019) and Ngah Essomba et al. (2019) reported the existence of well-preserved to variably retrogressed eclogite facies metamorphic rocks associated with greenstones belt in the Nyong unit. The SHRIMP U–Pb age of these eclogites was constrained at 2093 ± 45 Ma (Loose and Schenk, 2018). This date which is similar to that of their host rocks (2050 Ma, Lerouge et al., 2006) suggests that the Nyong Group underwent the same metamorphism by coupling field relationships with the contemporaneous zircon growth between both rock types during the Paleoproterozoic between 2100 and 2000 Ma (Bouyo Houketchang et al., 2019). The new findings allowed the reinterpretation of Paleoproterozoic Nyong unit as one of the oldest subducted oceanic slab or trace of a suture zone so far recorded within the West Central African Fold Belt (Ngah Essomba et al., 2019). Moreover, ca 600 Ma Pan-African high-grade recrystallization and static overgrowth was recorded in the western part of the Nyong unit. This suggests that this unit underwent a polycyclic evolution (Toteu et al., 1994; Lerouge et al., 2006; Ndema Mbongue et al., 2014).

(3) ***Archaean remnants in the Pan African domain***: These are isolated and often well-preserved blocks within Neoproterozoic (Pan-African) terranes in Cameroon. Archaean ages (~2.6 Ga) have been obtained in this domain in the Meiganga area, using 207Pb/206Pb single-zircon evaporation method (Ganwa et al., 2008a).Recent U–Pb dating indicates that the protoliths of some orthogneisses from the Adamawa-Yadé domain were emplaced during Tonalite-Trondhjemite-Granodiorite (TTG) suites in the Makénéné area and intruded at

ca.3.0–2.5 Ga, as well as Nomalé migmatitic gneiss that yielded an upper intercept age at 2980 ± 36 Ma (Tchakounté et al., 2017).

II.2.1.2 Proterozoic lithologies in Cameroon

The Proterozoic formations in Cameroon comprise the Paleoproterozoic rocks, which derived from old Archean rocks reactivated during the Eburnean metamorphic event and those generated during the same event and the Neoproterozoic rocks which are considered as rocks reactivated during the Panafrican metamorphic event between 550 and 650 Ma.

- **Paleoproterozoic lithologies in Cameroon**

Paleoproterozoic lithologies in Cameroon have been recorded mainly in the Ayna unit and the Nyong series described in section II.2.1.1. Therefore, recent studies also described remnants of Paleoproterozoic basement rocks within the Pan-African Central Africa Fold Belt(Penaye et al., 1989), where they are well preserved in some domains in the belt or displayed only as isolated blocks in other domains.The Paleoproterozoic ages within the Pan-African Central Africa Fold Beltare essentially recorded in rocks in the northern part of the belt (Poli region) and central part (Kékem, Banyo, Tibati, Makenene, Tonga, Meiganga and Mbé). In Meiganga,age determinations employing the 207Pb/206Pb single-zircon evaporation method yielded Late Archean (2.6 Ga) to Palaeoproterozoic (1.7 Ga) ages (Ganwa et al., 2008b). In the Bafia group, ca. 2.1-Ga zircon age (Paleoproterozoic) was recorded in orthogneiss from Makenene (Toteu et al., 2001; Nzolang, 2005) and in garnet-amphibolite and biotite-amphibole gneiss in the Tonga area (Tanko Njiosseu et al., 2005). Similar age was obtained inthe Mbé region to the north of Ngaoundéré where U–Pb dating on meta-igneous rocks (hornblende–biotite gneiss) gave an age around 2.1 Ga (Penaye et al., 1989).

- **Neoproterozoic lithologies in Cameroon**

The Pan-African Fold Belt (Nzenti et al., 1988; 2006; Ngnotué et al., 2000) is a major Neoproterozoic Orogen linked to the Trans-Saharan Belt of western Africa and to the Brasiliano Orogen of NE Brazil (Castaing et al., 1994; Neves et al., 2006). In Cameroon, the Pan-African Central Africa Fold Belt (Fig. 6) which is partly covered by basalts and trachytes of Tertiary to Recent age is subdivided into three domains (Nzenti et al., 1994; 1999; 2006; Ngnotué et al., 2000; Tanko Njiosseu et al., 2005): The southern domain (Yaounde domain), the central domain (Adamaoua-Yade domain) and the Northern domain.

The southern domain corresponds to the northern edge of the Congo Craton, formed by Neoproterozoic metasediments deposited in a passive margin environment and

metamorphosed under high pressure conditions at 616 Ma. This domain consists of the Yaoundé Group which is composed of the Yaoundé Series located at the centre, Mbalmayo-Bengbis –Ayos, Yokadouma and Bafia Series located to the South, East and North of the Yaoundé Series, respectively. They are Neoproterozoic volcanosedimentary series thrusted onto the Congo craton (Nzenti, 1987; Nzenti et al., 1984; 1988; 1998b; 1999; Nédéléc et al., 1986; Soba, 1989; Penaye et al., 1993). This southern domain shows a polyphased and monocyclic evolution (Nzenti et al., 1988; Nzenti and Tchoua, 1996; Ngnotué et al., 2000; Owona et al., 2010) with two main deformational phases contemporaneous with high temperature and high-pressure metamorphism. The early D_1deformational phase is responsible for a compositional banding.

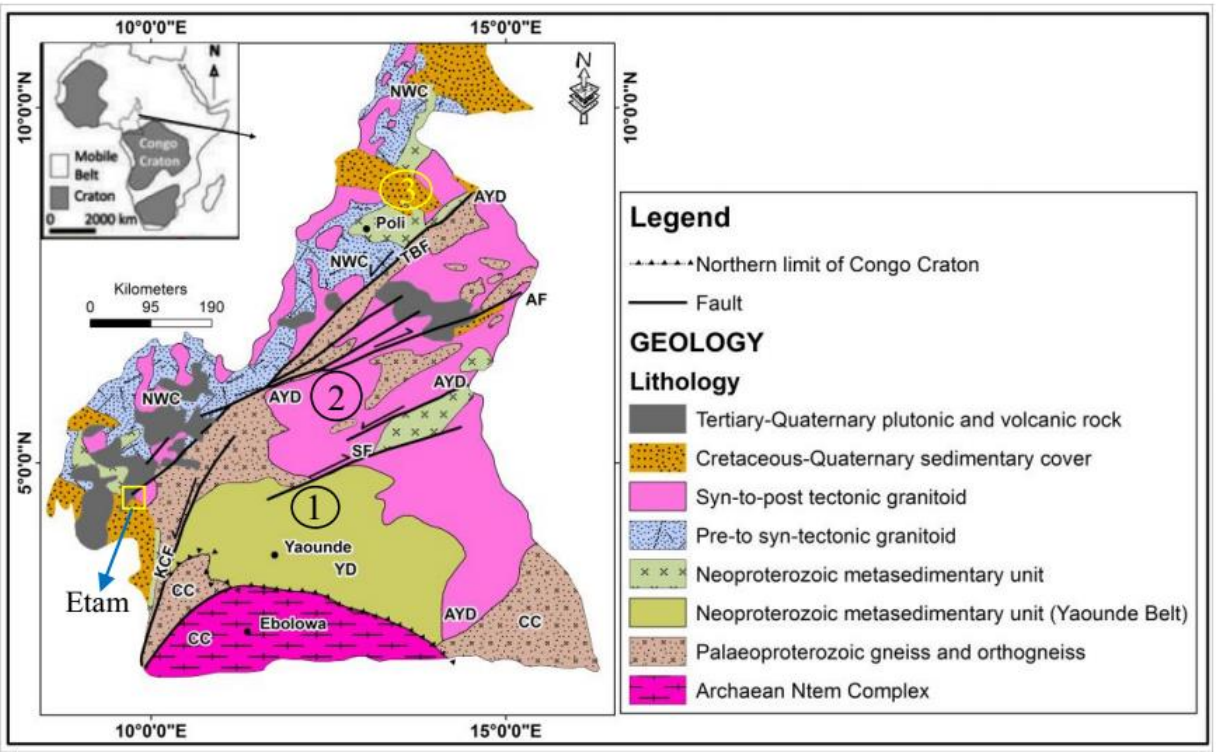

Figure 6:Geological map of Cameroon (modified from Toteu et al., 2001, Nzenti et al., 1994, Ngnotué et al., 2000, Kankeu et al., 2009 and Kankeu et al., 2012; Vishiti et al., 2015), showing three domains of Central African fold belt in Cameroon: (1) southern domain; (2) central domain; (3) northern domain. The Central African Shear Zone is defined by a system of NE-SW trending faults comprising Tchollire-Banyo Fault (TBF), Adamawa Fault (AF), Sanaga Fault (SF), and Kribi-Campo Fault (KCF). AYD, Adamwa-Yade Domain; YD, Yaoundé Domain; The location of the study area is marked by a yellow box.

The subsequent D_2deformation phase is characterized by tangential tectonics that resulted in thrusting onto the Congo craton (Nzenti et al., 1988; 1992; Ngnotué et al., 2000; Tadjou, 2004). It developed under granulites-facies metamorphism whose P and T are estimated at T = 800°C, P = 12Kb (Nzenti, 1987; Nzenti et al., 1984, 1988; Owona et

al.,2010) in the Yaoundé region. The southern domain probably corresponds to a continental margin. However, the presence of evaporitic compositional level and alkaline volcanictes strongly suggest a shallow water depositional environment during extensionnal tectonic processes (Nzenti et al., 1988; 1992; 1998b; Nzenti et Tchoua, 1996; Ngnotué et al., 2000). This domain may be considered as an extensional tectonic domain to the North of the Congo craton, generating fracturing of older crustal materials, which resulted in rift-related basins.

*The central domain*is a transition domain between the north and south domains, which stretches from the south of Bafia area to the south of Poli. It consists of (i) large strike-slip faults (Cameroon Central Shear Zone, CCSZ), Foumban-Tibati-Banyo fault considered as ductile transcurrent shear zone (Nzenti et al., 1988; Ngako et al., 1991; 2003; Abdelsalam et al., 2002), Bétaré-Oya ductile-brittle fault (Kankeu et al., 2009) and Sanaga Fault (Dumont, 1986); (ii) widespread syntectonic granitoids (leucogranites, granites, syenites) of aluminous to high-K calc-alkaline affinities (Nzenti et al., 1994; 1998; Nguiessi et al., 1997; Tagne Kamga, 2003; Tagne-Kamga et al., 1999; Nzolang et al., 2003; Njanko et al., 2006; Nzenti at al., 2006; 2010; Djouka-Fokwé et al., 2008; Njiekak et al., 2008; Kouankap Nono et al., 2010; Chebeu et al., 2010; Mosoh Bambi et al., 2013; Asaah et al., 2015; Ntieche et al., 2016; 2017), (iii) Neoproterozoic metasedimentary rocks (Soba, 1989; Tchaptchet Tchato et al., 2009, Bouyo et al., 2009) and (iv) 2100Ma Paleoproterozoic granulites (Nzenti 1987; Nzenti et al., 1998; Penaye, 1988; Toteu et al., 2001; Tanko Njiosseu et al., 2005; Ganwa et al., 2008a). Literature available (Nzenti et al., 1994; Tagne Kamga, 1994 Ngnotué et al., 2000; Kapajika, 2003; Nzolang et al., 2003; Tanko Njiosseu et al., 2005; Nzenti et al., 2006, 2007; Kouankap Nono et al., 2010; Chebeu et al., 2010; Nzenti et al., 2010) shows that the central domain is a polycyclic domain, it consists of three Neoproterozoic deformational phases developed under low to high grade amphibolites facies:

- D_1deformational phase is represented by S_1 foliation associated with L_1mineral lineation; shear plan C_1, shear band cleavages (S-C) structures associated with F_1 fold. This deformation phase is contemporaneous with low to medium grade amphibolites-facies metamorphism;

- D_2deformational phase is responsible for C_2shearing plane, F_2fold with S_2as axial plane schistosity, associated with a lineation L_2. It developed under high grade amphibolite-facies metamorphic conditions with P and T estimated at (5-7Kb, 700-800°C respectively). It is also coeval with the emplacement of some plutons in the central domain such as those of Tonga (Tanko Njiosseu et al., 2005), Bantoum (Nzolang et al., 2003), Bangangté, Batié (Njiekak et al., 2008), Kekem (Tchaptchet Tchato et al., 2009), Bafoussam (Djouka et

al.,2008), Bandja (Nguiessi et al., 1997), Banyo (Nzenti, 1998a), Kongolo (Lasserre et Soba, 1976), Koata-Tibati (Njanko, 1999; Njanko et al., 2006, Kapajika, 2003; Nzenti et al., 2006), Ngaoundéré (Tchameni et al., 2006), Banefo-Mvoutsaha (Kouankap Nono et al., 2010), Akum-Bamenda (Nzenti et al., 2010); Batié-Bapa (Chebeu et al., 2010);

- D_3 phase is mainly a brittle phase, characterized by C_3shearing plane associated with large scale folding F_3. The works of Nzenti et al. (1994; 1998 and 2007), Tanko Njiosseu et al. (2005) and Ganwa et al. (2008a and 2008b) revealed in this domain, the occurrence of 2100 Ma old Paleoproterozoic high grade gneiss intruded by 550 ± 50 Ma old Neoproterozoic plutons. According to these authors, the central domain represents an ancient continental domain reworked during Pan-African orogeny.

The northern domain is a polyphase and polycyclic domain (Toteu et al., 1987; Penaye et al., 1989; Nzenti et al., 1992; 1999), consisting of metasediments known as the Poli series, associated with subordinate 830 Ma-old volcanics of tholeiitic and alkaline affinities which have been interpreted as an extensional stage; metabasites and calc-alkaline orthogneiss interpreted as an accretion domain (Toteu et al., 1987; Danguené, 2003). The remnants of Paleoproterozoic crust dated at 2100 Ma (U/Pb zircon age, Penaye et al., 1993) are interlayed with orthogneiss. U/Pb and Sm/Nd geochronology data from the Buffle Noir and Mbé regions, located to the South East of Poli (Toteu et al., 2001; 2004) have revealed that these areas have experienced a long and complex crustal evolution from upper Archean (2900-3000 Ma) to Neoproterozoic (620-580 Ma), which is characterized by three successive deformational phases:

- The early D_1deformation corresponds to tangential tectonics dated at 800-700 Ma, (U/Pb zircon age, Toteu et al., 1990). Structures related to D_1deformation are most often obliterated by subsequent $D_2$and D_3deformation. It developed under amphibolite-facies conditions (650°C, 6-7Kb, Nzenti et al., 1992);

- D_2deformation phase, coeval with an intensive migmatization (Njel, 1988; Nzenti et al., 1992) and granitisation (Syn-D_2calc- alkaline granitoids dated at 580 Ma U/Pb Zircon age, Toteu et al., 1987; 1990), evolved both under amphibolite facies conditions (600°C, 5-7Kb) and green schist metamorphic conditions (550°C, 5Kb). This D_2deformation phase (Nzenti et al., 1992) is characterized by N-S or NW-SE oriented sinistral strike-slip fault, associated with thrusting and E-W to WSW-ENE in "echelon antiform and synform ". This stage is also contemporaneous with an important crustal melting;

- D_3deformation marked by E-W dextral strike –slip and E-W to N-S oriented drag fold, is associated with granitoids dated at 545 Ma (U/Pb zircon age, Toteu et al., 1987).

II. 2.2 Central Cameroon Shear Zone (CCSZ)

The CCSZ is a corridor of high strain rocks that extends across central Cameroon in a NE-SW direction (Dumont, 1986; Ngako et al., 2003) and continues into north-eastern Brazil as the Pernambuco shear zone (Fig. 4a, Castaing et al., 1994; Trompette, 1994; Neves et al., 2005). It is a set of an anastomosing transcurrent fault (Kankeu et al., 2009) and shows an important mylonitic band, low- to medium-grade with a variation of direction from N70°E to N30°E (Fig.4b). Deformation along the CCSZ is heterogeneous. Sinistral and dextral shear movement are separately recorded within the shear zone (Ngako et al., 2003). F_2 asymmetric fold consisting of boudinaged granitic veins and preferred orientation of feldspar phenocrysts oblique to concordant syn-kinematic vein characterise sinistral shear movement, while dextral shear movement is indicated by asymmetric boudins in granitic veins cross-cut by c' shear planes. An important relation has been indicated between CCSZ, generation and emplacement of granitic intrusions in the Pan-African North Equatorial Fold Belt (Ngako et al., 2003; Tagne Kamga, 1994; Nguiessi et al., 1997; Njanko, 1999; Njanko et al., 2006; Nzenti et al., 2006).

II.2.3 Previous studies in Tombel graben

Tombel area is located in the continental sector of the Cameroon volcanic line (CVL, Regnoult, 1986; Neba, 1987) also known as 'Cameroon Hot Line' (CHL, Deruelle, et al,. 2007). The metamorphic basement in the Tombel graben and its environs comprises gneisses, biotite-schists, migmatites and meta-granitoids (Njome and Suh., 2005). Gneisses and schists are low-grade metamorphic rocks evidenced by the appearance of biotite in the mode (Njome and Suh, 2003).

Structurally, the metamorphic basement in the Tombel graben region is marked by two major tectonic events, made up of a NE-SW mylonitic foliation reminiscent of ductile deformation along a sinistral strike-slip fault. The mylonitization event reworked an older N-S gneissose foliation and a younger brittle event marked by three principal sets of fractures: N140E-N150E, N120E-N130E and N90E-N110E. The mylonites have a distinct greenschist facies assemblage with the appearance of sericite + chlorite + epidote, and the silicification of the matrix (Njome et al., 2003). The sericite in the mylonite forms from the breakdown of feldspars in the precursor rocks and points to the fact that mylonitization was accompanied by fluid infiltration resulting in retrograde metamorphism. The tectonic evolution in the Tombel graben segment of the CASZ system follows a classical development of shear zone

describedby a number of works (e.g. Suh and Dada, 1997; Imber et al., 2001). It commenced with ductile deformation and terminated with brittle deformation.

The Etam area has mainly basalt, plutonic rocks (granitic and granodioritic) and metamorphic rocks including gneisses and migmatites. These lithologies are associated to a mylonitic band oriented N030 to N045 (Njome and Suh, 2003) termed the Etam shear zone (ESZ, Sigue et al., 2019) which constitutes a segment of CCSZ. The mylonitization event has been attributed to a Pan-african age (Njome and Suh, 2005) and has reworked the gneissic foliation. The basement rocks at Etam are extensively covered in some places by the basaltic lavas from the Cameroon Volcanic Line (CVL). All these lithologic units are cross-cut by several randomly oriented fracture sets and quartz veins. The quartz veins are few millimetres to several metres wide. Some quartz in this area show medium to high purity qualities with a great High-Tech use (Sigue et al., 2020).

III Overview of shear zone and High purity quartz

III.1 Shear zones and silica remobilization

Shear zones are generally known for their unique structural configuration which influences hydrothermal fluid flow and also acts as a conduit for granitoid emplacement (Hutton and Reavy, 1992; Lemos et al., 1992; Weinberg, 2004; Brown and Solar, 1998).

Alteration in brittle–ductile shear zones is mainly driven by syn-tectonic fluids (McCaig et al., 1990; Goncalves et al., 2012; Wintsch and Yeh, 2013). Spruzeniece et al., (2015) suggested that the fluid present in brittle–ductile shear zones is typically associated with a variety of weakening mechanisms: (1) chemical breakdown of feldspars into weak hydrous minerals (White and Knipe, 1978; Hippertt, 1998; Oliot et al., 2014); (2) reaction-controlled grain size reduction by growth of fine-grained metasomatic assemblages (White and Knipe, 1978; Kilian et al., 2011); (3) switch of the dominant deformation mechanisms from solid state power-law rheology to fluid facilitated Newtonian flow (Menegon et al., 2008; Wintsch and Yi, 2002; Brander et al., 2012); and (4) hydrolytic weakening in minerals deforming by crystal-plastic mechanisms (Tullis and Yund, 1980; Karato et al., 1986). Fluid-flow mechanisms in structural features within a shear zone have been extensively documented (Marquer 1989; Ferry and Gerdes 1998; Streit and Cox; 1998). A relationship

hasbeen noted between fluid–rock interaction processes and pervasive alteration of granitic rocks resulting in transport by diffusion (Cesare 1994; Watson & Wark 1997; Vidal & Durin 1999; Widmer & Thompson, 2001). Otherwise, the decrease in grain size through fracturing during cataclastic deformation, under certain metamorphic conditions, below 350°C and shadow pressure release Si, and reactions mostly responsible for that are: (1) breakdown of plagioclase to albite (2) formation of chlorite ± epidote and phengitic (Tullis and Yund, 1980; Evans, 1990; Fitz gerald and Stunitz, 1993; Kamineni et al., 1993; Suh and Dada, 1997). If it is attested that diffusional transport by fluids saturated in Si leads to the formation of small quartz vein, very large quartz vein formation mostly obey to different mechanisms. According to Bons (2001) and Lemarchand et al., (2012), a huge amount of quartz to be deposited in the same site requires conditions including pathways created by mobile hydrofracturing, very rapid ascent fluids flow bearing quartz and a pre-existing fracture or an anisotropy in the host rock.

III.2 Fault rocks

Several authors have suggested a definition for fault rocks (e.g. Sibson, 1977; White, 1982; Wise et al., 1984; Chester et al., 1985; Schmid and Handy, 1991). Fault rocks are mainly subdivided into ductile and brittle fault rocks according to the depth of formation within the crust (Fig. 7A).

1- Ductile fault rocks are represented by mylonites. They occur in high-strain zones known as mylonite zones, interpreted as exhumed, ‘fossil’ ductile shear zones (Passchier and Trouw, 2005). A mylonite is defined as a foliated and usually lineated rock that shows evidence of strong ductile deformation and normally contains fabric elements with monoclinic shape symmetry (Bell and Etheridge, 1973; Tullis et al., 1982; Hanmer and Passchier, 1991). Mylonites are classified according to the percentage of matrix and clasts in the rock. Matrix is considered to be clast less than 0.1mm (Sibson, 1977; Woodcock and Mort, 2008). This classification distinguishes three types of mylonites (Fig. 7B): (a) protomylonite (0-50% matrix), (b) mylonite (50-90% matrix) and (c) ultramylonite (90-100% matrix).

2- Brittle fault rocks (cataclasites, breccias, fault-gouge and pseudotachylites) are classified from low to high grade or from fast to slow strain rates. Brittle fault rocks are mostly represented by fault cataclasites and fault breccias which are difficult to distinguish at outcrop scale. Woodcock and Mort (2008) used clast size as the primary criterion for designating fault breccias. At least 30 % of the rock volume must be ‘large’ clasts, those defined here as greater than 2 mm in diameter. Therefore, three types of breccias are

definedaccording to the percentage of large clasts (>2mm) present (Fig 7C): crackle breccias (> 75% of large clast content); mosaic breccias (60-75% large clast content) and chaotic breccias (30-60% large clasts present). Cataclasites are cohesive and non-foliated rocks with less than 30% of clast greater than 2 mm in diameter.

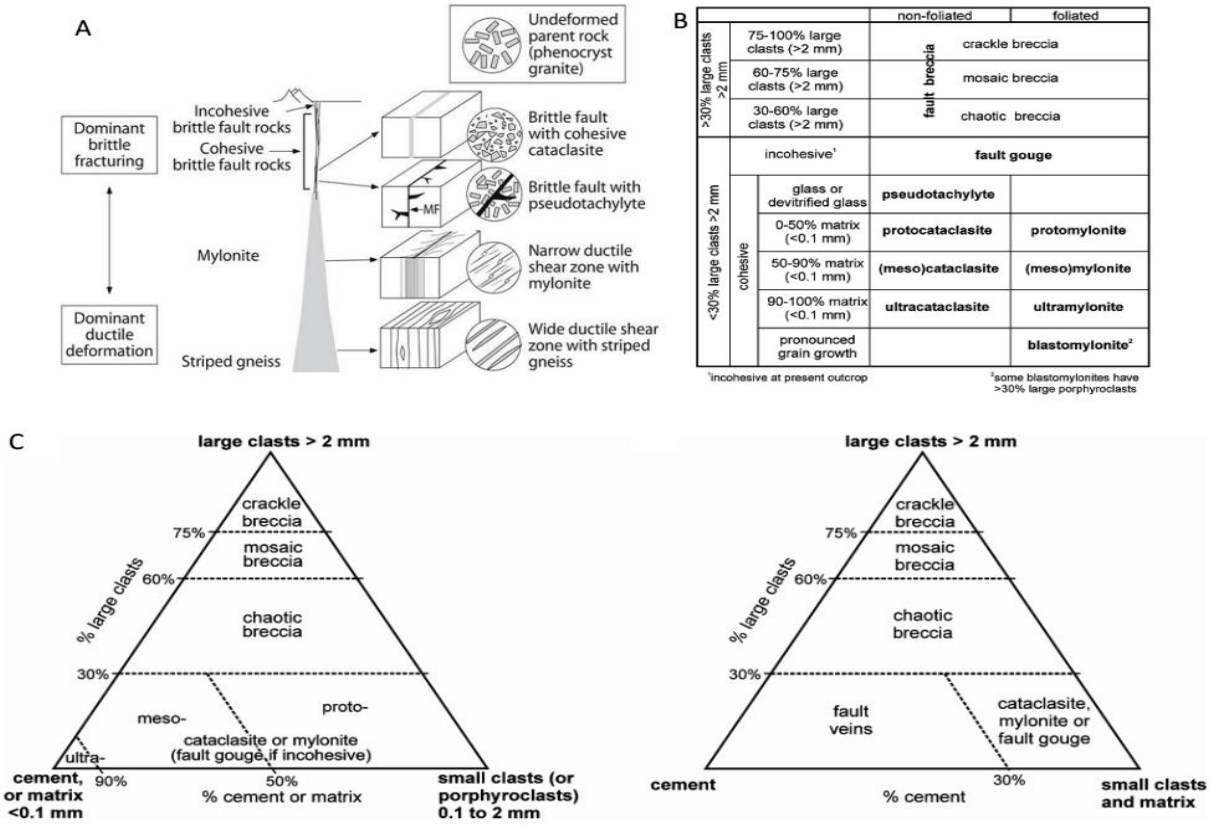

Figure 7: Classification of fault rock : A) Distribution of the main types of fault rocks with depth in the crust (Passchier and Trouw, 2005) : B) A revised classification of fault rocks and C) Ternary diagrams showing the two alternative graphical displays of the proposed fault rock classification. (B and C are after Woodcock et Mort, 2008).

III.3 Overview of High Purity Quartz (HPQ)

III.3.1 Impurities in quartz

High purity quartz has become one of today's key strategic minerals with applications in high-tech industries that include semiconductors, high temperature lamp tubing, telecommunications and optics, microelectronics, and solar silicon applications (Blankenburg et al., 1994; Haus, 2005 and 2010; Moore, 2005; Dal et al., 2011;Gao et al., 2011; Kodama et al., 2010).High-purity quartz (HPQ) defined as quartz with < 50 µg/g content of contaminating substances (Muller et al., 2010), is essentially pure quartz with very low levels of impurities and pigmenting agents.The maximum content of each element should be: Al <30µg/g, Ti < 10µg/g, Na <8µg/g, K < 8µg/g, Li < 5µg/g, Ca < 5µg/g, Fe < 3µg/g, P < 2µg/g

and B < 1µg/g whereby the sum of all elements should not exceed 50µg/g (Muller et al., 2012; Santos et al., 2015). The quality of HPQ products is a function of the impurities within quartz crystals (intracrystalline impurities), because they cannot be removed by conventional processing. These impurities include:

a) Lattice-bound trace elements which either substitute for Si^{4+} (Al^{3+}, Fe^{3+}, B^{3+}, Ti^{4+}, Ge^{4+}, P^{5+}) or occur at interstitial channel positions (Li^{+}, K^{+}, Na^{+}, H^{+}, Fe^{2+}). Thomas (2008) and Müller & Koch-Müller (2009), suggested that B^{3+} may substitute for Si^{4+} (Fig. 8). The determinations of the $(Al^{3+} + Fe^{3+} + B^{3+})/(P^{5+} + H^{+} + Li^{+} + Na^{+} + K^{+})$ ratio in natural quartzhas shown that electron defects have only a minor or no contribution to the charge balance (Müller and Koch-Müller, 2009). The equation is important for the determination of the chemical quality of quartz.

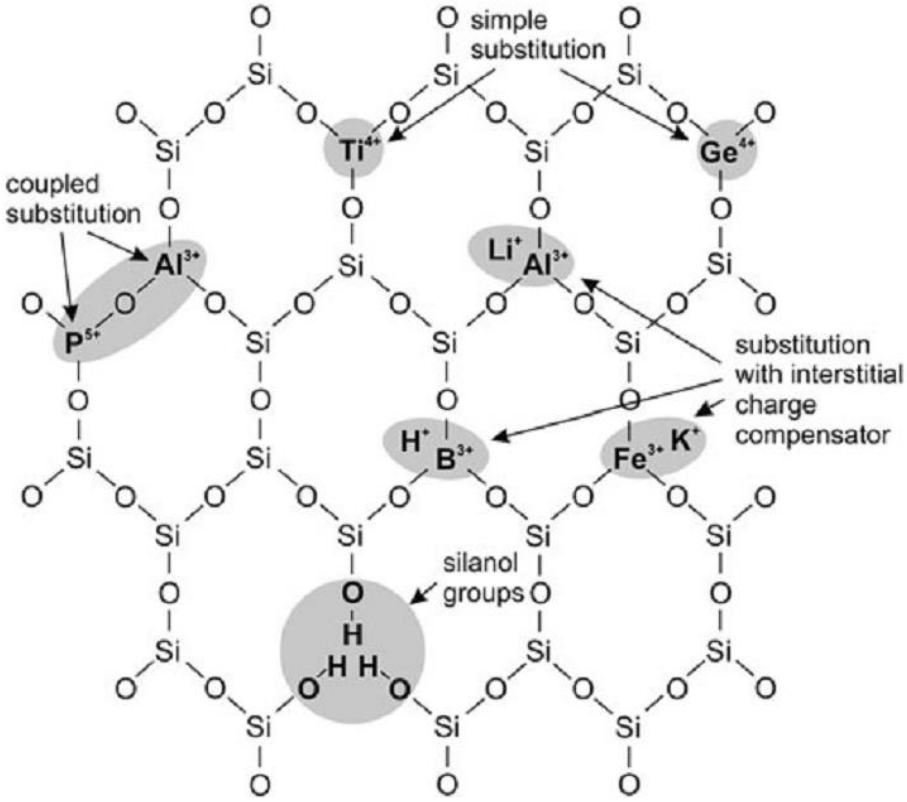

Figure 8: Schematic quartz structure showing the configuration of trace elements in the quartz lattice (from Götze, 2009).

McLaren et al. (1983) proposed the substitution of Si^{4+} by four H^{+} is possible (silanol groups). Because of the two-dimensional illustration the fourth H^{+} is not shown on the figure (Müller, 2012).

Aluminium is the most common trace element in natural quartz, in concentrations of up to several thousand lg g-1 and can thus be more easily determined by analytical methods than the other elements. If high Al concentrations are detected then concentrations of Li, K,

Na and H will be high as well and possibly also the concentrations of B and P. The Al concentration in quartz is thus an important quality indicator. A number of additional elements with concentrations < 0.01 lg g-1 have been detected in natural quartz (e.g. Gerler, 1990; Blankenburg et al., 1994; Monecke et al., 2002). Hydrogen is the only common trace element which is not listed because limited data exist (Fig.9).

b) Submicron inclusions <1 μm. They include so far rutile, ilmenite, mica, tourmaline and Al–Si phases which could represent Al_2SiO_5 polymorphs, AlOOH phases, or corundum (Zolensky et al., 1988; Seifert et al., 2011; Muller et al., 2012). The size, the chemical composition and the spatial distribution of inclusions and localization of isomorphic substitutional elements (e.g. Al, Ti) in the quartz crystal lattice determined the quality of the quartz raw material.

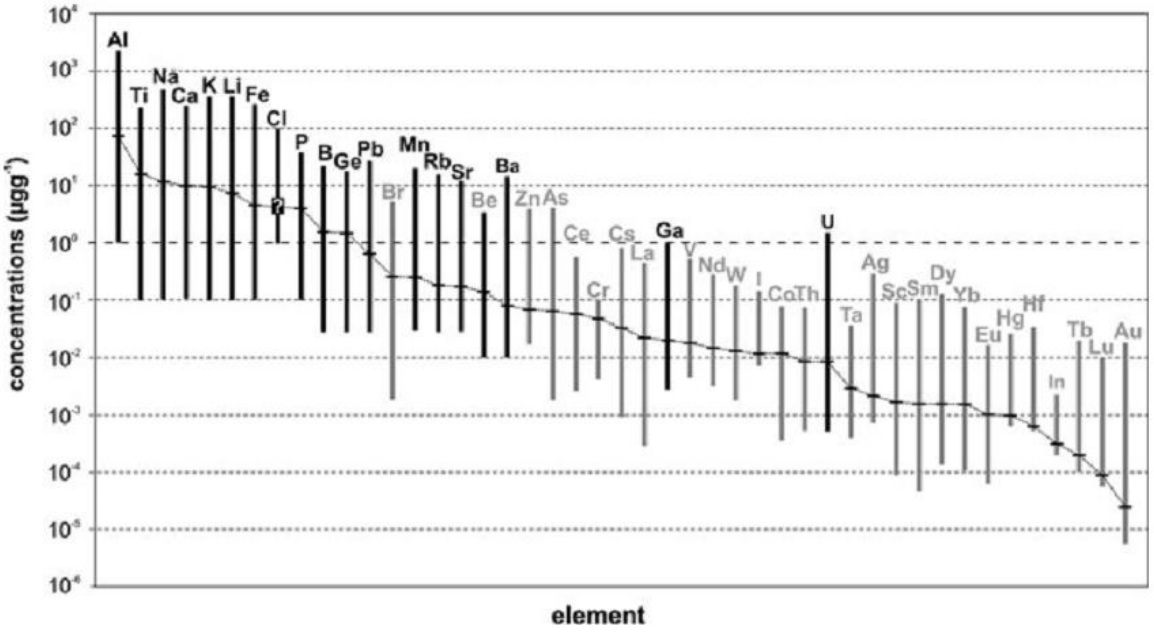

Figure 9: Average abundance and variations of trace elements in natural quartz. Data shown in grey are from Gerler, (1990); Blankenburg et al. (1994) and Götze. (2009). Data shown in black represent 2117 LA-ICP MS analyses of quartz carried out at Novegian Geological Survey (NGU) over the last 6 years. Concentrations of Cl are uncertain due to the very high detection limit of about 100 lg g-1. Cl is presented because Gerler, (1990); Blankenburg et al., (1994) and Götze, (2009) suggested that it occurs in considerable amounts in quartz.

c) Fluid micro inclusions (>1 μm). Fluid inclusions are formed during the primary crystallization of quartz from cooling rock forming fluids and also as a result of secondary (re)-crystallisation processes related to tectonic events (Roedder, 1984). They can be classified based on descriptive parameters like size, shape, color, refractive index, their origin (primary, secondary) and the number of physical phases (liquid (L), vapor (V), solid (S))

present within the inclusion (Van den Kerkhof and Hein, 2001). Liquid inclusions are commonly brines with elevated concentrations of alkalis which need to be removed to meet the chemical specification of the glass. The common types of fluid inclusions are: i) Water containing, biphasic inclusions liquid-gas rich liquid phase, negative crystal shape. ii) Coexistence rich inclusions in liquid and gas phase. iii) Fluid inclusions that define growth zones in peculiar quartz. iv) Decadent – broken inclusions in milk colored solid quartz, (Kilias et al., 2004; Santos et al., 2014). The disposition (oriented or scattered) of fluid inclusions is especially important since they may be aligned along tracks that will open during comminution or, if randomly scattered within the quartz crystals, their liberation by mechanical and physical processes will be prohibitively much more difficult. The chemical composition defines the impurity level when element concentrations enriched in the fluid inclusions are forced in the silica glass during the melting process. Fluid inclusions may form bubbles making the silica glass less valuable. Since silica glass melt is highly viscous, smaller bubbles are not able to rise to the surface of the melt and so survive to unacceptably impair the quality of the silica glass.

III.3.2 Commercial qualities of quartz

The commercial definition of quartz qualities, including high-, ultra- and hyper-qualities (Harben, 2002), is certainly the most widely used commercial qualities of synthetic and natural quartz (Fig. 10). This classification is based on qualities of processed quartz products available in the market. For the classification of high- and ultra-high qualities Harben utilized as a model the trace-element concentrations of the IOTA quartz products from Unimin (Jung, 1992; IOTA, 2011).According to Harben, high purity quartz concentrates are designated to contain less than 50 μg g-1 of contaminating trace elements. High-purity quartz is defined containing 8–50 μg g-1 impurities (see grey shaded field in Fig. 10). The lower limit of 8 μg g-1 is represented by the quartz product IOTA 8 which is the purest quartz product on the market produced from natural quartz.

III.3.3 Market demand of HPQ

Demand for HPQ is increasing strongly due to the rapid development and expansion of the HPQ consuming industry (Fig. 11a and b).The global outlook for high purity quartz-using industries is still positive with annual growth rates between 3 and 5% (Reiner et al., 2012). Certain applications as in the semiconductor industry are expected to growth at the level of 7% a year, while in the solar industry all signs point to further growth > 100% a year. Figure 12 shows a range of Global HPQ consumption structure by industries.

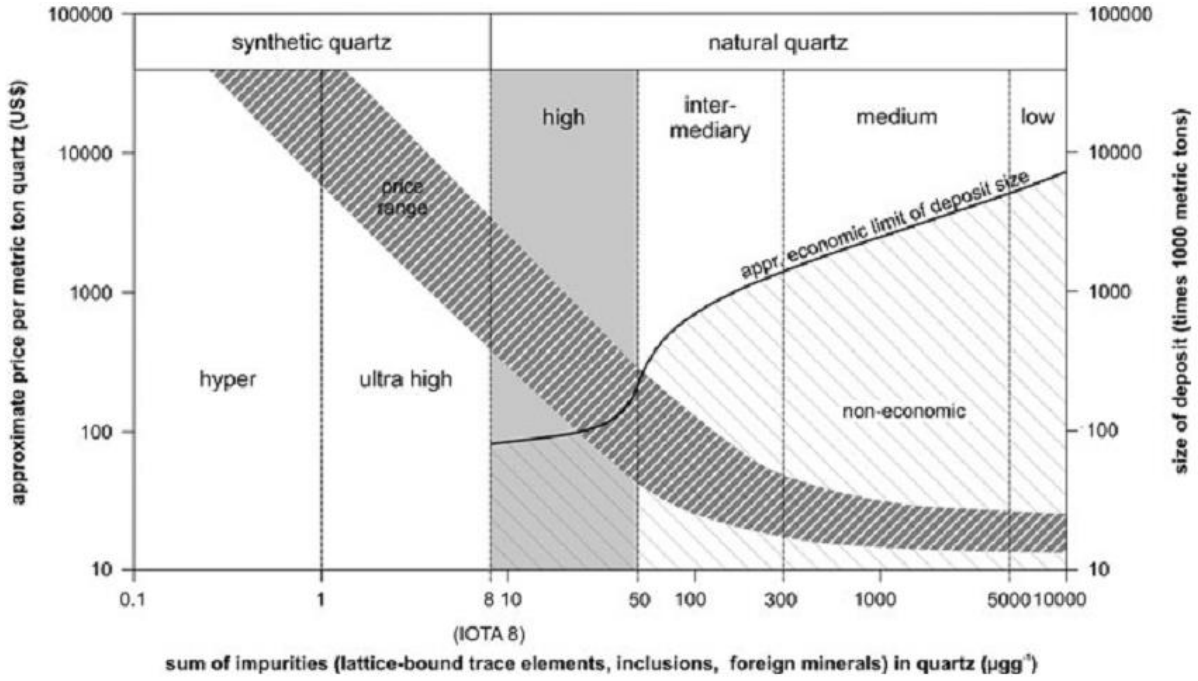

Figure 10: Classification of chemical quartz qualities (hyper to low) and their approximate price range according to Harben (2002). The lower limit of 8 lg g-1 is represented by the quartz product IOTA 8 which is the puriest quartz product on the market produced from natural quartz (IOTA, 2011). The approximate economic limit of the deposit size bases on data of active quartz mines.

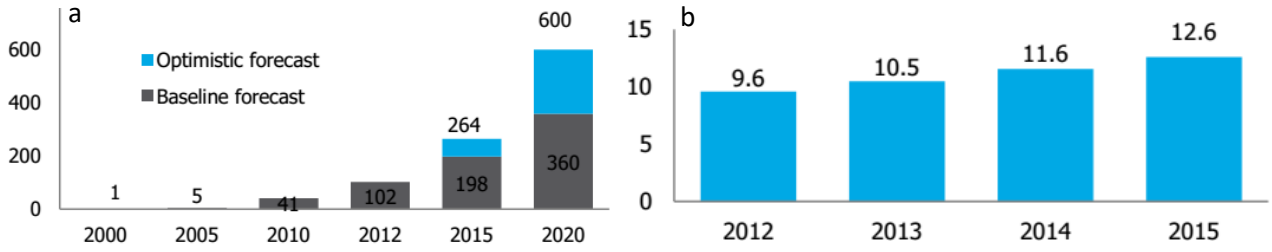

Figure 11: HPQ consuming industry: (a)-world solar energy installed (giga watt) (b) - Global electronic industry (http/www.serbia.mfa.gov.by).

III.3.4 Security and HPQ deposits around the world

To guarantee industries supply of quartz raw material necessitates the identification and characterization of new HPQ deposits all over the world. Expertise in geology, chemical analysis, and mineral processing is required to develop the full potential of a quartz deposit. Geological environments of world known HPQ deposit are manifold and the existing deposits of quartz raw material are related to magmatic and metamorphic events, hydrothermal activity or sedimentary processes (Table 1).

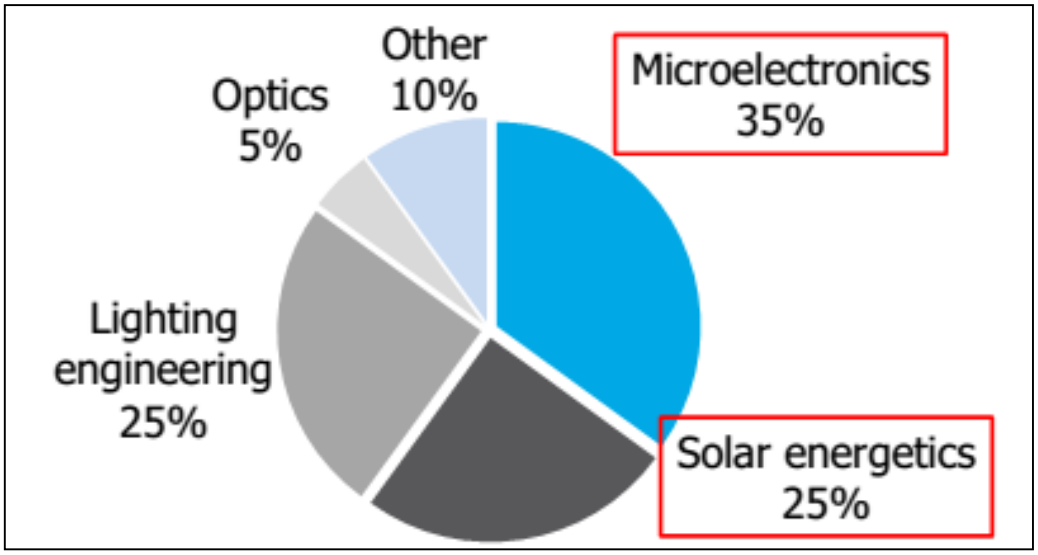

Figure 12: Global HPQ consumption structure (www.serbia.mfa.gov.by).

III.3.5 Guarantee HPQ quality

The HPQ materials are controlled by a range of laboratory techniques providing analytical support related to quality control. Analytical capabilities include wet chemistry, microwave digestion, atomic absorption, computer driven ICP and flame photometry. The laboratory also performs complete sample preparation including crushing, grinding and magnetic separation and can simulate all plant beneficiation methods.

Unimin Corporation is the world's leading high purity quartz producer (Fig. 13). They are fully integrated to ensure complete control over the quality and integrity of IOTA products from the mine to the customer from two unique ore bodies that produce a complete portfolio of quartz grades and custom products.

III.3.6 Mineral commodities in Cameroon

Substantial deposits of gold, diamond, bauxite, cobalt, iron ore, nickel, cassiterite, uranium, rutile, and nepheline have been found in many sites in Cameroon. A summary of the most important deposits of HPQ and their resource estimates are shown in Table 2. HPQ constitutes a new area that is still to be explored in Cameroon. This study brings for the first time the reflexion on the potential deposit of HPQ in the South-West Region of Cameroon.

Table 1: Some main deposits of high purity quartz over the world (magmatic, metamorphic, tectonic and sedimentary geologic context).

Deposit type	Geological environment	Location	Country	References
Kyanite quartzite	granitic gneisses of the Solør Complex	Solør, Surnadalen, Nasafjell and Skjomen	Norway	Muller et al., 2012
Kyanite quartzite	Green schist to amphibolites grade metamorphism	Forland	Norway	Muller et al., 2007
Hydrothermal quartz vein	Ductile shear zone	Nesodden	Norway	Muller et al., 2012
Pegmatite, quartz veins	Magmatic	Nedre Øyvollen	Norway	Muller et al., 2012
Pegmatitic quartz veins	Shear zone	Sierra de Comechigones	Argentina	Morteani et al., 2012
Quartz sand	Sedimentary (marine environment)	Santa Maria Eterna	Brasil	Santos et al., 2015
Quartz vein	Green schist grade metamorphism	Sierra de Santa Helena	Brasil	Santos et al., 2014
Quartz vein	desert area	Oum Agueneina	Mauritania	Feytis, 2010
pegmatite	Quartz vein	Spruce Pine	USA	SINOSI Group, (2013)
Pegmatite	Granitic pluton (Granodiorite)	Marwit Rod El Leqah	Egypt	Ibrahim et al., 2015
hydrothermal quartz vein	Sedimentary quartzite	farm Alt Seeis 133	Namibia	Carr, 1983
Quartz sand	Sedimetary	Far North Queensland	Australia	SSRG, 2019

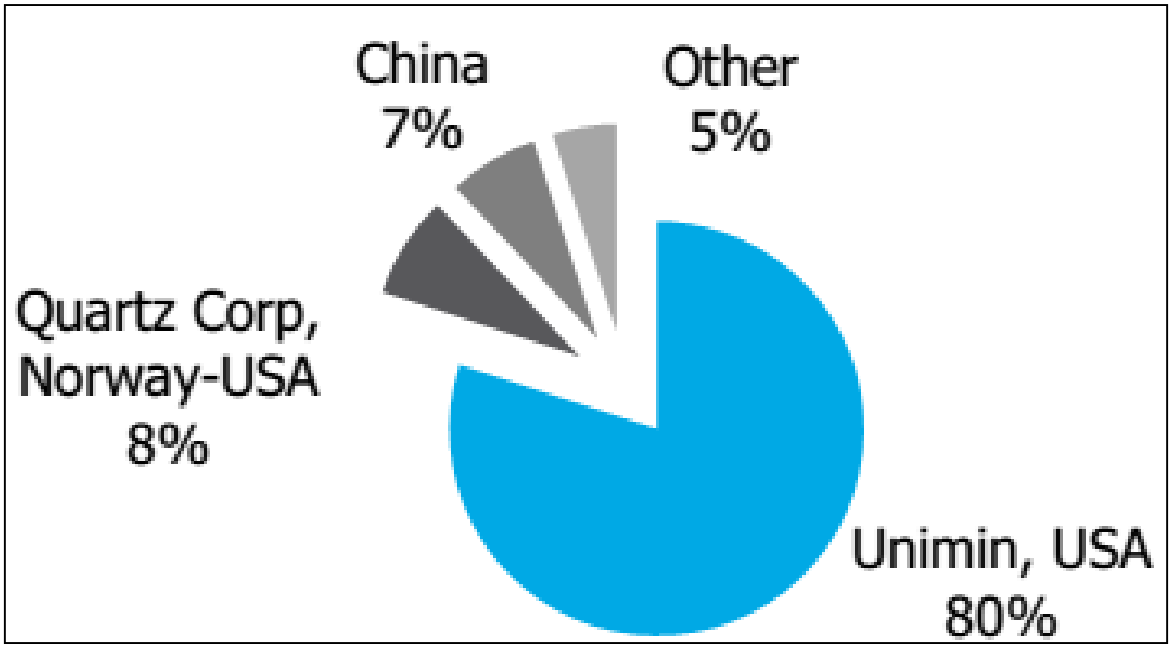

Figure 13: HPQ market (http/www.serbia.mfa.gov.by).

Table 2: Minerals commodity in Cameroon

Mineral commodity	locations	Reserve estimate	Deposit type	references

Diamond	Mobilong	3.78 billion carat	Conglomerate and alluvium	Gentry (2009)
Bauxite	Minim-Martap, Ngaoundal& Fongo Tongo	3 Gt	Paleogene to Quaternary volcanics	Milisi et al., (2006) Gentry (2009)
Co-Ni-Mn	Nkamouna, Mada, Kondong, Messea, North Mang, Rapodjombo and South Mang.	225 Mt (0.24% Co, 1.22% Mn, 0.72% Ni).	Laterite deposit hosted by Neoproterozoic (?) mafic-ultramafic magma complex.	Milési et al., (2006), Newman (2008), Gentry (2009).
Iron ore	Mbalam, Kribi and Nkout	Mbalam >800 Mt. (35–60 % Fe) Kribi ~330 Mt. (30 % Fe) Nkout (not defined).	Archaean-Palaeoproterozoic (?) BIF in greenstone belts.	Newman (2008), Ngako (2007), Milési et al.,(2006), African Aura Mining (2009), Gentry (2009).
Uranium	Kitongo, Lolodorf, Teubang, and Bantadje.	Kitongo=13,125 t. Lolodorf=1,200 t. Teubang (not defined). Bantadje=~10,000 t.	Mid-Proterozoic vein-related granite-metasediment contact, conglomerate and sandstone, microdiorite.	Newman, (2008), African Aura Mining (2009), Mega Uranium (2009).
Rutile	Eboundja Akonolinga	800 Mt. 3Mt 1% rutile	Quaternary alluvium reworked from Neoproterozoic nepheline-bearing-syenite.	Milési et al., (2006), Ngako (2007).
Tin	Mayo Darle	17 targets with one world class deposit.	Granitoids	Gentry (2009)
Wolframite	Goutchoumi	ca. 4,500 t.	Fault-related orogenic Neoproterozoic granite.	(Milési et al., 2006).
Gold	East Cameroon gold field	About 150 target areas		Department of Mines, MINIMIDT, (2013)
HPQ	Southwestern Cameroon	Km^3	Hydrothermal quartz vein	Sigue et al., 2019

IV Fluid inclusions and impact on HPQ quality

IV.1 Introduction

The growth of minerals from a fluid phase is considered to be one of the most important factors in the genesis of certain mineral deposits. Thus, it is common that when a crystal grows, it traps small amounts of the fluid phase with its soluble salts and its volatile phase. The relics of this fluid are called fluid inclusions. These are defined as microcavities trapped between the crystalline meshes of rock minerals and contain one or more solids. In other words, fluid inclusions are inclusions in minerals that are filled with fluids (gas and liquid), and sometimes with one or more solid phases. These micro-volume fluids are present throughout the history of the rock. The majority of fluid inclusions consist essentially of H_2O,

CO_2 and to a lesser extent NaCl, CH_4, and N_2 (Roedder, 1984; Shepherd et al., 1985; Bodnar, 1994; Andersen et al., 2001; Samson et al., 2003). Meanwhile, fluid inclusions are very useful in determining the physicochemical conditions that prevailed during the emplacement of the rock.

The main objective of the study of fluid inclusions in this work is to inform, in a qualitative and quantitative way, the global composition of the fluid trapped during the formation of quartz minerals.

IV.2 Classification of Fluid Inclusions

Goldstein (2003) defines a nomenclature of fluid inclusions based on their primary, secondary and pseudo-secondary inclusion trapping chronology. Indeed, the primary inclusions are contemporaneous with the crystallization of the host mineral, in our case that of quartz, their studies tell us about the physico-chemical conditions of rock formation. While secondary inclusions most often correspond to plans cementing old microfractures affecting the host mineral. They result from the circulation of fluids after the crystallization of minerals. As a result, they cut the grain boundaries. As for the pseudo-secondary inclusions, they are in the form of planes during crystallization of the host. In other words, these inclusions are formed during crystal fracturing episodes between episodes of crystal growth; the study of fluid inclusions, provide us with information on the P-T-X (pressure-temperature-composition) conditions that prevailed during the formation of the rock. Several terminologies are frequently used in the study of fluid inclusions, some important ones are shown in table 3.

IV.3Descriptive classification of fluid inclusions

Fluid inclusions can be described by visual parameters like size, shape, color, refractive index and particularly by the phases present at room temperature. The fluid inclusions may be somewhat captious since at room temperature and three phases can be present namely liquid phase (L) , gas or vapour phase (V) and eventually together with one or more solid phases (S), which may be accidentally trapped or formed as a daughter phase during cooling. The number and type of phases present at roomtemperatureis one of the most useful and widely applied criterion to describe fluid inclusions. The content of a fluid inclusion may be given by the phases and number of phases as a subscript. An inclusion containing liquid L, vapor V, and two salt crystals S_1 and S_2 can be typified as LVS_1S

Table 3 : Terminologies used in study of fluid inclusions

S/N	Terminology	Signification
1	Monophase Inclusions	The inclusions having a single phase at the room temperatures, *e.g.* liquid, gas
2	Two-phase Inclusions	The inclusions having two phases in the same inclusion at room temperature, *e.g.* liquid + gas; liquid + crystals
3	Polyphase Inclusions	The inclusions having more than two phases in the same inclusions at the room temperature; *e.g.* liquid + gas + crystals; liquid + vapor + solid(1)+solid(2)
4	Homogenous Inclusions	The inclusions composed of a single phase
5	Heterogenous Inclusions	The inclusions composed of multiple phases (more than one phase)

CHAPTER II

MATERIALS AND METHODS

I Presentation

Three field work campaigns, each three weeks long, were carried out in the study area. The modes of occurrence of rocks, the structural features, the alteration patterns of the various rocks' types were examined. Also, suitable samples were collected. Field work was subsequently followed by laboratory investigations.

II Field methods: Mapping and samples collection

The following material were mainly used during the field study:topographic map of the area,compass-clinometers (Sylva-type), Global Positioning system (GPS-Garmin), camera (SONY Cyber-Shot), hammers, hand lenses, markers, field note books, pens, pencils, measuring tape and sample bags**.**

Mapping was completed along transects running N-S, E-W, and NW-SE and NE-SW. The investigation of all outcrops, sub outcrops and some floats with emphasis on quartzitic rocks, and fault rocks in terms of their mode of occurrence, structural features, alteration patterns and various rock types was accomplished. To do this, identification, observation, measurement (length, wide, strike, dip, dip direction, trend, plunge, azimuth), photography, field description and field analysis were necessary. Representative samples were subsequently collected and the geographical coordinates of each location recorded.

III Laboratory methods

Representative rock samples collected were investigated in the laboratory following the steps presented below.

III.1 Petrographic studies

A set of 45 thin sections (20 for quartzite and quartz veins, 15 for mylonite, 6 for gneisses and 4 for granitoids) was prepared at the IRAD - Laboratory, Yaoundé. Representative samples for quartz, gneiss, and granitoids were polished down to ~ 30 µm thickness for thin sections. Mylonitic samples were cut perpendicular to the foliation (YZplane) and parallel to the stretching lineation (Xaxis). Each section has been polished down to ~ 30 µm thickness for thin sections.

Each quartz thin section was subsequently studied following the procedure outlined below:

i. Each quartz thin section was studied under the petrological microscope with focus on stages of quartz precipitation/recrystallization, microtectonics and alteration

ii. Polished chips of quartz were analysed by LA-ICP-MS along ‘rim to core to rim’ profiles, for trace element content.

iii. EDS analysis of spots on the quartz grains were also done.

III.2 Structural studies

Structural data obtained from the field were displayed as stereoplots, maps and other microtectonic structural interpretations made.

III.3 Whole rock chemical analyses (gneiss and granitoids) by ICP-MS

Major, trace and rare earth element concentrations of 05 gneiss samples and 08 granitoids samples were carried out by inductively coupled plasma mass spectrometry (ICP-MS) at Activation Laboratories Ltd. (Actlabs). Sample solutions were produced from ~ 30 mg of sample powder. Here, the powders were mixed with HF–HNO3–HCl in Teflon vials and placed on a hot plate at 150 °C for ~ 48 h. Subsequently the samples were dried down and taken back into solution using 3% HNO3 for final analysis. ICP-MS count rates were externally standardized by means of calibration curves based on the international standards (Actlabs). Reproducibility on replicate analyses and accuracy is of the order of 5% for all elements.

III. 4 Chemical analysis using inductively coupled plasma mass spectroscopy (ICP-MS) on quartz

Quartz samples of 0.1 g were dissolved using 0.5 mL of distilled HF in special vessels. The samples were then kept over a hot plate at 80°C for 1 hour in order to enhance the dissolution process. Afterwards, temperature was elevated to 110°C for evaporation. Subsequently, 0.5 mL of HF and 0.1 mL of HNO_3 were added and the system was kept closed for 24 hours. After this procedure, the samples were recovered using a nitric acid solution of 1% in mass. All solutions were prepared using ultra-pure water (18.2 MΩ.cm) obtained by Mili-Q system. All used acids were purified by sub-boiling. The vessels used were previously cleaned with a 5% nitric acid solution and washed with ultrapure water. All measurements were conducted by the ICP-MS technique using an X series II (Thermo) instrument, equipped with CCT

(collision cell technology) at the Analytical Geochemistry Laboratory, Institute of Geosciences, UNICAMP, Brazil(Santos et al., 2014).

III.4.1 Samples dilution

Samples were diluted gravimetrically to 10.0 g with ultrapure water. To all samples, 100 µL of a standard solution was added in order to compensate instrumental drift (In and Re concentrated at 200 µg/L).

III.4.2 Instrument optimization, measured isotopes and conditions

The instrument was adjusted according to the manufacturer instructions before each measurement. Isotopes 7Li, 9Be, 11B, 23Na, 25Mg, 39K, 43Ca, 85Rb, 88Sr, 89Y, 98Mo, 114Cd, 118Sn, 121Sb, 133Cs, 137Ba, 139La, 140Ce, 141Pr, 143Nd, 180Hf, 205Tl, 208Pb, 238U were measured using normal configuration. Isotopes 39K, 51V, 53Cr, 54Fe, 55Mn, 60Ni, 59Co, 63Cu were measured using CCT.

III.4.3 Instrument calibration

Calibration was done with multi-element solutions prepared gravimetrically from mono element standard solutions of 10 mg/L (High Purity Standards)

III.4.4 Quality control

Quality control was done by analyzing reference material BCS CRM 313 /1 (High Purity Silica) and details can be verified elsewhere (Santos *et al.*, 2014).

III.5 Chemical analysis using Laser ablation inductively coupled plasma mass spectroscopy (LA-ICP-MS) on quartz

Quartz composition was further evaluated using a New Wave Research Excimer Laser Ablation UP193FX and an Agilent 7500i quadrupole mass spectrometer. The laser had a pulse rate of 20 Hz, a speed of 15 µm·s^{-1}, a spot size of 50 µm and energy fluency of 5–7 mJ·cm−2 on the sample surface. Raster ablation was applied on an area of approximately 150 µm × 300 µm. The approximate depth of ablation was about 50 µm. The carrier gas for transport of the ablated material to the ICP-MS was He mixed with Ar. External calibration was performed using three silicate glass reference materials produced by the National

Institute of Standards and Technology, USA (NIST SRM 610, 612 and 614). In addition, the NIST SRM 1830 soda-lime float glass (0.1% *m*/*m* $Al2O_3$), the certified reference material BAM No.1 amorphous SiO_2 glass and the Qz-Tu synthetic pure quartz monocrystal were used. Measurements on commercially available IOTA HPQ material as well as reference material BSC CRM 313/1 (High Purity Quartz) were performed for further external calibration; reproducibility and accuracy.Each measurement comprised 15 scans of each isotope, with a measurement time varying from a 0.15 s/scan for K in high resolution to a 0.024 s/scan of, for example, Li in low resolution. A linear regression model, including several measurements of the different reference materials, was used to define the calibration curve for each element. For the calculation of P concentrations, the procedure of (Müller et al 2008) was applied. Ten sequential measurements on the Qz-Tu synthetic pure quartz monocrystal standard were used to estimate the limits of detection (LOD—3σ of 10 measurements). The analytical error ranges within 10% of the absolute concentration of the element.

III.6 Fluid inclusion observation using optical microscopy

For the fluid inclusion observation, a few quartz grains ranging in sized from 70 to 180 μm were placed on a microscope slide. In order to improve the observation of the grains, a film of kerosene was applied over them. Kerosene has a refractive index similar to that of the silica, which reduces undesired surface observations. A Nikon optical microscope operated at 500 x magnifications was used to acquire transmitted light photographs for fluid inclusion analysis, using a Nikon digital camera. All photographs were taken at room temperature. Using this methodology, it was possible to obtain insights on the nature of the fluid and mineral inclusions present in the grains. Although more complete analyses were not carried on, regarding homogenization temperature and other key properties of the inclusions, it was possible to obtain reliable data on mineral inclusions in the quartz grains. These data were vital in order to propose insights into the genesis of veins.

III.7 Fusion over silica plate

Samples were powdered using a silica mortar and sieved in nylon sieves at the Analytical Geochemistry Laboratory, UNICAMP, Brazil. Particle size distribution was selected between 80 and 200 mesh, i.e. 75 to 180 μm. The manufactured powders were then placed over a silica plate and an H_2/O_2 flame was applied over it using a premix torch. Flame conditions, burner distance to the sample and time of fusion were kept the same during all experiments, about 4 mm and 15 s respectively, although samples took different times until complete fusion. For bubble analysis, the silica plates were photographed using a mineralogical microscope. Photos of each fused plate were taken and then processed by computational analysis, in order to measure average bubble size and density on each photo. This is a common test conducted by several silica glass industries in order to evaluate the powder performance during glass making. Bubbles larger than 10 to 15 μm are highly undesired once they can affect the final glass' properties. This procedure is widely used in the literature (Santos et al., 2013; Santos et al., 2015: Griscom, 2006: Suzuki et al., 2012 and Santos et al., 2014)

III.8 Mineralogical quantitative analysis of quartz samples by SEM-EDS

Each quartz sample was crushed and panned in the laboratory. Grains were observed under a Scanning Electron Microscope (SEM) fitted with an Energy Dispersive Spectrometer (EDS) following procedures described by (Mărgărit et al., 2016). The EDS provided geochemical patterns reminiscent of the chemical composition of each phase identified.

CHAPTER III

RESULTS

I Petrogrphy

Etam area is constituted by magmatic (basalts and granitoids) and metamorphic (gneiss) rocks (Fig.14). Some of these rocks have undergone ductile or britle deformation during a tectonic event, giving rise to a shear zone and formation of fault rocks including mylonites and breccias. In this work, only host rocks (granitoids and gneiss) and fault rocks (Mylonites, quartz veins and quartzites) were studied.

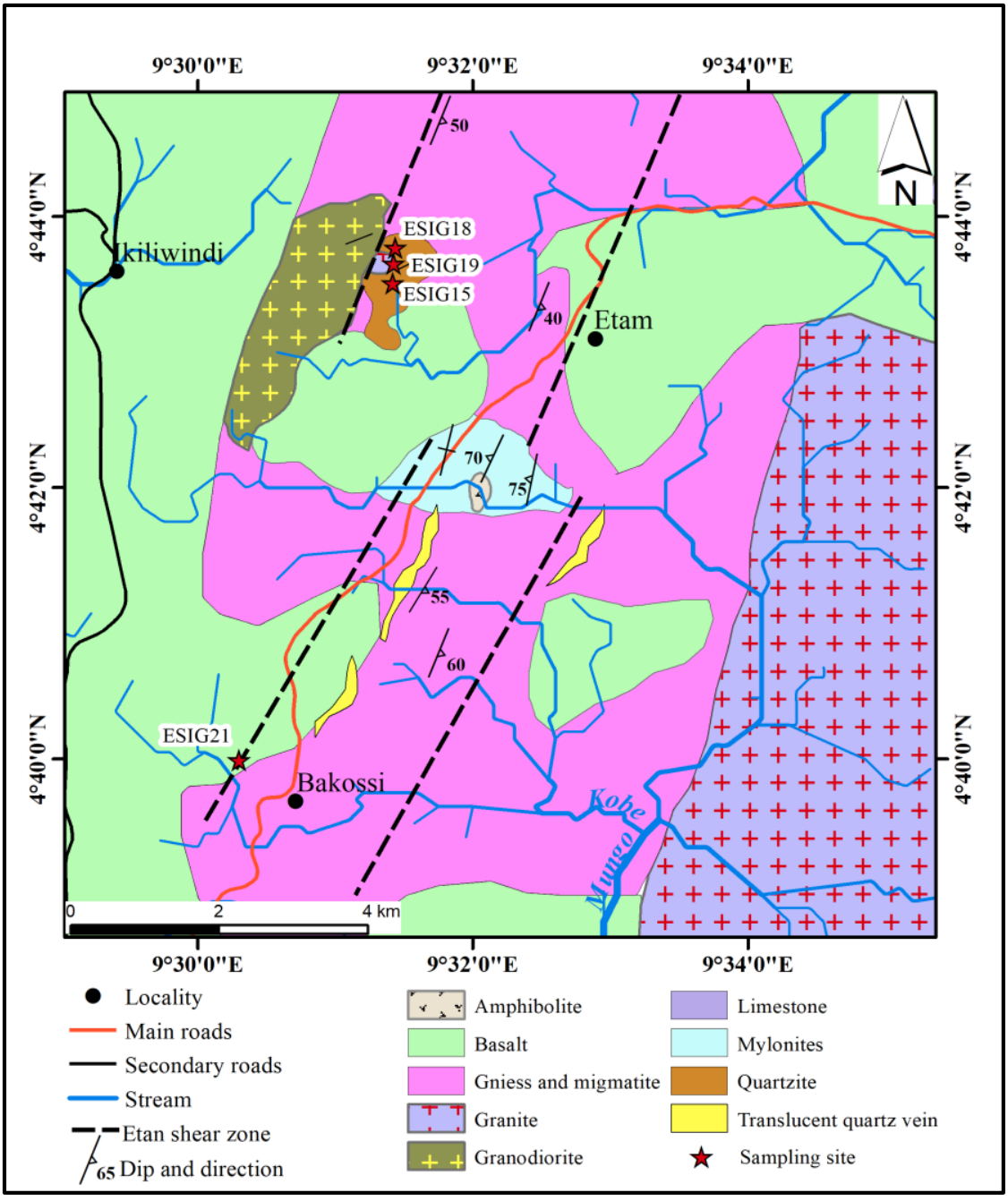

Figure 14: Geologic map of the study area

I.1 Magmatic rocks

The magmatic set comprises granodiorite, granites and basalts from Mount Cameroon recent eruptions.

I.1.1 Granodiorite

The granodiorite is a weakly deformed plutonic body. The pluton is elongated (4 km long and 1.8 km wide) and oriented N040E (Fig. 15a). The rock is massive despite the fact that it has undergone slight fracturing. It is dark-grey in color and coarse-grained (Fig.15b). Mineralogically, quartz, K-feldspar, plagioclase and biotite, referred in this study as Qtz_1, Kfs_1, Pl_1 and Bt_1, respectively define the magmatic constituents of the granodiorite. K-feldspar phenocrysts up to 10 cm can be observed without any visible preferred orientation. Quartz crystals of up to 2 cm fill the interstices and biotite flakes mark the discontinuous foliation planes. Accessory minerals include zircon and apatite.

The modal proportion estimated in thin sections using manually outlined optical microscope of these minerals is ~32% K-feldspar, ~30 % quartz, ~23% plagioclase, ~10% chlorite, ~2% biotite, and < 1% accessory minerals (apatite and zircon). Recrystalization produced ~2% of quartz (Qtz_2), alteration of Kfs_1 produced albite and chlorite ~1%.

- *Quartz:* Two types of quartz grains occur in this rock: the primary (igneous) quartz (Qtz_1) and the secondary (recrystallized) quartz (Qtz_2). Qtz_1 generally occurs as large grains (up to 2cm), subhedral and slightly elongated. In thin section, Qtz_1 commonly shows undulose extinction and the formation of a rim of subgrains (Fig. 15c). Large Qtz_1 grains are commonly strongly fractured and these fractures are filled by fine-grained Qtz_2 (Fig. 31d). Qtz_2 shows monocrystaline aggregates of quartz often equidimensional with milimetric dimensions. Qtz_2 is commonly observed surrounding large quartz grains and feldspar or filling microcracks (Fig. 15c). The total volume occupied by Qtz_2 in the granodiorite is about 2% and represents about 7% of the total volume of quartz present in the rock.
- *K-feldspar*: two categories are also observed: the primary K-feldspar (Kfs_1) and the recrystallized K-feldspar (Kfs_2). $Kfs_1$is randomly disposed. It occurs predominantly as mega (up to 10cm) euhedral or subhedral crystals showing several intragranular and/or transgranular pull apart microfractures, arranged often in sub-parallel or sub-perpendicular array and filled by fine equidimensional grains of Qtz_2 aggregates and Kfs_2 (Fig. 15d). Inclusions of euhedral plagioclase are common in the large K-feldspar clasts. Some large Kfs_1 are perthitic with albite lamellae covering about 30% of the area of the crystal (Fig.15e).

Around large Kfs_1 grains, alteration to albite is observed reminiscent of albitization. Kfs_2 is milimetric and encountered along microfractures.

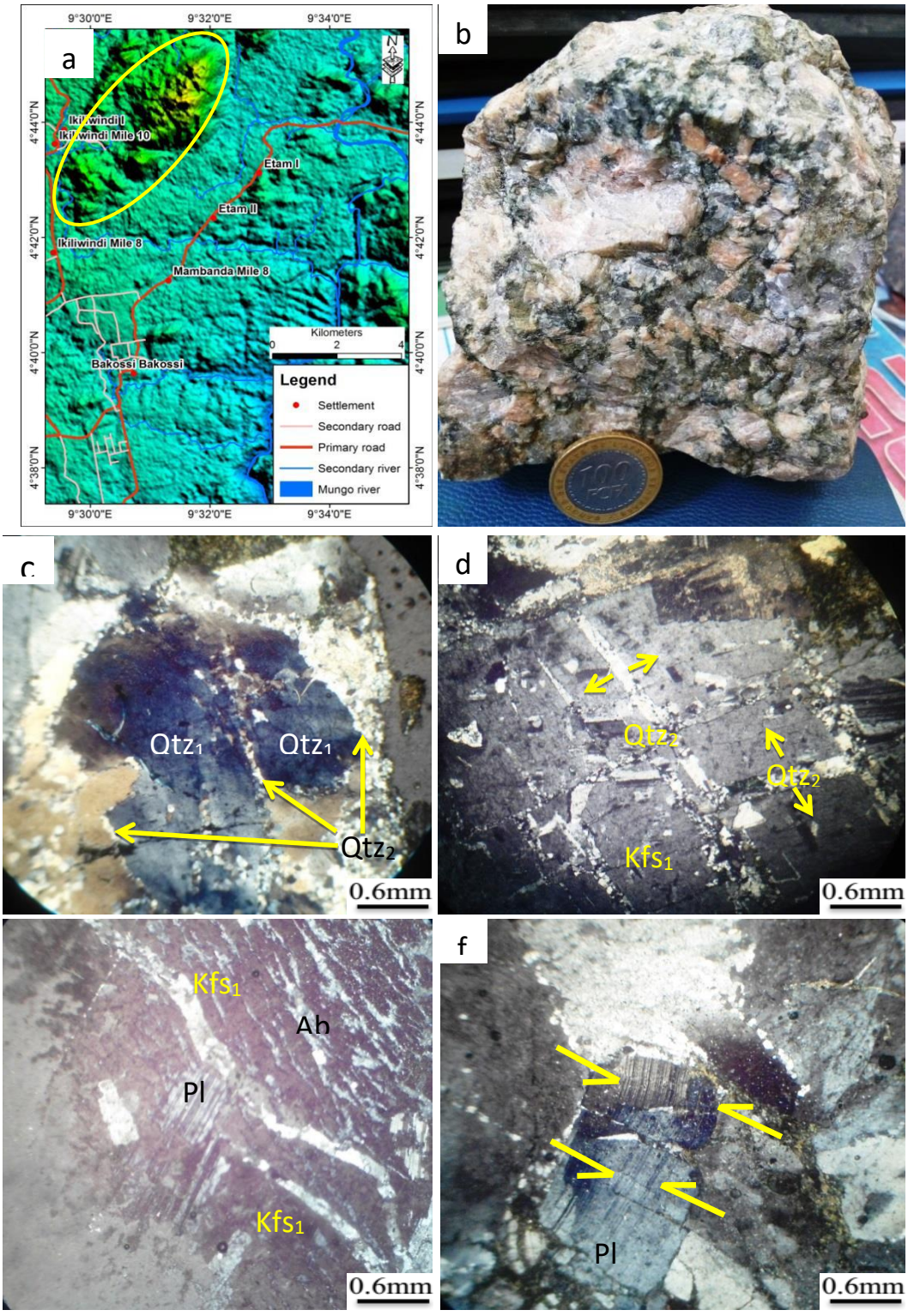

Figure 15: Photograph and photomicrograph of Etam granodiorite: a) Outcrop of granite, slightly elongated; b) Granodiorite sample showing coarse grain and elongated feldspar grains; c) Strongly recrystallized quartz (Qtz_2) surrounding Qtz_1; d) Kfs_1 showing several tensional micro-fractures filled by recrystallized equidimensional quartz aggregate; (e) Alteration of Kfs_1 to albite; f) Pl_1 showing bend or displacement cleavage plan.

Plagioclase presents similar characteristics as K-feldspar. In addition, Pl_1 is strongly chloritized along its boundaries and microfaults. Large crystals of Pl_1 have bent cleavages due to deformation and left lateral conjugate microfaults displacing the cleavages (Fig. 15f).

Biotite flakes have variable dimensions (0.1 to 0.6mm). It is observed commonly surrounding large quartz and K-feldspars. It shows alteration to chlorite at its margins.

Chlorite is up to 6mm in size, mostly developed at the expense of plagioclase and biotite.

I.1.2 Granites

Two types of granite namely fine-grained granite and biotite granite have been distinguished in the study area.

I.1.2.1 Fine-grained granite

The fine-grained granite is well exposed on the Mbossa river bed around Etam I area, where it is commonly associated with the migmatite gneiss. The rock is light in colour (Fig. 16a). Under the microscope, the rock is fine-grain with a granular texture (Fig. 16b) and composed essentially of K-feldspar (~40%), quartz (~40%), plagioclase (~12%) and biotite (~ 5%). Accessory (~3%) minerals include apatite. zircon and opaque.

Quartz is fine-grained (up to 1mm), subhedral to euhedral (Fig 32b). The grains are poly-crystalline aggregates.

K-feldspar is also fine- to medium-grained (up to 0.7cm) and commonly subeuhedral. Inclusions of apatite, biotite and zircon are present.

Plagioclase occurs as subeuhedral grains with variable dimensions (2mm x 8mm). The medium grains contain inclusions of quartz and plagioclase.

Biotite is interstitial or observed as inclusions in K-feldspar.

Apatite occurs as fine rectangular grains, mostly as inclusions in K-feldspar

Opaque minerals are rare. They are observed associated with biotite and K-feldspar.

I.1.2.2 Biotite granite

The biotite granite occurs as a large intrusion. The rock is dark-grey in colour and fine- to medium-grained (Fig. 16c). Under the microscope, the rock is slightly deformed and displays granular microstructure, made up of K-feldspar (~35%), plagioclase (~20%), quartz (~20%), biotite (~22%), apatite and opaque minerals.

Figure 16: Granite samples from Etam: a) Hand specimen of fine grained granite; (b) Photomicrograph showing equigranular microtexture in fine grained granite; c) Hand specimen of biotite granite; d) Photomicrograph showing microtexture aspect of biotite granite; e) Phenocrystal of plagioclase containig Qtz, Kfs as inclusion, f) Prefered orientation of biotite minerals in biotite granite.

Quartz is fine to medium grain slightly stretched (up to 1.5mm x 4mm), It occurs as subeuhedral or anhedral grain, small grains are interstitial occupied space between large quartz grains, k-feldspar and plagioclase (Fig.16d). Some crystals show undulose extinction.

Plagioclase presents medium to coarse grain (up to 3cm), elongated, also showing preferred orientation. Inclusions (Fig. 16e) of K-feldspars, plagioclase, quartz, apatite and biotite are common.

K-feldspar is stretched (up to 2.5cm) and shows prefered orientation. It occurs as medium sub to euheudral grain often showing undaluse extinction. Myrmekite are observed at the boundaries of some mineral. Inclusions of biotite and apatite are also commonly observed (Fig.16f).

Biotite is represented by reddish brown biotite. It occurs as small elongated flakes; generally with prefered orientation (Fig.16e).

Apatite presents fine rectangular grain as inclusion in feldspar, while opaques are associated with biotite mostly.

I.2 Metamorphic rocks

Metamorphic rocks described in this section are biotite gneiss, hosting quartzite or quartz Veins. They are widly spread in the study area (in Mabanda village, Bakossi and in the north of the study area). The rock is dark-grey to light-grey in color (Fig. 17a) with fine grains and presents granoblastic-heterogranular microstructure under microscope.

On the field the gneiss shows gneissose texture with centimetric dark bands, made up of biotite, amphibole, pyroxene and opaques mostly, in alternation with small (milimetric) light bands composed mostly of quartz and feldspar as minerals (Fig. 17b).

The rock is composed of quartz (~32%), K-feldspar (~30%), biotite (~20%), plagioclase (~10%), amphibole (~5%), zircon and opaques as accessory minerals.

- *Quartz* is anhedral with variable dimensions (0.1mm to 0.5mm). Some grains are stretched and display prefers orientation, mostly in the light bands. Some quartz grains are surrounded by biotite flakes in the dark bands. Undulatory extinction is often observed.
- *K-feldspar* displays sligthy stretched mineral with variable dimension (0.2mm to 0.7mm). The mineral is subhedral, commonly associated with hornblende and quartz. Myrmekite and undulose extinction are observed at the boundaries of some K-feldspar grains.
- *Plagioclase* occurs as sligthly elongated subhedral grains. Some crystals display myrmekite or inclusions of quartz, zircon and apatite.
- *Amphibole* is green horblende. The crystals are subhedral mantled by biotite and show Carlsbad twinning (Fig. 17c). Amphibole mineral fish is observed. Small grains are observed as inclusion in feldspar.

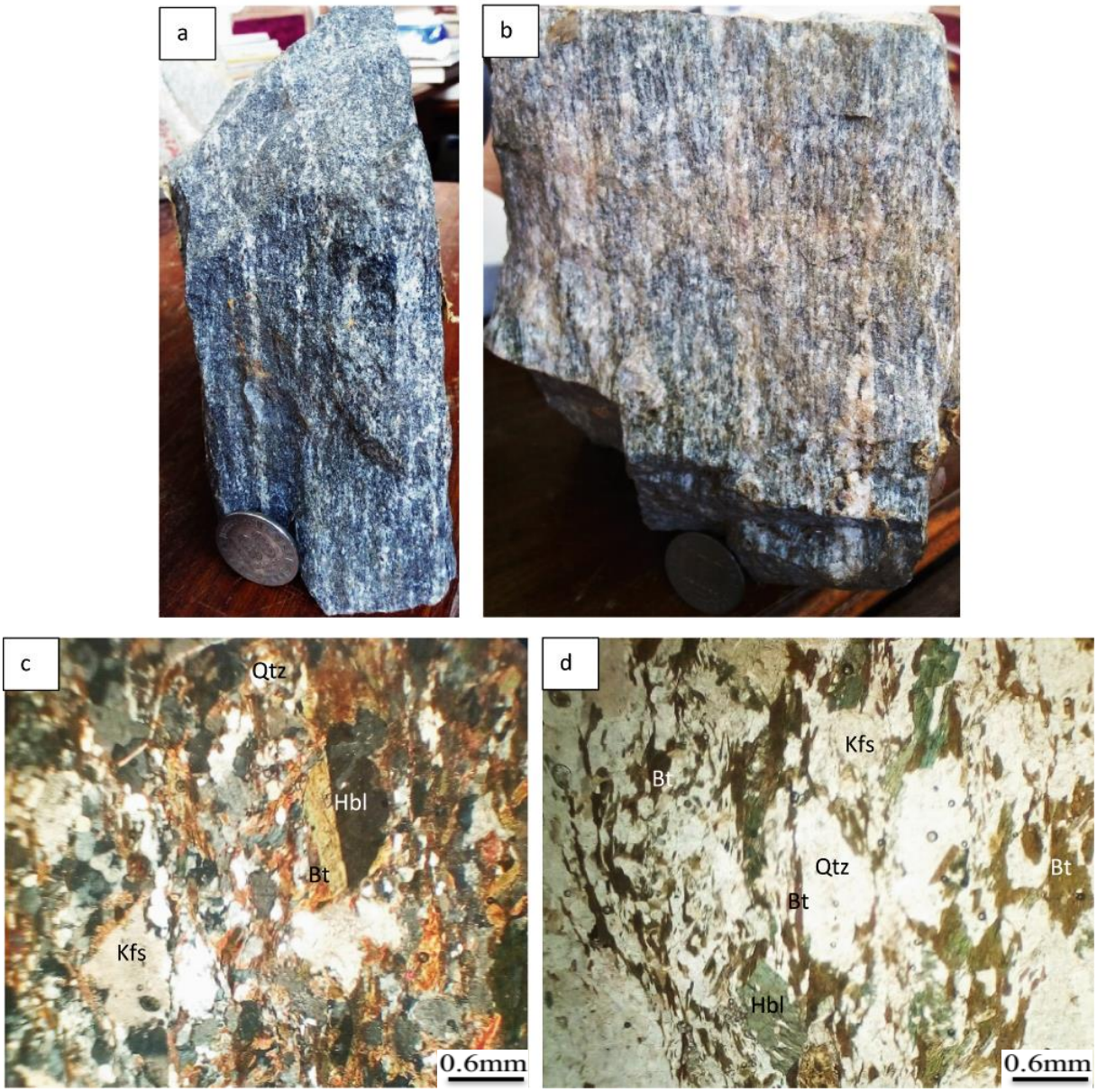

Figure 17: Photograph and photomicrograph of biotite gneiss sample from the study area: a) and b) Hand specimen c) photomicrograph showing granoblastic-heterogranular microstructure; d) Photomicrograph showing minerals prefer orientation note the amphibole fish.

Biotite is reddish brown and it shows elongated flakes up to 0.5cm in the dark bands. Biotite flakes are associated with amphibole and quartz and together they show a preferred orientation (Fig. 17d).

Zircon occurs as small euheudral crystals found as inclusion in biotite.

Opaque minerals display small crystals observed either in free form or as inclusions in other minerals.

I.3 Fault rocks

Structurally and mineralogically, two domains within the Etam shear zone have been distinguished: (1) a ductile zone where rock types include protomylonite, mylonites and ultramylonite and (2) a brittle zone showing quartzites mostly brecciated

I.3.1 Fault rocks in the ductile shear zone

This zone is represented by a mylonitic corridor. Within this zone, protomylonite, mylonite and ultramylonites are observed. The protolith of mylonitic rocks in Etam is granodioritic or gneiss. The limits between these zones are not clear due to the fact that the area is covered by volcanic rocks and vegetation. However, the variation in grain sizes and the gradual development of a continuous foliation, defined by preferred orientation of elongated lenses crystals and phyllosilicates indicates the transition between the various zones.

The terminology and classification of fault rocks used in this work are from Woodcock & Mort, 2008 (Fig.7b). Quartz, K-feldspar, plagioclase and biotite, referred in this study as Qtz_1, Kfs_1, Pl_1 and Bt_1 respectively define the magmatic constituents.

I.3.1.1 Protomylonites

Protomylonites are generally observed at the borders of the shear zone and they are mostly granodioritic mylonites. They are well exposed in Kobe River where they appear as blocks of rocks with variable dimensions (up to 10m large). Protomylonite in Etam shear zone (ESZ) are porphyroclastic, medium- to coarse-grained. The foliation is weak and is defined by preferred orientation of tabular to ellipsoidal feldspar porphyroclasts (fig. 18a).

The mineralogy of the protomylonites is mainly composed of quartz ~42%, K-feldspar ~28%, plagioclase ~15%, biotite, ~ 5%, epidote ~ 2%, muscovite ~1 % and zircon and apatite as accessories.

Quartz is represented by primary quartz (Qtz_1) and recrystallized quartz (Qtz_2). Qtz_1 shows slightly strectched porphyroclasts (up to 1.5 cm long) with lensoid shape. Intracrystalline deformation structures in clasts show undulose extinction, deformation lamellae and subgrains. Some clasts are rimmed by a layer composed by fine-grained aggregates of Qtz_2, Bt and recrystallized plagioclase (Pl_2) or show micro-fractures filled by Qtz_2.The secondary quartz (Qtz_2)is represented by polygonal or mosaic monocrystalline fine aggregate (~2µm), generated by bulging recrystallization (BLG). Qtz_2 is observed on the boundaries of larger clasts or filling micro-fractures and represent ~ 50% of the total volume of quartz in the protomylonite.

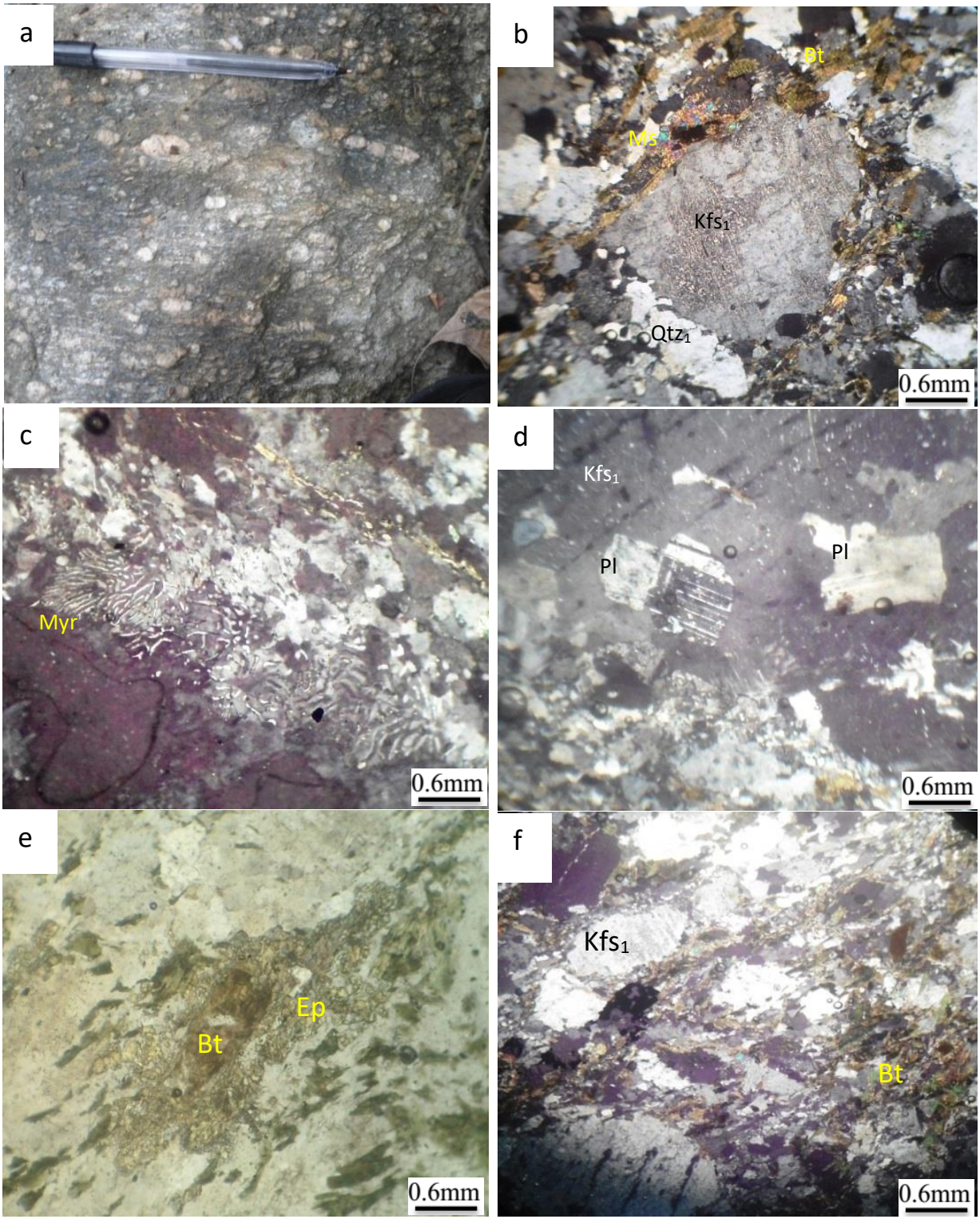

Figure 18: Photograph and photomicrographs of the ESZ protomylonite: (a) Outcrop of protomylonite, the feldspar clasts are slightly stretched and oriented. (b) Elongated feldspar and quartz with a rim of biotite and muscovite; (c) Myrmekite formation at feldspar clast boundaries; (d) plagioclase with bend cleavage due to sinistral shearing as inclusion in large Kfs_1 clast; (e) Alteration of large biotite to epidote; (f) Fine grained recrystallized green biotite surrounding feldspar clasts.

- *K-feldspar* displays large clasts (Kfs_1), up to 2.5cm (Fig. 18a). Kfs_1 is elongated and generally shows a shape preferred orientation following the mylonitic schistosity (Fig 18b). Micro-fractures filled by Qtz_2 are commonly observed and cut across the Kf_1 clasts.
- *Plagioclase* occurs as large clasts (2.5cm x 3cm) with myrmekitic microstructures (Fig 18c) commonly observed on their boundary. Some clasts show bent or kink cleavages due to sinistral shearing (Fig. 18d). Plagioclase is also observed as inclusion in Kfs_1.
- *Biotite* shows two types in the protomylonite, namely brown biotite and green biotite: (1) Brown biotite presents large flakes (0.7cm x 1.2cm). Alteration of biotite to epidote (Fig. 18e) is observed in some cases. (2) Green biotite occurs as small crystals (0, 1 cm x 0. 3cm) observed commonly on the boundary of Kfs_1, Qtz_1 and Pl_1(Fig. 17f).
- *Muscovite* derived from the intense alteration of brown biotite occurs as very fine grains (~8µm). It is also observed mostly surrounding Qtz_1 and Kfs_1 porphyroclasts. It is associated with biotite.
- *Zircon and apatite* occur in biotitet as inclusion.

I.3.1.2 Meso-mylonites

Meso-mylonites are granodioritic mylonites. They are medium-grained and display mylonitic texture, underlined by elongated feldspar and quartz clasts surrounded by biotite flakes and muscovite defining a continuous schistosity. S/C surfaces are well preserved (Fig 19a). The S-surfaces are defined by preferred orientation of elongated feldspar clasts, while C-surfaces show discrete shear bands that cross cut S-surfaces or displaced feldspar porphyroclasts.

The mineralogy of mylonites is generally composed of magmatic quartz $Qtz_1$and recrystallized quartz (Qtz_2 and Qtz_3) ~ 43 %, biotite ~22 %, K-feldspar ~10%, amphibole ~9%, plagioclase ~6%, muscovite 3%, calcite and zircon ~2%.

- *Quartz (Qtz_1)*presents stretched clasts due to an increase in deformation. Clasts are distinctly lensoid in shape with aspect ratio of 0.5-1.5. Qtz_1 is commonly fractured with recrystallized quartz aggregates filling the microfractures. Compared to protomylonite, the proportion of Qtz_1 decreases to ~25% of the total volume of quartz present in the rock. Under the microscope, Qtz_1 presents similar microstructures as in the protomylonite (undulose extinction, subgrains and deformation lamellae).

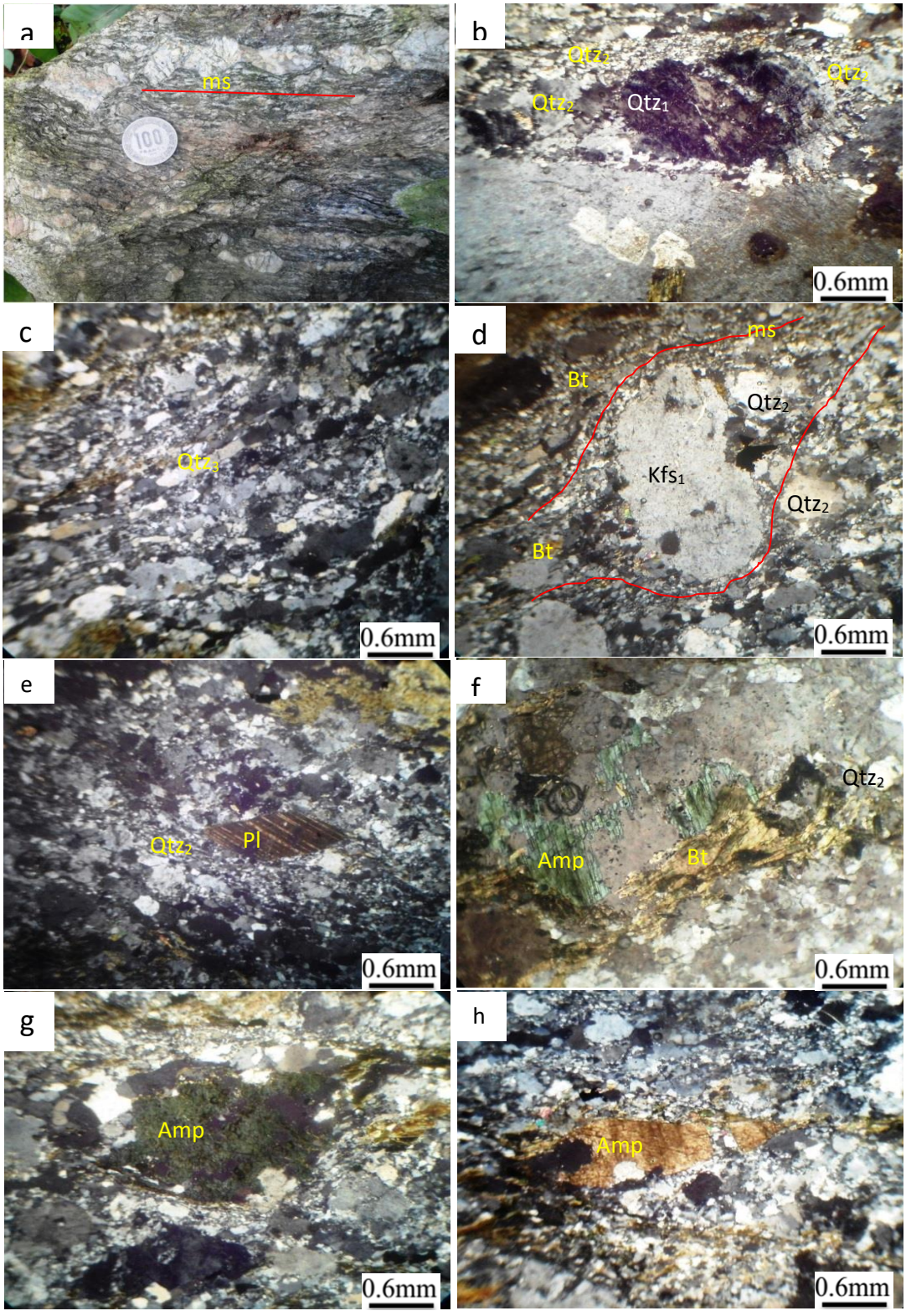

Figure 19: Photograph and photomicrographs of the ESZ mylonite: (a) Aspect of EZS mylonite, notice the boudinage and the sinistral shearing; (b) Quartz clast (Qtz_1) with formation of subgrain and recrystallized quartz (Qtz_2) rimming Qtz_1; (c) Dynamic recrystallization showing some singular strongly elongated quartz crystal; (d) rotated sub-euhedral Kfs_1 porphyroclast with cleavages oblique to mylonitic schistosity (e) Plagioclase fish lost in the quartz matrix; (f) Alteration of amphibole to biotite; (g) Amphibole fish; (h) Amphibole fish with pull apart structure

- *Quartz (Qtz_2)* is more abundant than in the protomylonite. It constitutes fine-grained (2µm) aggregate observed in thin layers rimming Qtz_1 large clasts (Fig. 19b) and amphibole clasts. Qtz_3 is produced by dynamic recrystallization. It shows quartz ribbons, made up of monomineralic fine-grained aggregates. Some Qtz_3 show strongly elongated single crystals (Fig. 19c) and define a strong crystal preferred orientation (CPO) similar to the porphyroclasts orientation.
- *K-feldspar* is elongated (aspect ratio 2-3.5) and commonly surrounded by quartz aggregates, fine-grained biotite and muscovite. Rotated sub-euhedral porphyroclasts with cleavages oblique to the mylonitic schistosity are observed (Fig. 19d). Porphyroclasts present common 'flame' perthite at their boundaries.
- *Plagioclase* displays some isolated mineral fish in a recrystallized quartz matrix with well-preserved polysynthetic twins (Fig. 19e). It is also observed as inclusion within the large K-feldspar. Intra granular micro-fractures are commonly observed.
- *Amphibole* shows large shreds due to deformation. It is mostly green hornblende, strongly altered to biotite at its boundary (Fig. 19f). Amphibole fish are rimmed by layers of recrystallized quartz aggregate (Fig. 19g), Often quartz layers made up of elongated quartz grains (Qtz_3), in alternation with layers composed of fine polygonal quartz aggregates (Qtz_2). Some mineral fish show micro-fractures or pull apart structures (Fig. 19h).
- *Biotite* is mainly concentrated along the mylonitic foliation. Biotite flakes have variable dimension (6 to 16mm long). Primary biotite (Bt_1) and recrystallized biotite (Bt_2) are observed. Bt_1 is brown biotite. It displays large crystals (up to 16mm long) with rare inclusions of zircon and apatite, often altered to chlorite and muscovite. Brown biotite is secondary from the alteration of large amphibole clasts (Fig. 19f). Bt_1 depicts generally large crystals fish textures.
- *Muscovite* is fine-grained (~2µm). It crystallized at the expense of brown biotite. Muscovite is generally concentrated in dark bands along the mylonitic foliation where it is associated with biotite.
- Accessory mineral phases include calcite at the boundaries of Kfs_1 and Pl_1 which underlines the starting stage of calcification of feldspars, and zircon which appears in biotite as inclusions.

I.3.1.3 Ultra-mylonites.

Ultramylonite appears as linear bands wrapped by mylonitic zones and show mylonitic texture defined by the strongly elongated feldspar clasts in light bands and biotite/muscovite and opaques in dark bands.

Ultramylonites are light in color compared to the protomylonite and mylonite. Asymmetric and symmetric boudins, σ and Φ types clasts are observed and define S-surfaces (Fig. 20a). The mineralogy of ultra-mylonites comprises quartz (~53 %) and biotite (~25 %), K-feldspar (~13%), plagioclase (~5%), muscovite (~2 %) and epidote (< 1%).

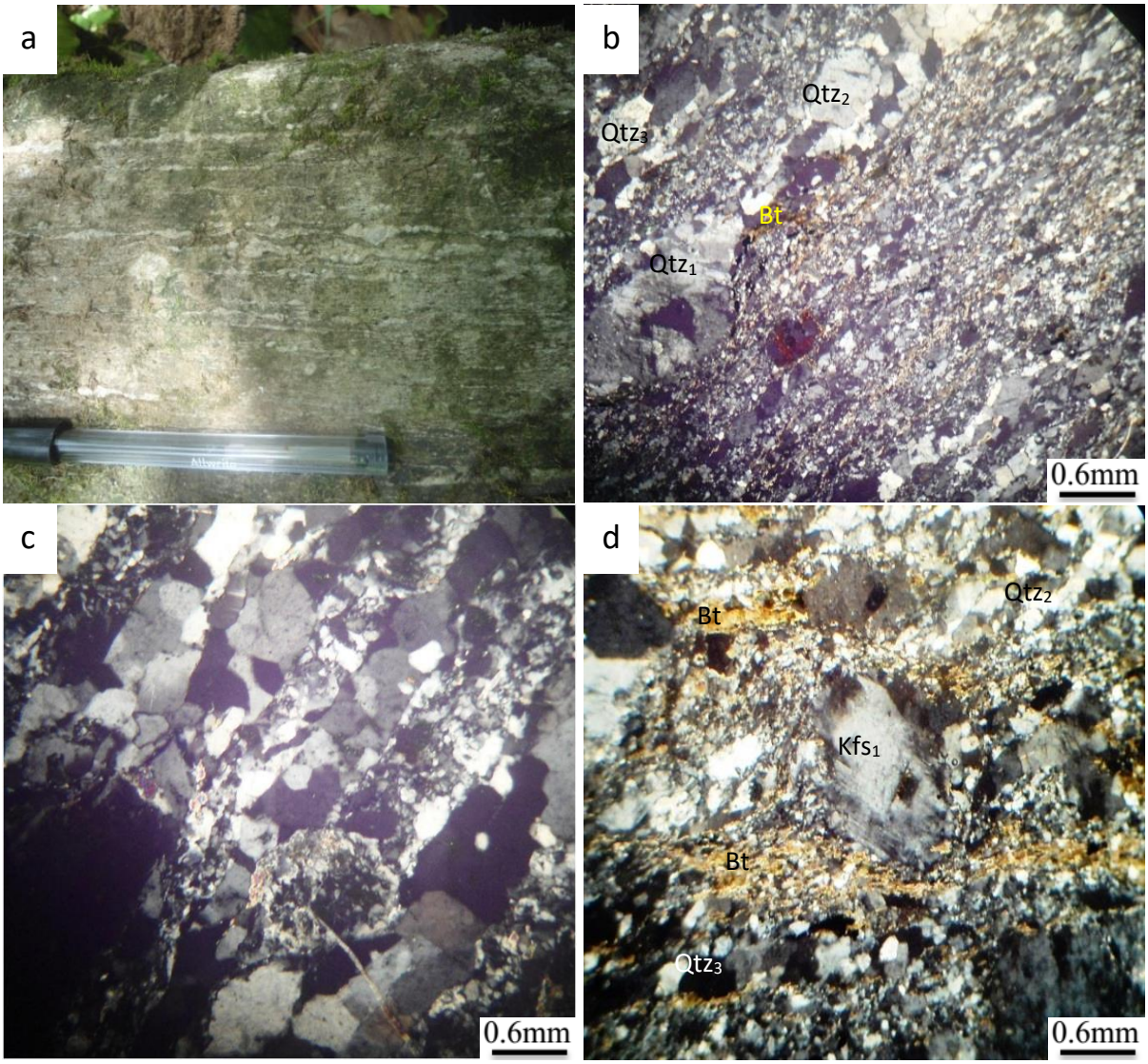

Figure 20: Photograph and photomicrographs of ESZ ultra-mylonites:(a) Outcrop showing strongly stretched Kfs clast; (b) Aspect of ultra mylonite under microscope: noticed quartz clast showing undulose extinction; (c) Alternating bands of fine grain Qtz_2 and Qtz_3; (d) continuous mylonitic foliation formed by the preferred orientation of biotite and muscovite surrounding feldspar clast oblique to the mylonitic schistosity.

- *Quartz (Qtz_1)* displays strongly elongated clasts with aspect ratios of 0.2-1.5. Sub-grains are common as well as undulose extinction in these quartz grains (Fig. 20b).
- *Quartz* Qtz_2 and Qtz_3 are fine-grained aggregates, concentrated in light bands and form alternating thick mantle aggregates (Fig. 20c) surrounding Qtz_1 and feldspar clasts. Recrystallized quartz (Qtz_2 and Qtz_3) represents ~88% of the total volume of quartz.

- *K-Feldspars* are strongly stretched (Fig. 20a). Large clasts display undulose extinction, intracrystalline micro-fractures filled mostly by Qtz_2 and pull apart features. They can also display rotated sub-euhedral porphyroclasts with cleavages oblique to the mylonitic foliation (Fig. 20d).
- *Plagioclase* is rare. It forms small elongated grains in the siliceous matrix or it is present as inclusions in K-feldspars.
- *Biotite* and muscovite are concentrated in ferromagnesian bands where they form continuous mylonitic foliation (Fig. 20d). They are fine-grained (2 µm x 6µm) with preferred orientation or rimming large clasts of Kfs_1 or Qtz_1.

I.3.2 Fault rocks in the brittle zone

The britle zone is marked by brecciated quartz blocks, observed in the northwestern corner of the fault zone and sandwiched between the wall rock, gneiss and the mylonitic corridor. Block of quartzitic bodies (Fig 21a) with variable dimensions (up to 20 m x 8 m), can be trace along strike for over 2.5 km in NNE-SSW to NE-SW direction. On some large blocks, joints and hydrothermal quartz veinlets (up to 15 cm wide) are observed arranged in sub-parallel arrays (Fig 21b). Most of these veinlets are characterized by a development of serrated elongated blocky grains recrystallization, where crystals grow from the wall inwards (Fig 21c and 21d). Generally, blocks are monomineralic and composed of milky quartz clasts that vary from < 0.5 mm to 8 cm in size. According to Woodcock and Mort (2008), breccias in Etam are classified into: i) crackle breccias (Fig.20e), with 75-100% clasts > 2mm, display small isolated blocks (1.2 x 0.8 m) in the brittle zone and represent about 5% of the quartzite blocks; ii) mosaic breccias (Fig. 21f) with 60-75% clasts > 2mm. The mosaic breccias are wide spread in the area and display blocks with variable dimensions, up to 20 x 8 m, cruss-cut by small quartz veins (centimetric width). They represent about 95% of the quartzite blocks.

I.3.2.1 Crackle breccias (75-100% clasts > 2mm)

They are characterized by large white and milky quartz clasts. Most of these breccias contain from ~95 to ~ 98% of clasts (Fig. 22a) with a siliceous matrix often less than 3%, and thus weakly cohesive. The clasts are angular and display sharp edges. The dimensions are variable and range from 2mm to 8cm long. The matrix comprises white fine quartz grains (< 2mm) between large clasts. Under the microscope, clasts are euhedral with sharp edges or straight edges (Fig. 22b).

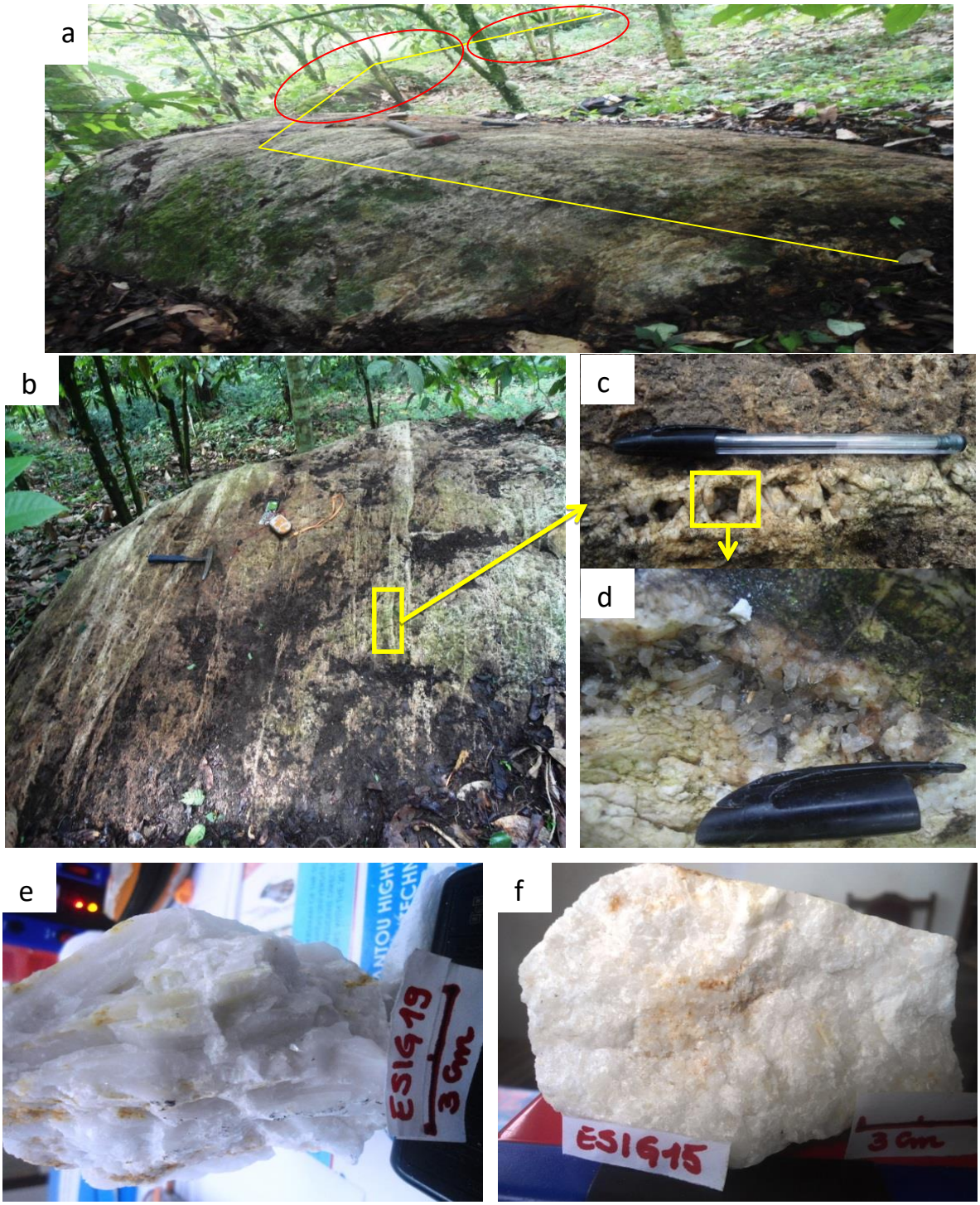

Figure 21:Photograph of EZS quartzitic rocks: a) Aspect of brecciated quartzite block trending N to NNE; b) Large block of breccias showing small quartz veins disposed in sub parallel array; (c) Small quartz veins with serrate elongated quartz minerals; (d) Transparent quartz clasts growing from the wall vein to the inner; (e) Aspect of crackle breccias; (f) Aspect of mosaic breccias, grains have shape edges.

I.3.2.2. Mosaic breccias (60-75% clasts> 2mm)

Mosaic breccias from Etam are cohesive and monomineralic, composed mainly of quartz clasts, neo-crystallized fine-grained quartz and matrix (Fig.22c).

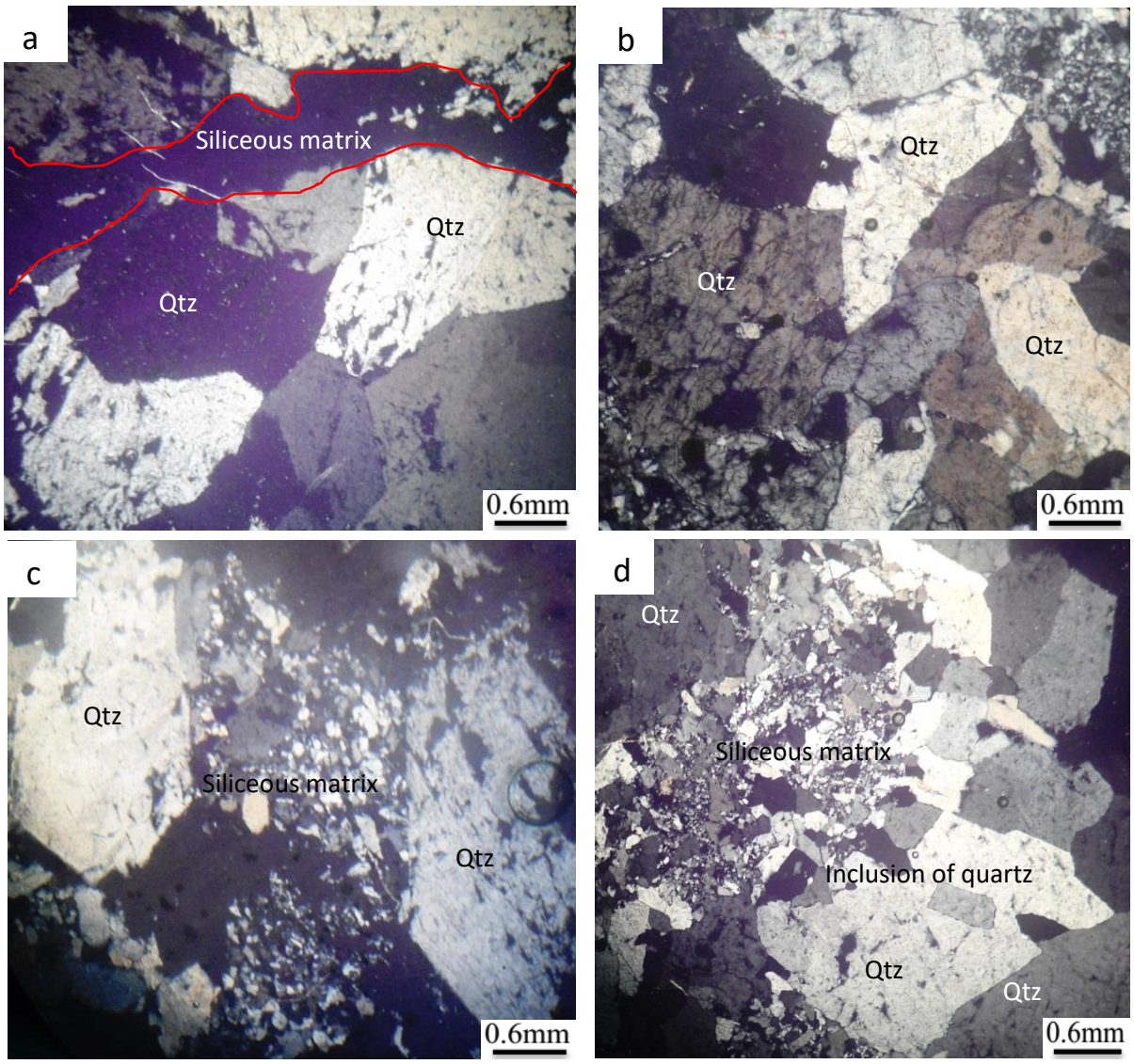

Figure 22: Photomicrographs of brecciated quartzit sample. a and b) crackle breccias showing euhedral large quartz clast and a silicified matrix often less than 3%. c) and d) mosaic breccias: quartz clasts are white or transparent with shape edges and present rare quartz inclusion.

Clasts occupy 65-70% of the volume of the rock and range from 0.6 mm to 1.2cm. Inclusions of recrystallized small quartz grains are observed in large quartz clasts (Fig.22d).

II.Geochemistry

II.1. Granitoids

Classification diagram of Middlemost (1977) show that Etam granitoids consiste of granodiorite and granites (Fig. 23). They are compared in this section with others panafrican fold belt granitoids in Cameroon (Magba and Ekomedjion) and in Brazil (Papanduva and Quiriri).

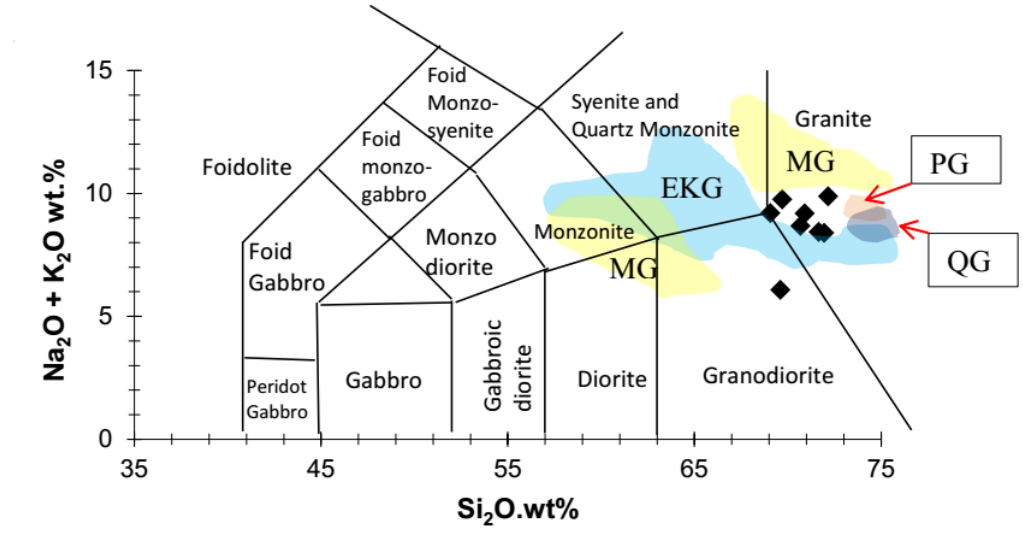

EKG Ekomedjion Granitoids, MG Magba Granitoids, PG Papanduva Granitoids
QG Quiriri Granitoids ◆ Etam Granitoids

Figure 23: Classification diagramm of Etam granitoids (after Middlemost, 1977), compared to the granitoids from: Magba (Ntieche et al., 2016): Papanduva and Quiriri (Vilalva and Vlach, 2014) and Ekomedjion (Bambi et al., 2012).

- ***Major elements***

Etam granodiorites show higher concentrations (Table 4) of TiO_2 (15.52 wt%), MnO (0.5 wt%), MgO (3.89 wt%) compared to granites: TiO_2 (mean 0.35 wt%), MnO (mean 0.03 wt%), MgO (mean 0.45wt%) respectively and lowest concentration of Al_2O_3 (2.24wt%), Fe_2O_3 tot (0.03 wt%), K_2O (0.26 wt%) compared to granites for the same elements: Al_2O_3 (means 14.69 wt%), Fe_2O_3 tot (mean 2.29 wt%), K_2O (mean 5.16 wt%) respectively.

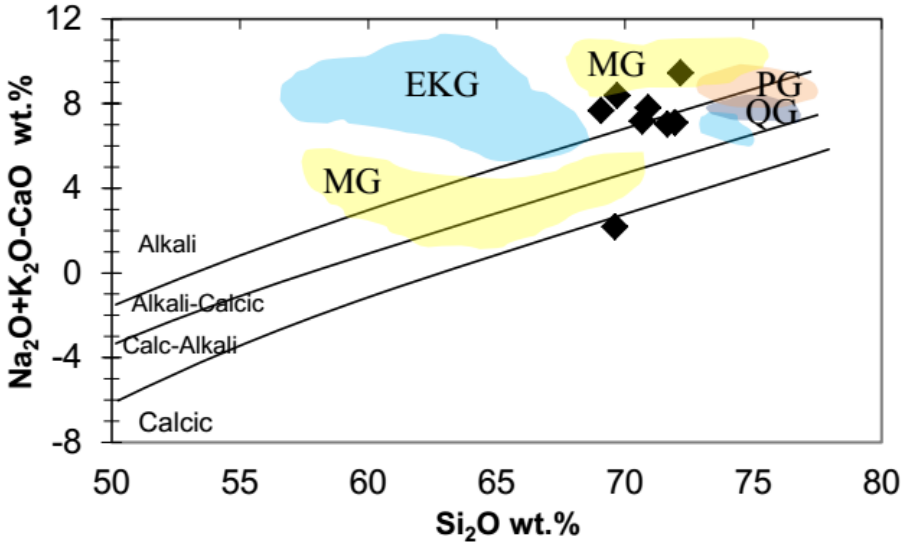

Figure 24: Diagramm (Na_2O + K_2O - CaO) - SiO_2 after Frost et al. (2001) for granitoids of Etam and granitoids from: Magba (Ntieche et al., 2016): Papanduva and Quiriri (Vilalva and Vlach, 2014) and Ekomedjion (Bambi et al., 2012).

Table 4: Major, trace and rare-earth element analyses of granitoids from Etam

	Granite							Granodioite
Sample No	**RG1**	**RG2**	**RG3**	**RG4**	**RG5**	**RG6**	**RG7**	**ESIG 20**
SiO_2	69.7	69.07	71.96	70.91	71.66	70.68	72.17	69.61
TiO_2	0.36	0.38	0.37	0.37	0.36	0.44	0.23	15.52
Al_2O_3	15.54	14.9	14.11	14.85	14.12	14.69	14.66	2.24
Fe_2O_{3t}	2.27	2.41	2.47	2.32	2.36	2.74	1.52	0.03
MnO	0.03	0.04	0.04	0.04	0.04	0.05	0.02	0.5
MgO	0.5	0.5	0.48	0.44	0.46	0.54	0.26	1.37
CaO	1.39	1.53	1.29	1.39	1.41	1.5	0.43	3.89
Na_2O	3.93	3.9	3.68	3.63	3.71	3.79	3.26	5.81
K_2O	5.83	5.3	4.71	5.56	4.72		4.88	0.26
P_2O_5	0.11	0.11	0.12	0.11	0.11	0.13	0.07	0.11
LOI	0.78	1.55	1.21	0.9	0.68	0.77	1.3	0.71
Total	**100.44**	**99.69**	**100.44**	**100.52**	**99.63**	**100.21**	**100.54**	**100.05**
V (ppm)	28	35	28	23	32	37	21	25
Sr "	211	202	143	242	188	200	190	209
Co "	9	13	6	DL	8	9	6	10
Zr "	173	186	143	181	175	189	119	171
Nb "	21	23	21	23	23	27	17	22
Ba "	946	892	615	916	721	788	1054	946
Rb "	258	215	210	224	226	246	222	255
Zn "	31	32	31	29	32	35	25	33
Y "	57	51	60	48	53	56	46	55
Ga "	15	15	15	15	15	16	15	13
Y + Nb	78	74	81	71	76	83	63	77
Y/Nb	2.71	2.21	2.85	2.08	2.30	2.07	2.70	2.5
La				54.5	51.9	49	34	56.5
Ce				107.9	116.7	123.4	73.2	108.1
Pr				11.37	11.62	11.62	7.49	11.36
Nd				38.7	42.3	44.4	24.1	39.2
Sm				5.8	7.1	7.6	4.2	6.8
Eu				0.78	0.9	0.79	0.64	0.77
Gd				4	5.29	5.18	2.55	3.9
Tb				0.68	0.95	0.96	0.48	0.58
Dy				3.41	4.76	4.69	2.23	3.42
Ho				0.61	0.86	0.89	0.44	0.61
Er				1.74	2.46	2.47	1.16	1.77
Tm				0.28	0.39	0.37	0.18	0.29
Yb				2.05	2.53	2.73	1.38	2.01
Lu				0.28	0.4	0.39	0.18	0.29
La/Lu				194.64	129.75	125.64	188.88	194.82
La/Yb				26.58	20.51	17.94	24.63	28.10
Ce/Yb				52.63	46.12	45.20	53.04	53.78
LaN/YbN				17.94	13.84	12.11	16.62	18.97
Eu/Eu*				0.49	0.44	0.38	0.59	0.37
Cs				2	13.6	15.8	2.9	2
Sn				11	12	13	7	
Ta				2.7	3.5	3.6	2	2.5
Th				32.8	34.2	38.5	24.9	32.8
U				10.8	13.5	12.9	8.9	10.8
W				1.2	31.4	12	0.7	1.2

The Etam samples plot within the alkali and alkali-calcic fields on the diagram of Frost et al., (2001) with the exception for granodiorite sample (ESIG20) which shows calcic composition (Fig. 24).

On the plot of A/NK vs A/CNK (A/CNK= molar ratio of $Al_2O_3/(CaO+Na_2O+K_2O)$ these rocks are peraluminous (Fig. 25).

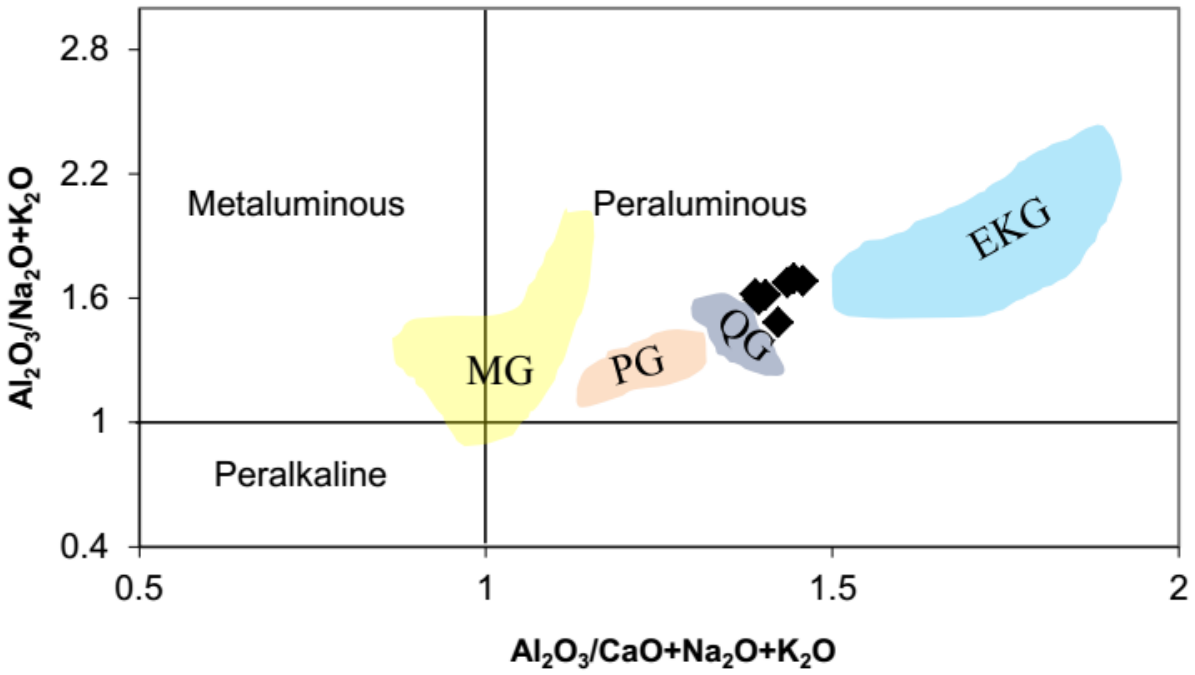

Figure 25: Molar ratioA/CNK= Al2O3/ (CaO + Na_2O+ K_2O) vs A/NK= $Al_2O_3/(Na_2O + K_2O)$

Etam granitoids are ferroan, akin to granitoids from Ekomedjion (Cameroon) and granitoids from Papanduva and Quiriri(southern Brazil), different from granitoids in Magba which fall within the magnesian and cordellian field in the FeOt/ (FeOt + MgO) vs SiO_2 diagramafter Frost et al (2001) (Fig. 26).

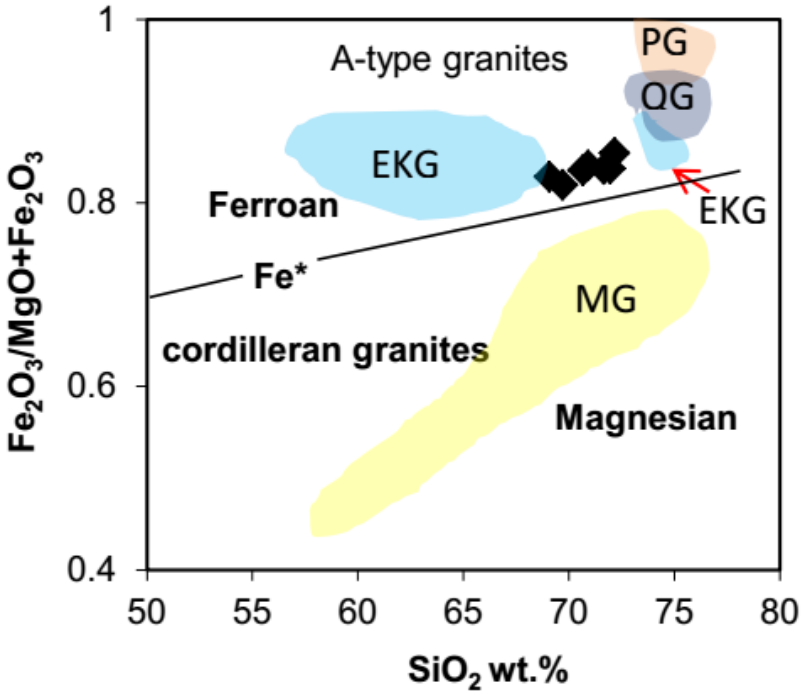

Figure 26: Diagramm FeOt/ (FeOt + MgO) vs SiO_2 after Frost et al (2001) for granitoids of Etam and some granitoids from panafrican fold belts in Cameroon and Brazil.

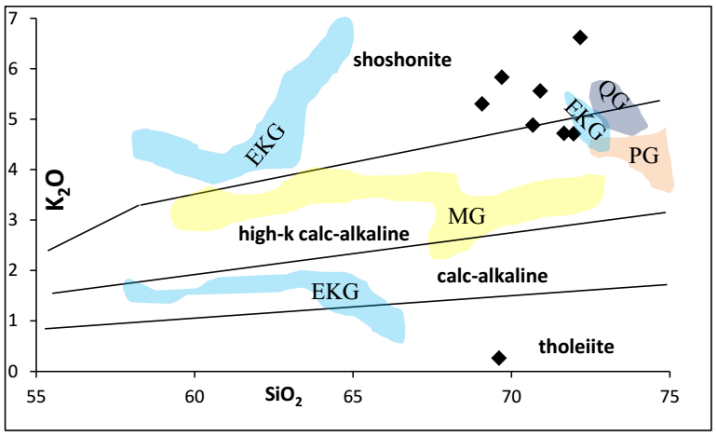

Figure 27: K_2O vs. SiO_2 diagramm illustrating high-K calc-alcaline to shoshonitic characters for granite samples

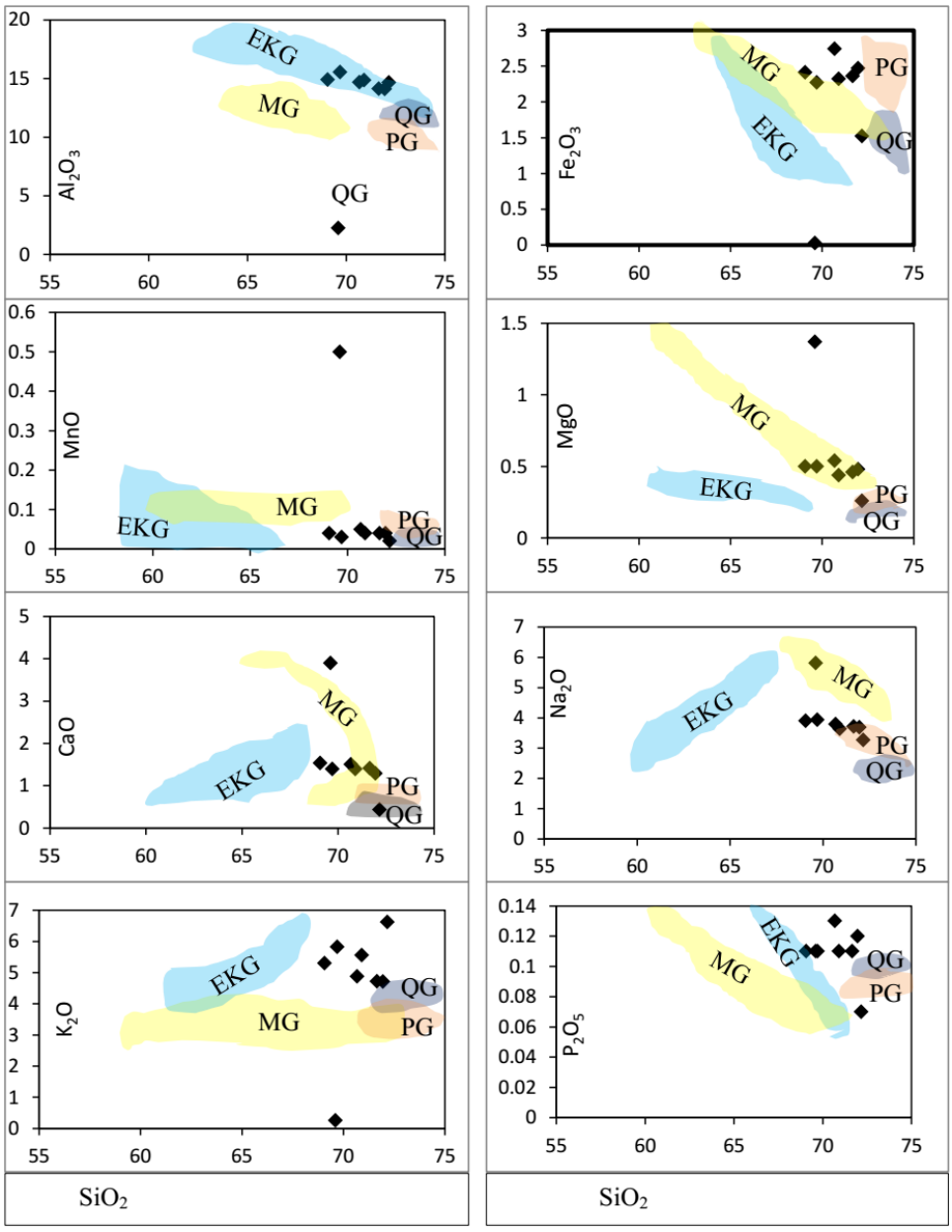

Figure 28: Harker diagrams (majors element vs SiO_2) for Etam granitoids compared to granite from Magba (Ntieche et al., 2016), Ekomedjion (Bambi et al., 2012) and (2) Brazil: Papanduva and Quiriri (Vilalva and Vlach, 2014).

The total alkali content ($Na_2O + K_2O$) is significally high (8.93 to 9.88 wt %) for Etams' granites and moderate in granodiorite (6.07 wt %). The sodic character of the Etam granitoids is shown by K_2O/Na_2O ratio (1.27-2.03 wt %). In the SiO_2 vs K_2O diagram of Peccerilo & Taylor (1976), Etamsgranites fall mostly in the shoshonitic field with few samples overlapping in the high-k-calc-alkaline field (Fig. 27). The Etam's granodiorite samples exhibit very low K_2O/Na_2O ratio (0.04 wt %) and plot in tholeitic field, also with a few Ekomedjion samples (Fig. 27). On Harker diagrams, most major oxides e.g Al_2O_3, Fe_2O_3 tot, MnO, P_2O_5, CaO and Na_2O show a slightly negative correlation with SiO_2 (Fig. 28).

- ***Trace elements***

Trace element compositions are characterized by high Ba, Nb, Y, Th, Rb. Sr, Ga and Zr are moderately low content (Table 4). Harker diagrams show negative correlation between SiO_2 vs Rb and SiO_2 vs Zr (Fig. 29).

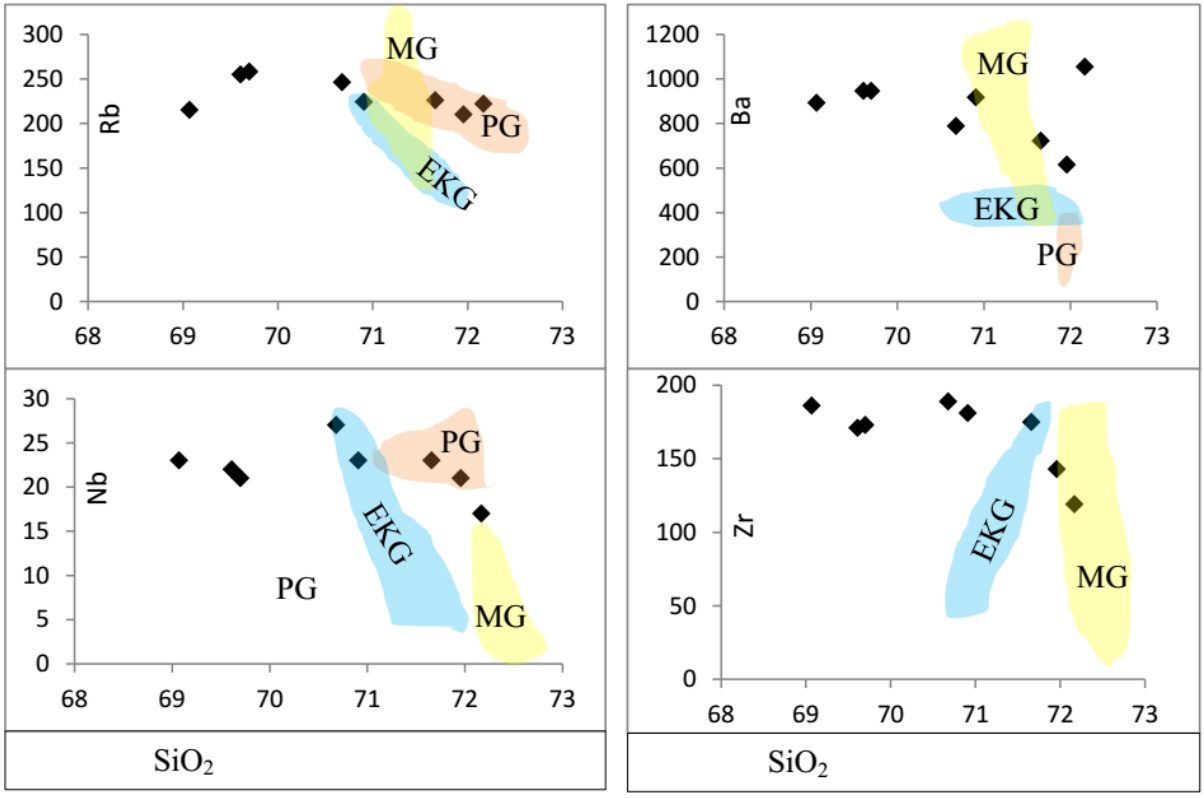

Figure 29: Harker diagrams (trace element vs SiO_2) for Etam granitoids compared to granite from Magba (Ntieche et al 2016), Ekomedjion (Bambi et al 2012) and (2) Brazil: Papanduva and Quiriri (Vilalva and Vlach, 2014).

Trace element distribution patterns (spidergrams), normalized to the values suggested by Thompson (1982) are characterized by negative anomalies at Ba, K, P and Ti (Fig. 30).

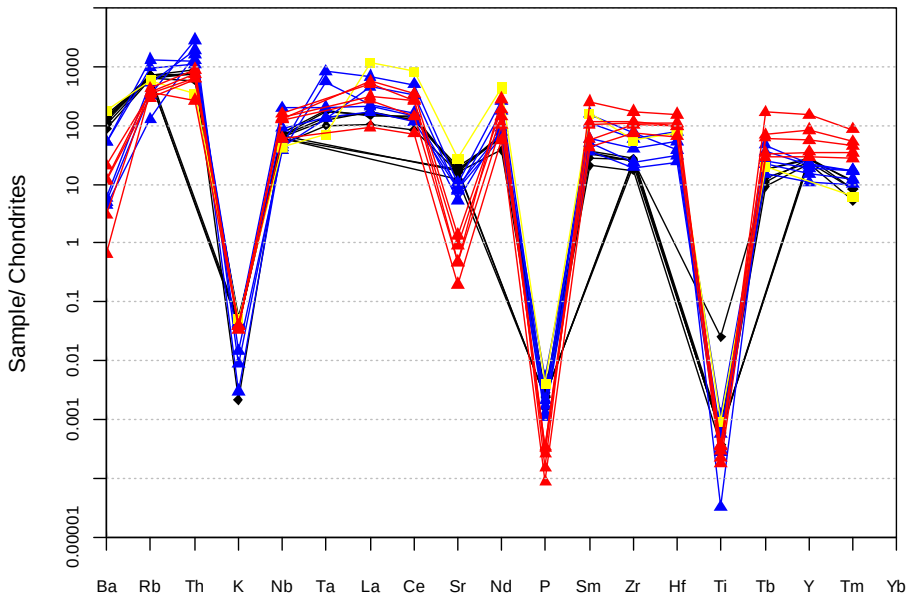

Figure 30:Chondrite-normalized multi-element diagram (Normalizing factors of Thompson (1984).

——— = Etam granitoids, ——— = EKG, ——— =PG, ——— =MG

These patterns are similar to granitoids from Ekomedjion, Quiriri and Papanduva in the Pan-African fold belt in Cameroon and Brazil, respectively.

The Etam granitoids fall in the 'Within Plate Granites' field (WPG, Fig. 31a) in the Y vs Nb diagram (Pearce et al., 1984) similarly with granite samples from Ekomedjion, few from Magba, and almost all granitoids samples from Papanduva and Quiriri.

On the (Y + Nb) vs Rb diagram (Pearce, 1996), they plot in the post-collisional granites (PCG) field, but close to the WPG (Fig. 31b) field. The Ekomedjion granitoids similarly to Etam granitoids plot in PCG field while Batouri granitoids are out of WPG field.

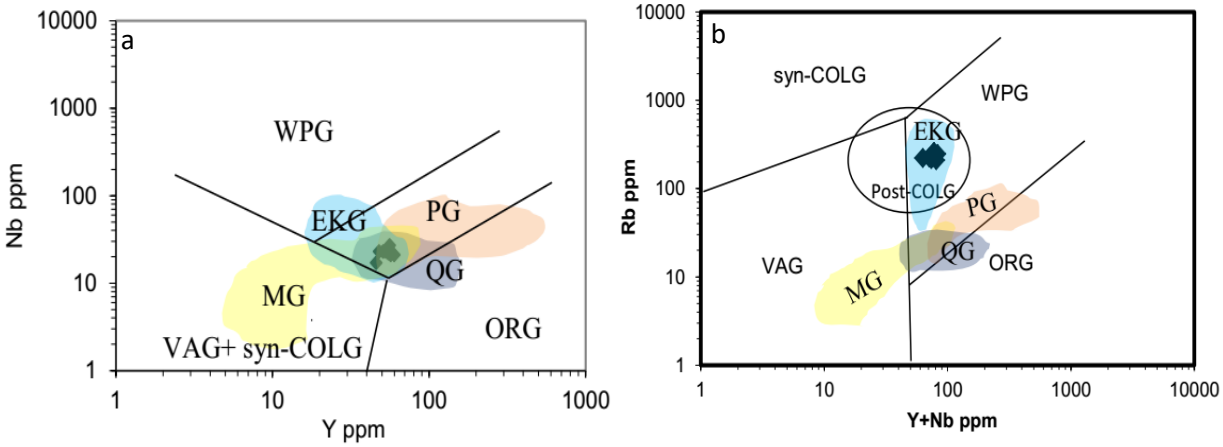

Figure 31: Etam granitoids fall in the 'Within Plate Granites' and in the post-collisional granites (PCG) field in a) Y vs Nb diagram (Pearce et al., 1984) and b) (Y + Nb) vs Rb diagram (Pearce, 1996) respectively.

- ***Rare earth elements***

The Etam granitoids are enriched in the LREE relative to the HREE with high (La/Yb)N ratios between 12.11 and 18.97 (table 4) and they are characterized by a negative Eu anomaly (Eu/Eu* ratio between 0.37 and 0.59, Fig. 32).

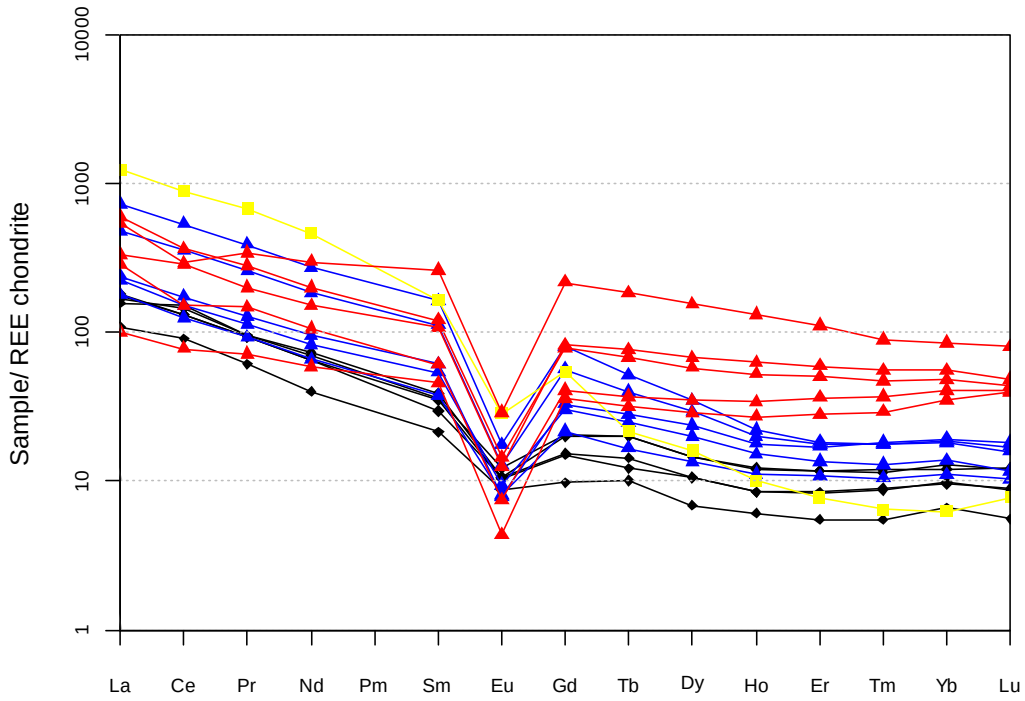

Figure 32: Rare Earth Element patterns of Etam granitoids samples, compared to granitoids from: Bambi et al., 2012 and Vilalva and Vlach, 2014 (Chondrite normalized Rare Earth Element patterns after Boynton. 1984).

= Etam granitoids, ——— = EKG, ——— =PG, ——— =MG

II.2. Gneiss

- ***Nature of the protolith***

The whole rock geochemical data for gneiss are presented in Table 5. These data from therepresentative's samples allow determining the main chemical characteristics of the metamorphic and mylonitic rocks in the Etam area. These data also permit to discuss about the protolith of the metamorphic basememt. The $Fe_2O_3t + TiO_2 + CaO$ vs. Al_2O_3 whole rock diagram (Fig. 33) of De la Roche (1965) is used to determine the protolith of the different petrographic units. On this diagram, gneisses as well as mylonites define a chemical trend parallel to the igneous rocks' origin (meta-igneous). They plot in the rhyolite and granodiorite fields.

Etam metamorphic rocks are compared to gneisses data from Eseka and Edea (Ndema et al., 2014) in the SiO_2 vs FeOt/MgO diagram of Miyashiro (1974).

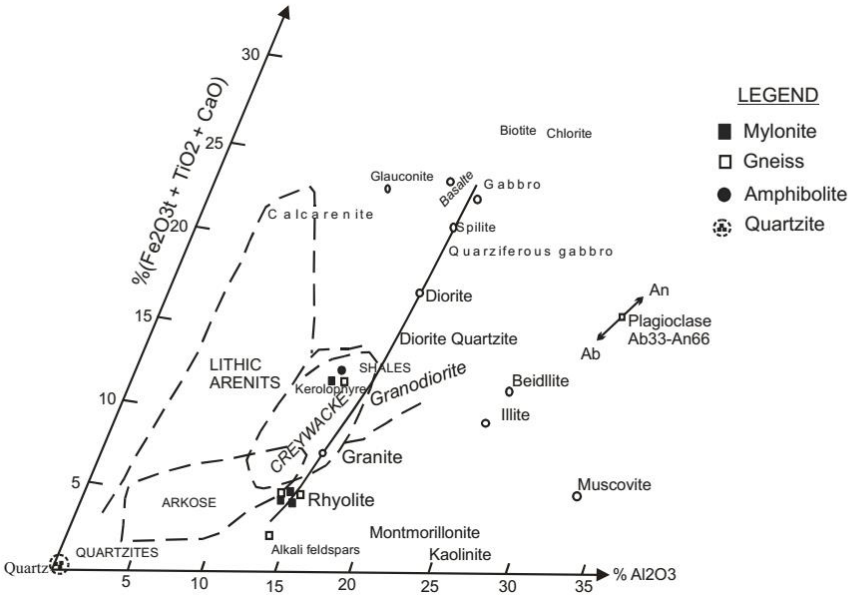

Figure 33: Fe2O3t + TiO2 +CaO vs Al2O3 diagram of De la Roche, (1965) shows the geochemical survival of the metamorphic study rocks.

This diagram shows that the Etam metamorphic rocks belong to the calc-alcaline series, with a few samples defining the tholeitic series (Fig. 34) similary to Eseka and Edea gneiss.

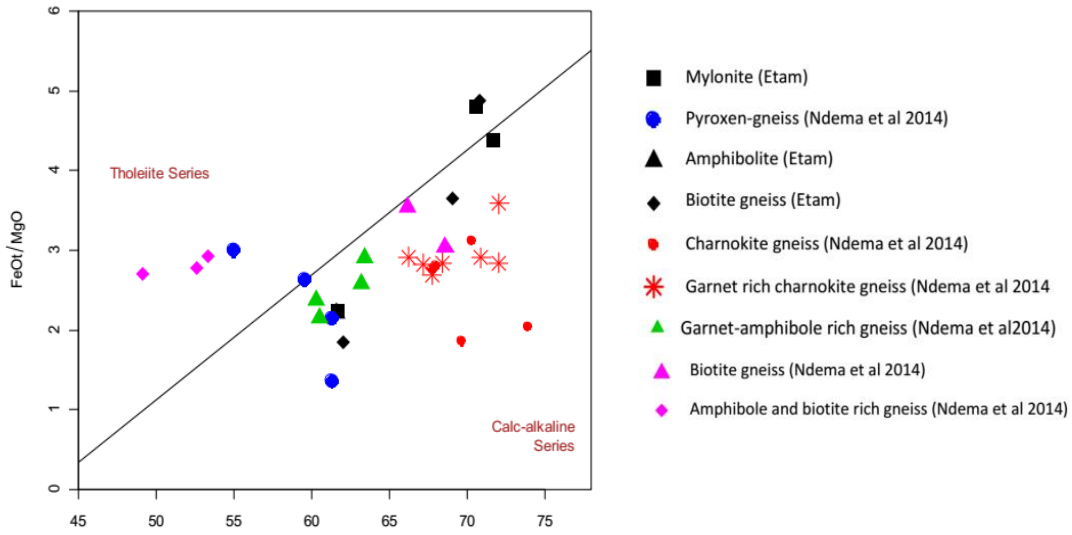

Figure 34: SiO_2-FeOt/MgO diagram of Miyashiro, (1974) showing double affinity, calc-alcaline series and tholeitic of mylonite and gneisses from Etam, compared to gneisses data from Eseka and Edea (Ndema et al., 2014).

- ***Major elements***

Gneiss in Etam display granitic composition (Table 5) with high SiO_2 content (62-72 wt %) and limited variation of Al_2O_3 (14-15 wt %).The concentrations of Fe_2O_3 (1.51-5.55 wt %), MnO (0.02-0.12 wt %), MgO (0.22-2.7 wt %),TiO_2 (0.21-1 wt%), CaO (0.4-4.6 wt%) and TiO_2 (0.21-1 wt%) are low, while alkalies show high concentration with K_2O + Na_2O range from 7.88 to 9.75 wt%.

Table 5: Major, trace and rare-earth element composition of Etam gneiss.

	ESIG 9	ESIG 30	STA7	STA6	ESIG 11
Major elements (w %)					
SiO_2	70.82	69.05	72.11	62.01	61.59
Al_2O_3	14.65	14.88	14.63	14.05	14.09
Fe_2O_3	2.22	2.43	1.51	5.55	5.62
MnO	0.04	0.04	0.02	0.12	0.13
MgO	0.41	0.6	0.22	2.7	2.29
CaO	1.39	1.54	0.39	4.58	4.68
Na_2O	3.61	3.9	3.23	3.46	3.6
K_2O	5.52	5.33	6.52	4.42	4.58
TiO_2	0.32	0.4	0.21	0.93	0.92
P_2O_5	0.11	0.13	0.12	0.41	0.45
LOI	0.9	1.57	0.9	1.78	1.99
Total	99.99	99.87	99.86	100.01	99.94
Trace elements (ppm)					
Be				7	4
Sc				15	11
V	21	38	19	91	79
Cr				46	51
Co	<2	11	5	9	17
Ni				18	22
Cu				<10	<10
Zn	28	30	22	89	103
Ga	18	17	15	19	22
Ge				2	2
As				<5	<5
Rb	224	213	232	138	151
Sr	246	199	210	1426	1444
Y	49	49	46	52	47
Zr	183	188	120	408	499
Nb	25	25	18	26.3	25.9
Mo				3	2
Ag				1.2	1.3
In				0.1	0.1
Sn				4	4
Sb				<0.2	<0.2
Cs	2.9	13.6	2.8	2.6	2.4
Ba	916	892	1054	2878	2799
Hf				9.9	12.2
Ta	2.2	3.9	2.9	0.99	2.01
W	0.7	31.4	11.3	<0.5	<0.5
Tl				0.69	0.71
Pb				41	33
Bi				0.2	0.2
Th	24.9	34.2	26.2	22.7	31
U	8.9	13.5	13.7	5.5	6.8
Rare Earth Element (REE)					
La	33.9	52	34.1	151	144
Ce	73.1	117.2	72.1	236	251
Pr	7.44	11.61	7.34	28.2	22.5
Nd	24.2	42.2	44.1	99	116
Sm	4.1	7.2	4.2	11	21
Eu	0.63	0.91	0.88	3.6	4.4
Gd	2.57	5.28	2.66	11.8	12.6
Tb	0.45	0.85	0.44	1.6	2.1
Dy	2.22	4.66	4.23	7.5	6.9
Ho	0.45	0.88	0.88	1.5	1.41
Er	1.18	2.46	1.17	2.9	3.5
Tm	0.19	0.38	0.21	0.5	0.5
Yb	1.38	2.53	2.1	3.1	3.7
Lu	0.2	0.4	0.2	0.55	1.1

There is a general negative correlation between SiO_2 and the other major elements (Fig. 35). Only K_2O exhibits positive correlation with SiO_2.

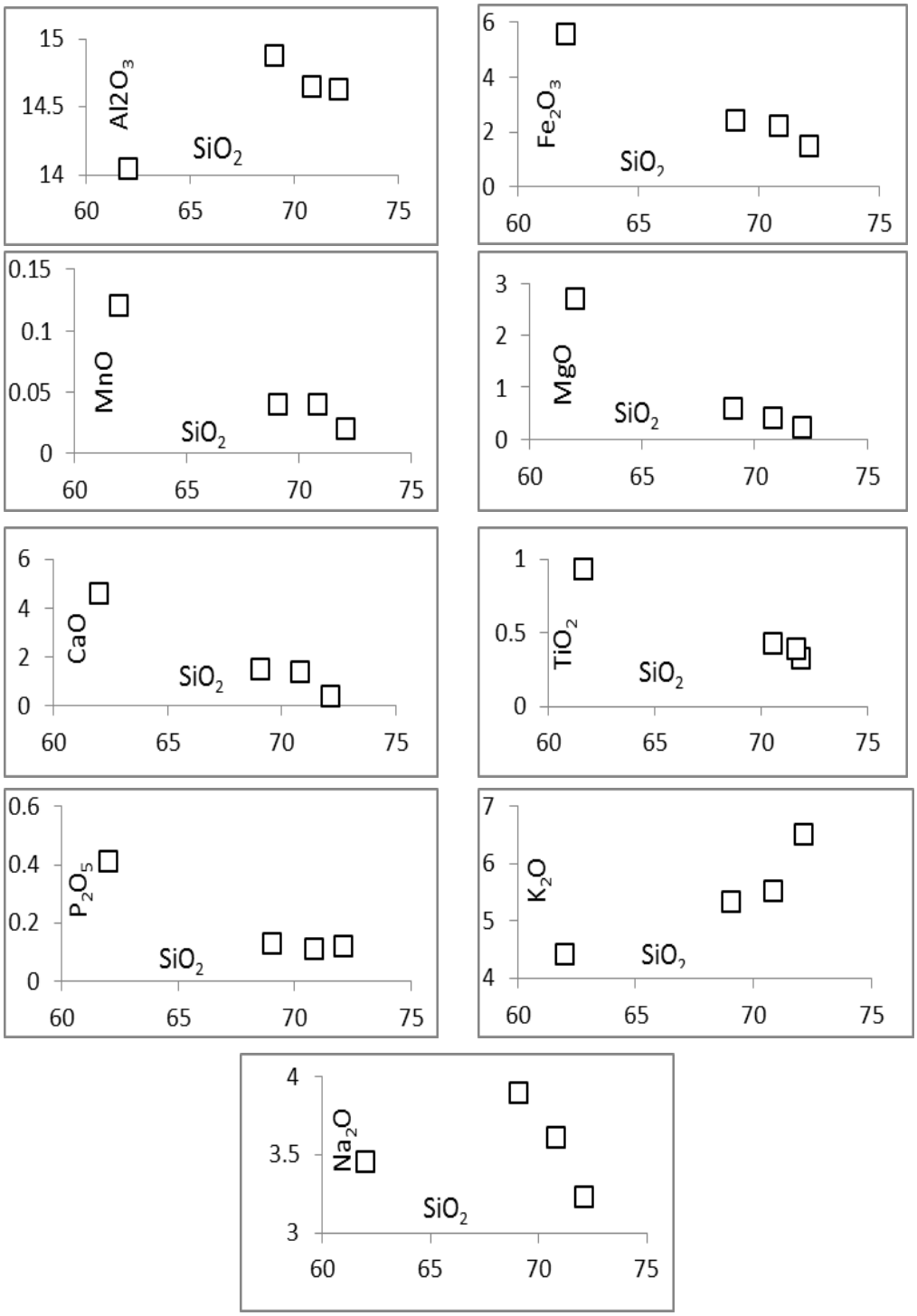

Figure 35: Harker variation diagrams of major elements of Etam gneisses

Trace elements

The Etam gneisses are enriched in Ba (892-2878ppm), Sr (199-1426 ppm), Rb (138-213 ppm) and Zr (120-408 ppm) and depleted with respect to V, Zn, Zr. There is positive correlation between SiO_2 vs Rb (Fig. 36). The spidergram displays anomalies with respect to Nb, Nd, Sm, Tm and Ta (Fig.37a).

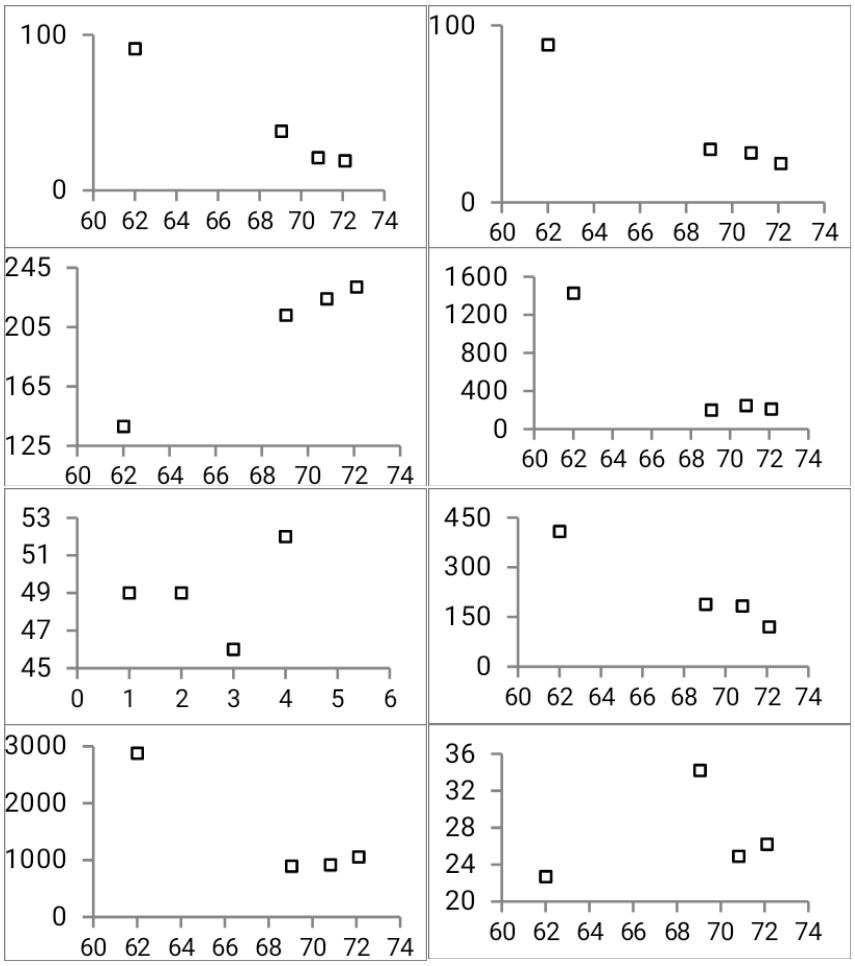

Figure 36: Harker diagrams for trace elements of biotite gneiss

Rare earth element

Chondrite-normalized rare-earth element patterns (Fig.37b) show fractionation (La_N/Yb_N = 10.96-32.87). They are characterized by enrichment in LREE (Ce_N/Sm_N=2.88-5.17) over HREE (GdN/SmN=1.02-3.07) and negative Eu anomalies (Eu/Eu*=0.45-0.96).

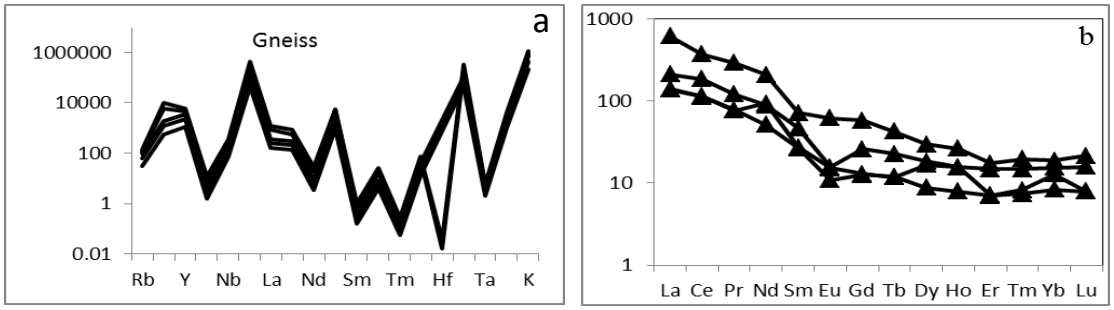

Figure 37: a) Chondrite-normalized patterns for biotite gneiss of Etam, b) spiderdiagram of trace elements

II.3 Mylonitic rocks

- ***Major elements***

Representative whole-rock major and trace elements analysis are given in Table 6.

Table 6: Chemical composition of mylonite from the ESZ.

	ESIG 23	ESIG 24a	ESIG 24b	ESIG 26	ESIG 27
Major elements (Wt %)					
SiO_2	70.58	61.66	61.66	71.68	71.89
Al_2O_3	14.66	14.06	14.06	14.14	14.12
Fe_2O_3	2.72	5.45	5.45	2.38	2.45
MnO	0.05	0.128	0.128	0.05	0.04
MgO	0.51	2.2	2.2	0.49	0.36
CaO	1.5	4.67	4.67	1.41	1.18
Na_2O	3.76	3.57	3.57	3.74	3.62
K2O	4.89	4.53	4.53	4.76	4.7
TiO_2	0.43	0.929	0.929	0.39	0.33
P_2O_5	0.12	0.44	0.44	0.12	0.11
LOI	0.77	1.97	1.97	0.68	1.2
Total	**99.99**	**99.6**	**99.607**	**99.84**	**100**
Trace elements (ppm)					
Be		10	4		
Sc		4	10	-	-
V	34	86	86	33	26
Cr	-	50	50		
Co	11	12	12	5	4
Ni	-	20	20	-	-
Cu	-	< 10	< 10	-	-
Zn	37	100	100	34	31
Ga	15	24	24	13	15
Ge		2	2	-	-
As		< 5	< 5	-	-
Rb	248	144	144	229	208
Sr	204	1466	1466	190	142
Y	57	43	43	55	58
Zr	190	477	477	177	145
Nb	29	28.6	28.6	23	19
Mo	-	3	3	-	-
Ag	-	1.3	1.3	-	-
In	-	0.1	0.1	-	-
Sn	-	4	4	-	-
Sb	-	< 0.2	< 0.2	-	-
Cs	14.9	2.8	2.8	13.4	15.8
Ba	788	2979	2979	721	615
Hf		11.6	11.6		
Ta	3.6	1.85	1.85	3.9	3.6
W	2	< 0.5	< 0.5	1.9	12
Tl	-	0.65	0.65	-	-
Pb	-	39	39	-	-
Bi	-	0.2	0.2	-	-
Th	33.4	25.8	25.8	32	38.5
U	12.4	6.2	6.2	11.1	12.9
Rare Earth Element (REE)					
La	49.3	149	149	52.1	49.1
Ce	131.3	249	249	117.1	122.3
Pr	10.63	29.7	29.7	11.52	11.63
Nd	39.4	110	110	24.5	43.9
Sm	6.9	19	19	7.1	7.5
Eu	0.6	4.42	4.42	1.1	0.8
Gd	5.15	12.9	12.9	5.22	5.17
Tb	0.87	1.6	1.6	0.57	0.97
Dy	4.4	8	8	5.11	4.71
Ho	0.46	1.35	1.35	0.87	0.85
Er	1.39	3.8	3.8	2.44	2.48
Tm	0.37	0.525	0.525	0.39	0.37
Yb	2.68	3.4	3.4	2.55	2.75
Lu	0.3	0.58	0.58	0.3	0.4
ΣREE	253.75	593.27	593.27	230.87	252.93
LaN/YbN	12.41	29.57	29.57	13.79	12.05
CeN/SmN	4.59	3.16	3.16	3.98	3.93
GdN/YbN	1.55	3.06	3.06	1.65	1.51
Eu/Eu*	0.3	0.86	0.86	0.55	0.39

The rocks show compositional ranges with 61.66–71.89 wt% SiO_2; limited variation of Al_2O_3 (14.01– 14.68 wt %); moderate to high concentration of alkalies: Na_2O (3.62 to 3.76 %) and K_2O (4.70 to 4.89 %). Major elements also show low concentrations of TiO_2 (0.33 to 0.92 %); CaO (1.5 to 4.47 %); MgO (0.36 to 202 %) and Fe_2O_{3t} (2.72 to 5.45 %). Harker diagram (Fig. 38) show that all major elements content decrease with increase in silica.

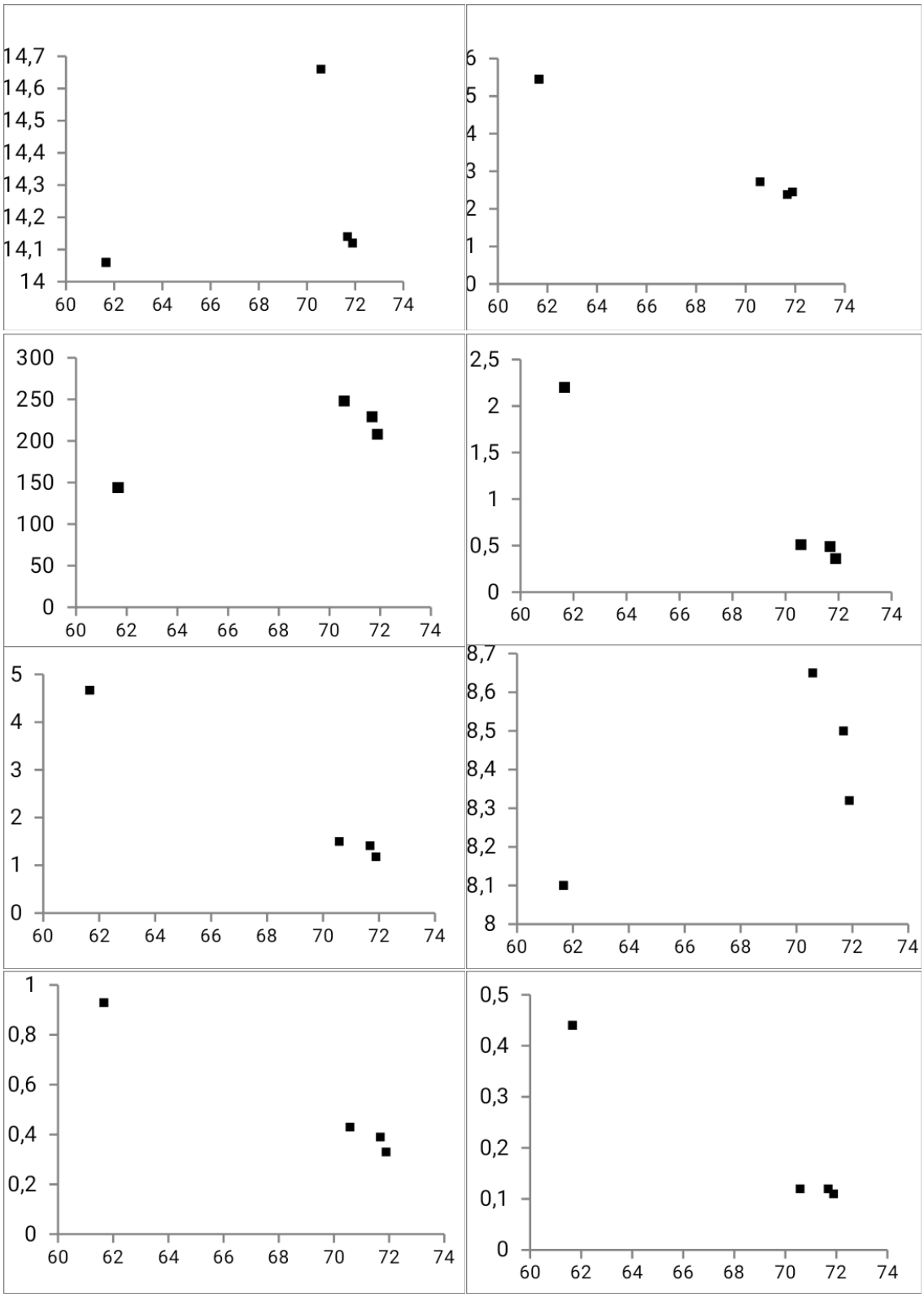

Figure 38: Harker variation diagrams for major elements of Etam mylonites

- ***Trace elements***

The Etam mylonitic samples exhibit variations in trace elements content and are enriched particularly in Ba (721-2979 ppm), Sr (204-1466 ppm), Rb (144–229 ppm), V(34-86 ppm), Zn(34-100 ppm), Cs(2.8-14.9 ppm), Th(25.8-33.4 ppm), U(6.2-12.4 ppm), Y(43-57 ppm). High field-strength elements (HFSE) (Zr: 177–477 ppm; Nb: 23-29 ppm; Ta: 1.85–3.9 ppm). Co (5-12 ppm), Ni (≤ 20 ppm), Cr (≤ 50 ppm), Sc (≤ 10 ppm), Ga (13–24 ppm), and Pb (≤ 39 ppm) contents are relatively low. Negative correlation is observed on the Harker diagrams for V, Zn, Sr, Zr, Ba while Y and Th correlate positively (Fig. 39). The overall trace element patterns (Fig. 40a) show Zr, Nd, Sm, Tm and Ta anomalies.

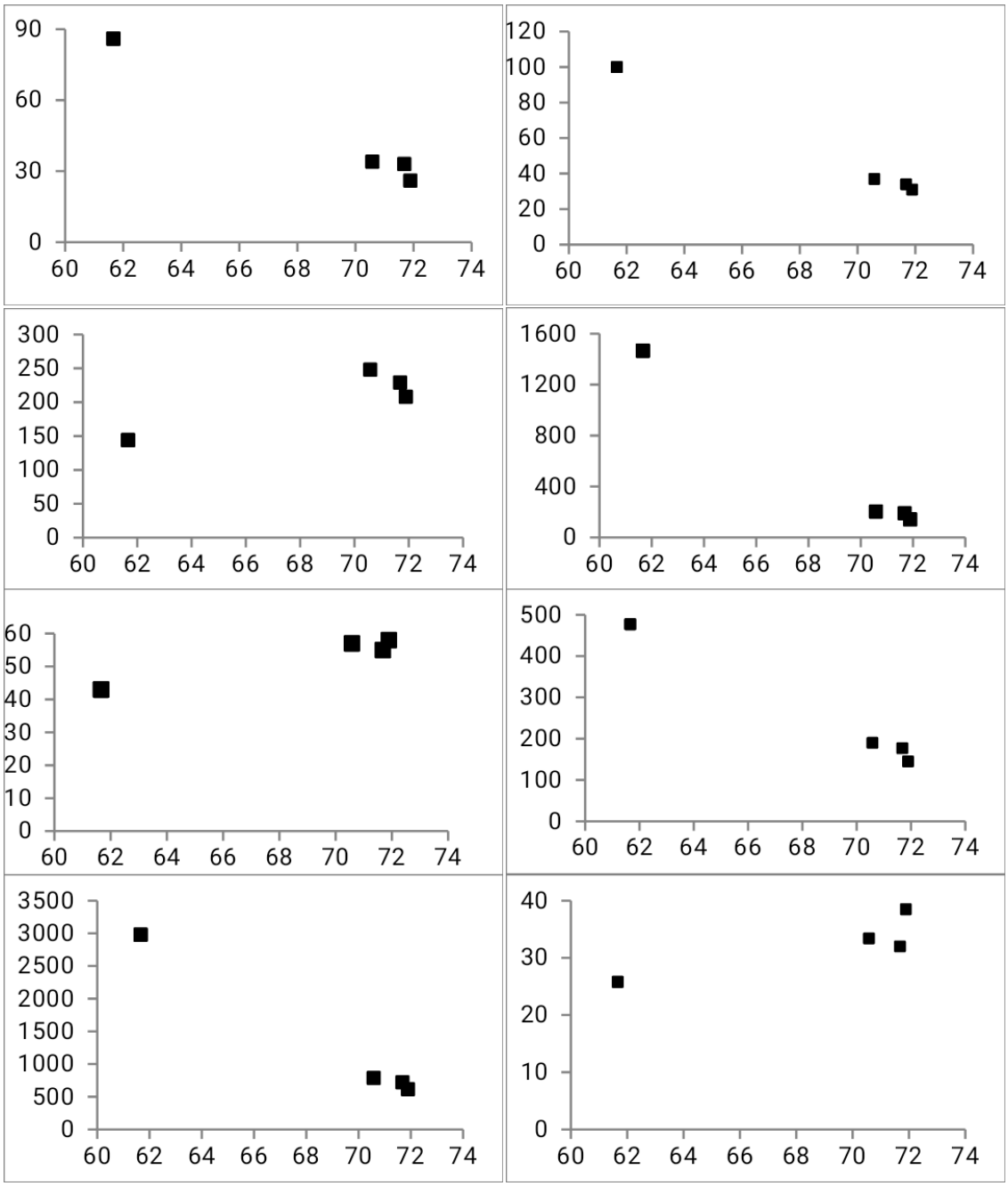

Figure 39: Harker diagrams of trace elements of mylonites

- ***Rare earth elements***

Chondrite-normalized rare-earth element patterns show strong fractionation (La_N/Yb_N= 12 to 29.6), an enrichement in LREE (Ce_N/Sm_N= 3-4.6) over the HREE (Gd_N/Yb_N= 1.55-3) and negative Eu anomalies (Fig. 40b, Eu/Eu*= 0.3 to 0.86).

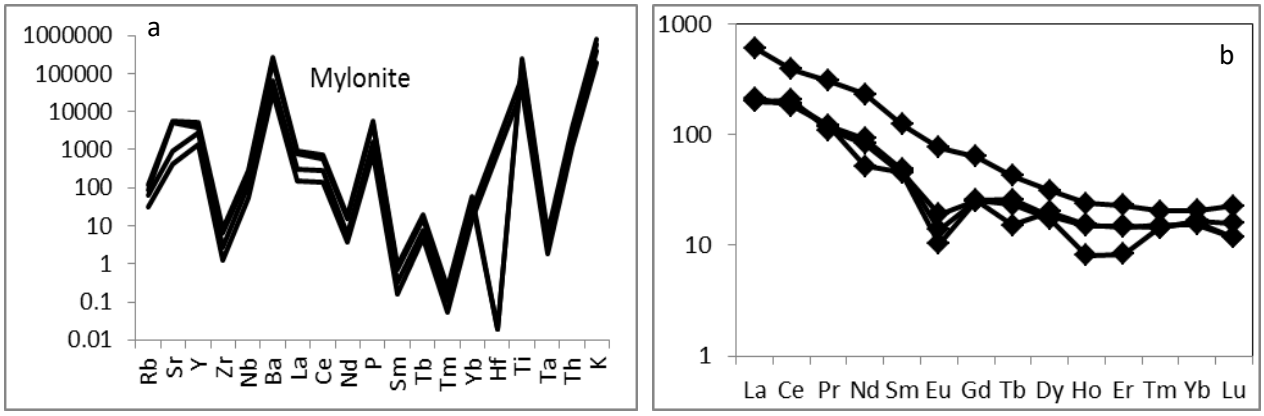

Figure 40: Chondrite-normalized patterns for mylonitic of ESZ: a) spiderdigram of trace elements b), REE (Normalized according to data of Eversen 1978).

III Structural analysis

The structural analysis of the Etam area combines the field data and microstructural studies. Structural features recorded during this work have been classified into two deformational phases: the first phase of deformation (D_1) and the second phase of deformation (D_2).

III.1 The first phase of deformation D_1.

This phase affects metamorphic rocks and it is characterized by foliation (S_1), intrafolial fold (F_1) and mineral lineation (L_1). The S_1 foliation is gneissosity, recorded in gneiss (Fig. 41a), migmatites and amphibolites (Fig. 41b).

The foliation (S_1) is defined by compositional banding, marked by the alternation of millimetric quartzo-feldspartic light bands and dark bands (5mm to 10cm) made up of stretched amphibole and biotite minerals mostly. In migmatites gneiss S_1 is reinforced by migmatitic foliation (Fig. 41c), where linear rock bands with light and dark color are observed. S_1 is also marked by elongated quartz and feldspar grains, biotite flakes and amphibole, with preferred orientation developed parallel to the compositional bands. The S_1 structures is generally oriented N10 to N22°E and dips 60-80°, generally to ESE (Fig. 41d) and it is progressively overprinted by S_2.

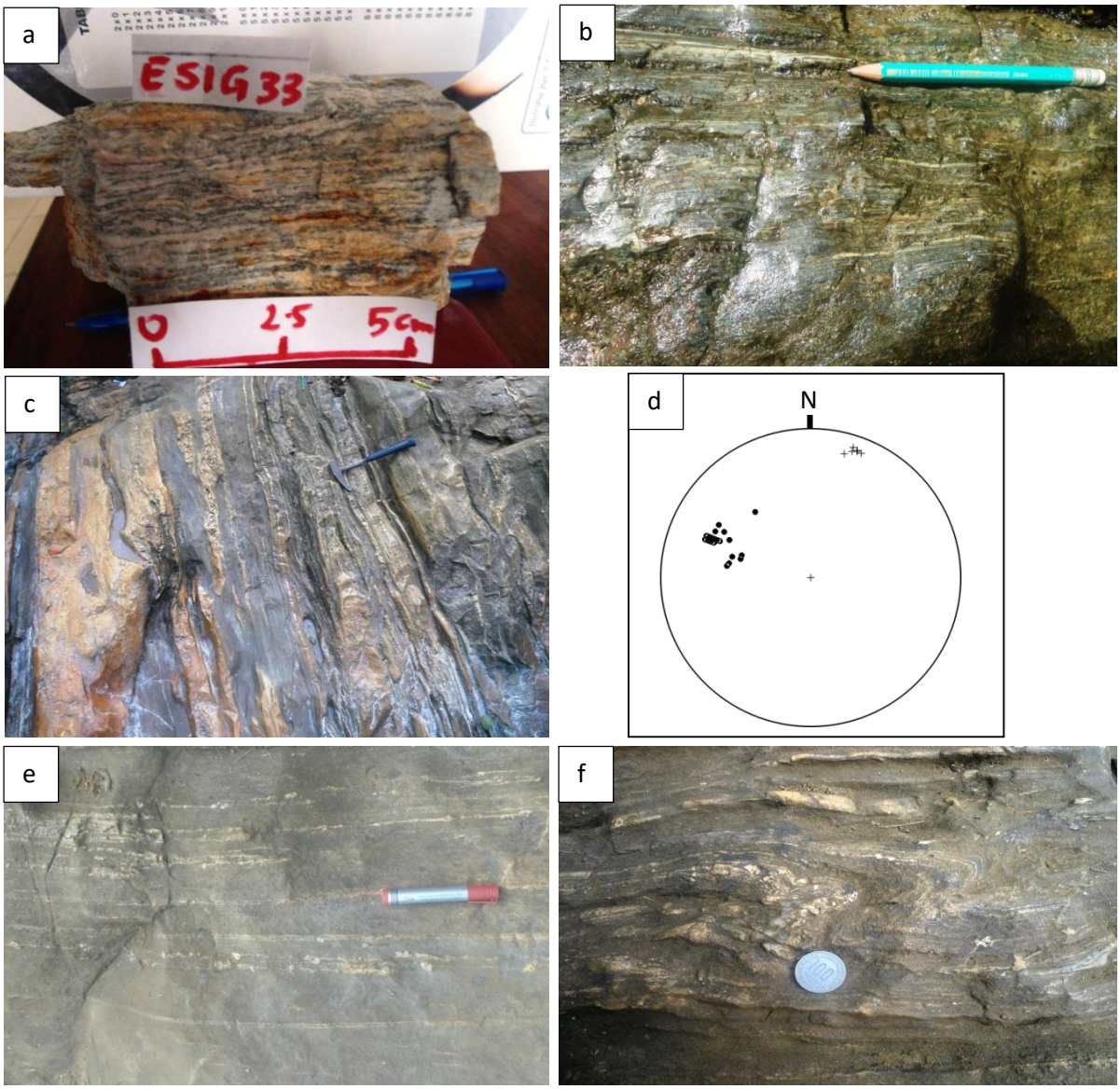

Figure 41: Structural elements of D_1 deformational phase, a) S_1 in gneiss, b) S_1 in amphibolite defining gnessosity,c) reinforcement of S_1 foliation by migmatitic banding, d) Stereographic representation of D_1 structures (S_1 and L_1): full cycle = S_1 and black cross = L_1,e) L_1 lineation define by stretching quartz and feldspar blasts, f) Intrafolial fold F_1 in biotite gneiss with axial plan oblique to S_1.

The L_1 lineation is a stretching mineral lineation, marked by elongated, often rotated feldspar porphyroblasts in gneiss (Fig. 41e), suggesting that the deformation was non-coaxial. L_1 lineation is associated to S_1 and trends NNE-SSW with average plunge 10° NE.

The F_1 folds are isoclinal folds, intrafolial with axial planes oblique to S_1 (Fig. 41f) and observed in the biotite gneiss having fold axis trend of N120E with plunge 115° ESE.

III.2 The second phase of deformation D_2.

The deformational D_2 phase is observed in the igneous and metamorphic rock units. This phase is associated with a development of mylonitic foliation (S_2), a ductile shear zones

and a shearing planes (C_2). Deformational D_2 phase also include boudin (β_2), folds (F_2) and a late brittle event.

In the igneous rocks, S_2 schistosity is observed in the granodioritic intrusion. It is marked by a preferred orientation of quartz crystals, k-feldspar crystals and biotite flakes defining a foliation trending N025E 65°SW (Fig. 42a.).

In gneisses, the S_2 mylonitic schistosity is almost parallel to S_1 gneissosity. In certain outcrops S_1 is reworked by S_2 and only relics of S_1 are preserved. S_2 is marked by a preferred orientation of stretched quartz blasts, sigmoidal feldspar blasts and biotite flakes.

The ductile zone is characterized by a gradual development of a mylonitic foliation (ms), from the protomylonite to ultramylonite. The mylonitic foliation is defined by stretched quartz and feldspar clasts, showing preferred orientation at outcrop scale (Fig. 42b).

Under the microscope, the mylonitic foliation is underlined by a preferred orientation of large and elongated clasts (quartz, K-felsdpar), as well as amphibole and mica fish. All these crystals are often surrounded by biotite and muscovite flakes, neocrystallized quartz and feldspar crystals. Those clasts constitute dark bands showing alternation with light bands made up of quartz and feldspar clasts.

C_2 constitutes one of the most prominent structures which characterize the second deformational phase (D_2). C_2 shearing planes are recorded in gneiss and mylonites. C_2 shearing planes transposed S_1, S_2 and Ms and display S/C fabric in some places (Fig. 42c) in mylonitic rocks. This event is generally oriented following N060E to N075E, and dip strongly W to NW. The shear planes are often empty but in some place, they are filled by injections of mafic minerals or quartz and feldspar, reminiscent of fluid-assisted deformation.

Small (5cm to 15 cm) quartz veins display asymmetric and symmetric boudins (β_2) (Fig. 42d) commonly observed in the mylonites and ultramylonite. Asymmetric β_2 boudins are the domino type and define a sinistral sense of shear. The symmetric boudins have their principal axes oriented parallel to the mylonitic foliation.

Sigmoidal tension gashes are often observed in *en echelon* arrays in blocks of breccias (Fig. 42e).

The F_2 folding event is observed in the gneiss and migmatite where it affects the S_1 regional foliation (Fig.42f). These are mostly asymmetric folds with axes that have an average trend of N110E with plunge 18° ESE.

L_2 is defined by preferred orientation of elongated quartz, feldspar and biotite flakes resulting in a stretching lineation trending N10-N40°E.

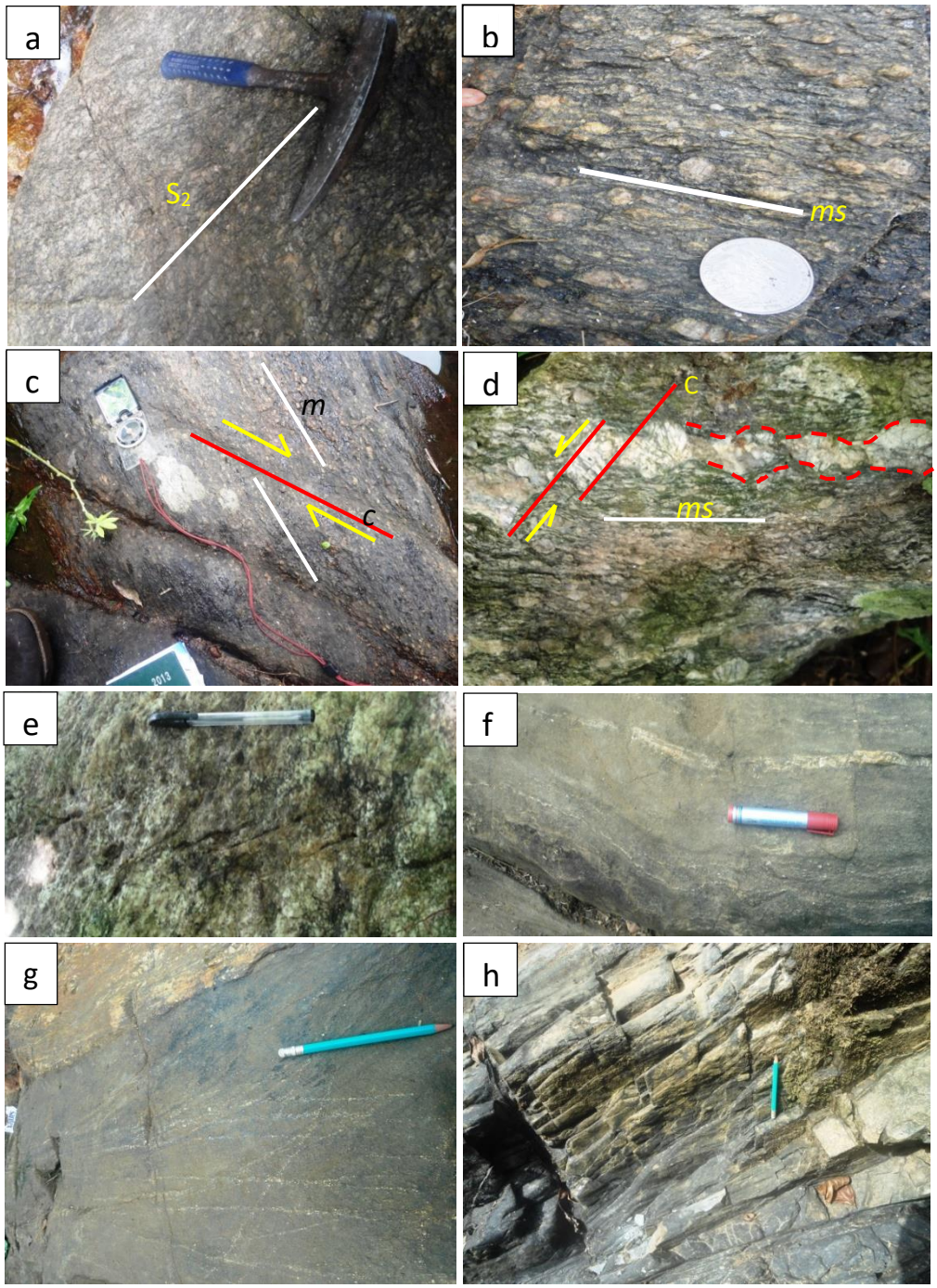

Figure 42: Structures related to D_2 deformational phase : a) S_2 Schistosity in granodiorite; b) Mylonitic schistosity (ms) in protomylonite marked by stretching feldspar and quartz clasts; c) C_2 schearing planes in mylonite: C_2 displace the mylonitic schistosity and both form S/C structures, Noticed dextral sens of schear; d) Domino type (assymetric) showing sinistral schearing and incomplete (symmetric) boudins in mylonite; e) Tension fissure in en echelon arrays with sigmoidal (S) shape in breccias' block; f) F_2 fold in gneiss; g) Fractures filled by quartz in biotite gneiss; h) joins and empty fractures in gneiss.

The fractures are quartzofeldspathic veins (Fig.42g) and joins (Fig. 42h). Four main fracture trends were observed: the first set is composed of NNW-SSE to N-S and N060E to

N065E fractures dipping strongly W to NW. The N060E to N065E fractures were encountered only in the brittle zone of the ESZ (Sigue *et al*., 2019) and they seem to be synchronous to the shear zone initiation.

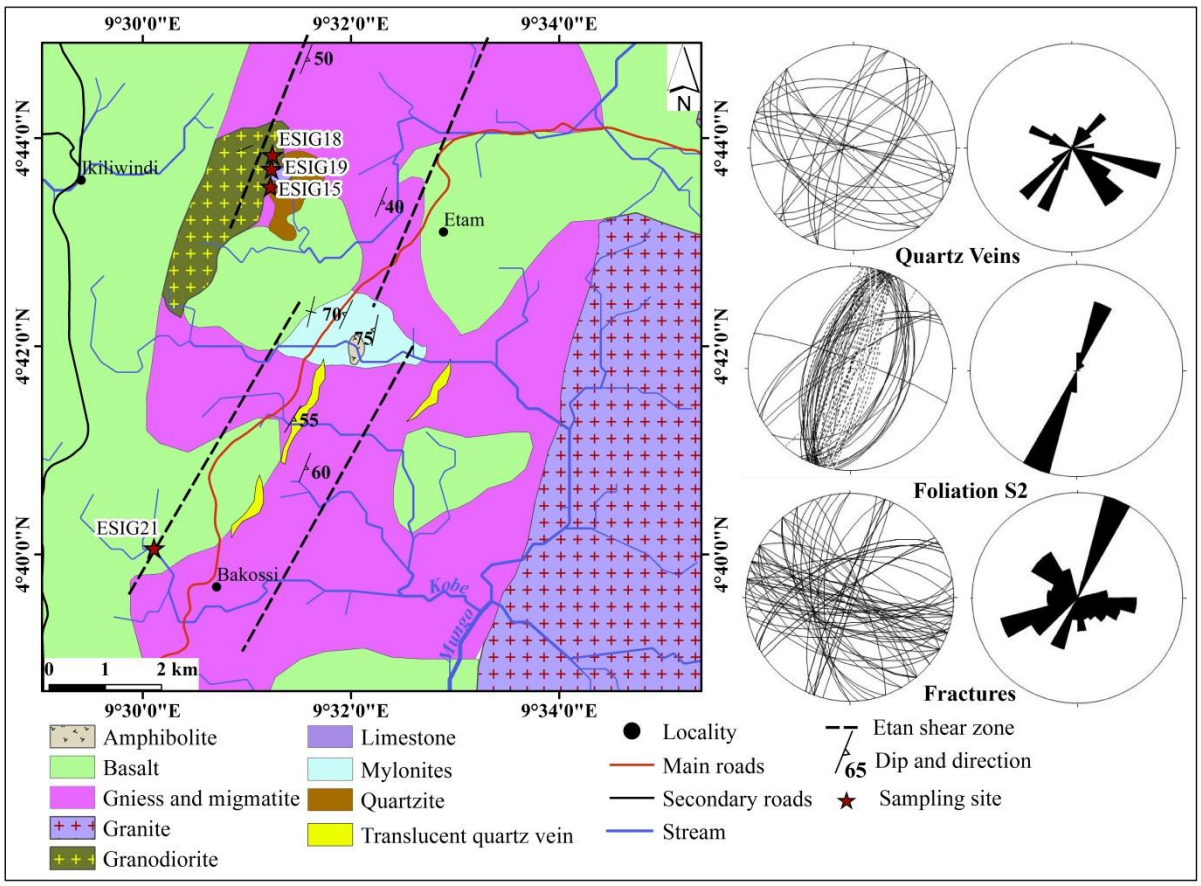

Figure 43: Structural map of study area.

The late fracture sets are sub-vertical structures which are oriented N120E to N140E and N100E to N110E and dip to the NW. S_2 generally strikes NNE-SSE and strongly dip either ESE or WNW, while the fracture event occurred randomly in the study Area (Fig. 43).

III.3 Microstructural analysis

In the study area, the microstructures of submagmatic deformation were observed in the granodiorite and gneiss and are characterized by microfractures of large feldspar and quartz crystals or clasts, filled with neo-recrystalized small quartz grains. Post magamatic deformation is also marked by mylonitic foliation in the granodiorite and defined by the preferred orientation of the slightly stretched quartz and feldspar clasts as well as biotite flakes. These features have been interpreted as representing synkinematic transition from magmatic to solid-state deformation in the shear zone (Neves and Vauchez, 1995). The undulose extinction of quartz porphyroclasts and the brittle behaviour of quartz grains also

suggest very low temperature condition of deformation in the area. Nevertheless, large feldspar porphyroclasts display several intragranular dilatant fractures and microcracks.

These structures sometimes distort cleavages in plagioclase clasts and suggest low confining pressure which enhances the deformation. The consistent albitization of K-feldspar by the formation of perthite suggest low-medium (400-500°C) conditions of metamorphism. In addition, the observation of myrmekite on the boundaries of large k-feldspar clasts suggests the temperature of deformation around 600°C (Passchier and Trouw, 2005; Dawai *et al.*, 2017).

IV Quartz-rich facies as HPQ source

IV.1 Field characteristics, petrographic and textural studies of quartzitic bodies

Several veins were observed in the study area. Most of these veins are quartz veins or quartzo-feldspathic veins (Fig. 43). They cross-cut various rock types (gneiss, mylonites, quartzite). In this work, two quartz veins were studied: (1) a large brecciated quartz vein, found in the brittle zone of the ESZ and, (2) a translucent quartz vein, observed within the biotite gneiss outcrop, at Mabanda village, which strikes N023E, parallel to the regional foliation.

IV.1.1 Petrography of the brecciated quartz bodies

The brecciated quartz bodies are situated in the northwestern corner of the Etam Shear Zone (ESZ). They are observed on about 150m wide and can be traced along strike for over 2.5km (Sigue et al,. 2019) in NNE-SSW to NE-SW direction. It shows blocks of breccia with variable dimensions (up to 20 m x 8 m) where small quartz veinlets/lenses (1 to 10 cm wide) are observed cuting across monomineralic blocks of quartzite (Fig. 44a). These late veinlets are randomly oriented or occur in sub-parallel arrays.

The brecciated quartzite blocks are composed mainly of milky quartz clasts that vary from < 0.2 mm to 8 cm in size (Fig. 44b). The quartz has the form of polygonal crystals showing sharp edges (Fig. 44c). The average clast size is between 1 and 5mm. Each quartz clast is locally strongly recrystallised (Fig.44d) due to post-crystallisation deformation related probably to shear zone (Central Cameroon Shear Zone) tectonics activities. The clasts are cemented by a silicified quartz matrix, composed of smaller quartz crystals, showing hexagonal small recrystallized quartz grain (Fig.44e, blue circle). The grain size of the cement ranges from 10 to 80 µm. The smaller quartz crystals some time form cluster of grains where red spots (colored material), probably Fe-bearing accessory minerals are observed (Fig.44f). The colored material is trapped within an aggregate of smaller quartz grains, and has no

apparent crystal habit. Fluid and mineral inclusions are common in the milky quartz. Detailed description of the petrographic characteristics of the milky quartz is provided in the paragraph on fluid inclusions below.

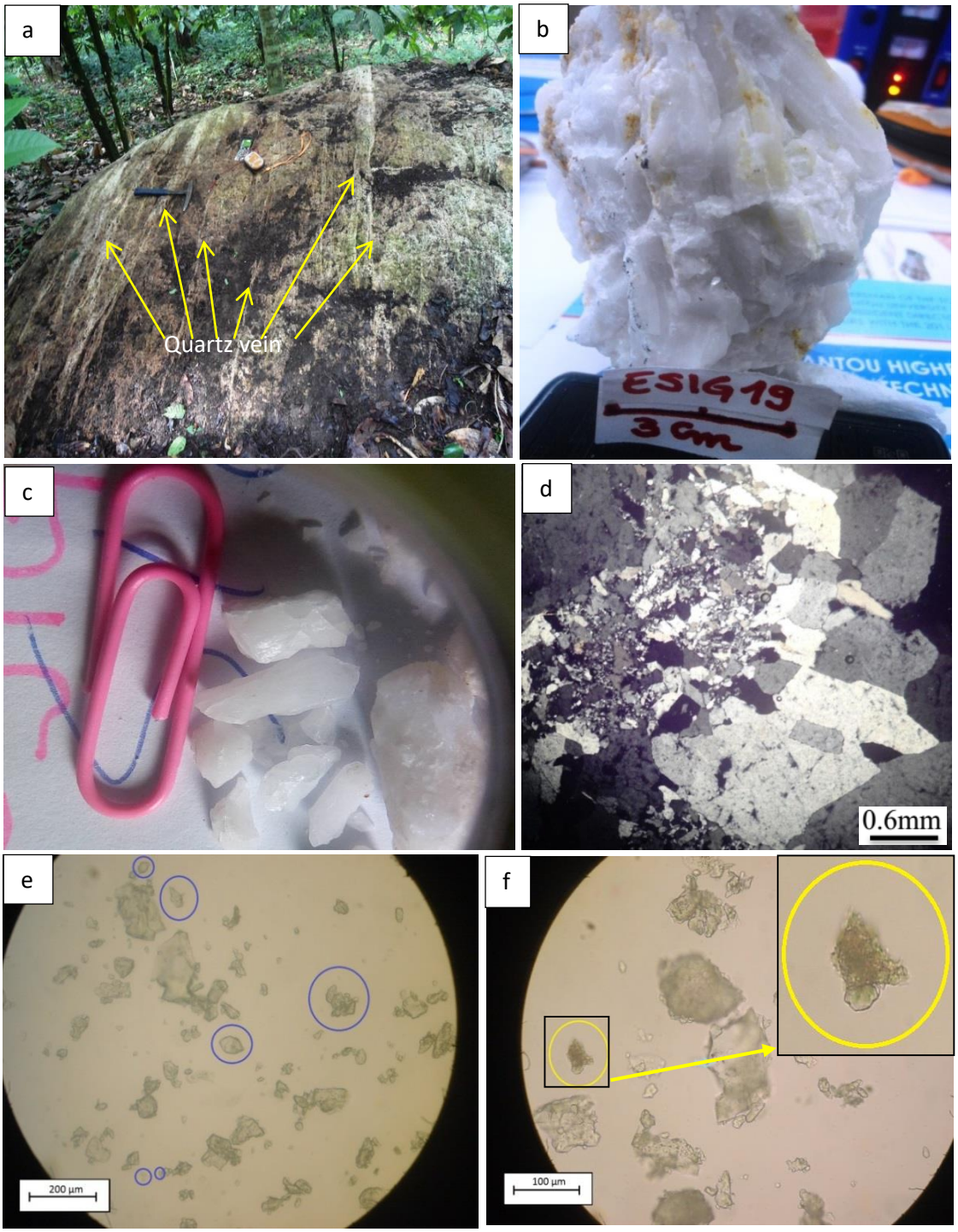

Figure 44: Field Features and petrography of the milky quartz: a) Brecciated quartzite block showing small quartz veins lenses, b) hand specimen of milky quartz clast, c) Milky quartz clast size (up to 12 cm), d) photomicrograph of milky quartz with quartz inclusion. e) Small recrystallized hexagonal quartz grain (blue circle). These grains constitute the siliceous matrix healding clasts. f) Cluster of small quartz grain contening red spot, probably iron oxide.

IV.1.2 Petrography of the translucent quartz vein

The translucent quartz vein is exposed at Mabanda village, southwestern sector of the study area. The vein is observed sandwich in the biotite gneiss outcrop which is partly covered by pioneer vegetation (Fig 45a). It is about 20 cm wide. The regional foliation in the gneiss and the vein are parallel and trend N023°E to N030°E with subvertical dip.

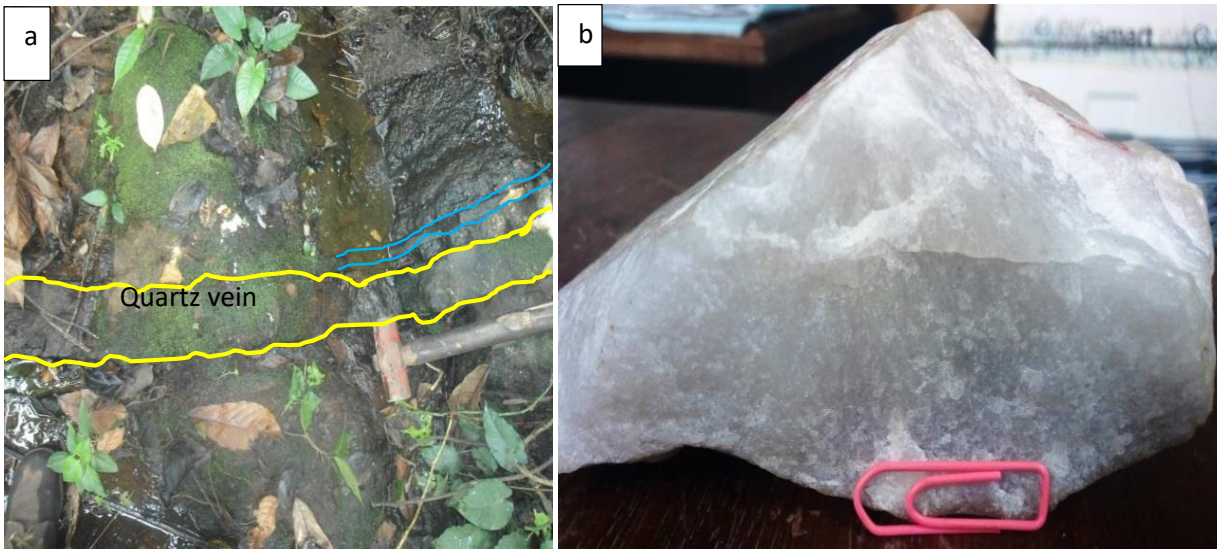

Figure 45: Aspect of translucent quartz vein: a) translucent quartz vein carried by the biotite gneiss outcrop (yellow lines), b) Hand specimen of the translucent quartz vein.

The vein is composed of highly homogeneous translucent fine-grained pure quartz (Fig.45b). They range from 1 to 3 µm in size, fluid and mineral inclusions are observed in some of the translucent quartz crystals. A detailed description of these features is also provided in the paragraph on fluid inclusions below.

IV.2 Geochemistry of Etam quartz

IV.2.1Whole rock geochemistry by ICP-MS

The whole rock chemistry of the Etam quartz samples is displayed in Table 7. The samples are characterised by high silica content with 98.46-99.75wt% SiO_2 and very low concentrations of the other major elements (Al_2O_3= 0.01 to 0.15wt%, Fe_2O_3tot =0.1 to 0.59wt%, MgO=0.01 to 0.02wt%, TiO_2=0.002 to 0.006wt% Na_2O=0.01 to 0.02). The concentration of K_2O (0.01 wt %) is constant. Most of the trace elements are below the detection limit. When present, their concentrations are low; e.g. Cr (55-220 ppm), Zr (3-4 ppm) and Ba (3-4 ppm).

Only four LREE are detected by ICP-MS analysis: La, Ce, Pr and Nd. The rest as well as the HREE are below the detection limit. The concentrations of light rare earth elements (LREE) vary slightly: La (0.2 to 0.4 ppm), Ce (0.3 to 0.4 ppm), Pr (0.03 to 0.05 ppm) and Nd (0.1 to 0.2 ppm).

IV.2.2 Trace elements concentration in Quartz by (LA-ICP-MS) Analysis

The results of the analysis ofrepresentative quartz samples are given in Table 8. Three quartz samples were selected from the brecciated quartz vein (milky quartz) and two samples from the translucent quartz vein. In order to better appreciate the chemical purity of the quartz, the elements' concentrations were converted to microgram/gramm ($\mu g g^{-1}$). The data illustrate that:

1) Milky quartz (samples ESIG15, ESIG18 and ESIG19) have high to very high concentrations of trace elements compared to average concentrations in natural quartz (Gotze, 2009; Muller *et al.*, 2012). Itis characterized by high and variable concentrations of Al (354 to 811 $\mu g.g^{-1}$), Ca (27.3 to 100 $\mu g.g^{-1}$), Fe (36.4 to 67.9 $\mu g.g^{-1}$) and K (89.9 to 261 $\mu g.g^{-1}$), moderately high Ti (3.64 to 7.38 $\mu g.g^{-1}$), Li (3.74 to 11.4 $\mu g.g^{-1}$) and low concentration for Zr (0.18 to 0.28 $\mu g.g^{-1}$) Ce (0.11 to 0.33 $\mu g.g^{-1}$) and Ge (0.12 to 0.17$\mu g.g^{-1}$).

2) Translucent quartz (ESG21a and ESIG21b) is characterized by relatively lower concentrations of trace elements compared to milky quartz: Al (mean 107$\mu g.g^{-1}$), Ca (mean 27.85) Fe (mean 26.05 $\mu g.g^{-1}$). An exception is observed for Ti concentration (mean 23.75$\mu g.g^{-1}$) which is consistently higher compared to Ti in milky quartz.The variability of concentrations in Ti between milky and translucent quartz is probably due to the difference of deformation temperature or the presence of mineral inclusions. Indeed, microscopic studies of transluscent quartz showed several rutile mineral inclusions in some translucent quartz grains which probably increase Ti concentration in this quartz. Similarly, the high concentration of Na and K in both quartz is reflected by the presence of several cubic salt crystals (NaCl) observed under the microscope. Lithium concentration is very low (0.51 $\mu g.g^{-1}$). This suggests the low participation of this element in the process of charge-balancing cation for Al, Fe, and P. Therefore the H^+ from hydrothermal fluid plays a greater role in the charge compensator for cation in translucent quartz.

Table 7: Major, trace and rare-earth element analyses of quartzite (analysis by ICP-MS)

	ESIG 1	ESIG 3	ESIG 4	ESIG 5	ESIG 10	ESIG 14	ESIG 15a
Majors Elements(wt %)							
SiO2	98.99	98.56	98.99	99.75	98.67	98.99	98.26
Al2O3	0.05	0.15	0.05	0.03	0.13	0.02	0.13
Fe2O3	0.55	0.5	0.59	0.1	0.39	0.51	0.49
MnO	0.006	0.005	0.006	0.006	0.005	0.006	0.005
MgO	0.02	0.01	0.02	0.02	0.01	0.02	0.01
CaO	0.02	0.02	0.01	0.02	0.02	0.02	0.02
Na2O	0.02	0.01	0.02	0.02	0.01	0.02	0.01
K2O	0.01	0.01	0.01	0.01	0.01	0.01	0.01
TiO2	0.005	0.002	0.005	0.004	0.002	0.006	0.002
P2O5	< 0.01	< 0.01	< 0.01	< 0.01	< 0.01	< 0.01	< 0.01
LOI	0.07	0.25	0.07	0.04	0.25	0.02	0.25
Total	**99.741**	**99.52**	**99.771**	**100**	**99.50**	**99.622**	**99.187**
Trace elements(ppm)							
Be	< 1	< 1	< 1	< 1	< 1	< 1	< 1
Sc	< 1	< 1	< 1	< 1	< 1	< 1	< 1
V	< 5	< 5	< 5	< 5	< 5	< 5	< 5
Cr	99	98	121	220	55	94	100
Co	< 1	< 1	< 1	< 1	< 1	< 1	< 1
Ni	< 20	< 20	< 20	< 20	< 20	< 20	< 20
Cu	< 10	< 10	< 10	< 10	< 10	< 10	< 10
Zn	< 30	< 30	< 30	< 30	< 30	< 30	< 30
Ga	< 1	< 1	< 1	< 1	< 1	< 1	< 1
Ge	1	< 0.5	1	1	< 0.5	1	< 0.5
As	< 5	< 5	< 5	< 5	< 5	< 5	< 5
Rb	< 1	< 1	< 1	< 1	< 1	< 1	< 1
Sr	< 2	< 2	< 2	< 2	< 2	< 2	< 2
Y	< 0.5	< 0.5	< 0.5	< 0.5	< 0.5	< 0.5	< 0.5
Zr	3	4	4	3	4	4	4
Nb	3.3	3.4	5	4.1	5.1	4.7	5.4
Mo	10	10	< 2	< 2	<2	<	10
Ag	< 0.5	< 0.5	< 0.5	< 0.5	< 0.5	< 0.5	< 0.5
In	< 0.1	< 0.1	< 0.1	< 0.1	< 0.1	< 0.1	< 0.1
Sn	< 1	< 1	< 1	< 1	< 1	< 1	< 1
Sb	< 0.2	< 0.2	< 0.2	< 0.2	< 0.2	< 0.2	< 0.2
Cs	< 0.1	< 0.1	< 0.1	< 0.1	< 0.1	< 0.1	< 0.1
Ba	4	4	4	4	3	3	4
Hf	< 0.1	< 0.1	< 0.1	< 0.1	< 0.1	< 0.1	< 0.1
Ta	< 0.01	< 0.01	< 0.01	< 0.01	< 0.01	< 0.01	< 0.01
W	< 0.5	< 0.5	< 0.5	< 0.5	< 0.5	< 0.5	< 0.5
Tl	< 0.05	< 0.05	< 0.05	< 0.05	< 0.05	< 0.05	< 0.05
Pb	< 5	< 5	< 5	< 5	< 5	< 5	< 5
Bi	< 0.1	< 0.1	< 0.1	< 0.1	< 0.1	< 0.1	< 0.1
Th	< 0.05	< 0.05	< 0.05	< 0.05	< 0.05	< 0.05	< 0.05
U	< 0.01	< 0.01	< 0.01	< 0.01	< 0.01	< 0.01	< 0.01
Rare Earth Element (ppm)							
La	0.4	0.2	0.2	0.4	0.2	0.3	0.2
Ce	0.3	0.4	0.4	0.3	0.4	0.4	0.4
Pr	0.05	0.05	0.03	0.03	0.05	0.05	0.05
Nd	0.1	0.2	0.2	0.2	0.2	0.2	0.2
Sm	< 0.01	< 0.01	< 0.01	< 0.01	< 0.01	< 0.01	< 0.01
Eu	< 0.005	0.01	0.01	< 0.005	0.01	0.01	0.01
Gd	< 0.01	< 0.01	< 0.01	< 0.01	< 0.01	< 0.01	< 0.01
Tb	< 0.01	< 0.01	< 0.01	< 0.01	< 0.01	< 0.01	< 0.01
Dy	< 0.01	< 0.01	< 0.01	< 0.01	< 0.01	< 0.01	< 0.01
Ho	< 0.01	< 0.01	< 0.01	< 0.01	< 0.01	< 0.01	< 0.01
Er	< 0.01	< 0.01	< 0.01	< 0.01	< 0.01	< 0.01	< 0.01
Tm	< 0.005	< 0.005	< 0.005	< 0.005	< 0.005	< 0.005	< 0.005
Yb	< 0.01	< 0.01	< 0.01	< 0.01	< 0.01	< 0.01	< 0.01
Lu	< 0.002	< 0.002	< 0.002	< 0.002	< 0.002	< 0.002	< 0.002

Table 7: continued

	ESIG 15b	ESIG 15c	ESIG 16	ESIG 17	ESIG 18	ESIG 19	ESIG 21a	ESIG 21b
Majors Elements								
SiO2	98.26	99.21	99.46	99.78	99.4	99.58	98.46	98.46
Al2O3	0.13	0.11	0.03	0.01	0.05	0.05	0.05	0.05
Fe2O3	0.49	0.32	0.32	0.11	0.36	0.21	0.58	0.58
MnO	0.005	0.005	0.006	0.006	0.006	0.006	0.006	0.006
MgO	0.01	0.01	0.02	0.02	0.02	0.02	0.02	0.02
CaO	0.02	0.02	0.02	0.02	0.02	0.01	0.02	0.02
Na2O	0.01	0.01	0.02	0.02	0.02	0.02	0.02	0.02
K2O	0.01	0.01	0.01	0.01	0.01	0.01	0.01	0.01
TiO2	0.002	0.002	0.006	0.002	0.005	0.006	0.006	0.006
P2O5	< 0.01	< 0.01	< 0.01	< 0.01	< 0.01	< 0.01	< 0.01	< 0.01
LOI	0.25	0.25	0.01	0.01	0.01	0.07	0.07	0.07
Total	**99.19**	**99.947**	**99.902**	**99.988**	**99.901**	**99.982**	**99.25**	**99.242**
Trace elements								
Be	< 1	< 1	< 1	< 1	< 1	< 1	< 1	< 1
Sc	< 1	< 1	< 1	< 1	< 1	< 1	< 1	< 1
V	< 5	< 5	< 5	< 5	< 5	< 5	< 5	< 5
Cr	100	81	77	220	199	216	220	220
Co	< 1	< 1	< 1	< 1	< 1	< 1	< 1	< 1
Ni	< 20	< 20	< 20	< 20	< 20	< 20	< 20	< 20
Cu	< 10	< 10	< 10	< 10	< 10	< 10	< 10	< 10
Zn	< 30	< 30	< 30	< 30	< 30	< 30	< 30	< 30
Ga	< 1	< 1	< 1	< 1	< 1	< 1	< 1	< 1
Ge	< 0.5	1	1	1	1	1	1	1
As	< 5	< 5	< 5	< 5	< 5	< 5	< 5	< 5
Rb	< 1	< 1	< 1	< 1	< 1	< 1	< 1	< 1
Sr	< 2	< 2	< 2	< 2	< 2	< 2	< 2	< 2
Y	< 0.5	< 0.5	< 0.5	< 0.5	< 0.5	< 0.5	< 0.5	< 0.5
Zr	4	3	4	3	3	4	3	3
Nb	5.4	3.9	3.8	3.1	3.1	3.1	3.1	3.1
Mo	10	<2	8	< 2	< 2	8	< 2	< 2
Ag	< 0.5	< 0.5	< 0.5	< 0.5	< 0.5	< 0.5	< 0.5	< 0.5
In	< 0.1	< 0.1	< 0.1	< 0.1	< 0.1	< 0.1	< 0.1	< 0.1
Sn	< 1	< 1	< 1	< 1	< 1	< 1	< 1	< 1
Sb	< 0.2	< 0.2	< 0.2	< 0.2	< 0.2	< 0.2	< 0.2	< 0.2
Cs	< 0.1	< 0.1	< 0.1	< 0.1	< 0.1	< 0.1	< 0.1	< 0.1
Ba	4	4	4	4	4	3	4	4
Hf	< 0.1	< 0.1	< 0.1	< 0.1	< 0.1	< 0.1	< 0.1	< 0.1
Ta	< 0.01	< 0.01	< 0.01	< 0.01	< 0.01	< 0.01	< 0.01	< 0.01
W	< 0.5	< 0.5	< 0.5	< 0.5	< 0.5	< 0.5	< 0.5	< 0.5
Tl	< 0.05	< 0.05	< 0.05	< 0.05	< 0.05	< 0.05	< 0.05	< 0.05
Pb	< 5	< 5	< 5	< 5	< 5	< 5	< 5	< 5
Bi	< 0.1	< 0.1	< 0.1	< 0.1	< 0.1	< 0.1	< 0.1	< 0.1
Th	< 0.05	< 0.05	< 0.05	< 0.05	< 0.05	< 0.05	< 0.05	< 0.05
U	< 0.01	< 0.01	< 0.01	< 0.01	< 0.01	< 0.01	< 0.01	< 0.01
Rare Earth Element (REE)								
La	0.2	0.3	0.2	0.4	0.4	0.4	0.4	0.4
Ce	0.4	0.3	0.4	0.4	0.4	0.4	0.4	0.4
Pr	0.05	0.05	0.04	0.03	0.04	0.03	0.03	0.03
Nd	0.2	0.1	0.2	0.1	0.2	0.1	0.1	0.1
Sm	< 0.01	< 0.01	< 0.01	< 0.01	< 0.01	< 0.01	< 0.01	< 0.01
Eu	0.01	<0.005	0.01	< 0.005	0.01	< 0.005	< 0.005	< 0.005
Gd	< 0.01	< 0.01	< 0.01	< 0.01	< 0.01	< 0.01	< 0.01	< 0.01
Tb	< 0.01	< 0.01	< 0.01	< 0.01	< 0.01	< 0.01	< 0.01	< 0.01
Dy	< 0.01	< 0.01	< 0.01	< 0.01	< 0.01	< 0.01	< 0.01	< 0.01
Ho	< 0.01	< 0.01	< 0.01	< 0.01	< 0.01	< 0.01	< 0.01	< 0.01
Er	< 0.01	< 0.01	< 0.01	< 0.01	< 0.01	< 0.01	< 0.01	< 0.01
Tm	< 0.005	< 0.005	< 0.005	< 0.005	< 0.005	< 0.005	< 0.005	< 0.005
Yb	< 0.01	< 0.01	< 0.01	< 0.01	< 0.01	< 0.01	< 0.01	< 0.01
Lu	< 0.002	< 0.002	< 0.002	< 0.002	< 0.002	< 0.002	< 0.002	< 0.002

Table 8:Trace elements concentrations (µg.g^{-1}) of samples from Etam (milky and translucent quartz).

		E-SIG15	E-SIG18	E-SIG19	E-SIG21a	E-SIG21b
Ag	µg.g^{-1}	0.002	0.003	0.004	0.011	0.009
Al	µg.g^{-1}	354	811	574	107	107
B	µg.g^{-1}	<LD	<LD	51	<LD	<LD
Ba	µg.g^{-1}	0.82	1.24	0.86	0.42	0.41
Be	µg.g^{-1}	0.07	0.10	0.05	0.03	0.03
Ca	µg.g^{-1}	64.3	47.8	100	27.3	28.4
Ce	µg.g^{-1}	0.11	0.19	0.33	0.08	0.06
Co	µg.g^{-1}	0.01	0.02	0.01	0.05	0.05
Cr	µg.g^{-1}	0.85	1.46	1.49	3.43	3.65
Cs	µg.g^{-1}	0.020	0.033	0.016	0.003	0.003
Cu	µg.g^{-1}	0.30	0.23	0.88	0.52	0.62
Dy	µg.g^{-1}	0.006	0.009	0.009	0.002	0.001
Er	µg.g^{-1}	0.004	0.004	0.005	0.001	0.001
Eu	µg.g^{-1}	0.001	0.003	0.003	0.001	0.001
Fe	µg.g^{-1}	36.4	67,8	67.9	26.5	25.6
Ga	µg.g^{-1}	0.06	0.15	0.05	0.02	0.02
Gd	µg.g^{-1}	0.004	0.016	0.010	0.003	0.002
Ge	µg.g^{-1}	0.15	0.12	0.17	0.83	0.84
Hf	µg.g^{-1}	0.004	0.009	0.008	0.04	0.04
Ho	µg.g^{-1}	0.001	0.001	0.002	< DL	< DL
K	µg.g^{-1}	89.9	261	< DL	81.0	83.8
La	µg.g^{-1}	0.07	0.36	0.11	0.04	0.04
Li	µg.g^{-1}	5.24	11.4	3.74	0.51	0.51
Lu	µg.g^{-1}	0.001	< DL	0.001	< DL	< DL
Mg	µg.g^{-1}	6.78	23.5	6.11	5.64	4.67
Mn	µg.g^{-1}	0.28	0.53	0.51	0.43	0.55
Na	µg.g^{-1}	37.2	32.3	41.0	34.7	34.8
Nb	µg.g^{-1}	0.04	0.04	0.02	< DL	< DL
Nd	µg.g^{-1}	0.03	0.16	0.08	0.02	0.02
Ni	µg.g^{-1}	0.44	0.71	0.73	1.82	1.87
Pb	µg.g^{-1}	0.18	0.17	1,59	0.19	0.11
Pr	µg.g^{-1}	0.01	0.05	0.02	0.01	0.01
Rb	µg.g^{-1}	0.95	3.15	0.40	0.38	0.33
Sb	µg.g^{-1}	0.002	0.002	0.012	0.003	0.004
Sc	µg.g^{-1}	< DL	< DL	< DL	< DL	< DL
Sm	µg.g^{-1}	0.006	0.02	0.02	0.004	0.003

Table 8: continued

		E-SIG15	E-SIG18	E-SIG19	E-SIG21a	E-SIG21b
Sn	µg.g^{-1}	< DL	< DL	< DL	< DL	< DL
Sr	µg.g^{-1}	1.43	1.50	1.34	0.26	0.26
Ta	µg.g^{-1}	< DL	< DL	< DL	< DL	0.02
Tb	µg.g^{-1}	0.001	0.002	0.002	< DL	< DL
Te	µg.g^{-1}	< DL	< DL	0.001	< DL	< DL
Th	µg.g^{-1}	0.02	0.04	0.05	< DL	< DL
Ti	µg.g^{-1}	6.60	7.38	3.05	23.3	24.2
Tl	µg.g^{-1}	0.006	0.017	0.002	0.002	0.001
Tm	µg.g^{-1}	0.001	< DL	0.001	< DL	< DL
U	µg.g^{-1}	0.007	0.010	0.02	0.007	0.008
V	µg.g^{-1}	0.13	0.20	0.05	0.02	0.02
W	µg.g^{-1}	< DL	0.002	< DL	< DL	0.002
Y	µg.g^{-1}	0.05	0.04	0.06	0.11	0.11
Yb	µg.g^{-1}	0.004	0.003	0.004	< DL	0.001
Zn	µg.g^{-1}	0.23	0.15	0.25	0.17	0.32
Zr	µg.g^{-1}	0.18	0.33	0.28	1.61	1.61

IV.2.3 Impurities evaluation in Transluscent quartz by LA-ICP-MS and EDS analysis

Samples of translucent quartz from Etam were furthermore analysed by LA-ICP-MS to better evaluate the chemical composition (quantity and quality) of these quartz samples.

Table 9: Major (wt %) and trace elements (ppm) analyses of translucent quartz (LA-ICP-MS) at Spot area 1

	ESIG21a1	ESIG21a2	ESIG21a3	ESIG21a4	ESIG21a5	ESIG21a6	ESIG21a7	ESIG21a8	ESIG21a9	ESIG21a10
Major elements (wt %)										
Al_2O_3	0.003	0.003	0.003	0.004	0.003	0.003	0.004	0.003	0.003	0.003
Fe_2O_3	0.001	0.001	0.002	0.001	0.003	0.001	0.001	0.001	0.001	0.001
MnO	<0.001	<0.001	<0.001	<0.001	<0.001	<0.001	<0.001	<0.001	<0.001	<0.001
CaO	0.043	0.045	0.047	0.048	0.043	0.042	0.054	0.059	0.062	0.068
Na_2O	0.101	0.084	0.075	0.091	0.087	0.101	0.124	0.116	0.097	0.117
K_2O	0.003	0.003	0.002	0.003	0.002	0.003	0.003	0.003	0.004	0.004
TiO_2	0.035	0.032	0.024	0.03	0.024	0.029	0.042	0.031	0.033	0.035
P_2O_5	0.017	0.02	0.021	0.024	0.02	0.021	0.023	0.048	0.03	0.036
Trace elements (ppm)										
Li	0.178	0.206	0.242	0.163	0.179	0.227	0.269	0.285	0.370	0.318
Be	0.079	0.076	0.068	0.069	0.075	0.081	0.094	0.104	0.106	0.091
B	2.980	3.250	2.850	2.860	2.660	2.860	3.970	3.440	3.250	3.850
S	348	331.7	329	340	328	318	349	335	322	340
Ge	2.32	1.43	1.32	1.28	1.30	1.30	1.46	1.57	1.53	1.60
Zr	126	145	100	127	169	123	167	197	194	199
Mo	0.122	0.131	0.099	0.113	0.132	0.131	0.157	0.163	0.156	0.163

Table 10:Major and trace elements analyses of translucent quartz (LA-ICP-MS) at spot area 2

	ESIG21b1	ESIG21b2	ESIG21b3	ESIG21b4	ESIG21b5	ESIG21b6	ESIG21b7	ESIG21b8	ESIG21b9	ESIG21b10
Major elements (wt %)										
Al_2O_3	0.007	0.008	0.005	0.007	0.007	0.005	0.005	0.007	0.007	0.004
Fe_2O_3	0.002	0.011	0.002	0.006	0.002	0.002	0.002	0.002	0.002	0.002
MnO	<0.001	<0.001	<0.001	<0.001	<0.001	<0.001	<0.001	<0.001	<0.001	<0.001
CaO	0.094	0.104	0.074	0.064	0.091	0.064	0.067	0.065	0.067	0.085
Na_2O	0.318	0.337	0.22	0.224	0.224	0.14	0.173	0.159	0.143	0.174
K_2O	0.005	0.006	0.004	0.004	0.006	0.003	0.003	0.004	0.005	0.004
TiO_2	0.079	0.071	0.063	0.055	0.063	0.049	0.05	0.057	0.052	0.049
P_2O_5	0.032	0.024	0.026	0.036	0.028	0.035	0.021	0.021	0.019	0.035
Trace elements (ppm)										
Li	0.536	0.476	0.437	0.630	0.494	0.392	0.328	0.360	0.282	0.319
Be	0.225	0.213	0.180	0.175	0.189	0.125	0.120	0.135	0.113	0.122
B	6.670	6.500	5.720	5.900	6.130	4.350	5.370	4.550	4.340	4.630
S	453	444	397	438	422	373	371	379	371	398
Ge	3.85	2.37	2.11	2.12	2.17	1.76	1.90	1.91	1.78	1.75
Zr	172	215	195	187	206	197	172	187	143	141
Mo	0.389	0.375	0.300	0.310	0.327	0.221	0.192	0.216	0.186	0.222

According to the data obtained by the ICP-MS investigation, this quartz type has the highest HPQ potential, thus it was selected for further testing by laser ablation. Sample ESIG21 was divided into two, ESIG21a and ESIG21b. Two spots were analysed in sample ESIG21a and three in sample ESIG21b. Ten spots replicate analyses were performed in each spot point area. In situ data (wt%) of Al_2O_3, Fe_2O_3, MnO, CaO, Na_2O, K_2O, TiO_2 and P_2O_5 and concentrations of some trace elements (ppm) of Li, Be, B, S, Ge, Zr and Mo for ESIG21a and ESIG21b are given in table 9 and table 10 respectively for ESIG21a and ESIG21b. Data show that, element concentrations determined by in situ LA-ICP-MS (table 9 and table 10) are generally lower than those determined with solution ICP-MS (table 7), probably due to the fact that during laser ablation the analysis of visible (>0.5 μm) micro-inclusions can be avoided by choosing clear inclusion-free areas for ablation. Therefore, it is assumed that concentrations measured by LA-ICP-MS reflect almost the values of lattice-bound trace elements (Gotze et al 2017).

This is furthermore observed by the quantitative and qualitative chemical analysis of these quartz samples shown in EDS spectra where spectra show that the translucent quartz is composed only of O and Si as indicated by the presence of consistent large peaks in all EDS spectra (Fig. 46 and 47). The absence of any peaks for other elements that could have been contributed by submicroscopic or nanoparticle mineral inclusions indicated that this quartz variety is free of contaminant mineral inclusions.

IV.3 Fluid inclusions petrography

Inclusions observed in the Etam quartz samples generally are of the fluid type. They are monophase inclusions and/or two-phase inclusions. In this study the fluid inclusion for the brecciated quartz samples are studied and their results presented separately from the data derived from samples of the translucent quartz vein.

IV.3.1 Fluid inclusions in milky quartz

In the milky quartz, most of the fused grains contain abundant inclusions with small size(Fig. 48) ranging from 2 to 12 µm and are randomly distributed in the grains (Fig. 49a). They are monophase or two-phase inclusions showing two distinct phases at room temperature: a solid daughter crystal phase and a fluid phase.

- ***Monophase fluid inclusions***

The monophase fluid inclusions are fewer in number compared to the two-phase fluid inclusions. They form negative crystals and sometimes bear inclusions (Fig. 49b, Orange arrow), which appear to be apatite crystals, because of the high Ca amounts observed in ICP-MS analysis (Table 7).

- ***Two-phase and three-phase fluid inclusions***

The majority of fluid inclusions in the milky quartz are two-phase fluid inclusions. Usually they are composed of liquid and gas although some have daughter crystals. The presence of halide crystals indicates that the liquid phase is probably brine while gas phase is CO_2. In this quartz, they often have a spherical gas bubble (Fig. 49c, black arrows). The volume of these bubbles ranges from 5 to 30% of the total volume of the inclusion. In shape, many two-phase inclusions are irregular (Fig. 49c, black arrows). Smaller regular inclusions are also observed with bubble, often larger than the liquid in terms of volume (Fig. 49c Blue arrow) compared to the irregular ones. Some two-phase inclusions have a negative hexagonal crystal-shape (Fig. 49d, black arrow).

Solid phases observed in the fluid inclusions mostly display cubic outlines(Fig. 49d and 49e, red arrow) which are probably salt crystals (NaCl), as attested by the high amount of Na present in the ICP-MS data (Table7). Melt inclusions are rare, larger (12µm) than mineral inclusions (Fig. 49e, green arrow) and are mostly irregular in sharp.

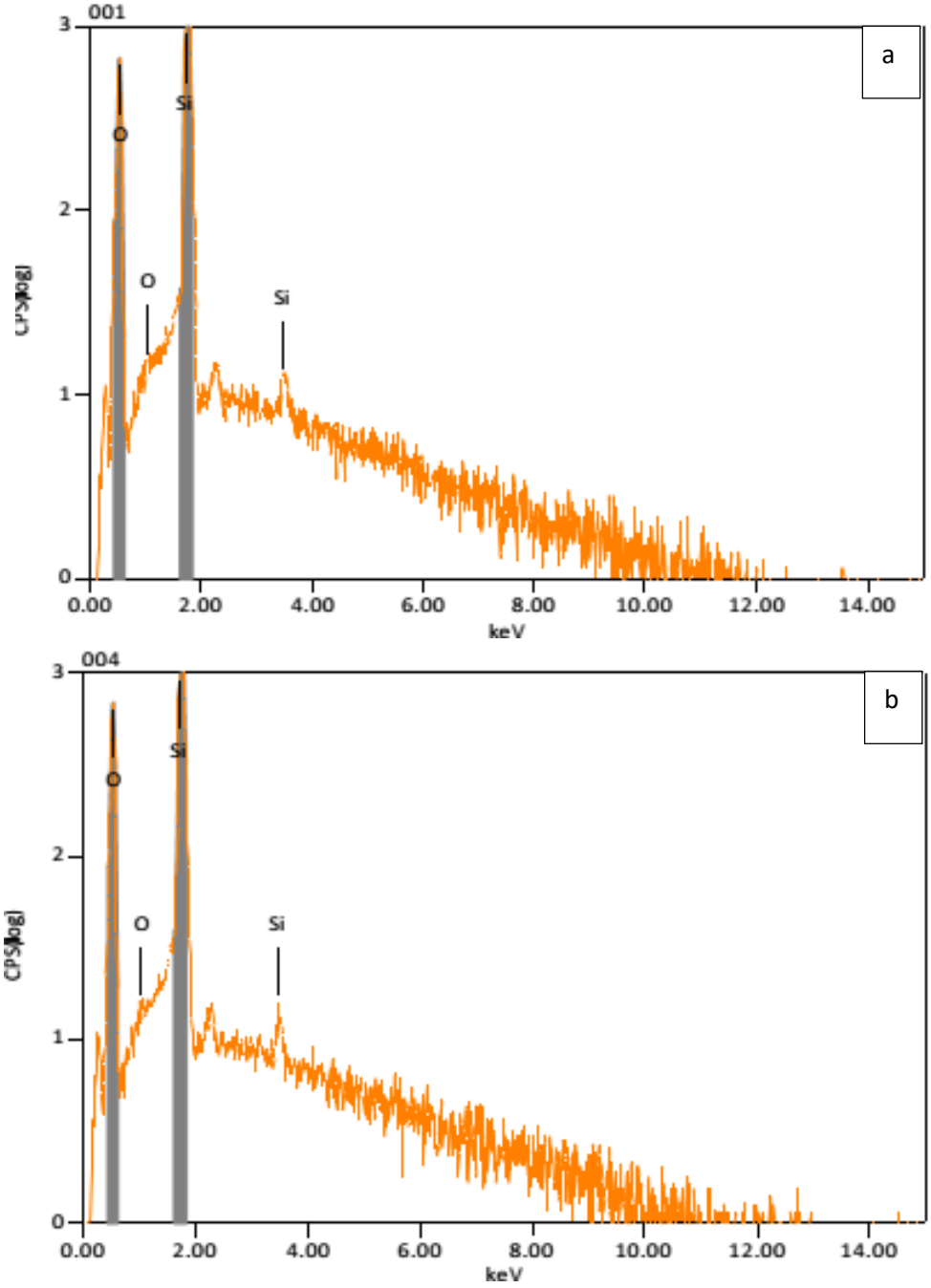

Figure 34: EDS patterns for transluscent quartz grain (ESIG21a): (a) pattern for quartz grain at point 1, (b) pattern for quartz grain at point 2.

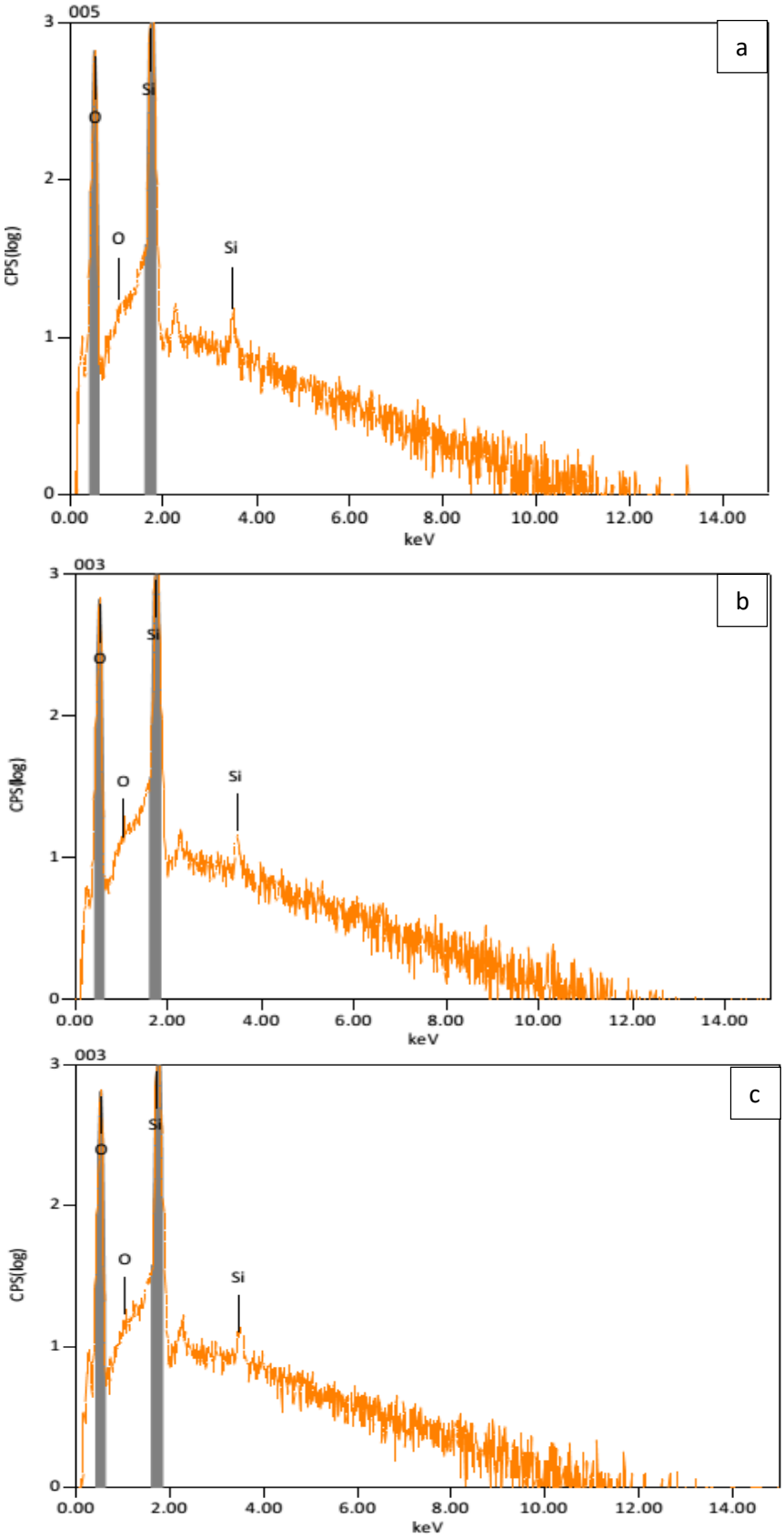

Figure 47: EDS patterns for transluscent quartz grain (ESIG21b): (a) pattern for quartz grain at point 1, (b) pattern for quartz grain at point 2 and (c) pattern for quartz grain at point 3

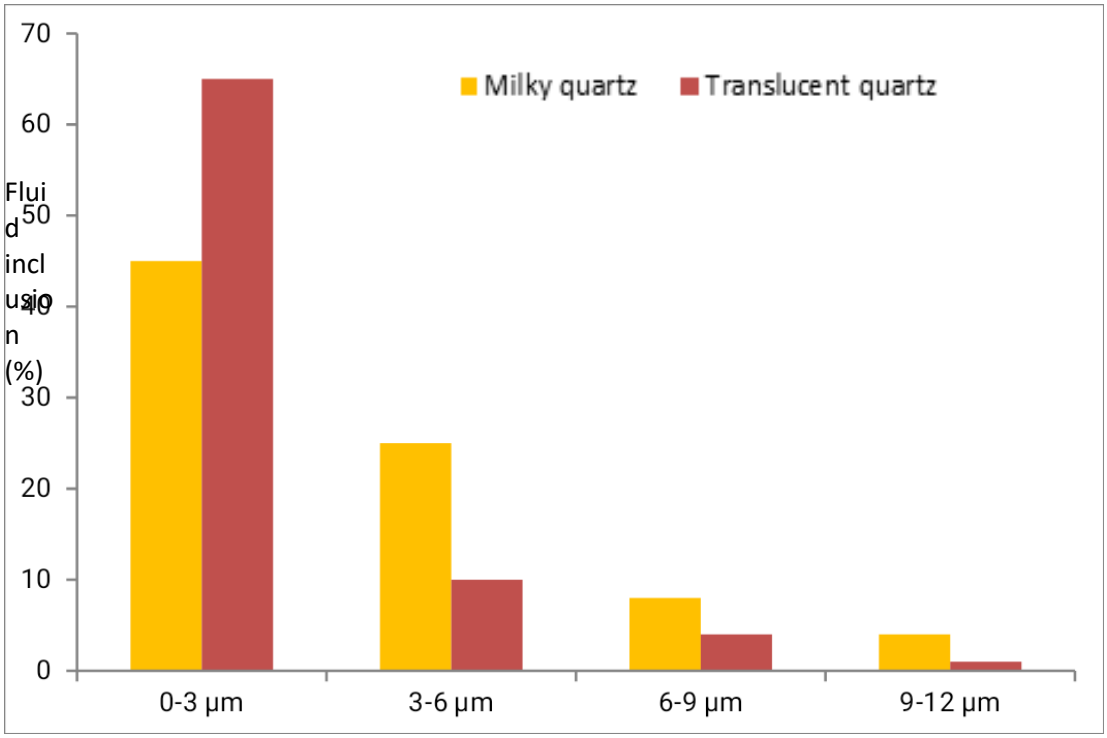

Figure 35: Histogram showing proportion of fluid inclusions in both milky and translucent quartz from Etam.

Some large inclusions are observed with small inclusions or satellite inclusions surrounding them (Fig. 49f, blue light arrow) in this quartz. Torantola et al (2010, 2012) showed that, due to deviatoric stress, inclusions can be deformed and dismembered, giving a large relic inclusion and a cluster of small neonate (satellite) inclusions around it (Fig. 50).

IV.3.2 Fluid inclusions in translucent quartz

Fluid inclusions in the translucent quartz are very few compared to the milky quartz (Fig. 48). Generally, they show features different from the milky quartz fluid inclusions. Some quartz have mineral inclusions, probably apatite. The shape is similar to the previous ones, but the size is much smaller. In these quartz samples, monophase inclusions are common and occur as dypiramidal monophasic inclusions (Fig. 51a, orange arrow). Two-phase inclusions are mostly the negative crystal type. They are small in size and generally form trails (Fig. 51b, black arrow and black line).

Mineral inclusions are represented by: 1) red hexagonal small mineral inclusions (Fig. 51a, pink arrow) which are probably iron-rich minerals, 2) needle-shaped mineral inclusions (Fig. 51c, grey arrow) which are suggested to be rutile because of the elevated concentration of Ti in ICP-MS analyses (Table 7). The acicular inclusions are common, small and randomly distributed in the grain.

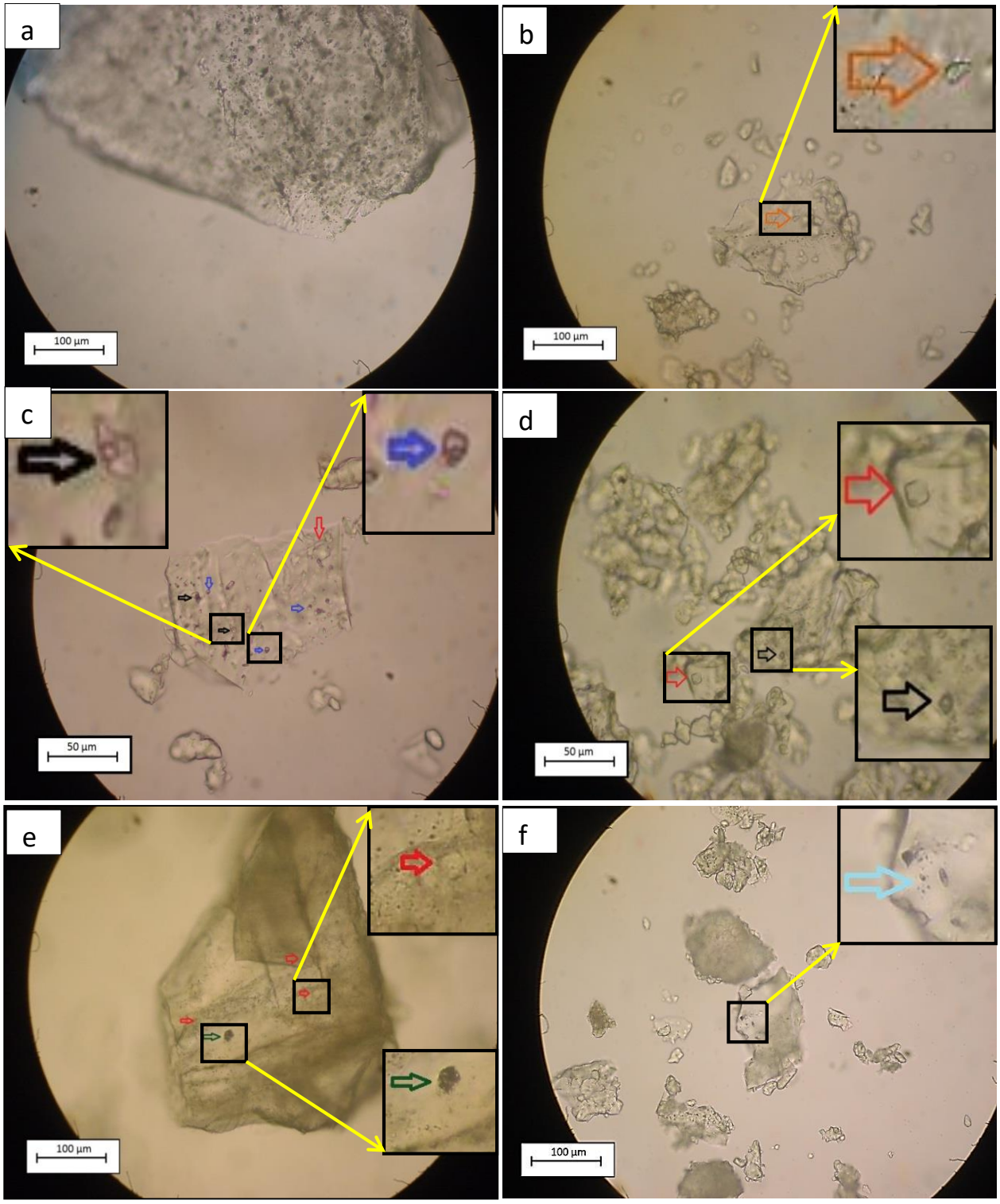

Figure 49: Fluid Inclusions in Milky quartz samples : a) Inclusions are large in quantities and small in size, b) dypiramidal monophasic inclusions probably apatite (orange arrow), c) Regular (black arrow) and Irregular (blue arrow) biphasic inclusion, d) negative quartz crystals (Black arrow) and cubic inclusion (Red arrow), e) Mineral inclusion (red arrow) and melt inclusion (green arrow), f) Fluid inclusion surrounded by small inclusion (satellite inclusions).

Figure 50: Fluid inclusion deformed by deviatoric stress, After Torantola et al., 2010

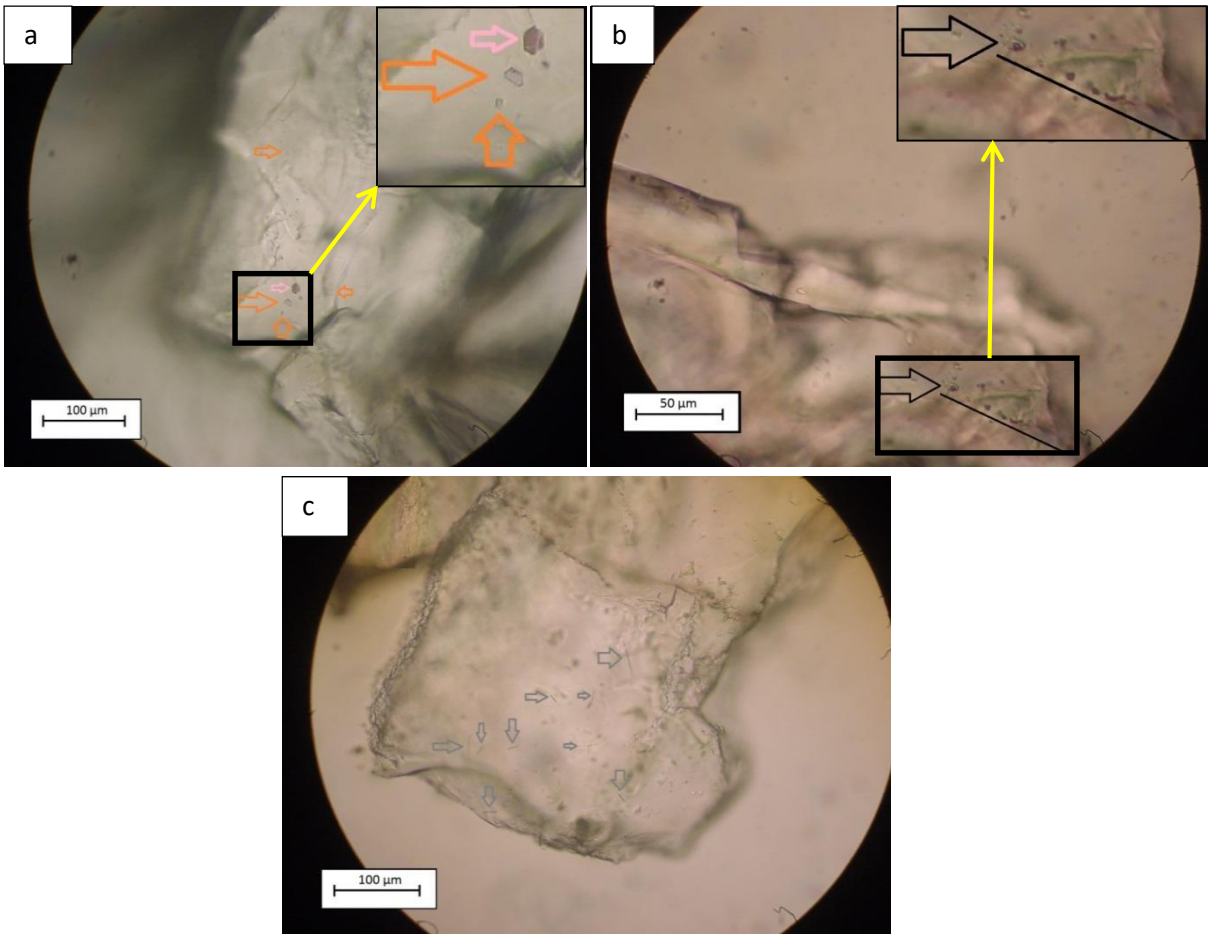

Figure 51: Fluid inclusion in translucent quartz: a) Dipyramidal monophasic fluid inclusion (orange arrow) and Mineral inclusion (pink arrow), b) Negative biphasic crystal incusion generally oriented, c) Needle mineral inclusion, probably rutile.

IV.4 Fusion of quartz grains over silica plate

IV.4.1 Bubbles formation

Fluid inclusions can contain several liquids and gasses, especially water and carbon dioxide (Götze et al., 2004; Santos et al., 2013; 2015), but can also contain salts, such as NaCl and KCl dissolved in water, which can produce chloride gas during the heating process for melting (Götze, 2009). Liquids and gasses present in the fluid inclusion are trapped within the silica melt and form the bubbles during the fusion. Those bubbles then tend to agglomerate and grow, as more time and energy are spent on the fusion process. It is has been shown that

the growth of air bubbles was more pronounced when the liquids were water and nonionic polymeric solution (Oliveira et al., 2014).

In this section the results of the quartz/silica plates tested for bubble formation are presented in the form of photos at various stages of heating. The images were then processed by computational analysis, in order to measure average bubble size and bubble density on each photo. Good HPQ material forms very few or no bubbles during this test.

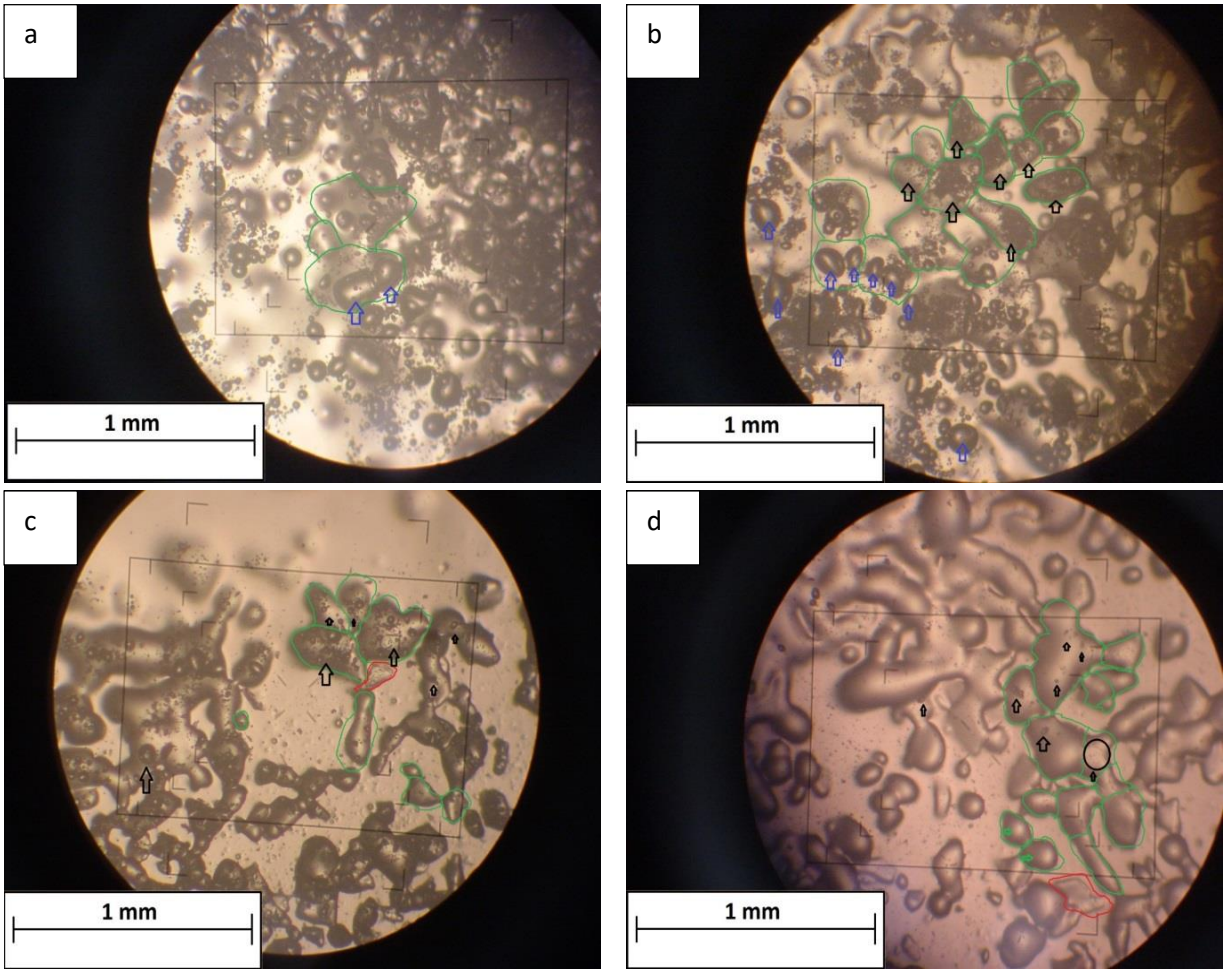

Figure 36: Photomicrographs of the fused quartz powders over silica plates where fused grains can be observed with formed bubbles inside. a) High quantity and very large bubble (blue arrow) formation in fused grains, b and c) Large quantity of bubble and clusters of small bubbles (Black arrow), d) Cleans fused grain with free bubble formation (green arrow) and small bubbles in grains (balack arrow). The green lines circles the grains that have been effectively fused, the red lines circles the "unfused" grains.

IV.4.2 Bubbles characterization

Three samples of milky quartz and two samples of translucent quartz were selected for silica fused analysis. The size and the average content of bubbles present vary among the samples:

1) Milky quartz samples (ESIG15, ESI18 and ESIG19) are from the brecciated quartz vein. The rock is brittle, and clasts are cemented by smaller quartz crystals. These small quartz crystals (10 to 80 μm in size) are separated upon grinding. Bubble characterization of all the milky quartz samples display large quantity of bubble formation in fused grain (The green lines encircle the grains that have been effectively fused, where one or more bubbles are shown inside) and bubble size distribution in the range of 10–240 μm with a mean diameter of 75 μm (fig. 520a and 52b, blue arrow). But, the majority (80%) of bubbles are from 50 to 80 μm in diameter while 90% were smaller than 140 μm.

Large clusters of small bubbles (less than 30 μm) were commonly observed in several fused grains of milky quartz (Fig.52b and 52c, Black arrow) and no bubble-free fused grains were observed in it. 2) Translucent quartz vein samples, Compared to the milky quartz samples shows an aspect of massive rock and they are not brittle. Figure 52d permit to observe grains before and after fusion. In fused state, the exact bubbles that form from each grain are distinctively observed. Translucent quartz samples do not produce many bubbles compared to the previous ones (milky quartz), and also the size of the bubble is drastically reduced. More than 90% of the bubbles are less than 10 μm (Fig. 52d Black arrow). Clean grains, that have not produced bubbles upon fusion are clearly identified (Fig. 52d, green arrows) and represent about 40%.

IV.4.3 Etam quartz fusion compared to other silica glass fusion

The results of the bubble formation test for the Etam translucent quartz (Fig. 53a) are compared here to the milky samples (Fig. 53b) and the transparent quartz (Fig. 53c) from Corinto and Olhos D'agua respectively (samples from the Serra de Santa Helena formation-Brazil, Santos et al., 2014), and to the commercial powder, IOTA powder (Fig. 53d).

The comparison shows that the milky quartz samples from Olhos D'agua formed more bubbles compared to the three other samples. Moreover, sample of translucent quartz, transparent quartz or the IOTA powder have formed small bubbles than the milky quartz sample during fusion over silica plate.

Between sample of translucent quartz from Etam, transparent quartz from Olhos D' agua or the IOTA powder, the variation of the size and amount of bubbles among the samples is negligible. These samples therefore seem similar from the point of view of bubbles formation after fusion over silica plate. A more careful observation shows that the translucent quartz sample from Etam has small bubbles formation, similar to the transparent quartz from Olhos D' agua which was concluded to be equivalent to commercial (IOTA) powder (Santos *et al.*, 2015).

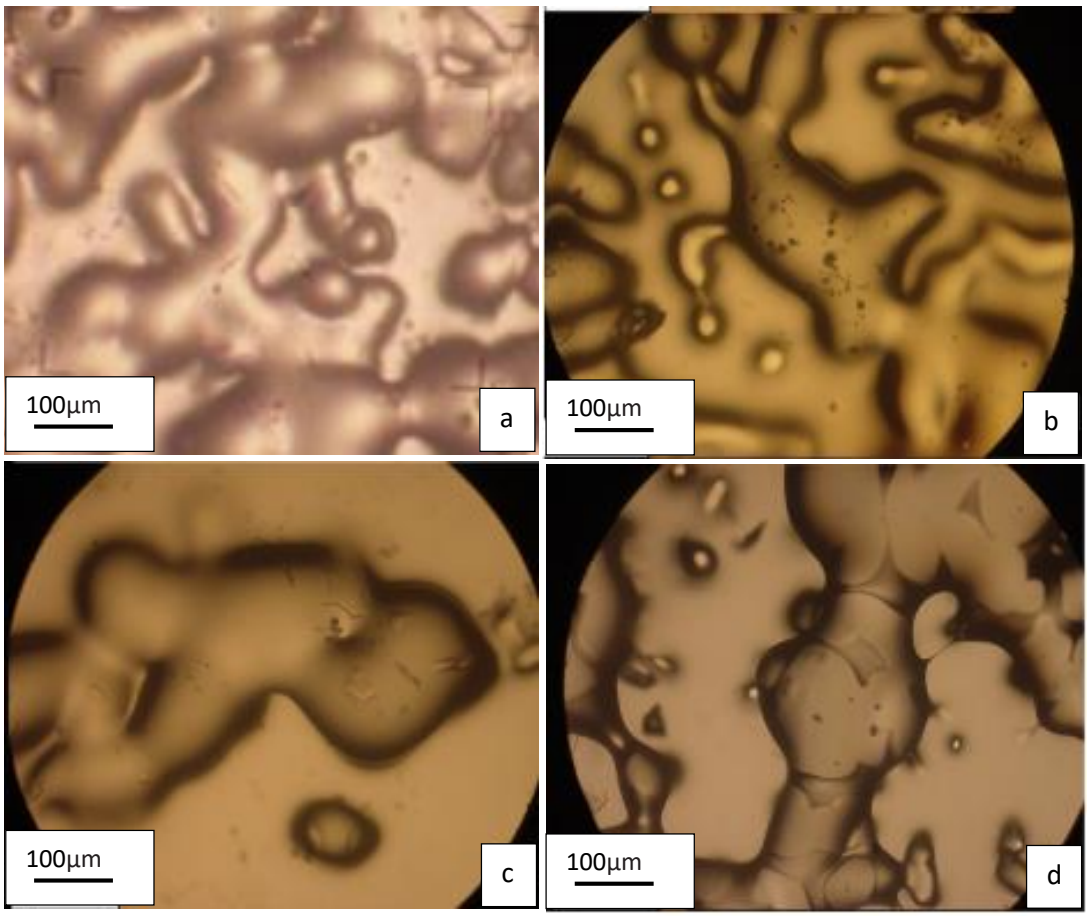

Figure 53: Compared photomicrographs of the fused quartz powders over silica plates: a) Translucente quartz from Etam, b) milky quartz from Olhos D'agua, c) transparent quartz from Corinto and d) Iota commercial powder (Santos et al., 2015). Small black dots represent bubbles.

CHAPTER IV

INTERPRETATIONS AND DISCUSSIONS

I Host rocks

I.1 Deformation and felsic plutonism

I.1.1 Origin of Etam Granites

The granitoids of Etam intruded a low to medium-grade metamorphic basement of greenschist to amphibolite facies. The geochemical characteristics of these granitoids show that they are high-k calc-alkaline affinity to shoshonitic and feroan, similar to some granitic rocks that have been studied in the Pan-African belt of Cameroon (Djouka-Fonkwe et al., 2008; Nzenti et al., 2006; Bambi et al., 2012). They are strongly peraluminous and belong to S-type granitoids (A / CNK ratio > 1.1). Although the majority of granitoids studied in the Pan-African belt of Cameroon are of the I-type, literature on S-type granitoids in this belt exist (Kalsbeek et al., 2001; Djouka et al,. 2008; Nzenti et al,. 2011; Kouankap Nono et al., 2018). The high SiO_2 (69.07-72.17) and Al_2O_3 (14.11-15.54) contents and the low MgO (0.26-0.5) and CaO (0.43-1.53) contents of the Etam granitoids are similar to some S-type granite studied in the Bamenda highlands (Nzenti et al., 2011; Kouankap Nono et al., 2018), also to metasediment melting liquids produeced experimentally (Patiño Douce and Johnston, 1991) and similar too to liquids from meta-igneous protoliths (Vielzeuf and Holloway, 1988). Their low Nb/U ratio (≤10) is typical of crustal granite (Hofmann et al., 1986). Further more, the high Rb/Sr (0.92 – 1.46) and low Sr/Ba (0.18 – 0.26) ratios coupled with strong negative Eu (Eu/Eu* = 0.37-0.59) anomalies characterized the lower degrees of vapour-absent crustal melting. These are features that suggest that the S-type granite in Etam have a pelitic protolith, and that, during the partial melting, melts were unfractionated and involved only felsic components from the upper crust (Harris and Inger, 1992; Kwékam et al., 2015).

I.1.2 Petrogenesis

In the molar CaO/(MgO + Fe_2O_3) versus molar $Al2O_3$/(MgO + FeO_{total}) diagram (Altherr, et al., 2000) the Etam samples plot in the domain that straddles the metapelite and metagreywacke fields (Fig. 54). The CaO/NaO_2 ratio point to a pelitic source to psammitic source (Sylvester, 1998). Figure 55 shows that granitoids from Etam were derived from mostly clay-poor, plagioclase-rich psammitic source material with high CaO/Na2O>3. These source rocks are predominantly found in the upper part of the continental crust and we suggest that the source for the Etam plutonic rocks was metamorphosed upper crustal metasedimentary rocks. The Na_2O/K_2O versus SiO_2 diagram of Gills (1981), shows that the Etam granitoids are K-granitoids (Fig. 56). Such granites often result from the partial melting of metamorphosed rocks (Gills, 1981; Nzenti et al., 2011). The relationship has been

observed between LREE enrichment in S-types granitoids and the process of partial melting of the source rock (Harris and Inger 1992, Nzenti et al., 2011). Indeed, the LREE enrichment in granite correlates negatively with the low degrees of partial melting although this effect is less important in metapelitic protoliths in the absence of vapors

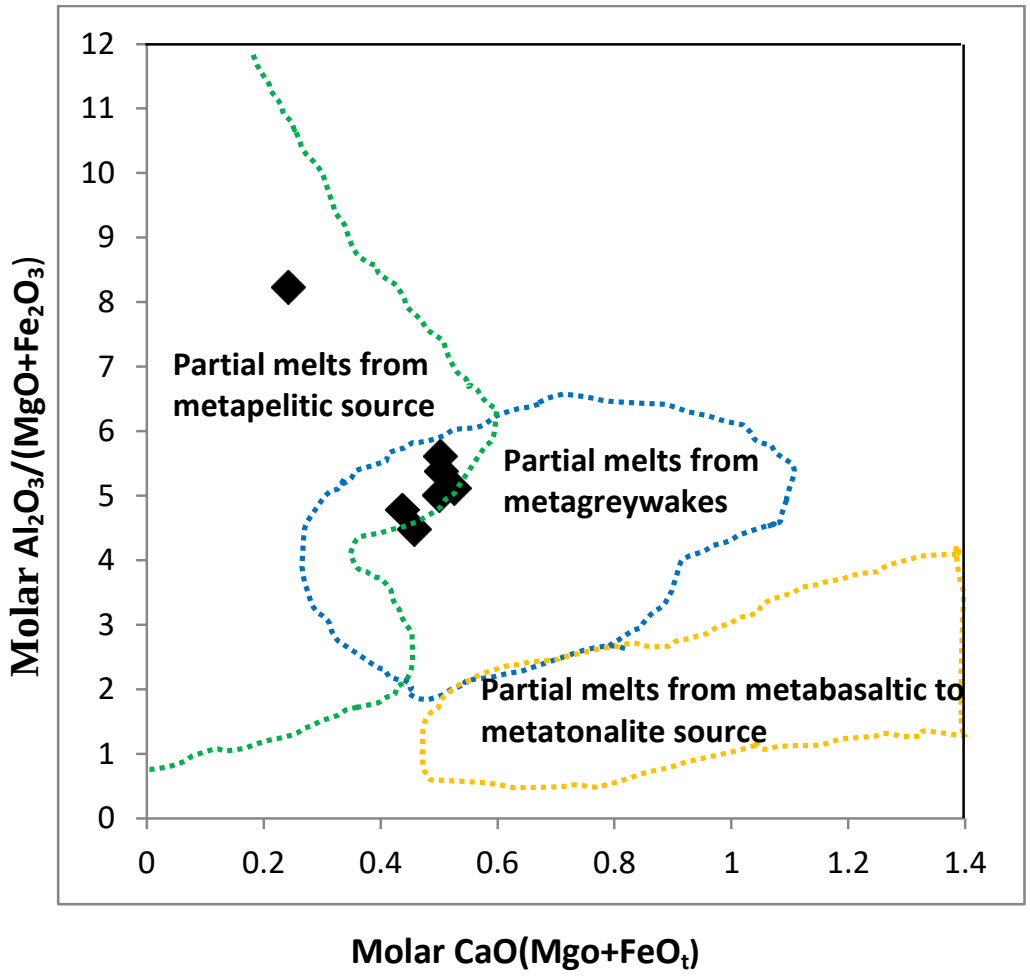

Figure 54: Molar diagram CaO/(MgO+FeOt) vs Al2O3/(MgO+FeOt) for the Etam granites.

The low Rb/Sr ratio and the negative Eu anomalies suggest the low hydrous conditions of partial melting and the participation of biotite during this process (Le Fort et al., 1987; Guillot and Le Fort., 1995; Guo and Wilson,. 2012; Nzenti et al., 2011). The depletion in Ba, Sr and Ti can be related to the composition of the protolith (Nzenti et al., 2011); these elements may have a low content in the source rock or retention in the residue during partial melting. Nzenti et al., (2011) stated that the large-scale melting of the source rocks could have been favoured by high heat flow during the Pan-African orogenesis or underplating of mantle-derived magmas into the crust.

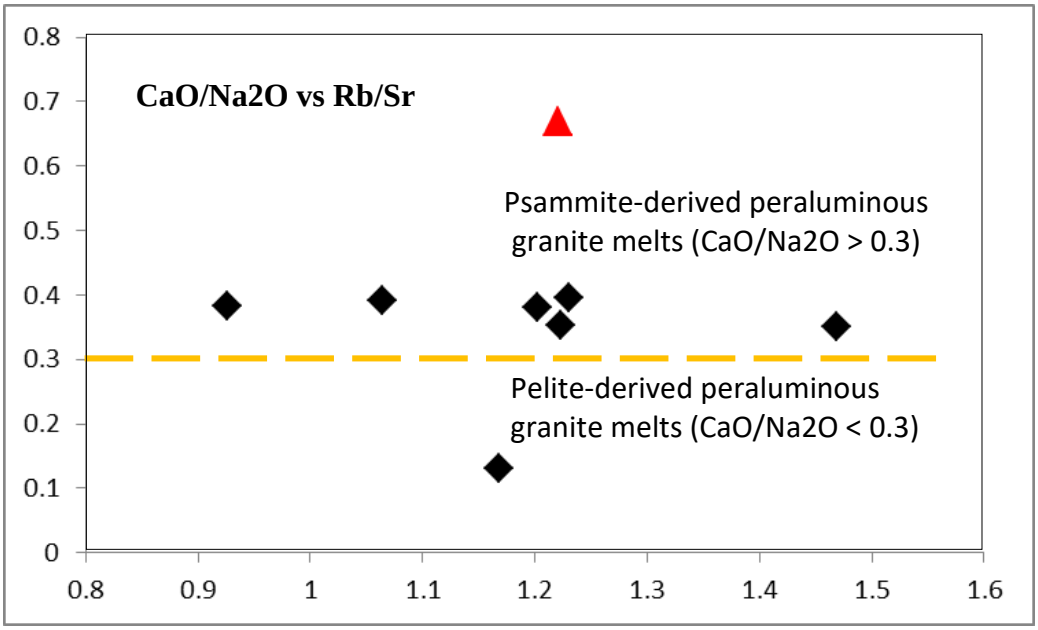

Figure 37: Rb/Sr versus CaO/Na2O ratios (Nzenti et al 2011) for the Etam granitoids granites.

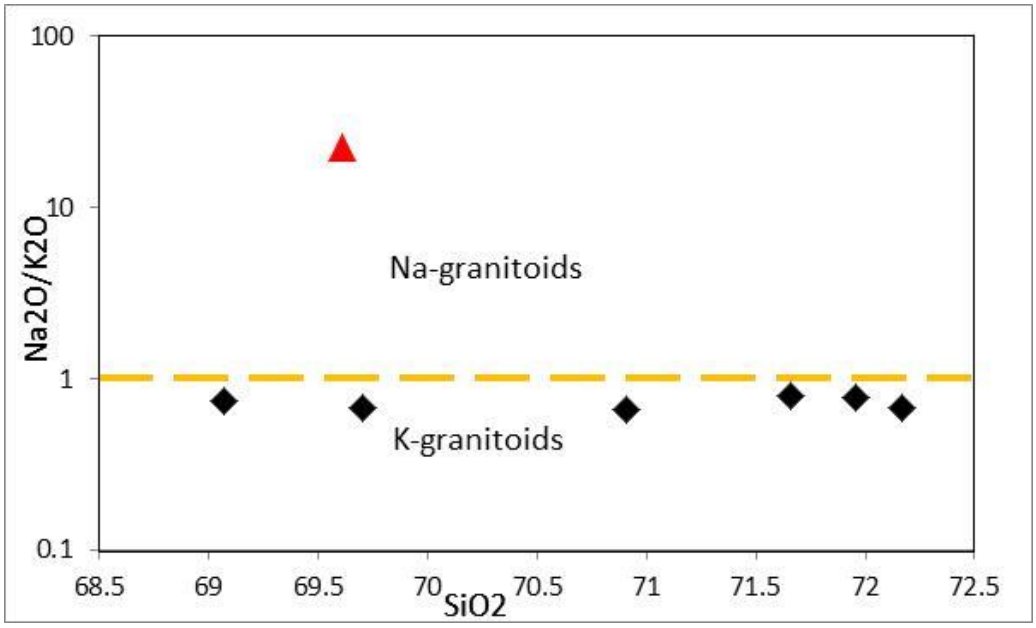

Figure 56: Na2O/K2O versus SiO2 diagram (Gills, 1981) defining Na-granitoids field and K-granitoids field

▲ = Granodiorite ◆ = Granite

I.1.3 Crystallization temperature and pressure

Estimates of crystallization temperature and pressure for granitic systems are abundant in the literature (Green and Pearson, 1986; Kalsbeek et al., 2001, Ferreira et al,. 2015; Kouankap et al,. 2018). Various methods are also used and depend on the rock chemistry. We used in this work (1) the diagram of TiO_2 vs SiO_2 of Green and Pearson

(1986) for hydrous mafic to felsic compositions at 7.5–30 kbar and 900–1100 °C. The authors observed a significant correlation between TiO_2 and silica content of a liquid coexisting with a Ti-rich accessory phase. This diagram (Fig. 57) indicates that Etam granitoids were formed at relatively low temperatures, probably < 900 °C.

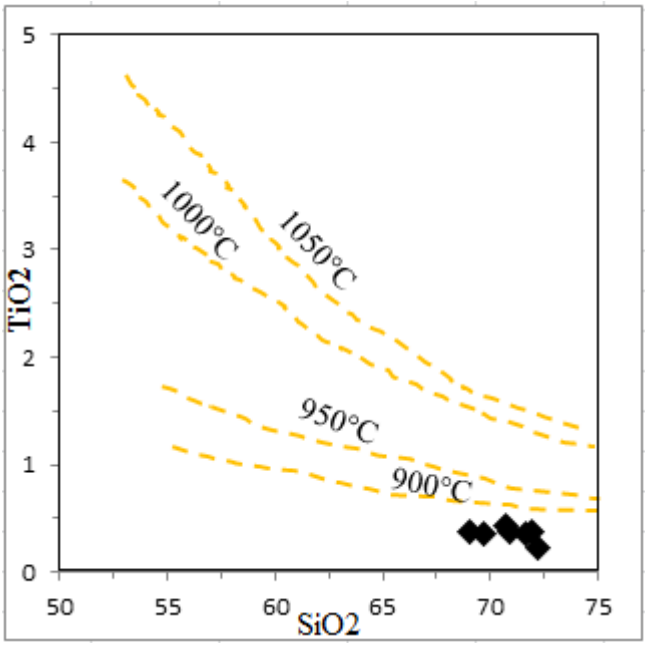

Figure 57: TiO2 vs SiO2 temperatures diagrams of Etam granitoids (Green and Pearson 1986)

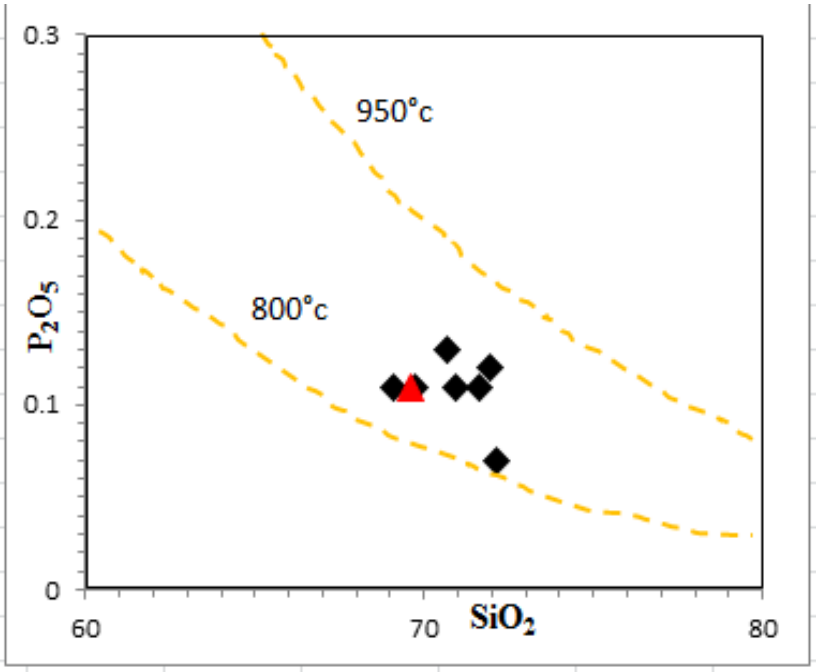

Figure 58: P_2O_5 vs SiO_2 Temperatures diagrams of Etam granitoids (Green and Watson., 1982): Black diamond= granites, red triangle= granodiorite

2) The P_2O_3 vs SiO_2 diagram (Green and Watson, 1982) where the authors studied the relationship between the solubility of apatite saturation in common magmas and temperature

and silica content of the magma at 750 kbar. The Etam granitoids are suggested to have crystallization temperature between 800 and 950 °C (Fig. 58), at 750 kbar.

II Fault rocks

II.1 Deformation characteristics: Grain size reduction in the fault rocks

Crystal-plastic deformation and recrystallization both constitute the most important style of grain size reduction in the wall rock (grnadiorite) and protomylonitic rocks of the Etam area. Within the mylonitic corridor, where Qtz_1 clasts are rare (e.g. ultramylonite), intracrystalline slip and recrystallization are commonly observed. In general, quartz is reduced mainly through dynamic recrystallization, while feldspar shows high fracturing in the high strain zone. The brecciated quartz blocks are cut by micro-fractures resulting in intragranular and transgranular segmentation (Ng Tham F, 1994). This process which contributed to grain size reduction in the shear zone led to high variation in clast size within the breccias ranging from 0.5 mm to 8 cm. The wall rock displays grain size up to 10 cm long (feldspar), while in the ultramylonites the remaining clasts rarely exceed 5 mm.

The microstructural evolution in the shear zone and the gradual grain size variation from the wall rock to the shear zone center as well as the mineralogical composition which presents very little changes from protomylonites to ultramylonites suggest that the granodioritic wall rock is the protolith for the shear zone fault rocks.

II.2 Quartz vein formation in shear zone

Quartz veins generally are produced by hydrothermal circulating fluids. Fourmier and Potter (1982) noted that because of the solubility of silica in water, often fluids are saturated in quartz even in shallow brittle shear zones. Fractures created during the brittle deformation act as pathways for fluid flow bearing and transporting quartz to eventually form veins. Small quartz veins can be formed by diffusional transport of quartz (Taber 1918; Fisher and Brantley 1992; Fisher et al., 1995; Bons and Jessell 1997). This mechanism mainly explains quartz transfer in the faults and shear zone (Oliver 1996; Jamtveit and Yardley 1997; Bons 2001). The Etam Shear Zone has several brittle features with various attitudes. Among them, a conspicuous transcurrent fault, trending N010E to N060E seems to limit the shear zone in the NW. This fault probably played a role during the formation of the major brecciated quartz bodies (vein) in Etam. It acted as an anisotropy which caused the precipitation of quartz carried by hydrothermal fluids saturated in silica in Etam. This suggests the mode of formation of quartz vein described in Bons (2001).

II.3 Mineral reactions due to deformation

Metasomatic reactions in the altered Etam rocks mostly include albitization of Kfs_1 and chloritization of Kfs_1, Pl_1, Bt. The alteration extends from the wall rock into the shear zone. The suggested reaction is: Pl + Kfs + H_2O = Qtz + Al + Ep + Chl. Previous studies have described the same reactions in the fluid-affected green schist facies shear zone: Pl + Kfs + Bt + H_2O = Ms + Qtz + Al + Ep, (Kerrich et al. 1980; Pryer and Robin 1995; Hippertt 1998; Wintsch and Yeh 2013; Spruzeniece et al. 2015). This reaction where feldspars break down to phyllosilicates or transform to albite is similar to mineral reactions occurring in ESZ. Njome and Suh (2003) previously suggested greenschist metamorphic conditions in the Tombel graben. The formation of flame perthite within K-feldspar in the wall rock can be justified by a multi-stage reaction sequence (Pryer and Robin 1995; Spruzeniece et al. 2015):

(1) Kfs+ $H_2O \rightarrow$ Ms + Qtz + K^+ + OH^-

(2) Pl + H_2O + K^+ + Fe^+ + Qtz$\rightarrow$ Pl + Ms + Ep,

Where intergranular fluids and pressure gradient are factors which control the transport of material. Such reactions particularly released quartz (Njome and Suh 2003; Spruzeniece et al., 2015) which is consistently dissolved during cataclasis and precipitated in strain shadow and fractures. The presence of several quartz veins and veinlets in ESZ suggest therefore, in this area a strong mobility of hydrothermal fluids saturated in silica. These fluids also carried K^+, Na^+, Ca^+, Fe^+, Al^+ released by the alteration of feldspars (albitization) and the metasomatic crystallization or recrystallization of secondary minerals such as K-feldspars, Plagioclase and epidote.

II.4 Deformation mechanism

The microstructural evolution within the ESZ shows incremental prograde deformation process. Quartz has been deformed both in cataclastic and ductile manner in the ESZ. The differential stresses resulting from the syntaxial quartz veins (Bons et al,.2012), observed in outcrop with prominent growth competition of elongated quartz grains from the wall inwards is relatively low (Etheridge 1983). Low confining pressure also played a role within this zone and created tension gashes and dilatants microfractures (Suh et Dada 1997), in which circulating fluids, saturated in silica flow (Bell and Etheridge 1973). The process of dislocation creep (White 1977; Poirier 1980; Urai et al., 1986) common in this zone is evidenced by undulose extinction in quartz, sub-grains boundaries and deformation lamellae present in quartz even within the ductile part of the shear zone. Nevertheless, bulging (BLG) recrystallization also accompanied the recrystallization of the polygonal quartz aggregates filling the microcracks or surrounding the porphyroclasts (Baily and Hirsch 1962; Drury et

al., 1985; Hirth and Tullis, 1992; Shigematsu 1999; Stipp et al., 2002) suggest the intervention of intergranular fluids during deformation (Mancktelow and pennacchioni, 2004).

Plagioclase, K-feldspars and quartz have several microfratures and chemical alteration microstructures. Quartz is the most stable phase and similar deformational sequences based on thermodynamic calculation of lifetime of minerals have been observed by Lasaga (1984). The microfractures are mostly dilatant and filled by equidimensional fine-grained quartz. Perthite with albite lamellae is observed in K-feldspar, indicating high stress around the boundaries of the clasts (Augustithitis 1973; Debat et al., 1978; Passchier et Trouw, 2005; Pryer, 1993; Pryer and Robin,1995). Myrmekite is also common at the boundary of K-feldspar. Indeed, according to Simpson and Wintsch (1989), myrmekite is commonly observed on K-feldspar pressure shadows on the side facing the shortening direction and thought to be often associated to high strain features. Mineral fish microstructures include plagioclase fish, mica fish and amphibole fish which are principally observed within a matrix of recrystallized quartz. The alteration of biotite to epidote observed in some cases suggests that equilibrium is not normally attained during hydrothermal alteration (Scharwtz, 2006). The kinematic markers such as boudins, sigmoidal porphyroclasts, mineral fish in mylonitic bands and S/C type structures defined a left lateral movement in ESZ, which constitutes the earlier sense of shear recorded in the CCSZ followed by dextral shearing (Njome et al., 2003; Ngako et al., 2003).

II.5Deformation conditions

Crystallo-plastic and cataclastic deformation affecting quartz and feldspar, respectively, are observed around the margins of the shear zone. Bulging (BLG) recrystalization (Baily and Hirsch 1962; Drury et al., 1985; Shigematsu 1999; Stipp et al., 2002; Hirth and Tullis 1992) indicate temperature during deformation around 300°C. The undulose extinction of quartz porphyroclasts and the brittle behaviour of quartz grains also suggest very low-grade metamorphic conditions in the ESZ, probably green schist stage, where epidote, sericite, neocrystalized quartz and chlorite assemblage are preserved. The consistent albitization of K-feldspar by the formation of perthite suggests low-medium (400-500°C) metamorphic conditions. Furthermore, the coexistence of such microstructures at different grades suggests that the deformation started at lower temperature of ~ 300 ^{o}C and ended at elevated temperatures of ~ 600 ^{o}C (Dawai et al., 2017).

III High Purity Quartz potential in Etam shear zone

III.1 Geochemistry and fluid inclusions

A number of factors played a role in the chemistry of the quartz studied in Etam. These are factors such as hydrothermal fluid composition, fluid and melt inclusions. Melt inclusions for example may contain high concentrations of F, Cl, B, P, Li, Cs, and Rb (Thomas et al., 2006). Trace elements concentrations are chiefly regulated by the crystallization temperature (Müller et al., 2012, Wark, and Watson, 2006), the extent of melt fractionation in igneous and pegmatitic quartz (Müller et al., 2002; Larsen et al., 2004; Breiter and Müller, 2009; Jacamon and Larsen, 2009; Beurlen et al., 2011) and the chemistry and acidity of the fluid from which the quartz crystallized in diagenetic and hydrothermal quartz (Rusk et al., 2008; Jourdan et al., 2009; Müller et al., 2010).

Monecko et al, (2002) defined Li, Al, K, Rb, Sr, and Y concentration in quartz as tools that allowed distinguishing quartz from metamorphic area and quartz of hydrothermal origin. The authors showed that, despite the variations, these elements generally have lower concentration in metamorphic quartz compared to hydrothermal quartz (Korneliussen et al., 2006 in Muller et al., 2007). According to Larsen et al (2004) the Ge/Ti, Ge/Be, P/Ge and P/Be ratios of quartz are strongly sensitive to the origin and evolution of the granitic melts. The Ge/Ti ratio therefore is the most suitable for analyzing and understanding petrogenetic processes in granitic igneous rocks.Research work discriminating sources of quartz deposit have been carried out previously world-wide and an abundant literature is available. Trace elements in quartz are then generally used as tools for differentiating pegmatite, igneous, hydrothermal and metamorphic quartz (Haus, 2005; Ihlen et al., 2007; Müller et al., 2007 and 2012; Gotze et al., 2004, Santos et al., 2014; Santos et al., 2015). These studies are used for bench-marking procedures and comparing results of this study.

From the ICP-MS or LA-ICP-MS analyses, the Etam quartz shows more or less variation between milky quartz and translucent quartz in terms of trace elements concentration.

Figure 59 shows similar trend variation in trace elements concentration for both quartz, and suggests the similar processes of formation of Etam quartz despite variations in trace element concentrations. The Al/Li ratio (means 209.8 μg·g−1) for translucent quartz is very high but similar to some metamorphic over printed quartz (Monecke et al., 2002). This ratio is different from the ratio in pegmatitic quartz, often <10 (Gotze et al., 2004; Santos et

al., 2014) and also that from hydrothermal quartz shown in data available (Monecke et al., 2002; Santos et al.,2017).

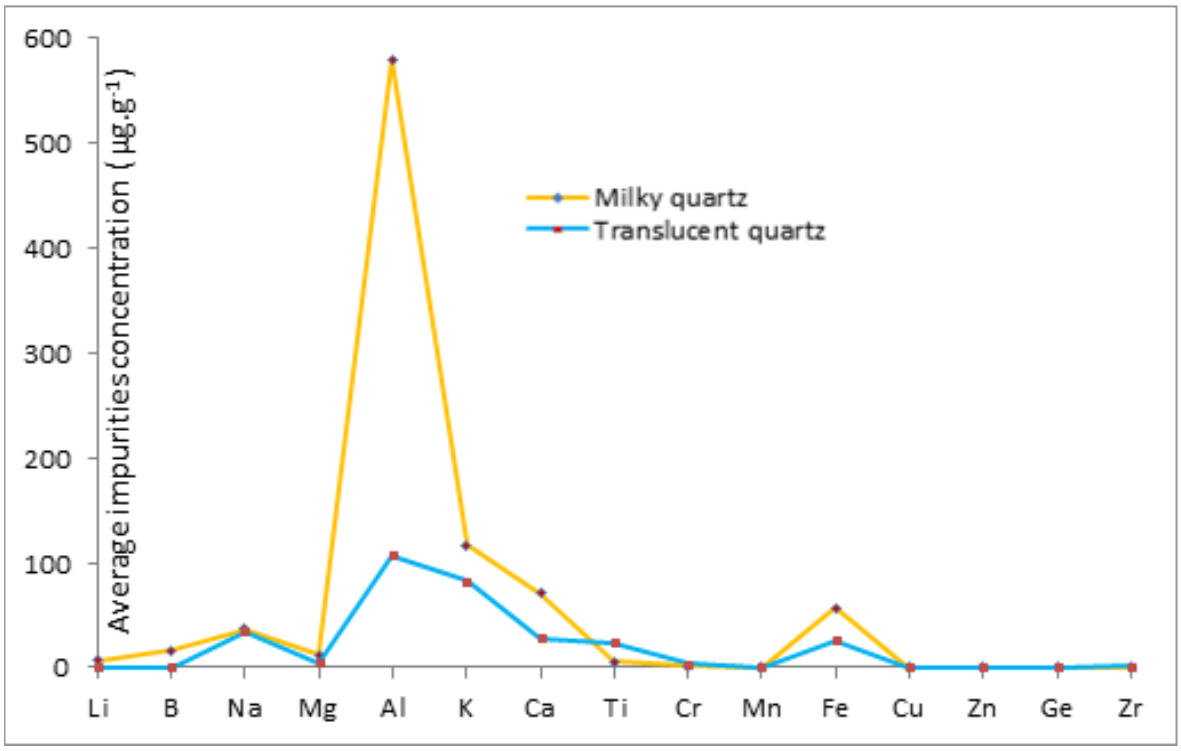

Figure 59: Spider diagram trace element concentration in Etam quartz. Notice that both patterns display similar trends with translucent quartz showing low concentration in all elements, except for Ti which is high compared to milky quartz.

Lithium, Rb, Sr, and Y show low concentration in these quartz samples, similar to most of the metamorphic quartz described in literature (Monecko *et al.*, 2002, Gotze *et al.*, 2017, Kempe *et al.*, 2012).

Monecke et al., 2002 discriminated metamorphic quartz from hydrothermal quartz by low concentration of Li, Al, K, Rb, Sr, and Y of recrystallized metamorphic quartz.

Although Ge and Fe show low concentrations in the milky quartz, the Ge/Fe ratio (means=0.0027) is very low in this quartz compared to translucent quartz (means= 0.031). It is equally low compared to hydrothermal quartz studied in Olhos D'agua (Ge/Fe =0.15) and Corinto (Ge/Fe =0.3) (Santos et al,. 2014), and much smaller compared to pegmatitic quartz which presents Ge/Fe ratio ranges from 4.5 to 0.1 (Gotze et al., 2004; Schron et al., 1982). This low Ge/Fe ratio suggests the early crystallisation stage of this quartz, containing high concentration of Fe (Schron et al., 1982), probably during metamorphic event. Furthermore, the REE distribution pattern of this quartz type shows the behaviour of typical metamorphic quartz samples with an enrichment of the light REE (LREE) (Fig 60, Monecke et al.,

2002;Kempe et al., 2012). The samples contain very low to negligible HREE and thus their chondrite-normalized REE cannot be shown on spider diagram. The absence of a positive Ce anomaly is suggested to reflect the igneous protolith of this quartz. This corroborates Njome and Suh (2003) and Sigue et al., (2019) who suggested that the protolith of the fault rocks is probably igneous rocks in Etam.

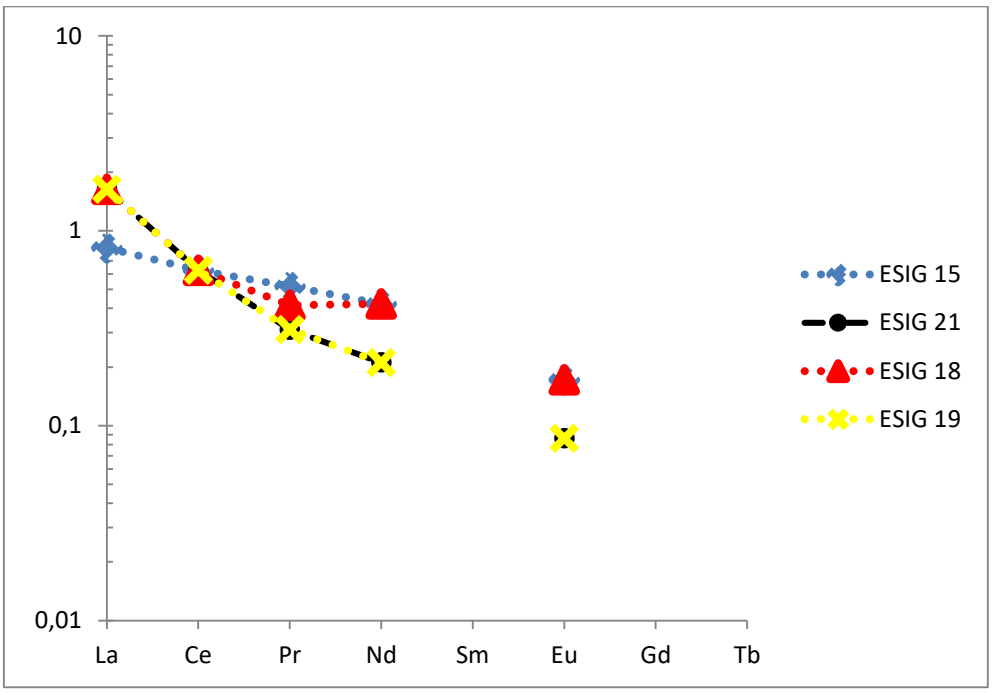

Figure 60: Chondrite-normalized rare earth element (REE) distribution patterns of Etam quartz (normalization according to data of Anders and Grevesse 1989)

The 10Ge-Al/50-Ti diagram is used here to plot representative samples of Etam quartz (Fig. 61). The samples from the translucent quartz vein fall in the hydrothermal quartz field and the samples from the milky quartz vein fall in quartz from granite field. This diagram is often useful to determine the origin of the quartz.

Fluid inclusions in milky quartz display features related to recrystallisation under metamorphic conditions as shown by the higher volume of two-phase fluid inclusion with irregular shapes containing brine and CO_2 (Heynke et al., 1992). However, the higher quantity and the variability of fluid inclusions suggest that this quartz benefitted from hydrothermal fluids inputs. Impurities contained in it are similar to some hydrothermal quartz data available (Monecke et al., 2002; Min et al., 2017). Therefore, it is suggested that quartz in Etam was probably formed during metamorphic processes implying circulation of hydrothermal fluid saturated in silica (Goetze et al., 2017), followed by silica precipitation and formation of hydrothermals vein.

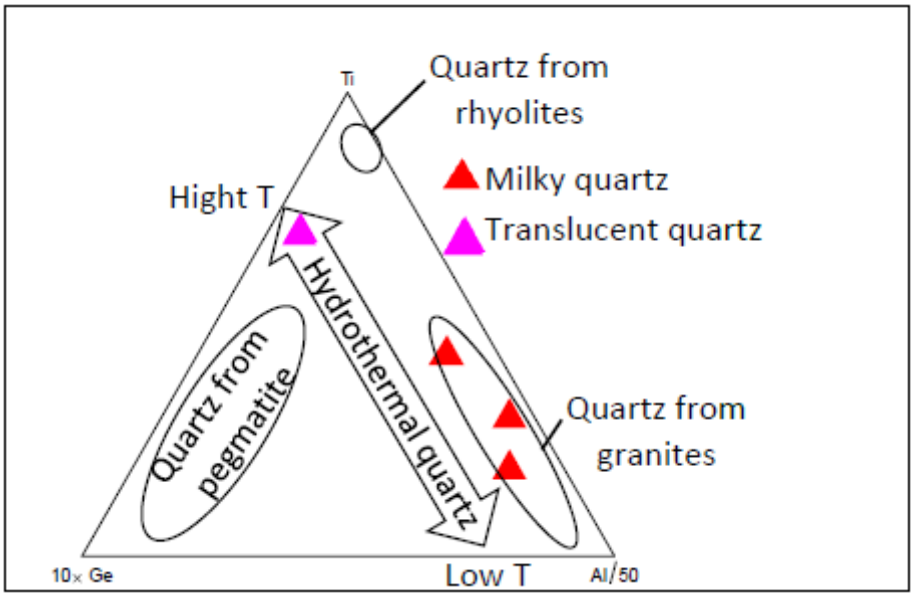

Figure 61: The 10Ge-Al/50-Ti diagram for representative sample of Etam quartz. The samples from translucent quartz fall in the Hydrothermal quartz field and the sample from milky quartz fall in quartz from granite fill (modified after, Santos et al,. 2014 and afte

III.2 Trace elements incorporation into quartz

The Al concentration in the Etam quartz samples varies (105.85 to 793.84 ppm, Table 11 shows Al and Ti concentration (ppm), extracted and converted from table 7). Figure 62 shows that Al and Ti concentrations have a negative correlation. Götze et al., (2001) and Rusk et al., (2006; 2008) demonstrated that high concentration of Ti and corresponding low concentration of Al are closely related to high temperature in hydrothermal quartz. The concentration of Ti in quartz reflects the temperature of recrystallization during metamorphism (Larsen et al., 2004; Spear and Wark, 2009; Wark and Watson, 2006; Müller et al., 2007). Ti concentration in milky quartz is similar to that of hydrothermal quartz described in the literature. The microscope studies of the Etam quartz did not show either regeneration of quartz by metamorphism as evidenced by the absence ofsecondary quartz, or rutile as inclusions in quartz. Therefore, the Ti concentration in milky quartz samples is presumably incorporated in the structure of the quartz and the hydrothermal fluids seem not to have played a major role in its genesis or the fluid was Ti poor. In the translucent quartz samples, the high content of Ti compared to the milky quartz is possibly related to mineral (rutile) microinclusions as observed in the thin sections.

The high Al concentration in quartz of hydrothermal origin could be induced during fluid-assisted metamorphism resulting in the development of new minerals at

hightemperature (Santos et al., 2014 and Monecke et al., 2002). Such phase transformations are widespread in the area (Njome and Suh 2005; Sigue et al., 2019).

Table 11: Al and Ti concentration (ppm) in Etam quartz: extracted and converted to ppm from table 7

Sample (ppm)	ESIG1	ESIG3	ESIG4	ESIG5	ESIG10	ESIG14	ESIG 15a	ESIG 15b	ESIG 15c	ESIG16	ESIG17	ESIG18	ESIG19	ESIG 21a	ESIG 21b
Al	264.61	793.84	264.61	158.77	688.00	105.85	688.00	688.00	582.15	158.77	52.92	264.61	264.61	264.61	264.61
Ti	69.94	11.98	29.95	23.96	11.98	35.94	11.98	11.98	11.98	35.94	11.98	29.95	35.94	41.93	47.92

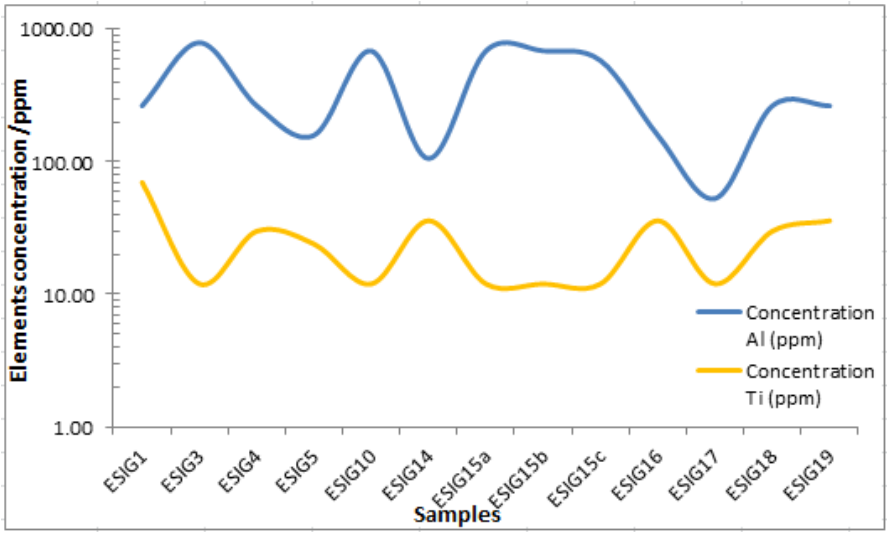

Figure 62: Inverse relations between Al and Ti concentrations in Etam quartz

Iron concentration is abnormally high in the translucent quartz. Muller et al., (2012) stated that quartz crystals in contact with Fe-rich minerals show high concentration of Fe. Thus, the Fe concentrations in quartz are predominantly diffusion-controlled. Indeed, clusters of small quartz grains containing red spots, probably iron oxide were observed in the fluid and mineral inclusion study (fig.44). The origin of these spots is not known, but probably hydrothermal fluids circulating in the area were Fe-rich.

Calcium, K, Mg and Na are generally carried in quartz by fluids inclusions (Santos *et al.*, 2015; Gotze *et al.*, 2017).

III.3 Technological aspect

Quartz in this study has mainly two-phase fluid inclusions containing water and gases (CO_2). The behavior of quartz upon fusion has been described by several authors (Santos et al., 2013; Griscom, 2006; Santos et al., 2014; 2015). The amount of gas liberated during fusion is related to the size and density of fluid inclusions. At Etam, the translucent quartz yielded better fusion test results than the milky quartz variety. The inclusions in both translucent and milky quartz varieties are different in size, quantity and types. This

observation suggests that, either the conditions/environments of formation of the two varieties were different and thus, experienced different geological events that could change the fluid inclusion characteristics, or inclusions were formed differently in these quartz probably due to the different cooling rate during metamorphism and hydrothermal alteration (Santos et al., 2014). In the case of the milky quartz, the host rock is a fault rock formed in a britle-ductile shear zone (Sigue et al., 2019). According to Tarantola et al., (2012); Schmatz and Urai, (2011); Romer et al., (2006); Schmidt et al., (2003); Vityk et al., (2000) and Roedder, (1984), pressure in such geological environments is often high and can induce fluid loss by causing deformation of the fluid inclusions. This is supported by the presence of some large inclusions observed surrounded by small inclusions or satellite inclusions. Indeed, Diamond et al., (2010) and Tarantola et al., (2010; 2012) showed that due to deviatoric stress, inclusions can be deformed and dismembered, giving a large relic inclusion and a cluster of small neonate (satellite) inclusions around them.

The chemical analysis in table 8 shows impurities in some of the Etam quartz samples. The results show the high to very high concentrations of various elements in the milky quartz.Nevertheless, the translucent quartz variety has more promising results for industrial applications, compared to the milky quartz. The principal elements with high concentrations in the translucent quartz are: Al (means 107 µg·g−1), K (means 82.4 µg·g−1), Fe (means=26.01). According to Santos et al., (2015) removing Al impurities from quartz by using HF or concentrated acid mixtures is costly and constitutes environmental hazards. Therefore, for quartz to be suitable as HPQ raw material, it should meet certain natural requirements, or the processing should be done by methods that are less hazardous and more efficient. Indeed, an efficient fluorine-free leaching system to purify quartz has been developed with an objective to establish a fluoride-free technology for improving quartz quality (Min et al., 2017). According to the authors, the method can consistently purify quartz by removing elements impurities up to 88.2 wt %, 99.0 wt % and 98.1 wt %, for the HCl-NH4Cl system, and 87.5 wt %, 98.1 wt % and 98.2 wt % for the H_2SO_4-NH_4Cl system, respectively for Al, K and Fe.

Based on chemical studies coupled with bubble formation characteristics in Etam quartz, the milky quartz can necessitate important and costly purification process to meet HPQ standard. The deposit therefore due to the high SiO_2 content (up to 99.75 wt%) can be used as raw materials for the refractory industry with a production of silica stone, silicon and silicon alloys. Translucent quartz in the other hand shows optimistic results as quartz raw material that can be used in some quartz applications industries without necessarily

purification processes. It can produce, for instance, silica glass which is common raw material largely used in optical and telecommunication industries.

III.4 Economic appraisal

According to the definition of HPQ the milky quartz from Etam does not meet the requirement of a high purity quartz deposit. The sum of the concentration of unwanted elements in this quartz type is ≥ 500 $\mu g \cdot g^{-1}$. The translucent quartz variety is fine-grained, translucent and massive. These aspects are often an indication of good fusion behavior (Santos et al., 2013). Regarding only the fusion behavior, this quartz type can be used to produce transparent glass. The problematic feature is the chemical purity. With the exception of Li (0.5 $\mu g \cdot g^{-1}$) and B (below detection limit), all the trace elements which determine the purity of quartz as per HPQ definition are above the required limits (Table 8)**.** The Ti and Fe are especially high. These impurities are probably located in the mineral inclusions which can easily be eliminated if proper processing tests are conducted. Translucent quartz shows similar characteristics to some samples from the Santa Helena quartz deposit (Santos et al., 2014) as shown by the fusion over silica plate and bubble formation. Therefore, further investigations for such quartz type in the Etam area are advised. Several veins as translucent quartz vein with similar orientation exist in the area. These veins crop mostly in metamorphic basement and are easily accessible. The volume of the milky and translucent quartz resource that defines the distinct Etam ridge above the surrounding peneplain is estimated at ~ 6 km^3 pointing to an exploitable deposit considering that drilling will only add to the subsurface volume

CONCLUSION AND PERSPECTIVES

Conclusion

Etam host rocks are granitoids and gneisses. Etam granitoids intruded a low to medium-grade metamorphic basement of greenschist to amphibolitic and migmatitic gneisses. These granitoids are syntectonic, S-type, high-k calc-alkaline affinity to shoshonitic and feroan with low Nb/U ratio (≤10) suggesting a typical of crustal granite. They show high Rb/Sr (0.92 – 1.46) and low Sr/Ba (0.18 – 0.26) ratio coupled with strong negative Eu (Eu/Eu* = 0.37-0.59) anomaly, thus they characterize the lower degrees of crustal melting that generated the melts. The S-type granites in Etam have a pelitic protolith and the melts upon the partial melting were unfractionated and involved only felsic components from the upper crust. Etam granitoids are derived from mostly clay-poor, plagioclase-rich psammitic source with the high $CaO/Na_2O>3$, therefore their source is suggested metamorphosed upper crustal metasedimentary rocks. The low Rb/Sr ratio and the negative Eu anomalies suggest the low hydrous conditions of partial melting and the participation of biotite during the process of formation of etam granitoids. These granitoids are suggested to have crystallization temperature between 800 and 950 °C at 750 kbar.

The shear zone in Etam area (ESZ) is an oblique-slip sinistral strike-slip shear zone oriented N010E to N060E with a ductile zone and a brittle zone. Three domains have been distinguished in ESZ: (1) the wall rock (shear zone margin) where quartz, K-feldspar, plagioclase and biotite, referred to as Qtz_1, Kfs_1, Pl_1 and Bt_1 respectively define the magmatic constituents. (2) a ductile zone within which protomylonitic rocks are porphyroclastic and medium- to coarse-grained, mylonite is medium-grained and ultramylonites appear as linear segments wrapped by mylonitic bands. (3) a brittle zone mark by brecciated large quartzite blocks showingtwo types of breccias (crackle breccias and mosaic breccias).

Crystal-plastic deformation and recrystallization are associated with micro-fracturing in ESZ. Metasomatic and alteration reactions particularly released quartz and K^+, Na^+, Ca^+, Fe^+, Al^+. The presence of several quartz veins in ESZ suggest therefore, a strong mobility of hydrothermal fluid saturated in silica. The deformation mechanism is suggested to be similar to that of the Cameroon Central Shear Zone (CCSZ). The metamorphic conditions are similar as indicated in Tombel Graben: green-schist facies with epidote, sericite, neocrystalized quartz and chlorite assemblage, low temperature grain boundaries (300 °C), or low-medium (400–500 °C) conditions metamorphism. The coexistence of microstructures at different grades suggests that the deformation started in the presence of a residual melt and ended after the full crystallization of the rock at high temperature. The sinistral strike-slip sense of shear has been recorded in the CCSZ follow by dextral shear sense. The N010E to N040E trend of

the mylonitic corridor in ESZ confirms how anastomosing the CCSZ is. Similar age as in Etam formation (Neoproterozoic) has been recorded in Panafrican fold belt in Cameroon and in the environment of the HPQ deposit is Brazil.

The investigation of Etam quartz samples in the southwest region (Cameroon) by the combination of ICP-MS, LA-ICP-MS, SEM-EDS resolved trace-element analysis and characterized in detail the type, the abundance of trace elements in quartz; the reconstruction of processes responsible for their formation and the amount of trace-element concentrations. The analyses show that the SiO_2 content is very high (98.46–99.75 wt%) with very low concentration of trace elements. The process of formation of both deposits type is suggested to be similar: The translucent quartz is clearly older than the milky quartz although both probably formed under metamorphic conditions and benefited from a contribution of hydrothermal fluids.

The translucent quartz of Etam show optimistic results as ore resource after analysis. Principal impurities in it are Al (mean 107µg.g-1), Ca (mean 27.85 µg.g-1) Fe (mean 26.05 µg.g-1) and Ti (mean 23.75 µg.g-1). According to the HPQ definition quartz from Etam does not meet the requirement of a high purity quartz deposit. Chemically and technologically the translucent quartz is medium purity quartz with good fusion behavior producing very little number of bubbles thus it could be used to produce transparent glass. Moreover, the main impurities in translucent quartz are mostly in fluid and mineral inclusions thus the purification using efficient method can purify this quartz and produced quartz crucibles with high purity qualities widely used in industries.

Perspectives

HPQ as a material for development is become today one of the most attractive ereas of interest world wide. This work which introduced for the first-time quartz mineral in mineral commodity in Cameroon should be furthermore continues and research around quartz deposit (HPQ deposit) intensified.

Etam quartz is syntectonic and show high concentration of trace element despite their metamorphic orign. The stress (shear zone) and the hydrothermal fluids rich in some elements, circulating in the area are probably responsible. it is therefore recommended that:

- Study to be carried out on syn- or pre-tectonic quartz hosting deposits. Such deposits should have been affected by metamorphism.
- The ages of these deposits should be pre-dating favourable metamorphic conditions.

- SEM and CL investigation of the sections complete with backscattered electron imaging (BSE) in order to elucidate the sequence of major quartz crystallisation stages.
- EMPA analysis of rutile inclusions in quartz along pre-determined profiles from core to rim are also recommended.

REFERENCES

Abdelsalam, J. M., Liegeois, J. P., Stern, J. R., 2002. The Saharan metacraton. Journal of African Earth Sciences 34, 119-136.

African Aura Mining., 2009. Batouri gold project, Cameroon. African Aura Resources (UK) Ltd., London. http://www.african-aura.com/s/Batouri.asp Accessed on March 7, 2009.

Almeida, F. F., Hasui, Y., Brito de Neves, B. B., Fuck, R. A., 1981.Brazilian structural provinces. Earth Sciences Review 17, 1-29.

Altherr F.F., Holl, A., Hegner, E., Langer, C., Kreuzer, H., 2000. High-potassium, calc-alkaline I-type plutonism in the European variscides: northern Vosges (France) and northern Schwarzwald (Germany). Lithos 50, 51-73.

Anders, E.; Grevesse, N., 1989. Abundances of the elements: Meteoritic and solar. Geochimistry Cosmochimistry Acta. 53, 197–214

Andersen, T., Frezzotti, M.L., and Burke, E.A.J., 2001. Fluid inclusions: Phase relationships - methods- applications (special issue). Lithos, 55, 320.

Asaah, A.V., Zoheirc, B., Lehmann, B., Frei, D., Burgess, R., Suh, C., E., 2015. Geochemistry and geochronology of the ~620 Ma gold-associated Batouri granitoids, Cameroon. International Geology Review 57, 1485–1509.

Augustithitis, S.S., 1973. Atlas of the textural patterns of granites, gneisses and associated rock types.Elsevier, Amsterdam

Baily, J.E., Hirsch, P. B., 1962.The recrystallization process in some polycrystalline metals. Proceedings of the Royal Society of London A, 267, 11–30.

Bell, T.H., Etheridge, M.A., 1976. The deformation and recrystallization of quartz in mylonite zone, central Australia.Tectonophysic 32, 235-267.

Beurlen, H., Müller, A., Silva, D., Da Silva, M.R.R., 2011. Petrogenic significance of trace-element data analyzed with LA-ICP-MS in quartz from the Borborema pegmatitic province, northeastern Brazil. Mineralogical Magazine 75, 2703-2719.

Blankenburg, H.-J., Götze, J. and Schulz, H., 1994.Quarzrohstoffe. Deutscher Verlag für Grundstoffindustrie: Leipzig-Stuttgart, 296. (in German).

Bodnar, R.J., 1994. Philosophy of fluid inclusions analysis.*In:* De Vivo and M.L. Frezzotti (Eds.), Fluid Inclusions in Minerals and Applications. Virginia Technology, Blacksburg, VA, 1 – 6.

Bons, P.D, Elburg M. A, Gomez-Rivas E., 2012.A review of the formation of tectonic veins and their microstructures.Journal of Structural Geology 43, 33- 62

Bons, P.D., 2001a. Development of crystal morphology during unitaxial growth in a progressively widening vein: I. The numerical model. Journal of Structural Geology 23, 865-872.

Bons, P.D., 2001b. The formation of large quartz veins by rapid ascent of fluids in mobile hydrofractures. Tectonophysics 336, 1–17.

Bons, P.D., Jessell, M.W., 1997. Experimental simulation of the formation of fibrous veins by localised dissolution-precipitation creep.Mineralogical Magazine 61, 53-63.

Bouyo Houkechang, M., Toteu, S.F., Deloule E., Penaye, J., Van Schumus, 2009. U-Pb and Sm-Nd dating of high-Pressure granulites from Tcholliré and Banyo regions: Evidence for a pan African granulite facies metamorphism in north-central Cameroon. Journal of African Earth Sciences 54, 144-154.

Bouyo Houketchang, M., Penaye, J., Mouri, H., Toteu, S.F,. 2019. Eclogite facies metabasites from the Paleoproterozoic Nyong Group, SW Cameroon: mineralogical evidence and implications for a highpressure metamorphism related to a subduction zone at the NW margin of the Archean Congo craton. J Afr Earth Sc 149:215–234

Boynton W. V., 1984. Cosmochemistry of the rare earth elements: meteorite studies, in Rare earth element geochemistry, Ed. by P. Henderson (Elsevier, Amsterdam,), 63–114

Brander, L., Svahnberg, H., Piazolo, S., 2012.Brittle-plastic deformation in initially dry rocks at fluid-present conditions: Transient behaviour of feldspar at mid-crustal levels, Contributions to Mineralogy and Petrology 163, 403–425.

Breiter, K., and Müller, A., 2009. Evolution of rare-metal granitic magmas documented by quartz chemistry. European Journal of Mineralogy, 21, 335–346.

Brito neves, B.B., Van schmus, W.R., Fetter, A., 2002. North-Western Africa-North estern Brazil: major tectonic links and correlation problems. Journal of African Earth Sciences 34, 275-278.

Brown, M., Solar, G. S., 1998. Shear zones and melts: Positive feedback in orogenic belts: Journal of Structural Geology 20, 211–227.

Castaing, C., Feybesse, J.L., Thieblemont, D., Triboulet, C., Chevremont, P., 1994. Paleogeographical reconstructions of the Pan-African/Brasiliano orogen: closure of an oceanic domain or intracontinental convergence between major blocks. Precambrian Research 69, 327-344.

Cesare, B., 1994. Syn-metamorphic veining: origin of andalusite-bearing veins in the Vedrette di Ries contact aureole, Eastern Alps, Italy. Journal of Metamorphic Geology 12, 643–653.

Chebeu, C., Ngo Nlend, C.D. Nzenti J-P. & Ganno, S., 2010. Neoproterozoic high-K calcalkaline granitoids from Bapa-Batié, North Equatorial Fold Belt, Central Cameroon: petrogenesis and geodynamic significance. The Open Geology Journal4, 112-131.

Chester, F., M., Friedman, M., Logan, J.,M., 1985. Foliated cataclasites. Tectonophysics 111, 139–146.

Chombong, N.N., Suh, E. C., Ilouga, C.D.C., 2013. New detrital zircon U-Pb ages from BIF-related metasediments in the Ntem Complex (Congo craton) of southern Cameroon, West Africa,Natural Science 5, 835-847.

Dal Martello, E., Tranell, G., Gaal, S., Raaness, OS., Tang, S.K, Arnberg, L., 2011. Study of pellets and lumps as raw materials in silicon production from quartz and silicon carbide.Metall MaterTrans B. 12

Danguene, Y.P., 2003. Nature des protholites et paléo-environnement des métabasites de Mindif (province de l´Extrême Nord au Cameroun). Mémoire de DEA, Université de Yaoundé I, 31p.

Dawaï, D., Tchameni, R., Bascou, J., Wangmene, S., A., Tchunte, F., P., M., Bouchez, J., L., 2017. Microstructures and magnetic fabrics of the Ngaoundere granite pluton (Cameroon): Implications to the late-Pan-African evolution of Central Cameroon Shear Zone. Journal of African Earth Sciences 129, 887-897.

De la Roche. H., 1965. Sur l'existence de plusieurs faciès géochimiques dans les schistes paléozoïques des Pyrénées luchonnaises. Geologische Rundscha, 55, 274-301

Debat, P., Soula, J.C., Kubin, L., Vidal, J.L., 1978. Optical studies of natural deformation microstructures in feldspars (gneiss and pegmatites from Occitania, Southern France). Lithos 11, 133-145.

Depine, M., Frimmel, H.E., Emsbo, P., Koenig, A.E., Kern, M., 2013. Trace element distribution in uraninite from MesoArcahean Witwatersrand conglomerates (South Africa) supports placer model and magmatogenic source. Mineralium Deposita 48, 423-435.

Déruelle B., Ngounouno I., Demaiffe D., 2007.The 'Cameroon Hot Line' (CHL): A unique example of active alkaline intraplate structure in both oceanic and continental lithospheres. Comptes Rendus Géoscience 339, 589-600

Diamond, L.W., Tarantola, A., Stünitz, H., 2010.Modification of fluid inclusions in quartz by deviatronic stress. II: experimentally induced changes in volume and composition. Contribution to Mineral Petrology 160, 845-864.

Djouka-Fonkwé, M.L., Schulz, B., Schüssler, U., Tchouankoué, J. P. and Nzolang, C., 2008. Geochemistry of the Bafoussam Pan-African I- and S- type granitoids in western Cameroon. Journal of African Earth Science 50, 148-167.

Drury M. R., Humphreys, F.J., White, S.H., 1985. Large strain deformation studies using polycrystalline magnesium as a rock analogue. Part II: dynamic recrystallization mechanisms at high temperatures. Physics of the Earth and Planetary Interiors 40, 208–222.

Dumont, J.F., 1986. Identification par télédétection de l'accident de la Sanaga (Cameroun). Sa position dans le contexte des grands accidents d'Afrique Centrale et de la limite nord du craton congolais. Géodynamique 1, 13-19.

Eteridge, M.A., 1983. Differential stress magnitudes during regional deformation and metamorphism: upperboundimposed by tensile fracturing. Geology 11, 232-234.

Evans, J.P., 1990. Textures, deformation mechanisms and the role of fluids in the cataclastic deformation of granite rocks. Geological Society London 54, 29–39.

Ferreira, V. P., Sial, A. N., Pimentel, M. M., Armstrong, R., Guimarães, I. P., da Silva Filho A.F., de Lima, M.M.C.. da Silva, T.R., 2015. Reworked old crust-derived shoshonitic magma: The Guarany pluton, Northeastern Brazil. Lithos, 232 150–161.

Ferry, J.M., Gerdes, M.L., 1998.Chemically reactive fluid flow during metamorphism. Annual Reviews of Earth and Planetary Sciences 26, 255–287.

Feybesse, J.L., Johan, V., Triboulet, C., Guerrot, C., Ma- yaga-Mikolo, F., Bouchot, V. and Ekondong, J., 1998. The West Central African belt: A model of 2.5-2.0Ga ac- cretion and two-phase orogenic evolution. Precambrian Research87, 161-216.

Feytis, A. 2010, Mauritanian quartz: Industrial Minerals, no. 512, 75.

Fisher, D., Brantley, S.L., 1992. Model of quartz overgrowth and vein formation: deformation and episodic fluid flow in an ancient subduction zone. Journal of geophysical Research 97, 20043-20061.

Fisher, D., Brantley, S.L., Everett, M., Dzvonik, J., 1995.Cycle fluid flow through a regionally extensive fracturing network within the Kodiak accretionary prism.Journal of geophysical Research 100, 12881-12894.

Fitz Gerald, J. D., Stünitz, H., 1993. Deformation of granitoids at low metamorphic grade I. Reaction and grain size reduction.Tectonophysics 221, 269–297.

Frost, B. R., Arculus, R. J., Barnes, C. G., Collins,W. J., Ellis, D. J. & Frost, C. D. (2001). A geochemical classification of granitic rocks. Journal of Petrology 42, 2033-2048

Ganno, S., Ngnotue, T., Kouankap Nono, G.K.D., Nzenti, J.P., Notsa, F.M., 2015. Petrology and geochemistry of the banded iron-formations from Ntem complex greenstones belt, Elom area, Southern Cameroon: implications for the origin and depositional environment. Chemie Erde - Geochemistry75, 375–387.

Ganno, S., Njiosseu Tanko, E.L., Kouankap Nono, G.D., Djoukouo Soh, A., Moudioh, C., Ngnotue, T., Nzenti, J.P,. 2017. A mixed seawater and hydrothermal origin of superior-type banded iron formation (BIF)-hosted Kouambo iron deposit, Palaeoproterozoic Nyong series, Southwestern Cameroon: constraints from petrography and geochemistry. Ore Geology Review 80, 860–875

Ganno, S., Tsozue, D., Kouankap Nono, G.D., Tchouatcha, M.S., Ngnotue T., Takam, G.R., Nzenti, J.P., 2018. Geochemical Constraints on the Origin of Banded Iron Formation-

Hosted Iron Ore from the Archaean Ntem Complex (Congo Craton) in the Meyomessi Area, Southern Cameroon. Resource Geology 68, 287–302

Ganwa, A., Frisch, W., Siebel, W., Shang, C.K., Mvondo, O.J., Satir, M., Tchakounte, N.J, 2008a. Zircon ^{207}Pb-^{206}Pb evaporation ages of Pan-African metasedimentary rocks in the Kombé-II area (Bafia Group, Cameroon): constraints on protolith age and provenance. Journal of African Earth Sciences 51, 77-88.

Ganwa, A.A., Frisch, W., Siebel, W., Ekodeck, G. E., Shang, C.K., Ngako, V. 2008b. Archean inheritances in the pyroxene–amphibole-bearing gneiss of the Méiganga area (Central North Cameroon): Geochemical and 207Pb/206Pb age imprints. Comptes Rendus Geoscience 340, 211–222

Gao, B., Nakano, S., Kakimoto, K., 2011. Influence of reaction between silica crucible and graphite susceptor on impurities of multicrystalline silicon in a unidirectional solidification furnace. Journal of Crystallography Growth 314, 239-245.

Gentry, C.F., 2009.Cameroon a new destination for mining investment in Africa, pp. 28, Yaounde.

Gerler, J., 1990. Geochemische untersuchungen an hydrothermalen, metamorphen, granitischen und pegmatitischen Quarzen und deren Flüssigkeitseinschlüssen. Ph.D. thesis, University Göttingen, p 169

Gills, J.B., 1981.Orogenic andesites and plates tectonics. Mineral and rocks 16,400p.

Goldstein, R. H., 2003. Petrographic analysis of Fluid Inlcusions. In: (Samson, I., Alderton, A., and Marshall, D. Eds.), Fluid Inclusions: Analysis and Interpretation. Mineralogical Association of Canada.

Goncalves, P., Oliot, E., Marquer, D., Connolly, J.A. D., 2012. Role of chemical processes on shear zone formation: An example from the grimselmetagranodiorite (Aar massif, Central Alps), Journal of Metamorphic Geology, 30, 703–722.

Götze, J,, Plötze, M., Habermann, D., 2001. Origin, spectral characteristics and practical applications of the cathodoluminescence (CL) of quartz—a review. Mineral Petrol 71:225–250

Götze, J,. 2009. Chemistry, textures and physical properties of quartz—geological interpretation and technical application. Mineralogical Magazine 73, 645–671.

Götze, J., Plötze, M., Graupner, T., Hallbauer, D.K., Bray, C.L., 2004. Trace element incorporation into quartz: a combined study by ICP-MS, electron spin resonance cathodoluminescence, capillary ion analysis, and gas chromatography. Geochimica Cosmochimica acta 68, 3741-3759.

Götze, J., Pan, Y., Müller, A., Kotova, E. L., Cerin, D., 2017. Trace Element Compositions and Defect Structures of High-Purity Quartz from the Southern Ural Region, Russia.Minerals7, 189; doi:10.3390/min7100189.

Green, T.H., Pearson, N.J., 1986.Ti-rich accessory phase saturation in hydrous mafic-felsic compositions at high P–T. Chemical Geology 54, 85–201.

Green, T.H., Watson, E.N., 1982. Crystallizations of apatite in natural magmas under high pressure, hydrous conditions, with particular reference to “orogenic” rocks series. Contributions to Mineralogy and Petrology 79, 96–105.

Griscom, D.L., 2006. Self-trapped holes in pure silica glass: a history of their discovery and characterization and an example of their critical significance to industry. Journal Non-crystalline Solids 3512, 2601-2617.

Guillot, S. and Le Fort P., 1995. Geochemical constraints on the bimodal origin of high Himalayan leucogranites. Lithos 35, 221-234.

Guo, Z., Wilson, M., 2012. The Himalayan leucogranites: Constraints on the nature of their crustal source region and geodynamic setting. Gondwana Research 22, 360–376.

Hanmer, S., and Passchier, C.W., 1991, Shear-sense indicators: A review: Ottawa, Ontario, Geological Survey of Canada, Paper 90-17.

Harben, P.W., 2002. The industrial mineral handybook—a guide to markets, specifications and prices, 4th edn.Industrial Mineral Information. Worcester Park, 412

Harris N.B.W., Inger, S., 1992. Trace element modeling of pelite-derived granites. Contrib. Mineral. Petrol., 110: 46-56.

Haus, R., 2005. High Demands on High Purity-Processing of High Purity Quartz and Diatomite. Industrial Minerals10, 62-67.

Haus, R., 2010. High-purity quartz resources. In: PHOTON's 8th solar silicon conference, Stuttgart

Heynke, U., Leeder, O. and Schulz, H., 1992. On distinguishing quartz of hydrothermal or metamorphogenic origin in different monomineralic veins in the eastern part of Germany.Mineralogy and Petrology, 46, 315_329.

Hippertt, J.F., 1998. Breakdown of feldspar, volume gain and lateral mass transfer during mylonitization of granitoid in a low metamorphic grade shear zone. Journal of Structural Geology 20, 175–193.

Hirth, G., Tullis, J., 1992. Dislocation creep regimes in quartz aggregates. Journal of Structural Geology 14, 145–159.

Hofmann, A.W., Jochum, K.P., Seufert, M., White, W.M., 1986. Nb and Pb in oceanic basalts: new constraints on mantle evolution. Earth and Planetary Science Letters 79, 33-45.

Hutton, D.H.W., Reavy, R.J., 1992. Strike-slip and granite petrogenesis. Tectonics, 11, 960-967.

Ibrahim, S., S., Shahien, M., G., Seliem, A., Q., Abukhadra, M., R., Zayed A., M., 2015. Marwit Rod El Leqah Quartz Deposits as a Strategic Source of High Purity Quartz, Journal of Geoscience and Environment Protection, 3, 41-47.

Ihlen, P., M., Muller, A., Larsen, R., B., and Henderson I., 2007.Transformation of igneous quartz to high-purity quartz in granitic pegmatites of South Norway Granitic Pegmatites. Paper presented at the State of the Art – International Symposium, Porto, Portugal. Retrieved from http://www.fc.up.pt/peg2007/files/ihlen.pdf

Ilouga, C.D.I., Suh, C.E. and Ghogomu, R.T., 2013. Textures and rare earth elements composition of Banded Iron Formations (BIF) at Njweng prospect, Mbalam Iron Ore District, Southern Cameroon.International Journal of Geosciences4, 146-165.

Imber, J., Holdsworth, R., E., Butler, C., A. and Strrachan, R., A., 2001. A reappraisal of the Sibson Scholz fault zone model: the nature of frictional to viscous ('brittle-ductile') transition along a long-lived crustal scale fault, Outer Hebrides Scotland, Tectonics 20, 601-624.

IOTA, 2011.IOTA_ high purity quartz. http://www.iotaquartz.com/techiota4data.html Accessed 20 May 2011

Jacamon, F., and Larsen, R.B., 2009, Trace element evolution of quartz in the charnockitic Kleivan granite, SW-Norway: the Ge/Ti ratio of quartz as an index of igneous differentiation: Lithos 107, 281–291.

Jamtveit, B., Yardley, B.W., 1997. Fluid flow and transport in rocks: an overview. In: Jamtveit, B., Yardle, B.W. (Eds), Fluid Flow and Transport in Rocks. Chapman & hall, London, 1-14.

Jourdan A.L., Vennemann T.W., Mullis J., Ramseyer, K., 2009. Oxygen isotope sector zoning in natural hydrothermal quartz. Mineral Magazine 73, 615–632

Jung, L,. 1992. High purity natural quartz. Part I: High purity natural quartz for industrial use. Part II: High purity natural quartz markets for suppliers and users. Quartz Technology, Liberty Corner, 657

Kalsbeek, F., Jepsen, H. F., Jones, K. A., 2001.Geochemistry and petrogenesis of S-type granites in the East Greenland Caledonides.Lithos 5, 91–109.

Kamineni, D. C., Kerrich R., Brown, A., 1993. Effects of differential reactivity of minerals on the development of brittle to semi-brittle structures in granitic rocks; textural and oxygen isotope evidence, Chemical Geology 105, 215-232.

Kankeu, B., Greiling, R.O., Nzenti, J.P., 2009. Pan-African strike-slip tectonics in eastern Cameroon-Magnetic fabrics (AMS) and structure in the Lom basin and its gneissic basement.Precambrian.Research. 174, 258–272.

Kankeu, B., Greiling, R.O., Nzenti, J.P., Bassahak, J., Hell, J.V., 2012. Strain partitioning along the Neoproterozoic Central Africa Shear Zone system: structures and magnetic fabrics (AMS) from the Meiganga area, Cameroon. Neues Jahrbuch fur Geologie und Palaontologie Abhandlungen, 265, 27-47.

Kapajika, B., 2003. Les granitoïdes calco-alcalins syn-cisaillement de l'Ouest de Tibati, dans la Chaîne Panafricaine Nord-Equatoriale. Pétrogenèse et structurogénèse. Thèse Doctorat, Université de Lubumbashi, 112p.

Karato, S.I., Paterson, M.S., FitzGerald, J.D., 1986. Rheology of synthetic olivine aggregates: Influence of grain size and water, Journal of Geophysical Research 91, 8151-8176.

Kempe, U., Gotze, J., Dombon, E., Monecke, T., Poutivtsev, M., 2012.Quartz regeneration and its use as a repository of genetic information. In: Gotze, J., Mockel, R. (Eds.), Quartz: Deposits, Mineralogy and Analytics. Springer, Berlin, 331-355.

Kerrich, R., Allison, I., Barnett, R. L., Moss, S., Starkey, J., 1980. Microstructural and chemical transformations accompanying deformation of granite in a shear zone at Mifiville, Switzerland; with implications for stress corrosion cracking and superplastic flow, Contribution to Mineralogy and Petrology 73, 221–242.

Kilian, R., Heilbronner, R., Stünitz, H., 2011. Quartz grain size reduction in a granitoid rock and the transition from dislocation to diffusion creep, Journal of Structural Geology 33, 1265–1284.

Kilias, S., Voudouris, P., Katerinopoulos, A., Kavouri S., 2004. "Study of fluid inclusions in alpine type quartz from discontinuity joints of Pentelic Mountain." Proceedings of the 10th International Congress"

Kodama, M., Kishi, H., Kanda, M., Japan Super Quartz Corp., 2010. Vitreous Sílica Crucible for Pulling Silicon Single Crystal.US Patent US2010/0251959.

Koglin N, Frimmel H.E., Lawrie Minter W.E., Brätz, H., 2010. Trace-element characteristics of different pyrite types in Mesoarchaean to Palaeoproterozoic placer deposits.Mineralium Deposita 45, 259–280

Korneliussen A, Wanvik J.E, Müller A, Ihlen P.M., 2006.Kystnære kvartsressurser i Hordaland. Geological Survey of Norway, Report 2006.045

Kouankap Nono G. D., Njiosseu Tanko E. L., Takodjou W. J. D., Kamguia W. B., Afahnwie Ngambu A., Fomena T. H., Folah M. C.L.,2018.Petro-Structural Characterization of Bonguen Area, Nyong Series, Cameroon: Insight into the Northern Extension of Kribi-Campo Shear Zone. *Earth Sciences*. Vol. 7, No. 5, 236-241. doi: 10.11648/j.earth.20180705.15

Kouankap Nono, G. D., Nzenti, J-P., Suh C. E., Ganno, S.**,** 2010. Geochemistry of ferriferous, high-K calc-alkaline magmas from the Banefo-Mvoutsaha Massif (NE

Bafoussam), Central Domain of the Pan-African Fold Belt, Cameroon. The Open Geology Journal, Vol.4, 21-34.

Kwékam. M., Hartmann, G., Njanko, T., Tcheumenak K. J., Fozing E. M., Njonfang, E., 2015. Geochemical and Isotope Sr-Nd Character of Dschang Biotite Granite: Implications for the Pan-African Continental Crust Evolution in West-Cameroon (Central Africa). Earth Science Research; 4, 88-102

Larsen, R.B., Henderson, I., Ihlen, P. M., Jacamon, F., 2004.Distribution and petrogenetic behaviour of trace elements in granitic pegmatite quartz from South Norway.Contribution to Mineral Petrology 147, 615–628.

Lasaga, A., 1984. Chemical kinetics of water-rocks interactions: Journal of Geophysical Research, 89, 4009–4025.

Lasserre et Soba 1976- Ages cambriens des granites de Nyibi et de Kongolo (Centre-Est Cameroun). Comptes Rendus de l'Académie des Sciences, 283, 1696-1698.

Lasserre, M., D., 1976. Age Libérien des granodiorites et des gneiss à pyroxènes du Cameroun Méridional. Bulletin BRGM 2, 17-32.

Le Fort, P., Cuney, M., Deniel, C., France-Lanord, C., Sheppard, S. M. F., Upreti, B. N. and Vidal, P., 1987.Crustal generation of the Himalayan leucogranites. Tectonophysics, 134, 39-57.

Lemarchand, J., Boulvais, P., Gaboriau, M., Boiron, M.C., Tartèse, R., Cokkinos, M., Bonnet, S., Jégouzo, P., 2012. Giant quartz vein formation and high-elevation meteoric fluid infiltration into the South Armorican Shear Zone: geological, fluid inclusion and stable isotope evidence. Journal of Geologycal Society 169, 17–27.

Lemos, R.S.D., Brown, M., Strachan, R.A., 1992. Granite ascent and emplacement within a transpressional orogen. Journal of Geologycal Society 149, 487-490.

Lerouge, C., Cocherie, A., Toteu, S.F., Penaye, J., Milési, J.P., Tchameni, R., Nsifa, E.N., Fanning, C.M. and Doloule, E., 2006. Shrimp U-Pb zircon age evidence for Paleoproterozoic sedimentation and 2.05Ga syntectonic plutonism in the Nyong Group, SouthWestern Cameroon: Consequences for the Eburnean-Transamazonian belt of NE Brazil and Central Africa. Journal of African Earth Sciences44, 413-427.

Li, X.-H., Chen, Y., Li, J., Yang, C., Ling, X.-X., Tchouankoue, J.P., 2016.New isotopic constraints on age and origin of Mesoarchean charnockite, trondhjemite and amphibolite in the Ntem Complex of NW Congo Craton, southern Cameroon.Precambrian Research 276, 14–23.

Loose, D., Schenk, V., 2018. 2.09 Ga old eclogites in the Eburnian- Transamazonian orogeny of southern Cameroon: significance for Palaeoproterozoic plate tectonics. Cameroon.Precambrian Research 304, 1–11

Mancktelow, N. S., Pennacchioni, G., 2004. The influence of grain boundary fluids on the microstructure of quartz-feldspar mylonites, Journal of Structural Geology., 26, 47–69.

Mărgărit M.N, Nicolae H, Simona Marchetti D, Bigi Simona, Gualtieri Alessandro .F., 2016.Progress in mineralogical quantitative analysis of rock samples: application to quartzites from Denali National Park, Alaska Range (USA). Powder Diffract 31:31–39

Marquer, D., 1989. Transferts de matieres et deformation des granitoıdes. Aspects methodologiques, Schweizrische Mineralogische und Petrographische Mitteilungen, 69, 13–33.

Maurizot, P., Abessolo, A., Feybesse, J.L., Johan, V. and Lecomte, P., 1986. Etude et prospection minière du Sud-Ouest Cameroon. Synthèse des travaux de 1978 à 1985. Geological and Mining Research Department (BRGM) Report, 85, 66.

McCaig, A. M., Wickham, S. M., Taylor, H. P., 1990. Deep fluid circulation in alpine shear zones, Pyrenees, France: field and oxygen isotope studies, Contribution to Mineralogy and Petrology 106, 41–60.

McLaren A., C., Cook R., F., Hyde S., T., Tobin R., C., 1983. The mechanisms of formation and growth of water bubbles and associated dislocation loops in synthetic quartz. Physic and Chemistry Mineral 9, 79–94.

Mega Uranium (2009). The official website of Mega Uranium. http://www.megauranium.com/main/index.php-cameroon Accessed on 25th October, 2009.

Menegon, L., Pennacchioni, G., Spiess, R., 2008. Dissolution precipitation creep of K feldspar in mid-crustal granite mylonites, Journal of Structural Geology., 30, 565–579.

Middlemost, E.A.K.,1977.Magmas, Rocks and Planetary Development. Longman, Harlow

Milesi, J., P., Toteu, S., F., Deschamps, Y., Feybesse, J., L., Lerouge, C., Cocherie, A., Penaye, J., Tchameni, R., Mo- loto-A-Kenguemba, G., Kampunzu, H.A.B., Nicol, N., Duguey, E., Leistel, J., M., Saint-Martin, M., Ralay, F., Heinry, C., Bouchot, V., Doumnang Mbaigane, J.C., Kan- da Kula, V., Chene, F., Monthel, M., Boutin, B., Cail- teux, J., 2006. An overview of thegeology and major ore deposits of Central Africa: Explanatory note for the 1: 4000,000 map "Geology and major ore deposits of Cen- tral Africa". Journal of African Earth Sciences, 44, 571- 595.

Min L., Zhenyu P,.Shaomin L,. 2017.Mineralogy and Processing of Hydrothermal VeinQuartz from Hengche, Hubei Province (China). Minerals 7, 161; doi:10.3390 /min7090161

Miyashiro, A., 1974. Volcanic rock series in island arcs and active continental margins.American Journal of Science, 274, 321–355.

Monecke, T, Kempe, U., GÖtze J., 2002. Genetic significance of the trace element content in metamorphic and hydrothermal quartz: a reconnaissance study. Earth and Planetary Science Letters 202, 709-724.

Moore P., 2005. High purity quartz. Ind Miner 8:54–57

Morteani, G., Eichinger, F., Götze, J., Tarantola, A., Müller, A., 2012. Evaluation of the Potential of the Pegmatitic Quartz Veins of the Sierra de Comechigones (Argentina) as a Source of High Purity Quartz by a Combination of LA-ICP-MS, ICP, Cathodoluminescence, Gas Chromatography, Fluid Inclusion Analysis, Raman and FTIR spectroscopy

Mosoh Bambi, C.K., Suh, C.E., Nzenti, J.P., Frimmel, H.E., 2012. U-Mo mineralization potential in Pan-African granites, southwestern Cameroon: Economic geology of the Ekomedion prospect, Journal of African Earth Sciences 65, 25–45.

Müller A, Herrington R, Armstrong R, Seltmann R, Kirwin D.J, Stenina N.G, Kronz A., 2010. Trace elements and cathodoluminescence of quartz in stockwork veins of Mongolian porphyry-style deposits. Mineralium Deposita 45, 707–727

Müller A, Lennox P, Trzebski R., 2002. Cathodoluminescence and micro structural evidence for crystallisation and deformation processes in quartz of S- and I-type granites in the Eastern Lachlan Fold Belt (SE Australia). Contrib Mineral Petrol 143, 510–524

Müller, A., Ihlen, P.M., Wanvik, J.E., Flem, B,. 2007. High-purity quartz mineralisation in kyanite quartzites, Norway. Mineralium Deposita 42, 523–535.

Müller, A., Koch-Müller, M., 2009.Hydrogen speciation and trace element contents of igneous, hydrothermal and metamorphic quartz from Norway. Min Mag 73:569–583.

Muller, A., Wanvik, J.E., Ihlen, P.M. 2012. Petrological and chemical characterisation of High-Purity Quartz deposits with examples from Norway. In: Gotze, J and Mockel, R., eds., Quartz: deposits, Mineralogy and Analytics, p.71-118, Springer Verlag, Heidelberg, natural hydrothermal quartz. Mineral Mag 73, 615–632.

Ndema Mbongue J., L., Ngnotue, T., Ngo Nlend, C., D., Nzenti, J., P., Cheo Suh, E., 2014. Origin and Evolution of the Formation of the Cameroon Nyong Series in the Western Border of the Congo Craton, Journal of Geosciences and Geomatics 2, 62-75.

Ndime E. N., Ganno S., Tamehea L. S., Nzenti J. P., 2018. Petrography, lithostratigraphy and major element geochemistry of Mesoarchean metamorphosed banded iron formation-hosted Nkout iron ore deposit, north western Congo craton, Central West Africa, Journal of African Earth Sciences 148, 80–98

Neba, A.S., 1987, Modern geography of the Republic of Cameroon, 2nd edition: Neba Publishers, Camden, New Jersey, 204.

Nédéléc, A., Macaudière, J., Nzenti, J.P., Barbey, P., 1986. Evolution structurale et métamorphique des schistes de Mbalmayo (Cameroun). Implications pour la structure de la zone mobile panafricaine au contact du craton du Congo. Comptes Rendus Academie des Sciences de Paris, Ser II, 303, 75–80.

Neves, S.P., and Vauchez, A., 1995. Successive mixing and minglinf of magmas in a plutonic complex of northeast Brazil. Lithos, 34, 275-299

Neves, S.P., Vauchez, A., Archanjo, C., 2006. Shear zone-controlled magma emplacement or magma-assisted nucleation of shear zones? Insights from northeast Brazil, Tectonophysics 262, 349-364.

Newman, H.R., 2008. The mineral industries of Cameroon and Cape Verde. In *USGS 2007 Minerals Yearbook - Area Reports: International*, 7.1-7.3. U.S. Department of the Interior, Washington D.C.

Nforba, M.T., Suh, C.E. and Kabeyene, K.V.K., 2010. Mbalam iron ore project, northern edge of the Congo cra- ton, southeast Cameroon. In: Goldfarb, R.J., Marsh, E.E. and Monecke, E., Eds., Proceedings of the Society of Economic Geologists on the Challenge of Finding New Mineral Resources: Global Metallogeny, Innovative Exploration and New Discoveries, SEG Extended Abstracts, Colorado, G-22.

Ng T. F., 1994. Microstructures of the deformed granites of the eastern part of Kuala Lumpur - implications for mechanism and temperature.Geological society of Malaysia, 35, 45-59.

Ngah Essomba T.P., Ganno, S., Tanko Njiosseu, E.L., Ndema Mbongue, J. L., Woguia, B. K., Tamehe, L. S., Takodjou Wambo, J. D., Nzenti, J. P., 2019. Geochemical constraints on the origin and tectonic setting of the serpentinized peridotites from the Paleoproterozoic Nyong series, Eseka area, SW Cameroon Acta Geochim, doi.org/10.1007/s11631-019-00368-4

Ngako V., 2007. Geology and mineral resources. In *Atlas of Cameroon* (eds. N. Houstin and C. Seignobos), pp. 60-61. Les Éditions Jeune Afrique, Paris.

Ngako, V., Affaton, P., Njonfang, E., 2008. Pan–African tectonic in northwestern Cameroon: Implication for history of western Gondwana. Gondwana Research 14, 509–522

Ngako, V., Affaton, P., Nnange, J.M., Njanko, T.H., 2003. Pan-African tectonic evolution in central and Southern Cameroon: transpression and transtension during sinistral shear movements, Journal of African Earth Sciences 36, 207-214.

Ngako, V., Jégouzo, P., Nzenti, J.P., 1991. Le Cisaillement Centre Camerounais. Rôle structural et géodynamique dans l'orogenèse panafricaine. Comptes Rendus de l'Académie des Sciences, Paris 313, 457–463.

Ngnotué, T. Nzenti, J.P. Barbey, P., Tchoua, M.F., 2000. The Ntui-Betamba High Grade Gneisse: A Northward Extension of the Pan-African Yaoundé Gneisses in Cameroon". Journal of African Earth Sciences 31, 369-381.

Nguiessi, T. C., Nzenti, J. P., Nsifa, E. N., Tempier, P., Tchoua, F. M., 1997. Les granitoïdes calco-alcalins, syncisaillement de Bandja dans la chaîne panafricaine nord-équatoriale au Cameroun. Comptes Rendus de l´Académie des Sciences de Paris 325**,** 95 - 101.

Njanko, T. 1999. Granitoïdes calco-alcalins syn-cisaillement de la région de Tibati (Domaine central de la chaîne panafricaine Nord-Equatoriale): leur signification géodynamique par rapport à la tectonique panafricaine. Thèse de Doctorat 3ème cycle, Université de Yaoundé I, 158p

Njanko, T., Nedélec, A., Affaton, P., 2006. Synkinematic high-K calc-alkaline plutons associated to the Pan-African central Cameroon shear zone (west-Tibati area: petrology and geodynamic significance. Journal of African Earth Sciences 44, 494-510.

Njel, U. O., 1988. Contribution à l'étude de l'orogenèse panafricaine. La ceinture volcanosédimentaire de Poli (Nord-Cameroun): lithostratigraphie, pétrographie, géochimie, minéralisations cuprifères associées. Thèse Doctorat de l'I.N. P. L., 220.

Njiekak, G., Dörr, W., Tchouankoue, J. P., Zulauf, G., 2008. U-Pb zircon and microfabric data of (meta) granitoids of western Cameroon: constraints on the timing of pluton emplacement and deformation in the Pan-African belt of Central Africa. Lithos 102, 460-477.

Njome, M.,S., and de Wit, M.,J., 2014. The Cameroon Line: Analysis of an Intraplate Magmatic Province Transecting Both Oceanic and Continental Lithospheres: Constraints, Controversies and Models. Earth-Science Reviews, 139, 168-194

Njome, M.S., Suh, C. E., Ghogomu, R.T., 2003. A microstructural approach to interpreting the structural setting of the Tombel graben, south western Cameroon, Geo Acta 2, 181-200.

Njome, M.S., Suh, C.E., 2005. Tectonic evolution of the Tombelgraben basement, southwestern Cameroon Episodes 28, 37-41.

Ntieche, B., Mohan, M. R., and Moundi A,. 2017. Granitoids of the Magba Shear Zone, West Cameroon, Central Africa: Evidence for Emplacement under Transpressive tectonic Regime. Journal Geological Society of India 89, 33-46.

Ntiéche, B., Mohan, M. R., Moundi, A., Mounjouohou, M. A., 2016. Petrogenesis and Geochemical Characterization of the Granitoids of the Magba Shear Zone West Cameroon Central Africa, Open Journal of Geology, 6, 812-839.

Nzenti J. P., Abaga B., and Suh C. E., 2011. Petrogenesis of peraluminous magmas from the Akum-Bamenda Massif, Pan-African Fold Belt, Cameroon. International Geology Review 53, 1121-1149.

Nzenti, J. P. et, Tchoua, F.M., 1996. Les gneiss scapolitiques de la chaîne nord-équatoriale au Cameroun : témoins au Précambrien d'une sédimentation évaporitique en bordure nord du craton du Congo. Comptes Rendus de l'Académie des Sciences 323, 289 - 294.

Nzenti, J. P., 1987. Pétrogenèse des migmatites de Yaoundé (Cameroun) : éléments pour un modèle géodynamique de la Chaîne Panafricaine Nord-Equatoriale. Thèse Doctorat, Université de Nancy I, 147.

Nzenti, J. P., Kapajika, B., Wörner, G. and Lubala, R. T., 2006.Synkinematic emplacement of granitoids in a Pan-African shear zone in Central Cameroon. Journal of African Earth Sciences 45, 74-86.

Nzenti, J.P., Barbey, P., Macaudiere, J., Soba, D., 1988a. Origin and evolution of the late Precambrian high grade Yaoundé gneisses (Cameroon), Precambrian Research 38, 91–109.

Nzenti, J.P., 1998b. L'Adamaoua panafricain (région de Banyo) : une zone clé pour un modèle de la chaîne panafricaine nord-équatoriale au Cameroun. Thèse Doctorat D'Etat, Université Cheikh Anta Diop –Université de Nancy I, 176p.

Nzenti, J.P., 1998c. Neoproterozoic alkaline meta-ignous rocks from the Pan-African North Equatorial Fold Belt (Yaounde Cameroon): biotites and magnetite rich pyroxenites. Journal of African Earth Sciences 26, n°1, 37-47

Nzenti, J.P., Barbey, P., Jegouzo, P. et Moreau, C., 1984. Un nouvel exemple de ceinture granulitique dans une chaîne Protérozoïque de collision: les migmatites de Yaoundé au Cameroun. Comptes Rendus de l'Académie des Sciences de Paris 299, 17**,** 1197 - 1199.

Nzenti, J.P., Barbey, P., Tchoua, F.M. 1999. Evolution crustale au Cameroun: éléments pour un modèle géodynamique de l'orogenèse néoproterozoïque. In Géologie et

environnements au Cameroun, Vicat J.P., Bilong P. (Eds.), collection GEOCAM 2, 397-407.

Nzolang, C., 2005. Crustal evolution of the Precambrian basement in west Cameroon: inference from geochemistry, Sr-Nd isotopes and experimental investigation of some granitoids and metamorphic rocks. Ph. D thesis, Niigata University, 206.

Nzolang, C., Kagami, H., Nzenti J.P. & Holtz, F., 2003. Geochemistry and preliminary Sr-Nd isotopic data on the Neoproterozoïc granitoids from the Bantoun area, west Cameroon: evidence for a derivation from a paleoproterozoïc to Archean crust. Polar Geoscience16, 196-226.

Oberthur, T. (2013): Comments on 'Trace element distribution in uraninite from MesoArchaean Witwatersrand conglomerates (South Africa) suppors placer model and magmatogenic source' by Depine et al. (Mineralium Deposita 48, 423-435, 2013). Mineralium Deposita, 48, 1047-1050.

Oliot, E., Goncalves, P., Schulmann, K., Marquer, D., Lexa, O., 2014. Mid-crustal shear zone formation in granitic rocks: Constraints from quantitative textural and crystallographic preferred orientations analyses, Tectonophysics, 612-613, 63–80.

Oliveira, C., Rodrigues, R. T., and Rubio.J., 2014.Nucleation, growth and coalescence phenomena of air bubbles on quartz particles in different aqueous solutions. Bubble Science, Engineering and Technology 5, 1-2

Oliver, N. H. S., 1996. Review and classification of structural controls on fluid flow during regional metamorphism. Journal of metamorphic Geology 14, 477-492.

Owona, S., Schulz, B., Ratschbacher, L., Mvondo Ondoa, J., Ekodeck, G.-E., Tchoua, M. F., Affaton, P., (2010).Pan-African metamorphic event in the southern Yaoundé Group (Oubanguide Complex, Cameroon) as revealed by EMP-monazite and thermobarometry of garnet metapelites. Journal of African Earth Sciences, doi: 10.1016/2010.09.003.

Pasava, J., Frimmel, H.E., Vymazalova, A., Dobes, P., Jukov, A.V., Koneev, R.I., 2013. A two-stage evolution model for the Amantaytau orogenic-type gold deposit in Uzbekistan. Minner deposita 48, 825-840.

Passchier, C.W. & Trouw, R.J., 2005. Microtectonics, Springer Berlin Heidelberg New York.

Patiño-Douce, A.E., Johnston, A.D., 1991. Phase equilibria and melt productivity in the pelitic system: implications for the origin of peraluminous granitoids and aluminous granulites. Contribution to Mineral Petrology 107, 202-218.

Pearce, J., A., Harris, N., W., Tindle, A., G., 1984. Trace element discrimination diagrams for the tectonic interpretation of granitic rocks. Journal of Petrology25, 956–983.

Pearce, J.,A., 1996. Source and setting of granitic rocks.Episode 19, 120–125.

Penaye, J. 1988. Pétrologie et structure des ensembles métamorphiques au Sud –Est de Poli (Nord-Cameroun). Rôles respectifs du socle protérozoique inférieur et de l'accrétion et de l'accrétion crustale panafricaine. Thèse de l'INPL, Nancy, 196p.

Penaye, J., Toteu, S. F, Michard, A., Bertrand, J. M., et Dautel, D., 1989. Reliques granulitiques d'âge Protérozoïque inférieur dans la zone mobile Panafricaine d'Afrique Centrale au Cameroun ; géochronologie U/Pb sur zircons. Comptes Rendus de l'Académie des Sciences Paris 309, 315-318.

Penaye, J., Toteu, S.F., Van Schmus, W.R. & Nzenti, J.P., 1993. U-Pb and Sm-Nd preliminary geochronologic data on the Yaoundé series, Cameroon: re-interpretation of the granulitic rocks as the suture of a collision in the "centrafrican" belt. Comptes Rendus de l'Académie des Sciences Paris 317, 789-794.

Poirier, J. P., 1980. Shear localization and shear instability in materials in the ductile field, Journal of Structural Geology 2, 135–142.

Pryer, L.L., 1993, Microstructures in feldspars from a major crustal thrust zone: The Grenville front, Ontario, Canada: Journal of Structural Geology, 15, 21–36.

Pryer, L.L., Robin, P.Y.F., 1995. Retrograde metamorphic reactions in deforming granites and the origin of flame perthite, Journal of metamorphic Geology 13, 645–658.

Regnoult, J.M., 1986, Synthese geologique du Cameroun: ImprimerieNational, Yaounde,. p 119.

Reiner, H., Prinz, S., Priess, C., 2012, Assesssment of high purity quartz resources. Götze, J and Möckel, R (eds.), Quartz: Deposites, mineralogy and analytics, 29-51.

Roedder, E., 1984. Fluid inclusions.Reviews in Mineralogy.Mineral.Soc. America, Washington, 12, 644.

Romer, R.,L., Franz, L., Wirth, R., 2006. Chemical and isotopic effects of retrogression

Rusk, B. G., Lowers, A. H., Reed M. H., 2008. Trace elements in hydrothermal quartz: Relationships to cathodoluminescent textures and insights into vein formation. Geological Society of America 36, 547–550;

Rusk, B., Reed, M., Dilles, J., and Kent, A., 2006. Intensity of quartz cathodoluminescence and trace element content of quartz from the porphyry copper deposit in Butte, Montana: American Mineralogist 91, 1300–1312.

Samson, I., Anderson, A. and Marshall, D. (Eds.), 2003.Fluid inclusions - Analysis and Interpretation.Mineralogical Association of Canada. Short Course Series, 32, 374p.

Santos, M.F.M., Fujiwara, E., De Paula, F.D., Suzuki, C.K., 2013. Opacity measurements on quartz and its influence on silica glass properties. International Journal of Mineral.Process. 124, 141-144.

Santos, M.F.M., Fujiwara, E., Schenkel, E. A., Enzweiler, J., Suzuki, C.K., 2015. Quartz sand resources in the Santa Maria Eterna formation, Bahia, Brazil: A geochemical and morphological study, Journal of South American Earth Sciences 62, 176-185.

Santos, M.F.M., Fujiwara, E., Schenkel, E.A., Enzweiler, J., Suzuki, C.K., 2014. Quartz resources in the Serra de Santa Helena formation, Brazil: a geochemical and technological Study. Journal of South America Earth Science 56, 328-338.

Scharwtz, G.M., 2006. Alteration of biotite under mesothermal conditions, American Geological Institute.Economic geology. Economic Geology (1958) 53 (2): 164-177

Schmatz, J., Urai, J.L., 2011. The interaction of migrating grain boundaries and fluid inclusions in naturally deformed quartz: a case study of a folded and partly recrystallized quartz vein from the Hunsrück Slate. German Journal of Structural Geology, 33, 468-480.

Schmid, S.M., and M.R. Handy. 1991. Towards a genetic classification of fault rocks: Geological usage and tectonophysical implications. In: Controversies in Modern

Geology, ed. K.J. Hsü, J. Mackenzie, and D. Müller, London: Academic Press, 339–361.

Schmidt, C., Bruhn, D., Wirth, R., 2003. Experimental evidence of transformation plasticity in silicates: minimum of creep strength in quartz. Earth Planet. Science Letter 205, 273-280.

Schron, W., Bauman, L., Rank, K., 1982.Zur Charakterisierung von Quartz- generationen in den postmagmatogenen Ertzformationen des Erzgebirges.Zeitschrifit für Geol (in german) Wiss.16, 229-244.

Seifert, W., Rhede, D., Thomas, R., Förster, H.J., Lucassen, F., Dulski, P., Wirth, R., 2011. On the origin of igneous blue quartz: inferences from a multi-analytical study of submicron mineral inclusions. Mineral Mag 75:2519–2534

Shang, C.K., Liégeois, J.P., Satirb, M., Frisch, W. and Nsifa, E.N., 2010. Late Archaean high-K granite geochronology of the northern metacratonic margin of the Archaean Congo Craton, Southern Cameroon: Evidence for Pb-loss due to non-metamorphic causes Gondwana Research18, 337-355.

Shang, C.K., Satirb, M. Siebelb, W. Nsifa, N.E. Taubald, H., Liegeois, J.P. and Tchoua F.M., 2004. TTG magmatism in the Congo craton; a view from major and trace element geochemistry, Rb-Sr and Sm-Nd systematics: case of the Sangmelima region, Ntem complex, Southern Cameroon. Journal of African Earth Sciences, 40, 61-79.

Shepherd, T.J., Rankin, A.H. and Alderton, D.H.M., 1985.A practical guide to fluid inclusion studies.BlackieGlasgow., 239p.

Shigematsu, N., 1999. Dynamic recrystallization in deformed plagioclase during progressive shear deformation, Tectonophysics 305:437–452.

Sibson, R., H., 1977. Fault rocks and fault mechanisms. Journal of Geology Society, London 133, 191-213.

Sigue, C., Moundi, A., Ndema Mbongue, J. L., Vishiti, A., Kedia, A. C., Suh, C.E.,and Nzenti, J.P., 2019.Quartz-Rich Fault Rocks as Potential High Purity Quartz Source (I) in a Sequence of the Central Cameroon Shear Zone(Etam Shear Zone): Geology and Structure.F. Rossetti et al. (eds.), The Structural Geology Contribution to the Africa-

Eurasia Geology: Basement and Reservoir Structure, Ore Mineralisation and Tectonic Modelling. https://doi.org/10.1007/978-3-030-01455-1_16.

Simpson, C., Wintsch, R. P., 1989. Evidence for deformation-induced K-feldspar replacement by myrmekite.Journal of Metamamorphic Geology 7, 261–275.

SINOSI 2013. High Purity Quartz Material, Version: HPQ-18-20130101

Soba, D., 1989**.** La série de Lom: étude géologique et géochronologique d´un bassin volcanosédimentaire de la chaîne panafricaine de l´Est du Cameroun**.** Thèse de Doctorat d´Etat, Université de Paris VI, France, 198.

Soh, T.L., Nzepang Tankwa, M., Chongtao, W., Ganno, S., Ngnotue, T., Kouankap Nono, G.D., Shaamu, J.S., Zhang, J., Nzenti, J.P., 2018. Geology and geochemical constrains on the origin and depositional setting of the Kpwa-Atog Boga banded iron formations (BIFs), northwestern Congo craton, southern Cameroon. Ore Geol Rev 95:620–638.

Spear, F.S., Wark, D. A., 2009.Cathodoluminescence imaging and titanium thermometry in metamorphic quartz. J metamorphic Geol, 27, 187–205

Spruzeniece L., Piazolo S., 2015. Strain localization in brittle–ductile shear zones: fluid-abundant vs.fluid-limited conditions (an example from Wyangala area, Australia). Solid Earth, 6, 881–901.

Stipp, M., Stünitz, H., Heilbronner, R., Schmid, S. M., 2002. The eastern Tonale fault zone: a "natural laboratory" for crystal plastic deformation of quartz over a temperature range from 250 to 700 °C. Journal of Structural Geology 24,1861–1884.

Streit, J.E., Cox, S.F., 1998. Fluid infiltration and volume change during mid-crustal mylonitizationof Proterozoic granite, King Island, Tasmania. Journal of Metamorphic Geology 16, 197–212.

Suh, C. E., Dada, S.S., 1997. Fault rocks and differential reactivity of minerals in the Kanawa violaine Uraniferous vein, NE Niegria, Journal of Structural Geology 19, 1037-1044.

Suh, C.E., Cabral, A.R., Shemang, E.M., Mbinkar, L. and Mboudou, G.G.M., 2008. Two contrasting iron-ore de- posits in the Precambrian mineral belt of Cameroon, West Africa. *Exploration and Mining Geology*, **17**, 197-207.

Suzuki, C.K., Santos, M.F.M., Ono, E., Fujiwara, E., 2012. Strategic high quality quartz supply for fusion into silica glass. In: Varshneya, A.K., Schaeffer, H.A., Richardson, K.A., Wightman, M., Pye, D. (Eds.), Processing Properties and Applications of Glass and Optical Materials: Ceramic Transactions. The American Ceramic Society, 69-74.

Sylvester, P.J., 1998. Post-collisional strongly peraluminous granites. Lithos 45, 29-44.

Taber, s., 1918. The origin of veinlets in the Silurian and Devonian strata of central new York. The Journal of Geology 6, 56-73.

Tadjou, J. M., 2004. Apport de la gravimetrie à l'investigation géophysique de la bordure septentrional du craton du Congo (Sud-Cameroun).Thèse Doctorat/PhD, Université de Yaoundé I, 178p.

Tagne-Kamga, G., 1994. Le complexe plutonique panafricain de Ngondo (Ouest Cameroun): Structure et pétrogenèse. Thèse Doctorat, Université Franche-comté, 236p.

Tagne-Kamga, G., 2003.Petrogenesis of the NeoproterozoicNgondo plutonic complex (Cameroon, West Central Africa): a case of late-collisional ferro-potassicmagmatism, Journal of African Earth Sciences 36, 149-171.

Tagne-Kamga, G., Mercier, E., Rossy, M., Nsifa, N.E., 1999. Synkinematic emplacement of the Pan-African Ngondo igneous complex (west Cameroon, central Africa). Journal of African Earth Sciences 28, 675-691.

Tanko Njiosseu, E.L., Nzenti, J.P., Njanko, T., Kapajika, B., Nédelec, A., 2005. New U-Pb zircon ages from Tonga (Cameroon): coexisting Eburnean-Transamazonian (2.1 Ga) and Pan-African (0.6 Ga) imprints. Comptes Rendus Géosciences 337, 551-562.

Tarantola, A., Diamond, L.W., Stunitz, H., 2010. Modification of fluid inclusions in quartz by deviatoric stress I: experimentally induced changes in inclusion shapes and microstructures. Contrib Mineral Petrol, 160, 825–843

Tarantola, A., Diamond, L.W., Stünitz, H., Thust, A., Pec, M., 2012. Modification of fluid inclusions in quartz by deviatoric stress III: influence of principal stresses on fluid inclusion density and orientation. Contribution to Mineralogy and Petrology 164, 537-550.

Tchakounté J., Eglinger A., Toteu S. F., Zeh A ., Nkoumbou C., Mvondo-Ondoa J., Penaye J., de Wit M ., Barbey P.,2017. The Adamawa-Yadé domain, a piece of Archaean crust

in the Neoproterozoic Central African Orogenic belt (Bafia area, Cameroon).Precambrian Research 299, 210–229

Tchameni R., Pouclet A., Penaye J., Ganwa A.A. and Toteu S.F., 2006. Petrography and geochemistry of the Ngaoundéré Pan-African granitoids in Central North Cameroon: Implications for their sources and geological setting? Journal of African Earth Science 44, 511-529.

Tchaptchet Tchato D., Schulz B., Nzenti J.P., 2009. Electron microprobe dating and thermobarometry of Neoproterozoic metamorphic events in the Kekem area, Central African Fold Belt of Cameroon. Neues Jahbür Minerolgy Abh.,186/1, 95- 109.

Thomas, R., Webster, J. D., and Davidson, P. (2006). Understanding pegmatite formation: the melt and fluid inclusion approach. In: Webster J. D. (Ed.), 120 Melt inclusions in plutonic rocks. Short Course Series 36, 189–210

Thomas, S.M., 2008. Wasserstoff in nominell wasserfreien Mineralen.PhD thesis. TU Berlin, D 83, Berlin, Germany, 134

Thompson, R. N., Morrisson, M. A., Hendry, G. L. and Parry, S. J. 1984- An assessment of the relative role of crust and mantle in magma genesis. An element approach. Philosophical Transactions of the Royal Society London, A310, 549-590.

Thompson, R., N., 1982. British tertiary volcanic province. Scottland Journal of Geology, 18, 49-107.

Toteu, S., F., Van Schmus, W., R., Penaye, J., Nyobe´, J., B., 1994. U–Pb and Sm–Nd evidence for Eburnean and Pan-African high-grade metamorphism in cratonic rocks of southern Cameroon. Precambrian Research 67, 321–347.

Toteu, S.F., Bertrand, J.M., Penaye, J., Macaudière, J., Angoua, S.,Barbey, P., 1991.Cameroon: a tectonic keystone in the Pan-African network. In the Early ProterozoicTrans-Hudson orogen of North America, Lewry, J.F. and Stauffer, M.R. Eds,. Geological Association of Canada, Special Paper 37, 483–496

Toteu, S.F., Penaye, J., Poudjom Djomani, Y.H., 2004. Geodynamic evolution of the Pan African belt in Central Africa with special reference to Cameroon.Canadian Journal of Earth Sciences 41, 73-85.

Toteu, S.F., Van Schmus, Penaye, J., Michard, A., 2001. New U-Pb and Sm-Nd data from North-Central Cameroon and its bearing on the pre- Pan-African history of CentralAfrica, Precambrian Research 108, 45-73.

Trompette, R., 1997. Geology of Western Gondwana (200–500 Ma) Pan-African Aggregation of South America and Africa. Bakelma, Rotterdam/Broofield, 350 p.

Trompette, R., 1997. Neoprotozoïc (600 Ma) aggregation of: western Gondwana a tentative Scenario. Precambrian Research 82, 101-112.

Tullis, J., Yund, R.A., 1980. Hydrolytic weakening of experimentally deformed Westerly granite and Hale albite rock, Journal of Structural Geology 2, 439–451.

Urai, J., Means, W. D., Lister, G. S., 1986. Dynamic recrystallization of minerals. In: Heard HC, Hobbs BE (eds) Mineral and rock deformation: laboratory studies. GeophysicalMonograph 36, 161–200.

Van den Kerkhof, A.M., Hein, U.F., 2001. Fluid inclusion petrography. Lithos 55:27–47

Vidal, O., Durin, L., 1999. Aluminium mass transfer and diffusion in water at 400–550 8^0C, 2 kbar in the K_2O–Al_2O_3–SiO_2–H_2O system driven by a thermal gradient or by a variation of temperature with time.Mineralogical Magazine 63, 633–647.

Vielzeuf, D., Kornprobst, J., 1984. Crustal splitting and the emplacement of the pyrenean lherzolites and granulites. Earth Planet Science Letter 67, 87-96

Vilalva,F., C., J., Vlach, S., R., F., 2014. Geology, petrography and geochemistry of the A-type granites from the Morro Redondo Complex (PR-SC), southern Brazil, Anais da Academia Brasileira de Ciências, 86, 85-116.

Vishiti, A., Suh, C.E., Lehmann, B., Egbe, J.A., Shemang, E.M., 2015. Gold grade variation and particle microchemistry in exploration pits of the Batouri gold district, SE Cameroon. Journal of African Earth Sciences 111, 1-13.

Vityk, M.O., Bodnar, R.J., Doukhan, J.-C., 2000.Synthetic fluid inclusions. XV. TEM investigation of plastic flow associated with reequilibration of fluid inclusions in natural quartz. Contributions to Mineralogy and Petrology, 139, 285-297.

Wark, D.A., Watson, E.B., 2006. TitaniQ: a titanium-in-quartz geothermometer. Contributions to Mineralogy and Petrology, 152, 743–754.

Watson, E.B., Wark, D.A., 1997. Diffusion of dissolved SiO_2 in H_2O at 1 GPa, with implications for mass transport in the crust and upper mantle. Contributions to Mineralogy and Petrology 130, 66–80.

Weinberg, R., 2004. Granite transport and Emplacement: a review. Ishihara Symposium: Granites and Associeted Metallogenesis.125-127.

White, S. H., Knipe, R. J., 1978. Transformation- and reaction enhanced ductility in rocks, Journal of Geological Society 135, 513–516.

White, S., 1977. Geological significance of recovery and recrystallization processes in quartz, Tectonophysics, 39, 143–170.

White, S., 1982. Fault rock of the Moine Thrust Zone: a guide to their nomenclature. Texture and microstructures.4, 211-21.

Widmer, T., Thompson, A.B., 2001.Local origin of high pressure vein material in eclogitefacies rocks of the Zermatt–Saas zone, Switzerland. American Journal of Sciences 301, 627–656.

Wintsch, R. P., & Yi, K., 2002. Dissolution and replacement creep: A significant deformation mechanism in mid-crustal rocks, Journal of Structural Geology 24, 1179–1193.

Wintsch, R., P., & Yeh, M.W., 2013. Oscillating brittle and viscous behavior through the earthquake cycle in the Red River Shear Zone: Monitoring flips between reaction and textural softening and hardening. Tectonophysics 587, 46-62.

Wise, D., U., Engelder, J., T., Geiser, P., A., Hatcher, R., D., Kish, S., A., Odom, A., L., Schamel, S., 1984. Fault –related rocks: suggestion for terminology. Geology 12, 391-4

Woodcock, N. H., Mort, K.,2008. Classification of fault breccias and related fault rocks.Geological Magazine145, 435–440.

Zolensky, M.E., Sylvester, P.J., Paces, J.B., 1988.Origin and significance of blue coloration in quartz from Llano rhyolite (llanite), north-central Llano County, Texas.Am Mineral

ANNEX

Annex 1: Foliation planes S_1

N020E 60°ESE X25	N022E 60°ESE X20	N030E60°ESE	N018E 40°E	N015E 45°E
N010E 46°E	N008E 47°E	N050E 48°E	N015E 40°E	N025E 50°E
N025E 50°E	N028E 55°E	N026E 60°ESE		

Annex 2: Foliation planes S_2

N011E 85°W X15	N012E 82°W X15	N010E 80°W X30	N008E70°W	N014E 75°W
N005E 87°W	N007E 84°W	N020E 72°WNW X25	N022E 79°WNW X6	N015E 75°WNW
N010E 80°W	N018E 74°WNW	N016E 78°W	N025E 70°WNW	N023E 76°WNW
N024E 65°WNW	N020E 60°WNW X15	N022E 60°WNW X10	N018E 65°WNW X4	N016E 58°W
N040E 85°SE X25	N010E 80°E	N020E 75°E	N026E 70°E	N022E 80°ESE
N025E 85ESE	N022E 86°ESE	N023E 80°E	N018E 75°E	N015E 70°E
N012E 78°E	N016E 72°E	N014E 82°E	N024E 84°E	N017E 79°E
N019E 87°E	N023E 62°W	N017E 68°W	N015E 65°W	

Annex 3: Fracture planes C_2

N065E 60°NNW	N060E 58°NW	N062E 60°NW	N064E 62°NNW	N025E 82°WNW
N085E 78°S	N092E 80°S	N150E 70°WSW X10	N110E 70°SW X20	N140E 60°SW X15
N110E 83°NNE	N020E 84°W	N058E 82°NW	N060E 60°NW x6	N080E 62°NW x4
N100E 40°S X16	N120E 50°SW X10	N080E 60°SSE X3	N140E62°SW	N120E 40°SW X5
N130E 80°SE	N062E 45°NE	N105E 70°SSW	N065E 75°NE	N023E 85°E
N110E 85°SW X6	N108E 85S°W X2	N100E 80°W X2	N095E75°W	N140E 60°SW X4
N015E 88°E	N140E 88°NE	N130E 85°NE	N120E 78°SW X4	N110E 78°SSW X3
N088E 70°SW	N120E 65°NE X5	N100E 80°N X3	N110E 65°SSW	N107E 60°S
N105E 76°SSW	N080E 68°SSE	N160E 80°ENE	N130E 80°NE	N080E 60°NNW X2
N120E65°SSW	N100E 65°S	N107E 65°S	N165E 55°WSW	N150E 60°WSW
N092E 60°N	N120E 80°SW X20	N115E 85°SSW X12	N-S 70°W	N-S 65°W X10
N145E 78°NE	N140E 78°NE	N140E 85°SW	N100E 85°SSW	N105E 85°SSW
N020E 65°WNW X5	N175E 60°WSW	N170E 60°WSW	N090E 78°S	N160E 50°SW

Annex 4: planes C_2 (Quartz Veins)

N045E 74°NW	N046E 85°NW	N110E 75°NNE	N105E 70°NNE	N065E 85°NW
N140E 40°SW	N130E 40°SW	N030E 65°SE	N050E 66°SE	N045E 65°SE
N050E 85NW	N110E 45°NNE	N040E 65°SE	N120E 42°NE	N020E 60°E
N012E 84°W x8	N020E 83°W x13	N010E 70°W x15	N-S 75° W	N140E 80°SW
N120E 45°SW	N100E 60°W	N-S 45°W	N020E 62°W	N010E 82°W X5
N135E 85°SW	N120E 82°SW	N020E 80°WNW	N040E 50°NW	N105E 50°W
N140E 60° WSW X4	N020E 70°WNW			

Annex 5: Publications

Sigue, C., Moundi, A., Ndema Mbongue, J. L., Vishiti, A., Kedia, A. C., Suh, C.E.,and Nzenti, J.P., 2019.***Quartz-Rich Fault Rocks as Potential High Purity Quartz Source (I) in a Sequence of the Central Cameroon Shear Zone (Etam Shear Zone): Geology and Structure.***F. Rossetti et al. (eds.): The Structural Geology Contribution to the Africa-Eurasia Geology: Basement and Reservoir Structure, Ore Mineralisation and Tectonic Modelling. https://doi.org/10.1007/978-3-030-01455-1_16.

Sigue, C., Moundi, A., Suh, C. E., Santos, M. F. M., Fujiwara, E., Suzuki, K. C., Ndema-Mbongue, J.L., 2020. ***Assessment of shear zone-derived quartz from the Etam area, south west Cameroon as potential high purity quartz resource: petrography, geochemistry and technological studies***. *SN Applied Sciences en 2020: DOI 10.1007/S42452-020-2301-7.*

Research Article

Assessment of shear zone-derived quartz from the Etam area, southwest Cameroon as potential high-purity quartz resource: petrography, geochemistry and technological studies

Cyrille Sigue[1,2] · Amidou Moundi[3] · Cheo Emmanuel Suh[1,5] · Murilo Ferreira Marques dos Santos[4] · Eric Fujiwara[4] · Carlos Kenichi Suzuki[4] · Jean Lavenir Ndema-Mbongue[1,2]

Received: 5 October 2019 / Accepted: 18 February 2020

Abstract
This study focuses on the evaluation of the high-purity quartz (HPQ) potential of a shear zone-hosted hydrothermal and metamorphic quartz deposit in Etam, southwest Cameroon. The shear zone quartz-rich rock is monomineralic and consists of both milky and translucent varieties. The combination of ICP-MS and LA-ICP-MS analytical techniques was used to assess the chemical purity of both quartz varieties. These compositional analyses show that all quartz samples have SiO_2 content of 98.46–99.75 wt% with very low concentrations of all the other elements. Translucent quartz when compared to the milky quartz variety shows low concentration of most of the elements including the following principal impurities: Al (mean 107 µg g^{-1}), Ca (mean 27.85 µg g^{-1}) and Fe (mean 26.05 µg g^{-1}). Bubble generation in the samples after flame fusion over a silica plate was assessed to test the suitability of the quartz in industrial uses. The results obtained from the chemical analyses and bubble formation tests indicate that all the samples investigated do not meet the HPQ requirement. However, the translucent quartz shows characteristics of medium-purity quartz and can produce silica glass for some industrial manufacturing even without further purification. In this study, the fluid inclusions in the samples were examined as this bears information on the economic viability of the deposit and provides clues on the genesis of the quartz vein. Also tiny mineral inclusions within individual quartz grains were identified by SEM–EDS. The results of these studies show that the deposit is probably of metamorphic origin marked by crystal-plastic deformation in quartz grains. The veins were later modified by hydrothermal fluid input. The results also indicate that the majority of impurities are likely hosted by fluid inclusions and thus the quartz can be upgraded to HPQ after purification by suitable methods.

Keywords Hydrothermal · Metamorphic · Cameroon · Shear zone · Silica glass · High-purity quartz (HPQ)

1 Introduction

The high-purity quartz (HPQ) market is presently characterized by a stable growth and annually increases by 3 to 5%. Despite this constant increase in the worldwide demand [1–3], quartz raw material resources with high purity are rare. An alternative solution to assure the HPQ supply for industries today can be the purification of medium- and low-purity quartz to upgrade the quartz grade. HPQ is an important raw material required for the production of silica glass [4, 5], and it is widely used in the electronics industry and advanced telecommunication and navigation devices.

✉ Cyrille Sigue, siguecyrille@gmail.com | [1]Economic Geology Unit, Department of Geology, University of Buea, P.O. Box 63, Buea, Cameroon. [2]Laboratory of Geosciences for Internal Formations and Applications, Department of Earth Sciences, Faculty of Science, University of Yaoundé I, P.O. Box 3412, Yaoundé, Cameroon. [3]Department of Earth Sciences, University of Yaoundé I, P.O. Box 3412, Yaoundé, Cameroon. [4]Laboratory of Photonic Materials and Devices, School of Mechanical Engineering, University of Campinas (UNICAMP), R. Mendeleyev 200, Campinas 13083-860, Brazil. [5]Department of Geology, Mining and Environmental Science, The University of Bamenda, P.O. Box 39, Bambili, North West Region, Cameroon.

SN Applied Sciences (2020) 2:551 | https://doi.org/10.1007/s42452-020-2301-7

Published online: 04 March 2020

SN Applied Sciences
A SPRINGER NATURE journal

Muller et al. [6] determined that for quartz to be classified as HPQ, the total impurity content should be less than 50 µg g^{-1}. The high content of some impurities such as Al, Ti, Ge and Fe affects drastically the quality of quartz [7–11]. For example, Al content can generate devitrification, resulting in cristobalite white spots, whereas Ti and Fe can contaminate the silicon melt [11] derived from HPQ during industrial applications. Another type of impurity in quartz is fluid inclusions. Despite the fact that fluid inclusions are less difficult to remove in quartz compared to metallic impurities (Ti, Fe, Ge), they can also jeopardize the suitability of quartz as an industrial raw material. Some characteristics of silica glasses made from HPQ also depend on the chemical purity and the amount of fluid inclusions in the raw material. Examples are the transparency in UV and visible ranges, resistance to radiation and mechanical strength [10, 12].

Purification of low-purity quartz using industrial processing is often very costly, laborious and constitutes environmental hazard [1, 11, 13, 14]. Medium-purity quartz with good technological behavior necessitates environment-friendly methods of contaminants removal that drastically reduced the treatment cost and time. Proper processing methods such as calcination pretreatment combined with ultrasound-assisted leaching [15] that increase SiO_2 content concentration up to 99.9% and methods using HCl–NH_4Cl and H_2SO_4–NH_4Cl reagents with removal rate between 88 and 99 wt% for some impurities (Al, K and Fe) have been developed [16] to upgrade quartz purity in order to meet industries' quartz glass requirements. In this regard, industries often prefer the application of purification techniques in medium- to high-purity resources.

In southwestern Cameroon, quartzitic rocks and quartz veins occur along major fault/shear zones and metamorphic rocks. The fault rocks range from breccias to mylonites, and most of them are monomineralic composed essentially of milky to transparent quartz. The potential of finding HPQ in these rocks has not been evaluated despite the widespread occurrence of these lithologies in the area. This is the aspect that constitutes the rationale of this study, and the expected results are of more than local importance considering that the potential of finding HPQ in the area exists.

2 Geological setting

2.1 Regional geological setting

Etam area is located in the southwestern sector of the Tombel Plain and belongs to the central domain of the Central African Fold Belt (CAFB) [17–19] in the southwest region of Cameroon. The CAFB is a megastructure, generally E–W oriented, and it is about 5000 km in length and about 300 km in width (Fig. 1a), running through Cameroon across the Atlantic Ocean into northeast of Brazil [20–25]. The central domain of CAFB in Cameroon comprises the Paleoproterozoic granulite [18, 26–28] and the Neoproterozoic metasedimentary rocks [29–31] intruded by syntectonic granitoids [25, 32–39] along thrust and shear zones (Fig. 1b), the most prominent being the Central Cameroon Shear Zone (CCSZ). The CCSZ is one of the most important and largest active strike-slip fault zones in Cameroon. It is part of the transatlantic shear zone system referred to as the Central African Shear zone (CASZ) that extends from the interior of Africa across the Atlantic into South America [40]. It is a set of anastomosing transcurrent faults [41] and shows an important mylonitic band trending N70°E to N30°E.

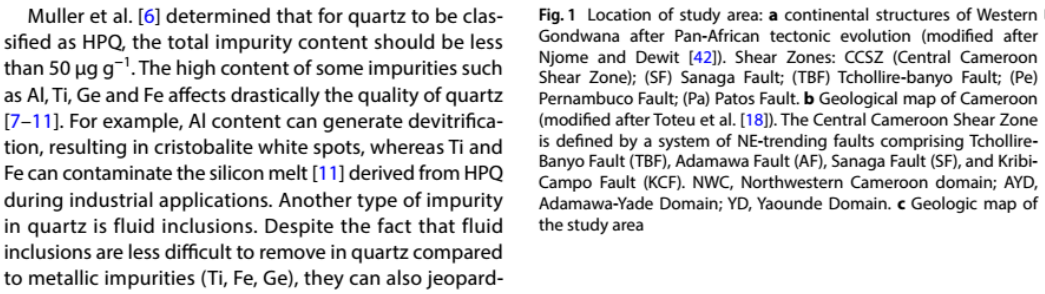

Fig. 1 Location of study area: **a** continental structures of Western Gondwana after Pan-African tectonic evolution (modified after Njome and Dewit [42]). Shear Zones: CCSZ (Central Cameroon Shear Zone); (SF) Sanaga Fault; (TBF) Tchollire-banyo Fault; (Pe) Pernambuco Fault; (Pa) Patos Fault. **b** Geological map of Cameroon (modified after Toteu et al. [18]). The Central Cameroon Shear Zone is defined by a system of NE-trending faults comprising Tchollire-Banyo Fault (TBF), Adamawa Fault (AF), Sanaga Fault (SF), and Kribi-Campo Fault (KCF). NWC, Northwestern Cameroon domain; AYD, Adamawa-Yade Domain; YD, Yaounde Domain. **c** Geologic map of the study area

2.2 Geology of Etam

The Etam area has mainly plutonic rocks (granitic and granodioritic) and metamorphic rocks including gneisses and migmatites. These lithologies are associated with a mylonitic band (Fig. 1c) oriented N030 to N045 [43] termed the Etam shear zone (ESZ) [44], which constitutes a segment of CCSZ. The mylonitization event has been attributed to a Pan-African age [40] and has reworked the gneissic foliation. The basement rocks at Etam are extensively covered in some places by the basaltic lavas from the Cameroon Volcanic Line (CVL). All these lithologic units are crosscut by several randomly oriented fracture sets and quartz veins. The quartz veins are few millimeters to several meters wide.

The studied quartz veins in this work are observed in ESZ. This is a clear white rock with no other rock-forming minerals than quartz similar to the Serra de Santa Helena high-purity quartz rock. [43, 44] suggested magmatic protoliths for the mylonitic rocks in Etam. These previous studies also indicated greenschist to amphibolitic metamorphic conditions between 300 and 450 °C in the surrounding country rocks, where epidote, neocrystallized quartz and chlorite minerals assemblage coupled with

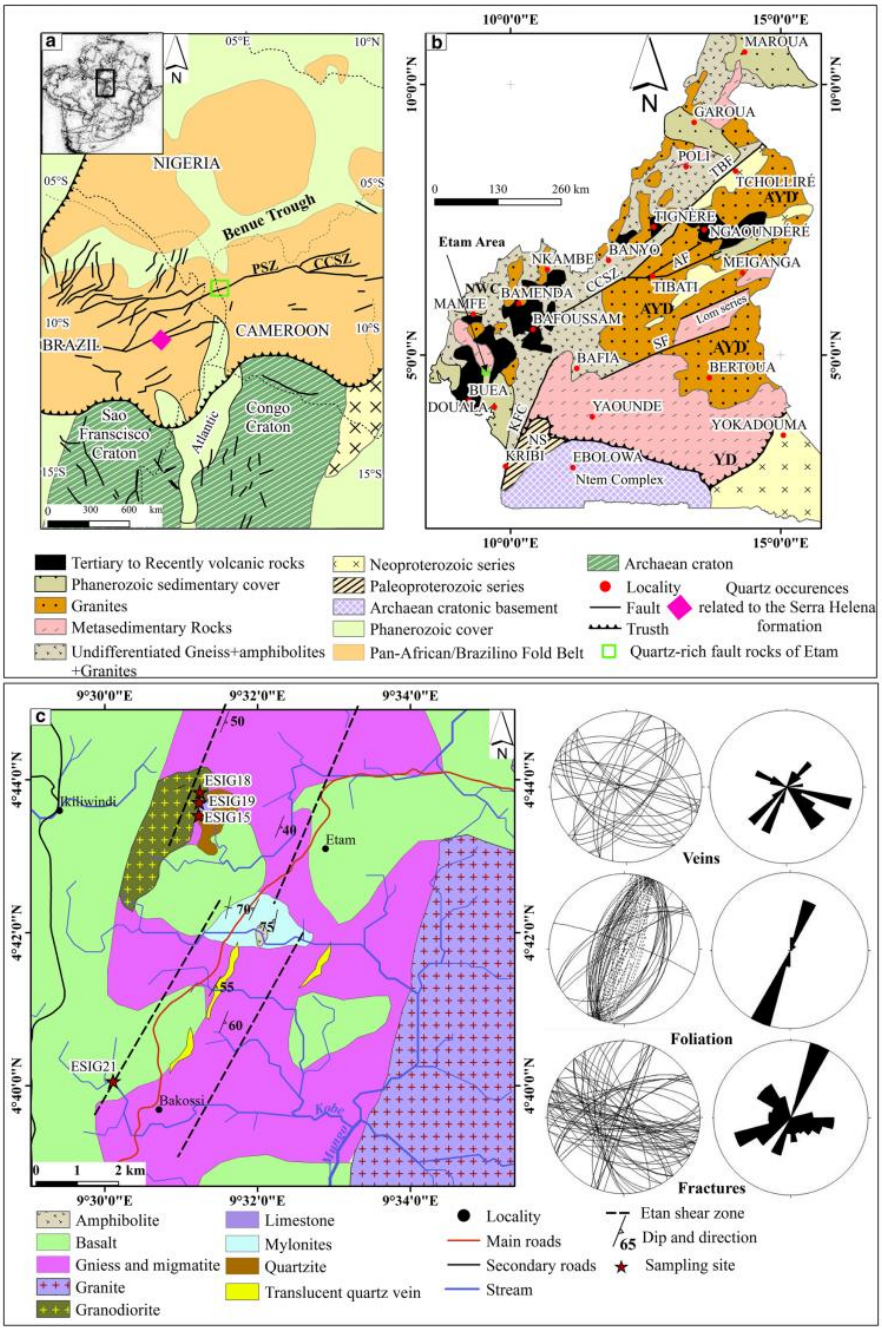
a
NIGERIA
Benue Trough
PSZ
CCSZ
CAMEROON
BRAZIL
São Franscisco Craton
Congo Craton
Atlantic
b
Etam Area
MAROUA
GAROUA
POLI
TCHOLLIRÉ
TIGNÈRE
NGAOUNDÉRÉ
BANYO
NKAMBE
MEIGANGA
TIBATI
BAMENDA
MAMFE
BAFOUSSAM
BAFIA
BERTOUA
BUEA
DOUALA
YAOUNDE
YOKADOUMA
KRIBI
EBOLOWA
Ntem Complex
AYD
YD
Lom series
Tertiary to Recently volcanic rocks
Phanerozoic sedimentary cover
Granites
Metasedimentary Rocks
Undifferentiated Gneiss+amphibolites +Granites
Neoproterozoic series
Paleoproterozoic series
Archaean cratonic basement
Phanerozoic cover
Pan-African/Brazilino Fold Belt
Archaean craton
Locality
Fault
Trusth
Quartz occurences related to the Serra Helena formation
Quartz-rich fault rocks of Etam
c
ESIG18
ESIG19
ESIG15
ESIG21
Ikiliwindi
Etam
Bakossi
Kribi
Lobe
Veins
Foliation
Fractures
Amphibolite
Basalt
Gniess and migmatite
Granite
Granodiorite
Limestone
Mylonites
Quartzite
Translucent quartz vein
Locality
Main roads
Secondary roads
Stream
Etan shear zone
Dip and direction
Sampling site

the albitization of K-feldspar and the formation of perthite were recorded.

The ESZ surrounding rock or wall rock (granodiorite) shows magmatic constituents (Kfs_1, Qtz_1, Pl_1 and Bt_1), recrystallized quartz (Qtz_2) and Ab + Chl as products of Kfs_1 alteration. The mylonites in the ductile zone in addition to primary igneous minerals also have secondary constituents (Qtz_2, Qtz_3, Pl_2, Bt_2, Ms) developed at the expense of Qtz_1, Pl_1 and Bt_1 through pervasive alteration and recrystallization. Other minerals include amphibole, muscovite, chlorite as well as iron oxide, pyrite and zircon. According to [44], the pervasive alteration in ESZ released K^+, Na^+, Ca^+, Fe^+ and Al^+ ions that circulated in hydrothermal fluids saturated in Si, precipitated in fractures and enriched the quartz veins.

For this study, two quartz veins were mapped and suitable quartz samples were collected for systematic laboratory analyses as detailed in the following sections.

3 Methods

3.1 Fluid inclusion observation using optical microscopy

For the fluid inclusion observation, a small amount of quartz grains sized 70 to 180 µm was placed on a microscope slide. In order to improve the observation of the grains, a film of kerosene was applied over them. The kerosene has a refractive index similar to that of the silica, which reduces undesired surface observations. A Nikon optical microscope operated at 500 × magnifications was used to acquire transmitted light photographs for fluid inclusion analysis, using a Nikon digital camera. All photographs were taken at room temperature. Using this methodology, it was possible to obtain insights on the nature of the fluid and mineral inclusions present in the grains. Although more complete analyses were not carried out, regarding homogenization temperature and other key properties of the inclusions, it was possible to obtain reliable data on mineral inclusions in the quartz grains. These data were vital in order to propose insights into the genesis of veins.

3.2 Fusion over silica plate

Samples were powdered using a silica mortar and sieved in nylon sieves at the Analytical Geochemistry Laboratory, UNICAMP, Brazil. Particle size distribution was selected between 80 and 200 mesh, i.e., 75 to 180 µm. The manufactured powders were then placed over a silica plate, and a H_2/O_2 flame was applied over it using a premix torch. Flame conditions, burner distance to the sample and time of fusion were kept the same during all experiments, about 4 mm and 15 s, respectively, although samples took different times until complete fusion. For bubble analysis, the silica plates were photographed using a mineralogical microscope. Photographs of each fused plate were taken and then processed by computational analysis, in order to measure average bubble size and density on each photograph. This is a common test conducted by several silica glass industries in order to evaluate the powder performance during glass making. Bubbles larger than 10 to 15 µm are highly undesired once they can affect the final glass' properties. This procedure is widely used in the literature [10–13, 45].

3.3 Chemical analysis using inductively coupled plasma mass spectroscopy (ICP-MS) on quartz

Quartz samples of 0.1 g were dissolved using 0.5 mL of distilled HF in special vessels. The samples were then kept over a hot plate at 80 °C for 1 h in order to enhance the dissolution process. Afterward, temperature was elevated to 110 °C for evaporation. Subsequently, 0.5 mL of HF and 0.1 mL of HNO_3 were added and the system was kept closed for 24 h. After this procedure, the samples were recovered using a nitric acid solution of 1% in mass. All solutions were prepared using ultrapure water (18.2 MΩ cm) obtained by Mili-Q system. All used acids were purified by subboiling. The vessels used were previously cleaned with a 5% nitric acid solution and washed with ultrapure water. All measurements were conducted by the ICP-MS technique using an X series II (Thermo) instrument, equipped with collision cell technology (CCT) at the Analytical Geochemistry Laboratory, Institute of Geosciences, UNICAMP, Brazil [45].

3.4 Chemical analysis using laser ablation inductively coupled plasma mass spectroscopy (LA-ICP-MS)

Quartz composition was further evaluated using a New Wave Research Excimer Laser Ablation UP193FX and an Agilent 7500i quadrupole mass spectrometer. The laser had a pulse rate of 20 Hz, a speed of 15 µm s^{-1}, a spot size of 50 µm and energy fluency of 5–7 mJ cm^{-2} on the sample surface. Raster ablation was applied on an area of approximately 150 µm × 300 µm. The approximate depth of ablation was about 50 µm. The carrier gas for transport of the ablated material to the ICP-MS was He mixed with Ar. External calibration was performed using three silicate glass reference materials produced by the National

Institute of Standards and Technology, USA (NIST SRM 610, 612 and 614). In addition, the NIST SRM 1830 soda-lime float glass (0.1% *m/m* Al2O_3), the certified reference material BAM No. 1 amorphous SiO_2 glass and the Qz–Tu synthetic pure quartz monocrystal were used. Measurements on commercially available IOTA HPQ material as well as reference material BSC CRM 313/1 (high-purity quartz) were performed for further external calibration; reproducibility and accuracy. Each measurement comprised 15 scans of each isotope, with a measurement time varying from a 0.15 s/scan for K in high resolution to a 0.024 s/scan of, for example, Li in low resolution. A linear regression model, including several measurements of the different reference materials, was used to define the calibration curve for each element. For the calculation of P concentrations, the procedure of [46] was applied. Ten sequential measurements on the Qz–Tu synthetic pure quartz monocrystal standard were used to estimate the limits of detection (LOD—3σ of ten measurements). The analytical error ranges within 10% of the absolute concentration of the element.

3.5 Mineralogical quantitative analysis of quartz samples by SEM–EDS

Each quartz sample was crushed and panned in the laboratory. Grains were observed under a scanning electron microscope (SEM) fitted with an energy-dispersive spectrometer (EDS) following procedures described by [47]. The EDS provided geochemical patterns reminiscent of the chemical composition of each phase identified.

4 Results and interpretation

4.1 Petrography and textural studies

Two quartz bodies are studied in this work: (1) quartzite body, showing blocks with variable dimensions (up to 20 m × 8 m) observed in the Etam Shear Zone (ESZ). The quartzite blocks are brecciated and can be traced along strike for over 2.5 km [44] in NNE–SSW to NE–SW direction. On some large blocks, joints and hydrothermal quartz veinlets (up to 15 cm wide) are observed arranged in subparallel arrays (Fig. 2a). The veinlets are characterized by a development of recrystallized serrate to elongated blocky quartz grains, where crystals grow from the wall inward (Fig. 2b). Generally, the blocks are monomineralic constituted by milky quartz clasts showing variable dimensions (< 0.2 mm to 8 cm in size) and having the form of polygonal crystals with sharp edges (Fig. 2c). Some are elongated and faceted, healed by a silicified quartz matrix (i.e., an optically continuous silica mass), composed of fine quartz crystals (10–80 µm) showing in some places red spots (Fig. 2d) of clustered grains (colored material), probably Fe-stained quartz grains trapped within an aggregate of smaller quartz grains.

Two types of breccias are observed in the Etam samples, both in hand specimen and under the microscope (see Table 1 for samples description): (a) Crackle breccias (75–100% clast > 2 mm, Fig. 2e) display small isolated monomineralic quartzite blocks (1.2 × 0.8 m) and represent ~ 5% of the quartzite in the area. They contain from ~ 85 to ~ 98% angular clasts with sharp edges, variable dimensions (2 mm to 8 cm, Fig. 2c) and a siliceous matrix often less than 3%. (b) Mosaic breccias (65–75% clast > 2 mm, Fig. 2f) which show blocks (up to 20 × 12 m) and are also monomineralic are widely spread in the study area, composed of slightly elongated quartz clasts (0.6 mm to 1.2 cm) and occupy 65–73% of the volume of the rock. Some wider intergranular zones are observed with very fine-grained cataclasite indicating sintered material. In some samples, fine-grained materials of the reformed grains show interlocking grain boundaries in some thin sections. (2) A translucent quartz vein (~ 20 cm wide, Fig. 2g) was mapped in the southwestern sector of the study area surrounded by a biotite gneiss country rock. The regional foliation and the vein are parallel and trend N023°E to N030°E with subvertical dips. The vein is composed of highly homogeneous translucent fine-grained pure quartz (Fig. 2h) and ranges from 1 to 3 µm in size. Fluid and mineral inclusions are observed in both deposits, and a detailed description of their petrographic characteristics is provided in the paragraph on fluid inclusions below.

4.2 Geochemistry of Etam quartz

4.2.1 Rock geochemistry by ICP-MS

The bulk rock chemistry of the Etam quartz samples is displayed in Table 2. The samples are characterized by 98.26–99.75 wt% SiO_2. The concentrations of the other major elements are very low (Al_2O_3 = 0.01 to 0.15 wt%, Fe_2O_3tot = 0.1 to 0.59 wt%, MgO = 0.01 to 0.02 wt%, TiO_2 = 0.002 to 0.006 wt% Na_2O = 0.01 to 0.02). The concentration of K_2O (0.01 wt%) is constant. Most of the trace elements are below the detection limit. When present, their concentrations are low, e.g., Cr (55–220 ppm), Zr (3–4 ppm) and Ba (3–4 ppm).

Only four light rare-earth elements (LREE) are detected by the ICP-MS analysis. Their concentrations vary slightly: La (0.2 to 0.4 ppm), Ce (0.3 to 0.4 ppm), Pr (0.03 to 0.05 ppm) and Nd (0.1 to 0.2 ppm. The quasi-totality of heavy rare-earth elements (HREE) is below detection limits.

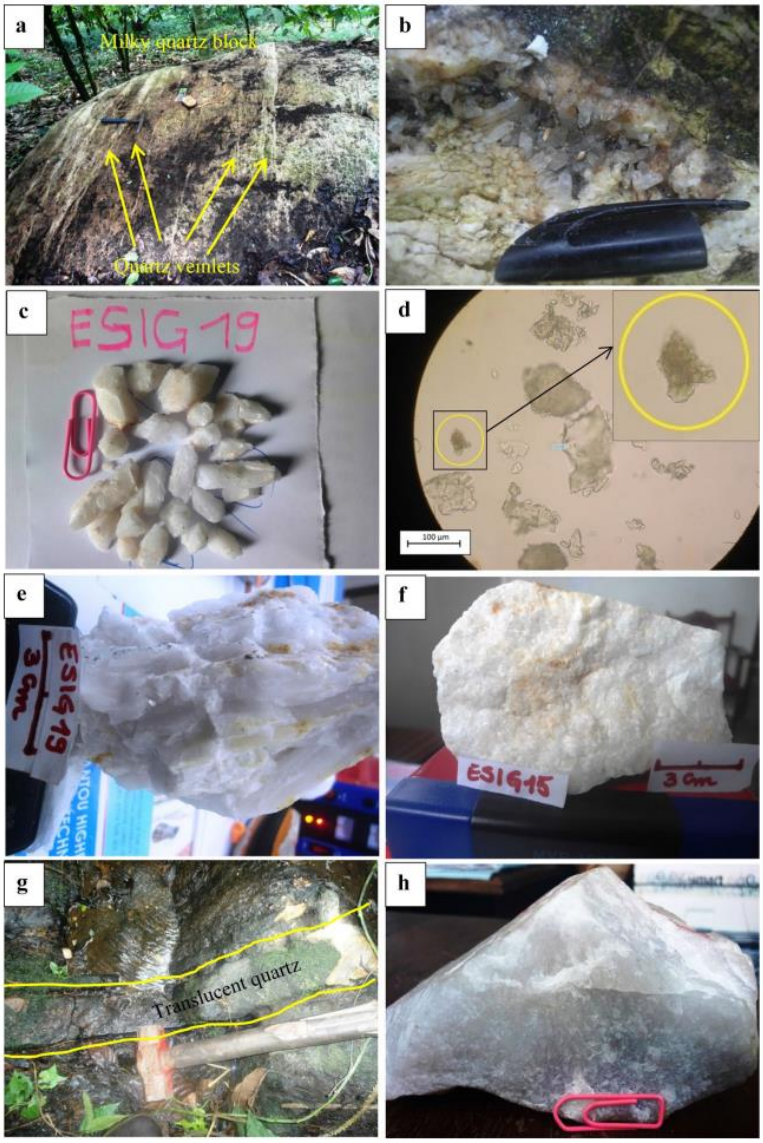

Fig. 2 Photograph and photomicrograph of the Etam quartz. **a** Brecciated quartzite block crosscut by quartz veinlets in subparallel array, **b** recrystallized quartz grain growing from the wall inward in quartz vein **c** milky quartz clast, faceted and elongated, up to 12 cm. **d** photomicrograph of cluster of small quartz grain containing red spot, probably iron oxide, **e** crackle breccia, **f** mosaic breccia, **g** aspect of translucent quartz vein translucent quartz vein on the outcrop (yellow lines), **h** hand specimen of the translucent quartz vein

4.2.2 Concentrations of impurities in the quartz determined by LA-ICP-MS

The analysis of representative quartz samples is given in Table 3. Three samples were selected from the brecciated quartz block (milky quartz) and two samples from the translucent quartz vein. A single spot was analyzed in each sample section. In order to better appreciate the chemical purity of quartz, the elements' concentrations were converted into µg g^{-1}. The data illustrated that: (1) milky quartz (samples ESIG15, ESIG18 and ESIG19) has high to moderately high concentrations of trace elements compared to average concentrations in natural quartz [6, 14]: Al (mean 579.66 µg g^{-1}), Ca (mean 70.7 µg g^{-1}), Fe (mean 57.36 µg g^{-1}), K (mean 116.96 µg g^{-1}), Ti (mean 5.67 µg g^{-1}), and low concentration for Zr (mean 0.26 µg g^{-1}) Ce (mean

Table 1 Representative investigated samples description

Sample no.	Sample description	Inclusion types
ESIG15	Averagely cohesive, crackle breccia, medium-size milky quartz clasts healed by very fine grains of siliceous matrix	Monophase, irregular and regular two-phase inclusion, mineral inclusion
ESIG18	Cohesive, mosaic breccia, milky fine quartz clasts cemented by small quartz crystal (10–80 µm)	Cubic crystal inclusion, irregular two-phase and cluster inclusions, mineral and satellite inclusions
ESIG19	Weakly cohesive, crackle breccias with milky large quartz clasts (up to 8 cm) often brittle + siliceous matrix	Dipyramidal monophasic and hexagonal negative crystal two-phase inclusions, mineral inclusion
ESIG21a	Massive, fine translucent quartz grains	Small inclusions, oriented biphasic negative crystal type, dipyramidal monophasic fluid inclusion, needle-like mineral inclusions

0.21 µg g^{-1}) and Ge (mean 0.14 µg g^{-1}). (2). The translucent quartz is characterized by low concentrations of trace elements compared to milky quartz: Al (mean 107 µg g^{-1}), Ca (mean 27.85 µg g^{-1}), Cr (mean 3.54 µg g^{-1}), Fe (mean 26.05 µg g^{-1}), Ge (mean 0.83 µg g^{-1}), K (mean 82,4 µg g^{-1}), Li (mean 0.51 µg g^{-1}), Mg (mean 5.15 µg g^{-1}), Na (mean 34.75 µg g^{-1}), Ni (mean 1.84 µg g^{-1}), Ti (mean 23.75 µg g^{-1}), Zr (mean 1.61 µg g^{-1}). In Etam quartz, Al, Ca, Cr, Fe, K, Mg, Na, Ni, Ti and Zr represent about 99% of the total impurities in this quartz. Other elements are below the detection limits. In HPQ, Fe is desirable to be under 10 ppm and Ca below 10 ppm as well. All the trace elements in HPQ put together should be less than 50 ppm [6, 14].

In the translucent quartz, the concentration of trace elements is low compared to the milky quartz. An exception is observed for Ag, Co, Cr, Ni, Zn, Zr and Ti. Aluminum is the most important impurity in this quartz, and it is highly variable (107–811 µg g^{-1}) between samples (Table 3). It commonly substitutes Si in quartz structure or is incorporated in quartz by the hydrothermal fluids. Titanium concentration is consistently higher in translucent quartz compared to Ti in milky quartz. The variability of Ti concentrations between milky and translucent quartz is probably related to the difference in deformation temperature or the presences of mineral inclusions [48, 49]. Indeed, microscopic studies of translucent quartz permit to observe several rutile mineral inclusions in translucent quartz, which increase their bulk (whole rock) Ti concentration [50]. Potassium content is highly variable in milky quartz. Sample E-SIG19 shows K concentration below the detection limit, and in sample ESIG15, the K content is 261 in µg g^{-1}. The concentration of Na in both quartz varieties is reflected by the presence of several cubic salt crystals (NaCl) within fluid inclusions (daughter crystals) observed under the microscope. The calcium and Mg contents are high in all the samples and variable (Ca/Mg ratio varies between from 2.03 to 16.36). Usually, the concentration of these elements is related to mineral inclusions in the quartz crystals or halite phases in the fluid inclusions [11, 14, 51, 52] reflecting the crystallization of quartz in saline environments [11, 51, 53]. The concentration of Fe is high in all samples. According to [6], the high concentrations of Fe in quartz are predominantly diffusion-controlled. Therefore, ferromagnesian minerals in contact with quartz can induce high Fe content in this quartz. Microscopic observation permitted to distinguish spots of Fe-rich mineral inclusions in quartz grains attesting the accumulation of Fe in the milieu. Lithium shows low concentration (mean 0.51 µg g^{-1}) in the translucent quartz compared to the milky quartz (mean 6.79 µg g^{-1}), thus suggesting that Li is probably associated with submicroscopic mineral inclusions in the milky quartz [54]. This suggests therefore the low participation of Li in the process of charge-balancing cation for Al, Fe and P. Therefore, the H^+ from the hydrothermal fluid plays a greater role in the charge compensator for cation in the translucent quartz. SEM/EDS analyses were conducted to better understand the aspects of possible mineral inclusions in the translucent quartz, once the whole rock analysis and the fusion tests indicated that this quartz variety is the most promising. Two points (P_1 and P_2) were selected in sample ESIG21a (Fig. 3a) and three (P_1, P_2 and P_3) in sample ESIG21b (Fig. 3b).The resulting EDS spectra for samples ESIG 21a [Fig. 3a, ESIG21a (P_1) and (P_2)] and ESIG 21b (Fig. 3b, ESIG21b (P_1), (P_2) and (P_3) show high peaks for O and Si. The absence of any peaks for other elements that could have been contributed by submicroscopic or nanoparticle mineral inclusions indicated that this quartz variety is free of contaminant mineral inclusions.

4.3 Fluid inclusion petrography

Fluid inclusions observed in the Etam quartz samples generally are monophase or two-phase inclusions (Table 1). In this study, the fluid inclusions for the milky quartz samples are studied and the results presented separately from the data derived from samples of the translucent quartz.

Table 2 Major, trace and rare-earth element analyses of Etam quartzite (ICP-MS)

	Milky quartz								Translucent quartz	
	ESIG 5	ESIG 10	ESIG 14	ESIG 15a	ESIG 15b	ESIG 15c	ESIG 18	ESIG 19	ESIG 21a	ESIG 21b
Major elements (wt%)										
SiO_2	99.75	98.67	98.99	98.26	98.26	99.21	99.4	99.58	98.46	98.46
Al_2O_3	0.03	0.13	0.02	0.13	0.13	0.11	0.05	0.05	0.05	0.05
Fe_2O_3	0.1	0.39	0.51	0.49	0.49	0.32	0.36	0.21	0.58	0.58
MnO	0.006	0.005	0.006	0.005	0.005	0.005	0.006	0.006	0.006	0.006
MgO	0.02	0.01	0.02	0.01	0.01	0.01	0.02	0.02	0.02	0.02
CaO	0.02	0.02	0.02	0.02	0.02	0.02	0.02	0.01	0.02	0.02
Na_2O	0.02	0.01	0.02	0.01	0.01	0.01	0.02	0.02	0.02	0.02
K_2O	0.01	0.01	0.01	0.01	0.01	0.01	0.01	0.01	0.01	0.01
TiO_2	0.004	0.002	0.006	0.002	0.002	0.002	0.005	0.006	0.006	0.006
P_2O_5	< 0.01	< 0.01	< 0.01	< 0.01	< 0.01	< 0.01	< 0.01	< 0.01	< 0.01	< 0.01
LOI	0.04	0.25	0.02	0.25	0.25	0.25	0.01	0.07	0.07	0.07
Total	100	99.50	99.622	99.187	99.19	99.947	99.901	99.982	99.25	99.242
Trace elements (ppm)										
Be	< 1	< 1	< 1	< 1	< 1	< 1	< 1	< 1	< 1	< 1
Sc	< 1	< 1	< 1	< 1	< 1	< 1	< 1	< 1	< 1	< 1
V	< 5	< 5	< 5	< 5	< 5	< 5	< 5	< 5	< 5	< 5
Cr	220	55	94	100	100	81	199	216	220	220
Co	< 1	< 1	< 1	< 1	< 1	< 1	< 1	< 1	< 1	< 1
Ni	< 20	< 20	< 20	< 20	< 20	< 20	< 20	< 20	< 20	< 20
Cu	< 10	< 10	< 10	< 10	< 10	< 10	< 10	< 10	< 10	< 10
Zn	< 30	< 30	< 30	< 30	< 30	< 30	< 30	< 30	< 30	< 30
Ga	< 1	< 1	< 1	< 1	< 1	< 1	< 1	< 1	< 1	< 1
Ge	1	< 0.5	1	< 0.5	< 0.5	1	1	1	1	1
As	< 5	< 5	< 5	< 5	< 5	< 5	< 5	< 5	< 5	< 5
Rb	< 1	< 1	< 1	< 1	< 1	< 1	< 1	< 1	< 1	< 1
Sr	< 2	< 2	< 2	< 2	< 2	< 2	< 2	< 2	< 2	< 2
Y	< 0.5	< 0.5	< 0.5	< 0.5	< 0.5	< 0.5	< 0.5	< 0.5	< 0.5	< 0.5
Zr	3	4	4	4	4	3	3	4	3	3
Nb	4.1	5.1	4.7	5.4	5.4	3.9	3.1	3.1	3.1	3.1
Mo	< 2	<2	<	10	10	<2	< 2	8	< 2	< 2
Ag	< 0.5	< 0.5	< 0.5	< 0.5	< 0.5	< 0.5	< 0.5	< 0.5	< 0.5	< 0.5
In	< 0.1	< 0.1	< 0.1	< 0.1	< 0.1	< 0.1	< 0.1	< 0.1	< 0.1	< 0.1
Sn	< 1	< 1	< 1	< 1	< 1	< 1	< 1	< 1	< 1	< 1
Sb	< 0.2	< 0.2	< 0.2	< 0.2	< 0.2	< 0.2	< 0.2	< 0.2	< 0.2	< 0.2
Cs	< 0.1	< 0.1	< 0.1	< 0.1	< 0.1	< 0.1	< 0.1	< 0.1	< 0.1	< 0.1
Ba	4	3	3	4	4	4	4	3	4	4
Hf	< 0.1	< 0.1	< 0.1	< 0.1	< 0.1	< 0.1	< 0.1	< 0.1	< 0.1	< 0.1
Ta	< 0.01	< 0.01	< 0.01	< 0.01	< 0.01	< 0.01	< 0.01	< 0.01	< 0.01	< 0.01
W	< 0.5	< 0.5	< 0.5	< 0.5	< 0.5	< 0.5	< 0.5	< 0.5	< 0.5	< 0.5
Tl	< 0.05	< 0.05	< 0.05	< 0.05	< 0.05	< 0.05	< 0.05	< 0.05	< 0.05	< 0.05
Pb	< 5	< 5	< 5	< 5	< 5	< 5	< 5	< 5	< 5	< 5
Bi	< 0.1	< 0.1	< 0.1	< 0.1	< 0.1	< 0.1	< 0.1	< 0.1	< 0.1	< 0.1
Th	< 0.05	< 0.05	< 0.05	< 0.05	< 0.05	< 0.05	< 0.05	< 0.05	< 0.05	< 0.05
U	< 0.01	< 0.01	< 0.01	< 0.01	< 0.01	< 0.01	< 0.01	< 0.01	< 0.01	< 0.01
Rare-earth element (ppm)										
La	0.4	0.2	0.3	0.2	0.2	0.3	0.4	0.4	0.4	0.4

Table 2 (continued)

Rare-earth element (ppm)										
Ce	0.3	0.4	0.4	0.4	0.4	0.3	0.4	0.4	0.4	0.4
Pr	0.03	0.05	0.05	0.05	0.05	0.05	0.04	0.03	0.03	0.03
Nd	0.2	0.2	0.2	0.2	0.2	0.1	0.2	0.1	0.1	0.1
Sm	< 0.01	< 0.01	< 0.01	< 0.01	< 0.01	< 0.01	< 0.01	< 0.01	< 0.01	< 0.01
Eu	< 0.005	0.01	0.01	0.01	0.01	<0.005	0.01	< 0.005	< 0.005	< 0.005
Gd	< 0.01	< 0.01	< 0.01	< 0.01	< 0.01	< 0.01	< 0.01	< 0.01	< 0.01	< 0.01
Tb	< 0.01	< 0.01	< 0.01	< 0.01	< 0.01	< 0.01	< 0.01	< 0.01	< 0.01	< 0.01
Dy	< 0.01	< 0.01	< 0.01	< 0.01	< 0.01	< 0.01	< 0.01	< 0.01	< 0.01	< 0.01
Ho	< 0.01	< 0.01	< 0.01	< 0.01	< 0.01	< 0.01	< 0.01	< 0.01	< 0.01	< 0.01
Er	< 0.01	< 0.01	< 0.01	< 0.01	< 0.01	< 0.01	< 0.01	< 0.01	< 0.01	< 0.01
Tm	< 0.005	< 0.005	< 0.005	< 0.005	< 0.005	< 0.005	< 0.005	< 0.005	< 0.005	< 0.005
Yb	< 0.01	< 0.01	< 0.01	< 0.01	< 0.01	< 0.01	< 0.01	< 0.01	< 0.01	< 0.01
Lu	< 0.002	< 0.002	< 0.002	< 0.002	< 0.002	< 0.002	< 0.002	< 0.002	< 0.002	< 0.002

4.3.1 Milky quartz

In the milky quartz, most of the fused grains contain abundant inclusions with small size (Fig. 4, yellow color) ranging from 2 to 12 µm and randomly distributed (Fig. 5a). They are monophase or two-phase inclusions showing two distinct phases at room temperature: a solid daughter crystal phase and a fluid phase.

- Monophase fluid inclusions

The monophase fluid inclusions are fewer in number compared to the two-phase fluid inclusions. Rarely, they are dipyramidal monophasic inclusions (Fig. 5b, orange arrow). Most are irregular and some have the shape of negative crystals.

- Two-phase and three-phase fluid inclusions

The majority of fluid inclusions in the milky quartz are two-phase fluid inclusions. Usually, they are composed of liquid and gas although some have daughter crystals. The presence of halide crystals indicates that the liquid phase is probably brine while gas phase is CO_2. Often here, fluid inclusions show spherical gas bubbles (Fig. 5c, black arrows) with a range from 5 to 30% of the total volume of the inclusion. Many two-phase inclusions are irregular (Fig. 5c, black arrows) in shape. Smaller regular inclusions are observed with bubbles, often larger than the liquid volume (Fig. 5c, blue arrow). Some two-phase inclusions showing negative hexagonal crystal-shape (Fig. 5d, black arrow) are observed in this quartz.

Solid phases observed in the fluid inclusions mostly display cubic outlines (Fig. 5d, e, red arrow), which are probably salt crystals (NaCl), as attested by the high amount of Na present in the ICP-MS data analysis (Table 3). Other fluid inclusions are rarely observed, mostly irregular in shape and larger (12 µm) than the solid phases encountered in some inclusions (Fig. 5e, green arrow). Figure 5f (blue light arrow) shows large inclusions with smaller fluid inclusions (satellite inclusions) surrounding it. Tarantola et al. [55, 56] showed that, due to deviatoric stress, inclusions can be deformed and dismembered, giving a large relic inclusion and a cluster of small neonate (satellite) inclusions around it.

4.3.2 Translucent quartz

The inclusions present in the translucent quartz are different from those of the milky quartz samples. The fluid inclusions are much smaller compared to those of milky quartz (Fig. 4) and oriented. Figure 6a shows this orientation (represented by the black line). Most of these oriented inclusions are of the negative crystal type but much smaller. Monophase inclusions are common and occur as dipyramidal monophase inclusions (Fig. 6b, orange arrow). Several needle-shaped mineral inclusions (Fig. 6c, gray arrow) which are suggested to be rutile because of the elevated concentration of Ti in LA-ICP-MS analyses (Table 3) are observed in this quartz sample as well as small acicular inclusions, randomly distributed in the grains.

4.4 Fusion of quartz grains over silica plate: bubble formation and bubble characterization

In this section, the results of the quartz/silica plates tested for bubble formation are presented in the form of photographs at various stages of heating. The images were then processed by computational analysis in order to measure average bubble size and bubble density on each

Table 3 Impurities concentrations in quartz samples (LA-ICP-MS)

		Milky quartz			Translucent quartz	
		ESIG15	ESIG18	ESIG19	ESIG21a	ESIG21b
Ag	$\mu g\ g^{-1}$	0.002	0.003	0.004	0.011	0.009
Al	$\mu g\ g^{-1}$	354	811	574	107	107
B	$\mu g\ g^{-1}$	< LD	< LD	51	< LD	< LD
Ba	$\mu g\ g^{-1}$	0.82	1.24	0.86	0.42	0.41
Be	$\mu g\ g^{-1}$	0.07	0.10	0.05	0.03	0.03
Ca	$\mu g\ g^{-1}$	64.3	47.8	100	27.3	28.4
Ce	$\mu g\ g^{-1}$	0.11	0.19	0.33	0.08	0.06
Co	$\mu g\ g^{-1}$	0.01	0.02	0.01	0.05	0.05
Cr	$\mu g\ g^{-1}$	0.85	1.46	1.49	3.43	3.65
Cs	$\mu g\ g^{-1}$	0.020	0.033	0.016	0.003	0.003
Cu	$\mu g\ g^{-1}$	0.30	0.23	0.88	0.52	0.62
Dy	$\mu g\ g^{-1}$	0.006	0.009	0.009	0.002	0.001
Er	$\mu g\ g^{-1}$	0.004	0.004	0.005	0.001	0.001
Eu	$\mu g\ g^{-1}$	0.001	0.003	0.003	0.001	0.001
Fe	$\mu g\ g^{-1}$	36.4	67.8	67.9	26.5	25.6
Ga	$\mu g\ g^{-1}$	0.06	0.15	0.05	0.02	0.02
Gd	$\mu g\ g^{-1}$	0.004	0.016	0.010	0.003	0.002
Ge	$\mu g\ g^{-1}$	0.15	0.12	0.17	0.83	0.84
Hf	$\mu g\ g^{-1}$	0.004	0.009	0.008	0.04	0.04
Ho	$\mu g\ g^{-1}$	0.001	0.001	0.002	< LD	< LD
K	$\mu g\ g^{-1}$	89.9	261	< LD	81.0	83.8
La	$\mu g\ g^{-1}$	0.07	0.36	0.11	0.04	0.04
Li	$\mu g\ g^{-1}$	5.24	11.4	3.74	0.51	0.51
Lu	$\mu g\ g^{-1}$	0.001	< LD	0.001	< LD	< LD
Mg	$\mu g\ g^{-1}$	6.78	23.5	6.11	5.64	4.67
Mn	$\mu g\ g^{-1}$	0.28	0.53	0.51	0.43	0.55
Na	$\mu g\ g^{-1}$	37.2	32.3	41.0	34.7	34.8
Nb	$\mu g\ g^{-1}$	0.04	0.04	0.02	< LD	< LD
Nd	$\mu g\ g^{-1}$	0.03	0.16	0.08	0.02	0.02
Ni	$\mu g\ g^{-1}$	0.44	0.71	0.73	1.82	1.87
Pb	$\mu g\ g^{-1}$	0.18	0.17	1.59	0.19	0.11
Pr	$\mu g\ g^{-1}$	0.01	0.05	0.02	0.01	0.01
Rb	$\mu g\ g^{-1}$	0.95	3.15	0.40	0.38	0.33
Sb	$\mu g\ g^{-1}$	0.002	0.002	0.012	0.003	0.004
Sc	$\mu g\ g^{-1}$	< LD	< LD	< LD	< LD	< LD
Sm	$\mu g\ g^{-1}$	0.006	0.02	0.02	0.004	0.003
Sn	$\mu g\ g^{-1}$	< LD	< LD	< LD	< LD	< LD
Sr	$\mu g\ g^{-1}$	1.43	1.50	1.34	0.26	0.26
Ta	$\mu g\ g^{-1}$	< LD	< LD	< LD	< LD	0.02
Tb	$\mu g\ g^{-1}$	0.001	0.002	0.002	< LD	< LD
Te	$\mu g\ g^{-1}$	< LD	< LD	0.001	< LD	< LD
Th	$\mu g\ g^{-1}$	0.02	0.04	0.05	< LD	< LD
Ti	$\mu g\ g^{-1}$	6.60	7.38	3.05	23.3	24.2
Tl	$\mu g\ g^{-1}$	0.006	0.017	0.002	0.002	0.001
Tm	$\mu g\ g^{-1}$	0.001	< LD	0.001	< LD	< LD
U	$\mu g\ g^{-1}$	0.007	0.010	0.02	0.007	0.008
V	$\mu g\ g^{-1}$	0.13	0.20	0.05	0.02	0.02
W	$\mu g\ g^{-1}$	< LD	0.002	< LD	< LD	0.002
Y	$\mu g\ g^{-1}$	0.05	0.04	0.06	0.11	0.11

Table 3 (continued)

		Milky quartz			Translucent quartz	
		ESIG15	ESIG18	ESIG19	ESIG21a	ESIG21b
Yb	µg g^{-1}	0.004	0.003	0.004	< LD	0.001
Zn	µg g^{-1}	0.23	0.15	0.25	0.17	0.32
Zr	µg g^{-1}	0.18	0.33	0.28	1.61	1.61

photograph. HPQ material forms very few or no bubbles during this test.

Three samples of milky quartz and two samples of translucent quartz were selected for silica fused analysis. The size and the average content of bubbles present vary among the samples: 1) Milky quartz samples (ESIG15, ESI18 and ESIG19) are from the brecciated quartz vein. The rock is brittle, and clasts are cemented by smaller quartz crystals. These small quartz crystals (10 to 80 µm in size) are separated upon grinding. Bubble characterization of all the milky quartz samples displays large quantity of bubble formation in fused grains (the green lines encircle the grains that have been effectively fused, where one or more bubbles are shown inside) and bubble size distribution in the range of 10–240 µm with a mean diameter of 75 µm (Fig. 7a, b, blue arrow). However, the majority (80%) of bubbles are from 50 to 80 µm in diameter while about 90% were smaller than 140 µm. Large clusters of small bubbles (less than 30 µm) were commonly observed in several fused grains of milky quartz (Fig. 7b, c, black arrow), and no bubble-free fused grains were observed in this quartz. 2) In translucent quartz, Fig. 7d permits to observe grains before and after fusion. In the fused state, the exact bubbles that form from each grain are distinctively observed. Translucent quartz samples do not produce many bubbles compared to the milky quartz, and also the size of each bubble is drastically reduced. More than 90% of the bubbles are less than 10 µm (Fig. 7d black arrow). Clean grains that have not produced bubbles upon fusion are also identified (Fig. 7d, green arrows) and represent about 40% of volume.

5 Discussion

5.1 Geochemistry and fluid inclusions

A number of factors likely played a role in the chemistry of trace elements in quartz studied in Etam. These are factors such as metamorphism and hydrothermal fluid action. Trace elements concentrations are chiefly regulated by the crystallization temperature [6, 57], the extent of melt fractionation in igneous and pegmatitic quartz [58–60] and the chemistry and acidity of the fluid from which the quartz crystallized in diagenetic and hydrothermal quartz [61–63].

Monecke et al. [64], Baron et al. [65] define Li, Al, K, Rb, Sr, and Y concentration in quartz as tools that allow distinguishing quartz from metamorphic processes from quartz of hydrothermal origin. Korneliussen et al. [66], Müller et al. [67] show that, despite variations, the previous elements have generally lower concentration in metamorphic quartz compared to hydrothermal quartz. According to [58], the Ge/Ti, Ge/Be, P/Ge and P/Be ratios of quartz are strongly sensitive to the origin and evolution of the granitic melts. The Ge/Ti ratio therefore is the most suitable for analyzing and understanding petrogenetic processes in granitic igneous rocks. Research work discriminating sources of quartz deposit have been carried out previously worldwide and abundant literature is available [3, 6, 11, 45, 52, 67, 68]. Trace elements in quartz are then generally used as tools for differentiating pegmatite, igneous, hydrothermal and metamorphic quartz. These studies are used for benchmarking procedures and comparing results of this study.

From the ICP-MS or LA-ICP-MS analysis, Etam quartz samples show more or less variation between milky and translucent quartz trace elements concentration. Figure 8 a shows similar trend variation in trace elements concentration for both quartz and suggests the similar processes of formation of Etam quartz. Data available [14, 69, 70] show that Al^{3+}, Ti^{3+} and Ge^{3+} commonly substitute Si^{4+} in quartz structure and the charge defect created by these substitutions is compensated by monovalent ions Li^{+}, Na^{+}, K^{+} and H^{+}.

The Al/Li ratio is often used to constrain crystallization conditions of quartz [52, 65, 72]. This ratio varied from 67.55 to 153.47 in milky quartz and is 209.8 in translucent quartz samples. Thus, the Al/Li value in Etam quartz is far from the Al/Li ratio in pegmatitic quartz, often < 10 [45, 52] and also far from hydrothermal quartz studied elsewhere [11, 64]. Monecke et al. [64] distinguished metamorphic quartz from hydrothermal quartz by low content of Li, Al, K, Rb, Sr and Y in recrystallized metamorphic quartz. Lithium, Rb, Sr and Y show low concentrations in Etam quartz, similar to most of the metamorphic quartz described in the literature [64, 73, 74]. Aluminum and K concentrations are high and comparable to some pegmatite quartz studied in the world [52], except for sample E-SIG 19 which shows K

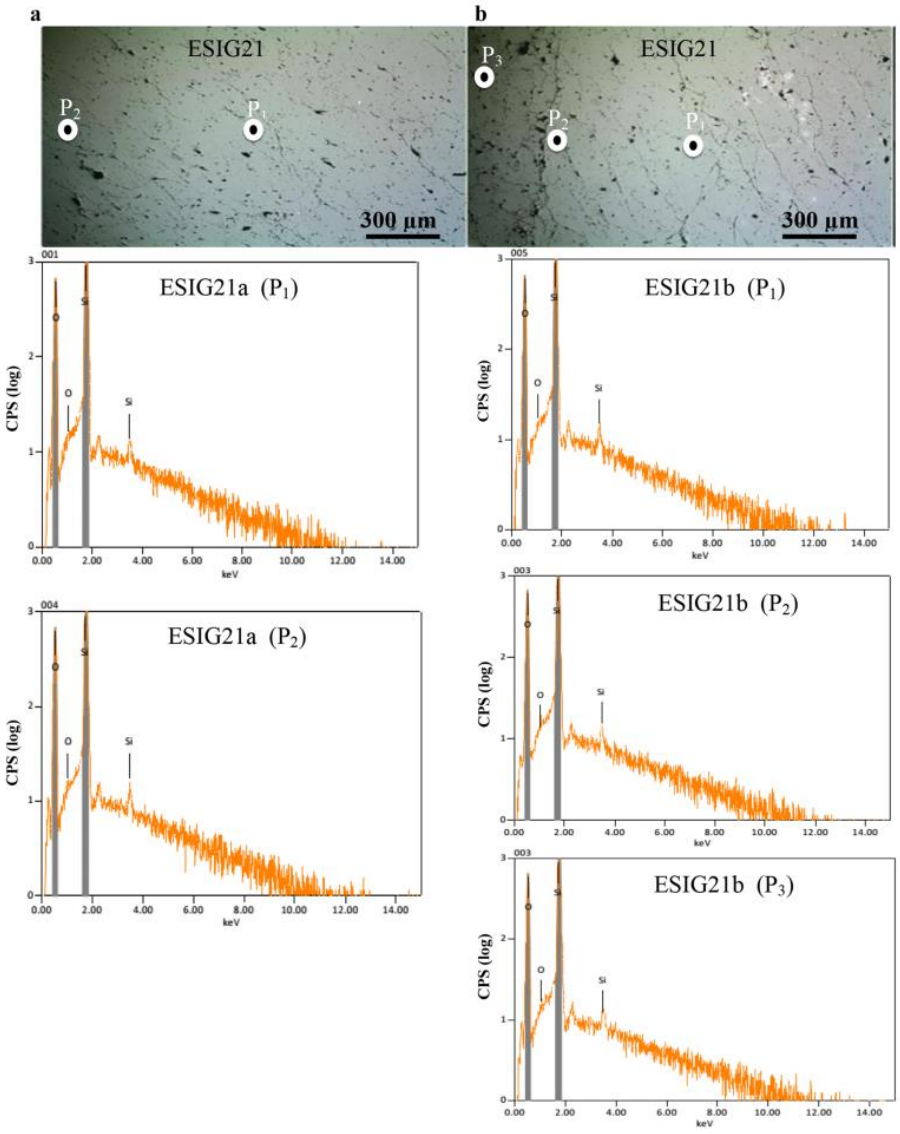

Fig. 3 SEM-EDS images and patterns for translucent quartz: **a** image for sample ESIG21a and EDS patterns at point 1 (P_1) and 2 (P_2), **b** image for sample ESIG21b and EDS patterns at points 1 (P_1), 2 (P_2) and 3 (P_3)

below detection limit. Daughter crystals in fluid inclusions in this quartz are mostly salts, and therefore, Al is probably incorporated in the quartz structure added by hydrothermal fluid circulating during metamorphic events. Indeed, milky quartz in Etam was probably (re)crystallized under greenschist to amphibolitic metamorphic condition [44] in the shear zone. The relative low concentration of Na and K coupled with the low Al/Li ratio suggests that the charge balances are compensated mainly by H^+ [75] from hydrothermal fluid in milky and translucent quartz, since either

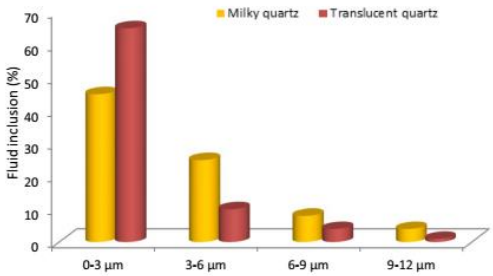

Fig. 4 Histogram showing proportion of fluid inclusions in milky and translucent quartz in Etam

a metamorphic event or the brittle nature of the rock has enhanced fluid flow in the area.

The Ge/Fe ratio (mean = 0.0027) is very low in milky quartz compared to translucent quartz (mean = 0.031) and to hydrothermal quartz studied in Olhos D'agua (Ge/Fe = 0.15) and Corinto (Ge/Fe = 0.3 [45]. It is also much smaller compared to pegmatitic quartz which presents Ge/Fe ratio ranges from 4.5 to 0.1 [52, 76]. According to [76], this low Ge/Fe ratio suggests the early crystallization stage of quartz probably during metamorphic event and containing high concentration of Fe. Furthermore, the rare-earth elements (REE) distribution pattern of this quartz type shows the characteristics of typical metamorphic quartz samples [64, 74] with an enrichment of LREE (Fig. 8b). The samples contain very low to negligible HREE when compared to standard HPQ values [6, 51], and thus

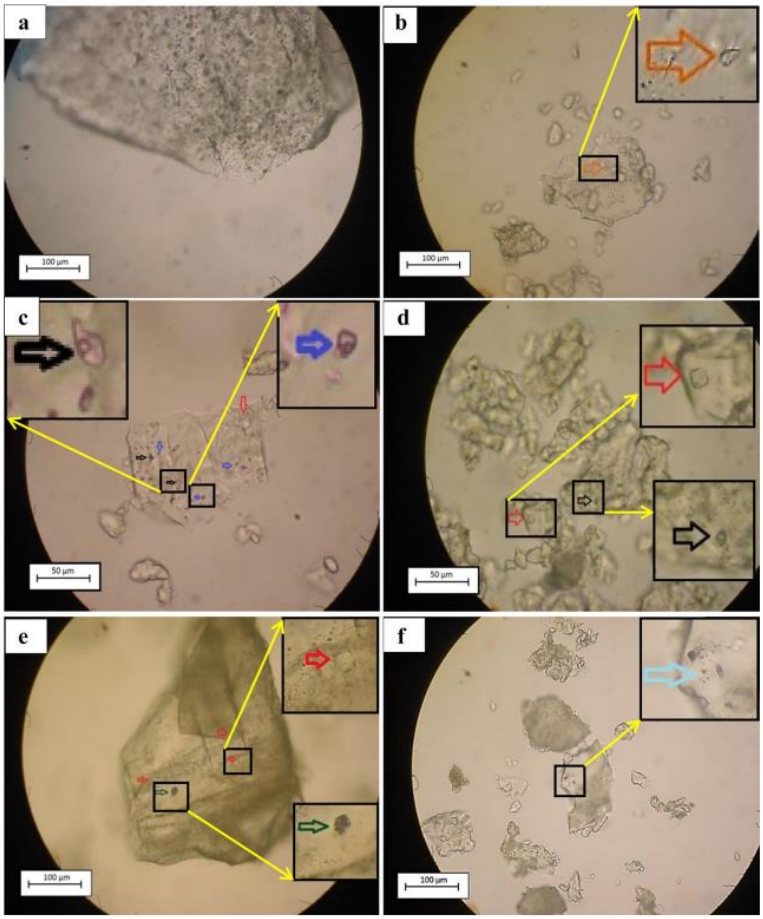

Fig. 5 Photomicrographs of fluid inclusions in milky quartz samples: **a** large in quantities and small in size fluid inclusions in milky quartz, **b** dipyramidal monophasic inclusions probably apatite (orange arrow), **c** Irregular (black arrow) and regular (blue arrow) two-phase inclusions, **d** negative quartz crystals (black arrow) and cubic inclusion (red arrow), **e** mineral inclusion (red arrow) and melt inclusion (green arrow), **f** fluid inclusion surrounded by small inclusion (satellite inclusions)

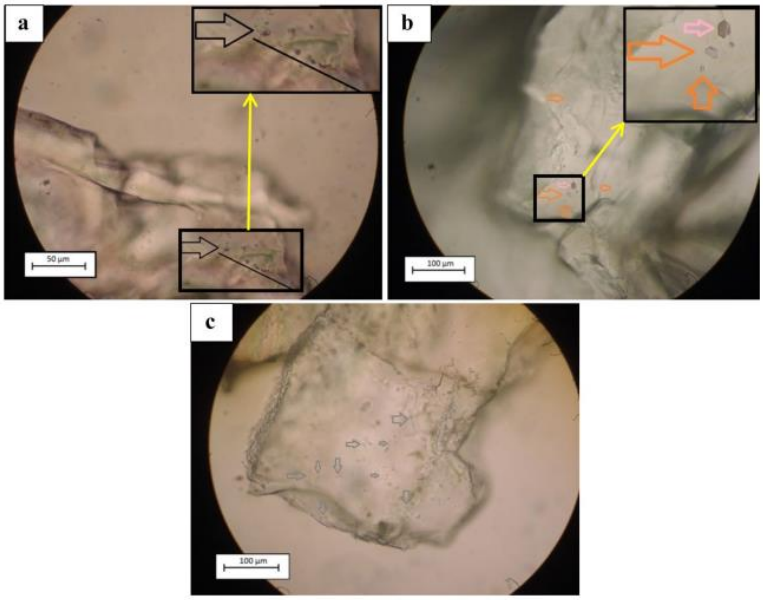

Fig. 6 Photomicrographs of fluid inclusions in translucent quartz: **a** Negative biphasic crystal inclusions generally oriented, **b** dipyramidal monophasic fluid inclusion (orange arrow) and mineral inclusion (pink arrow), **c** needle mineral inclusion, probably rutile (gray arrows)

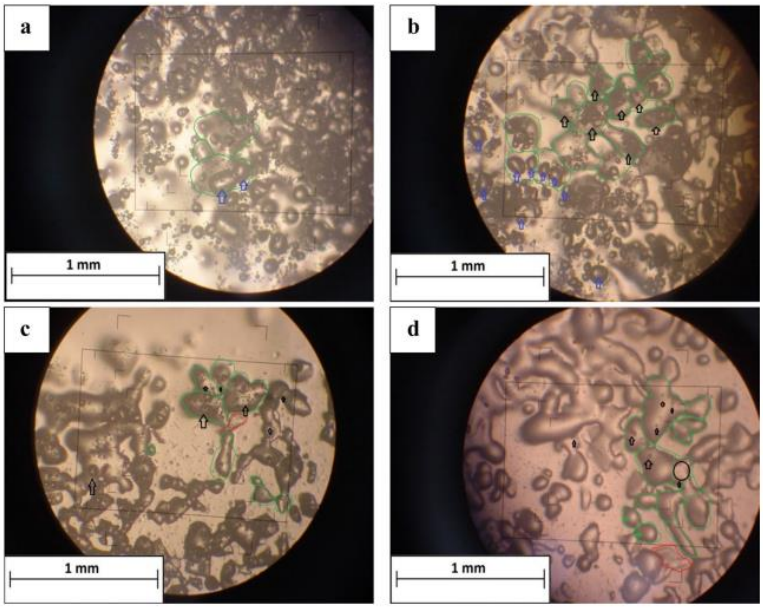

Fig. 7 Photomicrographs of the fused quartz powders over silica plates where fused grains can be observed with formed bubbles inside. **a** High quantity and very large bubble (blue arrow) formation in fused grains in milky quartz, **b**, **c** large quantity of bubble and clusters of small bubbles (black arrow) milky quartz, **d** cleaned fused grain with free bubble formation (green arrow) and small bubbles in grains (black arrow) in translucent quartz. The green lines circle the grains that have been effectively fused; the red lines circle the "unfused" grains

their chondrite-normalized REE patterns cannot be shown on spider diagram. The absence of a positive Ce anomaly is suggested to reflect the igneous protolith of this quartz. This corroborates [43, 44] who suggested that the protolith of the fault rocks is probably igneous rocks in Etam.

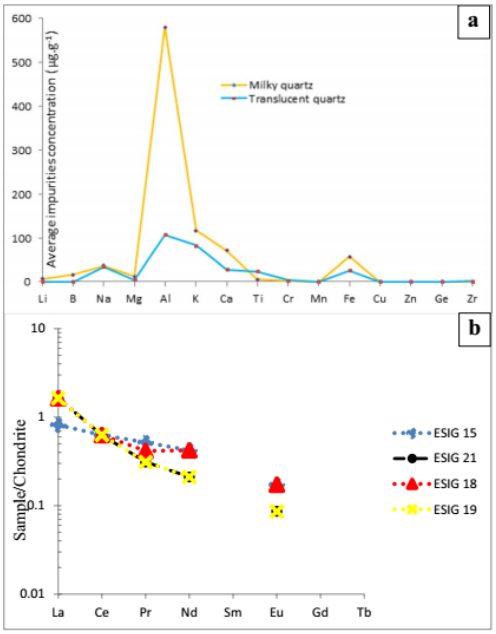

Fig. 8 Trace elements and REE variation in Etam quartz: **a** some trace element concentration average in Etam quartz, milky and translucent quartz patterns display similar trends with translucent quartz showing low concentration in all elements, except for Ti, **b** chondrite-normalized rare-earth element (REE) distribution patterns of Etam quartz (normalization according to data of Anders and Grevesse [71])

Fluid inclusions in milky quartz display features related to recrystallization under metamorphic conditions as shown by the higher volume of two-phase fluid inclusion with irregular shapes containing brine and CO_2 [77] and the alignment of the inclusions to define trails. However, the abundance and the variability of fluid inclusions suggest that this quartz benefitted from hydrothermal fluids inputs. Impurities contained in it are similar to some hydrothermal quartz data available [16, 64]. Therefore, it is suggested that quartz in Etam was probably formed during metamorphic processes implying circulation of hydrothermal fluid saturated in silica [73], followed by silica precipitation and formation of hydrothermal veins. Some data available [45] reveal that hydrothermally formed quartz of Pan-African age was submitted to some degree of metamorphism. These conditions are similar to the geological context at Etam environment. Furthermore, the Etam area and Santa Helena (Olhos D'_agua and Corinto) in Brazil are situated in N070E-oriented thrust zone (Fig. 1a) and were probably subjected to the same metamorphic degree during Pan-African event. Along shear zones, crystal-plastic deformation is an important process in the purification of quartz. Quartz has the capacity to response to stress along ductile shear zones in a combined brittle–ductile manner. Ductile failure results in quartz ribbons, deformation lamellae and undulose extinction and fracture-controlled slip. These features are observed in the pure quartz grains in the Etam shear zone.

5.2 Trace elements incorporation into quartz

The Al concentration in the Etam quartz samples varies (107 to 811 µg g^{-1}, Table 3). Rusk et al. [61], Götze et al. [78], Rusk et al. [79] demonstrated that high concentration of Ti and corresponding low concentration of Al are closely related to high temperature in hydrothermal quartz. The concentration of Ti in quartz reflects the temperature of recrystallization during metamorphism [48, 49, 57, 58, 67, 80]. Titanium concentration in milky quartz is similar to that of hydrothermal quartz described in the literature. The microscope studies of the Etam quartz did not show rutile as inclusions in milky quartz. Therefore, the Ti concentration in this quartz samples is presumably incorporated in the structure of the quartz and the hydrothermal fluids seem not to have played a major role in its genesis or the fluid was Ti poor. In the translucent quartz samples, the high content of Ti compared to the milky quartz is possibly related to mineral inclusions as needles that seem to be rutile inclusions were abundantly observed under the microscope study. The absence of Ti–Fe-rich mineral (e.g., ilmenite) in this geological environment suggests that Ti was probably added by Ti–rich hydrothermal fluids from other environment.

The high Al concentration in Etam quartz was probably induced during hydrothermal fluid-assisted metamorphism at elevated temperature [45, 64]. Such phase transformations are widespread in the area [40, 44]. Iron concentration is abnormally high in the translucent quartz compared to that of HPQ [6, 51]. Also [6] stated that quartz crystals in contact with Fe-rich minerals show high concentration of Fe. Thus, the Fe concentrations in quartz are predominantly diffusion-controlled. Indeed, clusters of small quartz grains containing red spots, probably iron oxide, were observed in the fluid and mineral inclusion study. The origin of these spots is not known, but probably hydrothermal fluids circulating in the area were Fe-rich.

The high concentration in quartz of Ca, K, Mg and Na is sometimes due to saline environment. But generally these elements are carried in quartz by fluids inclusions or mineral inclusions [11, 73]. Indeed, the microscope observation shows several NaCl crystal inclusions in Etam quartz that probably carried some of these elements.

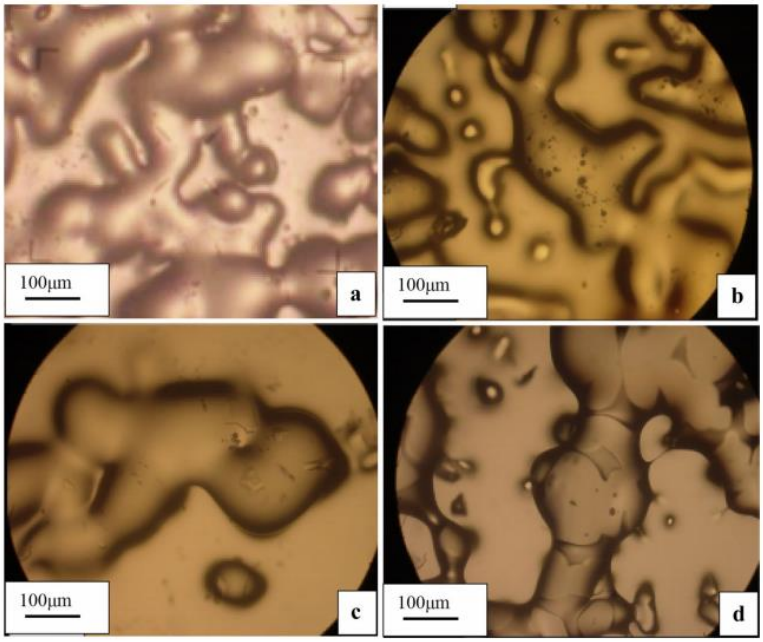

Fig. 9 Photomicrographs of the fused quartz powders over silica plates. **a** Translucent quartz from Etam, **b** milky quartz from Olhos D'agua, **c** transparent quartz from Corinto, **d** Iota commercial powder [11]. Small black dots represent bubbles

5.3 Technological aspect

Quartz in this study has mainly two-phase fluid inclusions containing saline water and CO_2. The behavior of quartz upon fusion has been described by several authors [10–12, 45]. The amount of gas liberated during fusion is related to the size and density of fluid inclusions. At Etam, the translucent quartz yielded better fusion test results compared to the milky quartz variety. The results of the bubble formation test for the Etam translucent quartz (Fig. 9a) are compared here to the milky samples (Fig. 9b) and the transparent quartz (Fig. 9c) from Corinto and Olhos D'agua, respectively (samples from the Serra de Santa Helena formation-Brazil) [45], and to the commercial powder, IOTA powder (Fig. 9d).

The comparison shows that the milky quartz samples from Olhos D'agua formed more bubbles compared to the three other samples. Moreover, samples from Etam translucent quartz, transparent quartz or the IOTA powder have formed small bubbles compared to the milky quartz samples during fusion over silica plate. Between sample of translucent quartz from Etam, transparent quartz from Olhos D'agua or the IOTA powder, the variation in terms of bubble size and bubble volume is negligible. These samples therefore seem similar from the point of view of bubbles formation after fusion over silica plate. Furthermore, the translucent quartz sample from Etam has few bubbles formed, similar to the transparent quartz from Olhos D' agua, which was concluded to be equivalent to commercial IOTA powder [11].

The inclusions in both quartz varieties are different in size, in quantity and types. This observation suggests that either the two quartz varieties were subjected to different geological events (hydrothermal action or metamorphism) that could modify fluid inclusion features in it or inclusions were initially formed differently due to different processes [45]. Furthermore, high-stress tectonic geological environment can induce fluid inclusion deformation due to fluid loss [56, 81–85]. Milky quartz in Etam developed along a brittle–ductile shear zone [44] and shows large inclusions observed surrounded by small inclusions or satellite inclusions. This can be supported by [86] and [55, 56] who showed that due to deviatoric stress, inclusions can be deformed and dismembered, giving a large relic inclusion and a cluster of small neonate (satellite) inclusions around them.

The chemical analysis in Table 3 shows impurities in some Etam quartz samples. The translucent quartz variety has more promising results for industrial applications, compared to the milky quartz. According to [45], impurities in fluid inclusions are less hard to eliminate than the incorporated ones in quartz structure. Therefore, the

most principal elements with high concentrations in the translucent quartz are: Al (means 107 µg g^{-1}), K (means 82.4 µg g^{-1}), Fe (means 26.01 µg g^{-1}). According to [11], removing Al impurities from quartz by using HF or concentrated acid mixtures is costly and constitutes environmental hazards. Therefore, for quartz to be suitable as HPQ raw material, it should meet certain natural requirements, or the processing should be done by methods that are less hazardous and more efficient. Indeed, an efficient fluorine-free leaching system to purify quartz has been developed with an objective to establish a fluoride-free technology for improving quartz quality [16]. According to the authors, the method can consistently purify quartz by removing elements impurities up to 88.2 wt%, 99.0 wt% and 98.1 wt%, for the HCl–NH4Cl system, and 87.5 wt%, 98.1 wt% and 98.2 wt% for the H_2SO_4–NH_4Cl system, respectively, for Al, K and Fe.

Based on chemical studies coupled with bubble formation characteristics in Etam quartz, the milky quartz can necessitate important and costly purification process to meet HPQ standard. The deposit therefore due to the high SiO_2 content (up to 99.75 wt%) can be used as raw materials for the refractory industry with a production of silica stone, silicon and silicon alloys [51]. Translucent quartz in the other hand shows optimistic results as quartz raw material that can be used in some quartz applications industries without necessarily purification processes. It can produce, for instance, silica glass which is common raw material largely used in optical and telecommunication industries.

5.4 Economic appraisal

According to the definition of HPQ, the milky quartz from Etam does not meet the requirement of a high-purity quartz deposit. The sum of the concentration of unwanted elements in this quartz type is ≥ 500 µg g^{-1}. The translucent quartz variety is fine-grained, translucent and massive. These aspects are often an indication of good fusion behavior [10]. Regarding only the fusion behavior, this quartz type can be used to produce transparent glass. The problematic feature is the chemical purity. With the exception of Li (0.5 µg g^{-1}) and B (below detection limit), all the trace elements which determine the purity of quartz as per HPQ definition are above the required limits (Table 3). The Ti and Fe are especially high. These impurities are probably located in the mineral inclusions which can easily be eliminated if proper processing tests are conducted. Translucent quartz show similar characteristics to some samples from the Santa Helena quartz deposit [45] as shown by the fusion over silica plate and bubble formation. Therefore, further investigations for such quartz type in the Etam area are advised. Several veins as translucent quartz vein with similar orientation exist in the area. These veins crop mostly in metamorphic basement and are easily accessible. The volume of the milky and translucent quartz resource that defines the distinct Etam ridge above the surrounding peneplain is estimated at ~ 6 km^3 pointing to an exploitable deposit considering that drilling will only add to the subsurface volume.

6 Conclusion

The investigation of Etam quartz samples in the southwest region (Cameroon) by the combination of ICP-MS, LA-ICP-MS, SEM–EDS resolved trace-element analysis and characterized in detail the type, the abundance of trace elements in quartz and the reconstruction of processes responsible for their formation and the amount of trace-element concentrations. The analyses show that the SiO_2 content is very high (98.46–99.75 wt%) with very low concentration of trace elements. The process of formation of both deposit types is suggested to be similar: The translucent quartz is clearly older than the milky quartz although both probably formed under metamorphic conditions and benefited from a contribution of hydrothermal fluids.

The translucent quartz of Etam shows optimistic results as ore resource after analysis. Principal impurities in it are Al (mean 107 µg g^{-1}), Ca (mean 27.85 µg g^{-1}) Fe (mean 26.05 µg g^{-1}) and Ti (mean 23.75 µg g^{-1}). According to the HPQ definition, quartz from Etam does not meet the requirement of a high-purity quartz deposit. Chemically and technologically, the translucent quartz is medium-purity quartz with good fusion behavior producing very little number of bubbles; thus, it could be used to produce transparent glass. Moreover, the main impurities in translucent quartz are mostly in fluid and mineral inclusions; thus, the purification using efficient method can purify this quartz and produce quartz crucibles with high-purity qualities widely used in industries.

Acknowledgements This paper is part of ongoing Ph.D. thesis by the first author. This work has been financially supported by the Ministry of Higher Education, Cameroon, through the Special Allocation for the Modernization of Research (SAMR) granted to the first author. Authors thank the Conselho Nacional de Desenvolvimento Cientifico e Tecnologico (CNPq) for the financial support. We highly appreciate the support of Prof. Nzenti Jean Paul who suggested constructive revisions to the various versions of the manuscript. The incisive comments of two anonymous reviewers and the Editor are much appreciated.

Authors' contributions CES, CS and MA were involved in study conception and design. CES, CS and MJLN were involved in acquisition of data. CES, CKS, CS, EF and MFMS contributed to analysis and interpretation. CS drafted the manuscript. CES, CKS, EF and MFMS were involved in critical revision of the manuscript. All authors read and approved the final manuscript.

Funding This study received financial support from the Ministry of Higher Education, Cameroon, through the Special Allocation for the Modernization of Research (SAMR) granted to CS and CES. MFMS, EF and CKS received financial support from Conselho Nacional de Desenvolvimento Cientifico e Tecnologico (CNPq).

Compliance with ethical standards

Conflict of interest The authors declare that they have no conflict of interest.

References

1. Haus R, Prinz S, Priess C (2012) Assessment of high purity quartz resources. In: Götze J, Möckel R (eds) Quartz: deposits, mineralogy and analytics. Springer, Berlin, pp 29–51
2. Moore P (2005) High purity quartz. Ind Miner 455:53–57
3. Haus R (2005) High demands on high purity. Ind Miner 10:62–67
4. Barkhudarov EM, Christofi N, Kossyi IA, Misakyan MA, Sharp J, Taktakishvili IM (2008) Killing bacteria present on surfaces in films or in droplets using microwave UV lamps. World J Microl Biotechnol 24:761–769
5. Wait IW, Johnston CT, Blatchley ER (2007) The influence of oxidation reduction potential and water treatment process on quartz lamp sleeves fouling in ultraviolet disinfection reactors. Water Res 41:2427–2436
6. Muller A, Wanvik JE, Ihlen PM (2012) Petrological and chemical characterisation of High-Purity Quartz deposits with examples from Norway. In: Gotze J, Mockel R (eds) Quartz: deposits, mineralogy and analytics. Springer, Heidelberg, pp 71–118 **Natural hydrothermal quartz. Mineral Mag 73:615–632**
7. Minami T, Maeda S, Higasa M, Kashima K (2011) In-situ observation of bubble formation at silicon melt-silica glass interface. J Cryst Growth 318:196–199
8. Yahamara K, Huang X, Sakai S, Utsonomiya A, Tsurita Y, Hoshikawa K (2001) Surface of silica glass reacting with silicon melt: effect of raw materials for silica crucibles. Jpn J Appl Phys 40:1178–1182
9. Huang X, Kishi H, Oishi S, Watanabe H, Sanpei K, Sakai S, Hoshikawa K (1999) Expansion behavior of bubbles in silica glass concerning Czochralski (CZ) Si growth. Jpn J Appl Phys 38:353–355
10. Santos MFM, Fujiwara E, De Paula FD, Suzuki CK (2013) Opacity measurements on quartz and its influence on silica glass properties. Int J Miner Process 124:141–144
11. Santos MFM, Fujiwara E, Schenkel EA, Enzweiler J, Suzuki CK (2015) Quartz sand resources in the Santa Maria Eterna formation, Bahia, Brazil: a geochemical and morphological study. J S Am Earth Sci 62:176–185
12. Griscom DL (2006) Self-trapped holes in pure silica glass: a history of their discovery and characterization and an example of their critical significance to industry. J. Non Cryst Solids 3512:2601–2617
13. Suzuki CK, Santos MFM, Ono E, Fujiwara E (2012) Strategic high quality quartz supply for fusion into silica glass. In: Varshneya AK, Schaeffer HA, Richardson KA, Wightman M, Pye D (eds) Processing properties and applications of glass and optical materials: ceramic transactions. The American Ceramic Society, Baltimore, pp 69–74
14. Götze J (2009) Chemistry, textures and physical properties of quartz—geological interpretation and technical application. Miner Mag 73:645–671
15. Yang C, Li S, Bai J, Han S (2018) Advanced purification of industrial quartz using calcination pretreatment combined with ultrasound-assisted leaching. Acta Geodyn Geomater 15:187–195. https://doi.org/10.13168/AGG.2018.0014
16. Lin M, Pei Z, Lei S (2017) Mineralogy and processing of hydrothermal vein quartz from Hengche, Hubei Province (China). Minerals 7:161. https://doi.org/10.3390/min7090161
17. Penaye J, Toteu SF, Van Schmus WR, Nzenti JP (1993) U–Pb and Sm–Nd preliminary geochronologic data on the Yaoundé series, Cameroon: re-interpretation of the granulitic rocks as the suture of a collision in the "centrafrican" belt. C R Acad Sci Paris 317:789–794
18. Toteu SF, Van Schmus Penaye J, Michard A (2001) New U–Pb and Sm–Nd data from North-Central Cameroon and its bearing on the pre-Pan-African history of Central Africa. Precambrian Res 108:45–73
19. Toteu SF, Penaye J, Poudjom Djomani YH (2004) Geodynamic evolution of the Pan African belt in Central Africa with special reference to Cameroon. Can J Earth Sci 41:73–85
20. Almeida FF, Hasui Y, Brito de Neves BB, Fuck RA (1981) Brazilian structural provinces. Earth Sci Rev 17:1–29
21. Castaing C, Feybesse JL, Thieblemont D, Triboulet C, Chevremont P (1994) Paleogeographical reconstructions of the Pan-African/Brasiliano orogen: closure of an oceanic domain or intracontinental convergence between major blocks. Precambrian Res 69:327–344
22. Neves SP, Vauchez A, Archanjo C (2006) Shear zone-controlled magma emplacement or magma-assisted nucleation of shear zones? Insights from northeast Brazil. Tectonophysics 262:349–364
23. Ngako V, Affaton P, Nnange JM, Njanko TH (2003) Pan-African tectonic evolution in central and Southern Cameroon: transpression and transtension during sinistral shear movements. J Afr Earth Sci 36:207–214
24. Ngako V, Affaton P, Njonfang E (2008) Pan-African tectonic in northwestern Cameroon: implication for history of western Gondwana. Gondwana Res 14:509–522
25. Njiekak G, Dörr W, Tchouankoue JP, Zulauf G (2008) U–Pb zircon and microfabric data of (meta) granitoids of western Cameroon: constraints on the timing of pluton emplacement and deformation in the Pan-African belt of Central Africa. Lithos 102:460–477
26. Penaye J (1988) Pétrologie et structure des ensembles métamorphiques au Sud–Est de Poli (Nord-Cameroun). Rôles respectifs du socle protérozoique inférieur et de l'accrétion et de l'accrétion crustale panafricaine. Thèse de l'INPL, Nancy
27. Tanko Njiosseu EL, Nzenti JP, Njanko T, Kapajika B, Nédelec A (2005) New U-Pb zircon ages from Tonga (Cameroon): coexisting Eburnean-Transamazonian (2.1 Ga) and Pan-African (0.6 Ga) imprints. C R Géosci 337:551–562
28. Ganwa A, Frisch W, Siebel W, Shang CK, Mvondo OJ, Satir M, Tchakounte NJ (2008) Zircon 207Pb–206Pb evaporation ages of Pan-African metasedimentary rocks in the Kombé-II area (Bafia Group, Cameroon): constraints on protolith age and provenance. J Afr Earth Sci 51:77–88
29. Soba D (1989) La série de Lom: étude géologique et géochronologique d´un bassin volcanosédimentaire de la chaîne panafricaine de l´Est du Cameroun. Thèse de Doctorat d´Etat, Université de Paris VI, France
30. Tchaptchet Tchato D, Schulz B, Nzenti JP (2009) Electron microprobe dating and thermobarometry of Neoproterozoic metamorphic events in the Kekem area, Central African Fold Belt of Cameroon. Neues Jahbür Minerol Abh 186:95–109
31. Bouyo Houkechang M, Toteu SF, Deloule E, Penaye J, Schumus Van (2009) U–Pb and Sm–Nd dating of high-pressure granulites from Tcholliré and Banyo regions: evidence for a pan African

granulite facies metamorphism in north-central Cameroon. J Afr Earth Sci 54:144–154
32. Nzenti JP, Kapajika B, Wörner G, Lubala RT (2006) Synkinematic emplacement of granitoids in a Pan-African shear zone in Central Cameroon. J Afr Earth Sci 45:74–86
33. Tagne-Kamga G (2003) Petrogenesis of the Neoproterozoic Ngondo plutonic complex (Cameroon, West Central Africa): a case of late-collisional ferro-potassic magmatism. J Afr Earth Sci 36:149–171
34. Kouankap NGD, Nzenti JP, Suh CE, Ganno S (2010) Geochemistry of ferriferous, high-K calc-alkaline magmas from the Banefo-Mvoutsaha Massif (NE Bafoussam), Central Domain of the Pan-African Fold Belt, Cameroon. Open Geol J 4:21–34
35. Mosoh BCK, Frimmel HE, Ze A, Suh CE (2012) Age and origin of Pan-African granites and associated U-Mo mineralization at Ekomedion, southwestern Cameroon. J Afr Earth Sci 88:15–37
36. Ngnotué T, Nzenti JP, Barbey P, Tchoua MF (2000) The Ntui–Betamba high grade gneisse: a northward extension of the Pan-African Yaoundé Gneisses in Cameroon. J Afr Earth Sci 31:369–381
37. Asaah AV, Zoheirc B, Lehmann B, Frei D, Burgess R, Suh CE (2015) Geochemistry and geochronology of the ~ 620 Ma gold-associated Batouri granitoids, Cameroon. Int Geol Rev 57:1485–1509
38. Ntiéche B, Mohan MR, Moundi A, Mounjouohou MA (2016) Petrogenesis and geochemical characterization of the granitoids of the Magba shear zone west Cameroon central Africa. Open J Geol 6:812–839
39. Ntiéche B, Mohan MR, Moundi A (2017) Granitoids of the Magba shear zone, west Cameroon, Central Africa: evidence for emplacement under transpressive tectonic regime. J Geol Soc India 89:33–46
40. Njome MS, Suh CE (2005) Tectonic evolution of the Tombelgraben basement, southwestern Cameroon. Episodes 28:37–41
41. Kankeu B, Greiling RO, Nzenti JP (2009) Pan-African strike–slip tectonics in eastern Cameroon–Magnetic fabrics (AMS) and structure in the Lom basin and its gneissic basement. Precambrian Res 174:258–272
42. Njome MS, De Wit MJ (2014) The Cameroon line: analysis of an intraplate magmatic province transecting both oceanic and continental lithospheres: constraints, controversies and models. Earth-Sci Rev 139:168–194
43. Njome MS, Suh CE, Ghogomu RT (2003) A microstructural approach to interpreting the structural setting of the Tombel graben, south western Cameroon. GeoActa 2:181–200
44. Sigue C, Moundi A, Ndema MJL, Vishiti A, Kedia AC, Suh CE, Nzenti JP (2019) Quartz-rich fault rocks as potential high purity quartz source (I) in a sequence of the central cameroon shear zone (Etam Shear Zone): geology and structure. In: Rossetti F et al (eds) The structural geology contribution to the Africa-Eurasia geology: basement and reservoir structure, ore mineralisation and tectonic modelling. https://doi.org/10.1007/978-3-030-01455-1_16
45. Santos MFM, Fujiwara E, Schenkel EA, Enzweiler J, Suzuki CK (2014) Quartz resources in the Serra de Santa Helena formation, Brazil: a geochemical and technological study. J S Am Earth Sci 56:328–338
46. Müller A, Ihlen PM, Kronz A (2008) Quartz chemistry in polygeneration Sveconorwegian pegmatites, Froland, Norway. Eur J Miner 20:447–463
47. Mărgărit MN, Nicolae H, Simona Marchetti D, Bigi Simona, Gualtieri Alessandro F (2016) Progress in mineralogical quantitative analysis of rock samples: application to quartzites from Denali National Park, Alaska Range (USA). Powder Diffract 31:31–39
48. Nachlas WO, Whitney DL, Teyssier C, Bagley B, Mulch A (2014) Titanium concentration in quartz as a record of multiple deformation mechanisms in an extensional shear zone. Geochem Geophys Geosyst 15:1374–1397
49. Nachlas WO, Thomas JB, Hirth G (2018) TitaniQ deformed: experimental deformation of out-of equilibrium quartz porphyroclasts. J Struct Geol 116:207–222
50. Nachlas WO, Teyssier C, Whitney DL, Hirth G (2018) Diffusion geospeedometry in natural and experimental shear zones. Earth Planet Sci Lett 498:129–139
51. Götze J, Möckel R (2012) Quartz deposits, mineralogy and analytics. Springer, Berlin, p 360. ISBN 978-3-642-22161-3
52. Götze J, Plötze M, Graupner T, Hallbauer DK, Bray CL (2004) Trace element incorporation into quartz: a combined study by ICP-MS, electron spin resonance cathodoluminescence, capillary ion analysis, and gas chromatography. Geochim Cosmochim Acta 68:3741–3759
53. Fruth M, Blankenburg HJ (1992) Charaketerisierung von authigenen idiomorphen Kohle- und Salinarquartzen durch Einschlussuntersuchungen. Neues Jahrbuch Mineralogie. Abhandlungen 165:53–64 **(in German)**
54. Spear FS, Selverstone J (1983) Water exsolution from quartz: implications for the generation of retrograde metamorphic fluids. Geology 11:82–85
55. Tarantola A, Diamond LW, Stünitz H (2010) Modification of fluid inclusions in quartz by deviatoric stress I: experimentally induced changes in inclusion shapes and microstructures. Contrib Mineral Petrol 160:825–843
56. Tarantola A, Diamond LW, Stünitz H, Thust A, Pec M (2012) Modification of fluid inclusions in quartz by deviatoric stress III: influence of principal stresses on fluid inclusion density and orientation. Contrib Miner Petrol 164:537–550
57. Wark DA, Watson EB (2006) TitaniQ: a titanium-in-quartz geothermometer. Contrib Miner Petrol 152:743–754
58. Larsen RB, Henderson I, Ihlen PM, Jacamon F (2004) Distribution and petrogenetic behaviour of trace elements in granitic pegmatite quartz from South Norway. Contrib Miner Petrol 147:615–628
59. Breiter K, Müller A (2009) Evolution of rare-metal granitic magmas documented by quartz chemistry. Eur J Miner 21:335–346
60. Beurlen H, Müller A, Silva D, Da Silva MRR (2011) Petrogenic significance of trace-element data analyzed with LA-ICP-MS in quartz from the Borborema pegmatitic province, northeastern Brazil. Miner Mag 75:2703–2719
61. Rusk BG, Lowers H, Reed MH (2008) Trace elements in hydrothermal quartz; relationships to cathodoluminescent textures and insights into hydrothermal processes. Geology 36:547–550
62. Jourdan AL, Vennemann TW, Mullis J, Ramseyer K (2009) Oxygen isotope sector zoning in natural hydrothermal quartz. Miner Mag 73:615–632
63. Müller A, Herrington R, Armstrong R, Seltmann R, Kirwin DJ, Stenina NG, Kronz A (2010) Trace elements and cathodoluminescence of quartz in stockwork veins of Mongolian porphyry-style deposits. Miner Depos 45:707–727
64. Monecke T, Kempe U, GÖtze J (2002) Genetic significance of the trace element content in metamorphic and hydrothermal quartz: a reconnaissance study. Earth Planet Sci Lett 202:709–724
65. Baron MA, Stalder R, Konzett J, Hauzenberger CA (2015) OH-point defects in quartz in B-and Li-bearing systems and their application to pegmatites. Phys Chem Miner 42:53–62
66. Korneliussen A, Wanvik JE, Müller A, Ihlen PM (2006) Kystnære kvartsressurser i Hordaland. Geological Survey of Norway, Report 2006.045
67. Müller A, Ihlen PM, Wanvik J, Flem B (2007) High-purity quartz mineralisation in kyanite quartzites, Norway. Miner Depos 42:523–535

68. Ihlen PM, Muller A, Larsen RB, and Henderson I (2007) Transformation of igneous quartz to high-purity quartz in granitic pegmatites of South Norway Granitic Pegmatites. Paper presented at the State of the Art—International Symposium, Porto, Portugal. Retrieved from http://www.fc.up.pt/peg2007/files/ihlen.pdf. Accessed July 2019
69. Weil JA (1993) A review of EPR spectroscopy in alpha-quartz: the decades of 1982–1992. In: Helms CR, Deal BE (eds) Physics and chemistry of SiO_2 and the Si-SiO_2 interface, vol 2. Plenum Press, New York, pp 131–144
70. Weil JA (1984) A review of electron spin spectroscopy and its application to the study of paramagnetic defects in crystalline quartz. Phys Chem Miner 10:149–165
71. Anders E, Grevesse N (1989) Abundances of the elements: meteoritic and solar. Geochim Cosmochim Acta 53:197–214
72. Iwasaki H, Iwasaki F, Oliveira VAR, Hummel DCA, Pasquali MA, Guzzo PL, Watanabe N, Suziki CK (1991) Impurity content characterization of Brazilian quartz lasca. Jpn J Appl Phys 30:1489–1495
73. Götze J, Pan Y, Müller A, Kotova EL, Cerin D (2017) Trace element compositions and defect structures of high-purity quartz from the Southern Ural Region, Russia. Minerals 7:189. https://doi.org/10.3390/min7100189
74. KempeULF GötzeJ, Dombon E, MoneckeT Poutivtsev M (2012) Quartz regeneration and its use as a repository of genetic information. In: Götze J, Möckel R (eds) Quartz: deposits, mineralogy and analytics. Springer, New York. https://doi.org/10.1007/978-3-642-22161-3_15
75. Stalder R, Konzett J (2012) OH defects in quartz in the system quartz–albite–water and granite–water between 5 and 25 kbar. Phys Chem Miner 39:817–827
76. Schron W, Bauman L, Rank K (1982) Zur Charakterisierung von Quartz- generationen in den postmagmatogenen Ertzformationen des Erzgebirges. Zeitschrifit für Geol Wiss 16:229–244 **(in German)**
77. Heynke U, Leeder O, Schulz H (1992) On distinguishing quartz of hydrothermal or metamorphogenic origin in different monomineralic veins in the eastern part of Germany. Miner Petrol 46:315–329
78. Götze J, Plötze M, Habermann D (2001) Cathodoluminescence (CL) of quartz: origin, spectral characteristics and practical applications. Miner Petrol 71:225–250
79. Rusk B, Reed M, Dilles J, Kent A (2006) Intensity of quartz cathodoluminescence and trace element content of quartz from the porphyry copper deposit in Butte, Montana. Am Miner 91:1300–1312
80. Spear FS, Wark DA (2009) Cathodoluminescence imaging and titanium thermometry in metamorphic quartz. J Metamorph Geol 27:187–205
81. Schmatz J, Urai JL (2011) The interaction of migrating grain boundaries and fluid inclusions in naturally deformed quartz: a case study of a folded and partly recrystallized quartz vein from the Hunsrück Slate. Ger J Struct Geol 33:468–480
82. Romer RL, Franz L, Wirth R (2006) Chemical and isotopic effects of retrogression in metamorphic fluid inclusions. Contrib Mineral Petrol 151(2):174–186
83. Schmidt C, Bruhn D, Wirth R (2003) Experimental evidence of transformation plasticity in silicates: minimum of creep strength in quartz. Earth Planet Sci Lett 205:273–280
84. Vityk MO, Bodnar RJ, Doukhan JC (2000) Synthetic fluid inclusions. XV. TEM investigation of plastic flow associated with reequilibration of fluid inclusions in natural quartz. Contrib Miner Petrol 139:285–297
85. Roedder E (1984) Fluid inclusions. Reviews in mineralogy, vol 12. Mineralogical Society of America, Washington
86. Diamond LW, Tarantola A, Stünitz H (2010) Modification of fluid inclusions in quartz by deviatronic stress. II: experimentally induced changes in volume and composition. Contrib Miner Petrol 160:845–864

Quartz-Rich Fault Rocks as Potential High Purity Quartz Source (I) in a Sequence of the Central Cameroon Shear Zone (Etam Shear Zone): Geology and Structure

Cyrille Sigue, Amidou Moundi, Jean Lavenir Ndema Mbongue, Akumbom Vishiti, Arnold Chi Kedia, Cheo Emmanuel Suh, and Jean Paul Nzenti

Abstract

The Etam shear zone is the NNE-SSE to NE-SW trending fault zone with coexistence of a sinistral shearing mylonitic corridor and a brecciated quartz vein. The mylonitic zone is evidence of progressive deformation. Primary minerals include Qtz_1 + Kfs_1 + Pl_1 + Bt_1. These minerals increasingly and gradually reduce from the wall rock towards the shear zone center. Quartz recrystallization also gradually increases in the same direction. Microstructures observed include: recrystallization, sub-grain boundary, myrmekites and undulose extinction. Mica-chlorite-epidote assemblages define the greenschist assemblage, but the observation of amphibole in the mylonite and the presence of flame perthite in feldspar suggest a transitional greenschist-amphibolite metamorphic condition in the Etam Shear Zone. The brecciated quartz vein has dimensions of about 2.5 × 0.5 km and shows several quartzitic blocks, mainly composed of milky to transparent quartz clasts and a siliceous matrix. Quartz clasts are pure and the observation of thin sections of these quartz under polarized microscope shows grains free of microstructures or displays small micro quartz veins and rare feldspar inclusions. These are some criteria, which can lead to a preliminary assessment of the purity of quartz in Etam area.

Keywords

Etam • Fault zone • Quartz vein • Pure quartz Inclusions

1 Introduction

An abundant literature in fluid-flow mechanisms in structural features within a shear zone is available [1, 2]. Alteration in brittle–ductile shear zones is mainly driven by syn-tectonic fluids which are associated with a variety of weakening mechanisms [3]. The process of grain size reduction through fracturing during cataclastic deformation often releases Si through breakdown of albite or the formation of chlorite ± epidote and phengite [4]. Fluid saturated in Si can then circulates by diffusional transport [5] and form small quartz veins or by mobile hydrofracturing with very ascent fluids flow and form large quartz veins [6].

In southwestern Cameroon numerous quartz-rich rocks of metamorphic and fault-related origin have been described [7]. These rocks lie essentially along the Central Cameroon Shear Zone (CCSZ). Although this structure has witnessed numerous structural and economic studies [8], no previous studies have focused on these quartz-rich fault rocks whose contribution to the overall evolution of the shear zone and potential role as High Purity Quartz (HPQ) source is of more than local significance.

This study which is typically descriptive with preliminary geochemistry data examines the mineralogy and textural context of fault rocks and associated wall rock within the ESZ. The preliminary results obtained can constitute the commencement of the assessment of the potential HPQ in these rocks.

C. Sigue (✉) · J. L. N. Mbongue · A. Vishiti · A. C. Kedia
C. E. Suh
Economic Geology Unit, Department of Geology, University of Buea, P.O. Box 63 Buea, Cameroon
e-mail: siguecyrille@gmail.com

C. Sigue · J. L. N. Mbongue · J. P. Nzenti
Laboratory of Geosciences for Internal Formations and Applications, Department of Earth Sciences, Faculty of Science, University of Yaoundé I, Messa-Yaoundé, P.O. Box 3412 Cameroon

A. Moundi
Department of Earth Sciences, University of Yaoundé I, P.O. Box 3412 Messa-Yaoundé, Cameroon

A. Vishiti
Higher Institute of Science, Engineering and Technology, Cameroon Christian University Institute, P.O. Box 5 Bali, North West Region, Cameroon

F. Rossetti et al. (eds.), *The Structural Geology Contribution to the Africa-Eurasia Geology: Basement and Reservoir Structure, Ore Mineralisation and Tectonic Modelling*, Advances in Science, Technology & Innovation, https://doi.org/10.1007/978-3-030-01455-1_16

2 Methods of Study

The Etam shear zone was mapped in details. Representative mylonitic and quartz samples were cut and polished down to ~30 μm in thicknesses in preparation of thin sections in the IRGM laboratory, Nkolbisson-Yaounde. The polished samples were examined with the aid of a polarized light microscopy at the Geology laboratory, University of Buea. Petrographic studies involved the description of mineralogical features, microtectonics and alteration pattern. Structural data were displayed as stereoplots and the regional geological maps compiled to show the principal shear zone. All the data were built into a GIS platform in the Remote sensing Unit University of Buea (both field and laboratory) for easy retrieval and comparative studies.

All chemical analysis measurements were conducted by the ICP-MS technique using an X series II (Thermo) instrument, equipped with CCT (collision cell technology) in Analytical Geochemistry Laboratory, Campinas State University-Brazil.

3 Results: Texture, Mineralogy, Microstructures and Geochemistry

3.1 Wall Rock, Ductile Zone and Brittle Zone

The wall rock is a weakly deformed elongated (4 km long and 1.8 km wide) plutonic body, oriented N040E. The rock is massive, coarse grained, and made up of magmatic constituents (Kfs_1, Qtz_1, Pl_1 and Bt_1). Recrystallization produced 2% of quartz (Qtz_2), alteration of Kfs_1 produced albite and chlorite. The ductile zone consists of medium to coarse-grained protomylonite, medium grain mylonite and ultramylonites wrapped by mylonitic bands. Qtz_2 and Qtz_3, Pl_2, Bt_2 increased in volume in expense of Qtz_1, Pl_1 and Bt_1 through recrystallization. Microstructures include: Macro-fracturing, undulose extinction, Bulging (BLG) recrystallisation, Flame perthite, Myrmekitic and minerals fish. The brittle zone shows a large quartz vein (0.150 × 2.5 km), brecciated (Fig. 1a). Blocks of this vein are composed mainly of milky to transparent quartz clasts, <0.5 mm to 8 cm in size (Fig. 1 b and c). Microstructures are restricted to microfractures and rare Mineral small inclusion of feldspar (Fig. 1d–f).

3.2 Whole Rock Geochemistry by ICP-MS

ICP-MS analysis shows quartz composition range with 98.46–99.75 wt% SiO_2. Very low concentrations of the overall other major elements (Al_2O_3 = 0.01 to 0.15 wt%, Fe_2O_3tot = 0.1 to 0.59 wt%, MgO = 0.01 to 0.02 wt%, TiO_2 = 0.002 to 0.006 wt% Na_2O = 0.01 to 0.02, K_2O = 0.01 wt%). Trace elements and REE are under detection limit (LD), Except for: Cr (55–220 ppm), Zr(3–4 ppm), Ba (3–4 ppm), La(2–4 ppm), Ce (3–4 ppm), Pr (0.03–0.05 ppm) and Nd (0.1–0.2 ppm).

3.3 Structural Context of the Shear Zone Deformation

Quartz shows evidence of crystal-plastic deformation, while K-feldspar and plagioclase are deformed in a plastic and brittle manner. ESZ define an oblique-slip with a mylonitic schistosity, trending N10°E in the south of the shear zone although turn elsewhere to N40°E towards the north. Asymmetric boudin, C-type, C'-type and S/C structures define a sinistral strike-slip sense of shear. During brittle deformation, ESZ experienced a N060E to N065E fracture event, formed earlier in the zone follow by N120E to N140E and N100E to N110E (Fig. 1a) [9].

4 Discussion

Crystal-plastic deformation and recrystallization are associated with micro-fracturing in ESZ suggesting the greater role played by stress. Metasomatic and alteration reactions particularly released quartz and K^+, Na^+, Ca^+, Fe^+, Al^+ [3, 4]. The presence of several quartz veins in ESZ suggest

Fig. 1 **a** Geologic map of Etam, **b** and **c** photograph of Milky quartz, **d** and **e** photomicrograph of milky quartz free of mineral inclusion, **f** photomicrograph with mineral inclusion

therefore, a strong mobility of hydrothermal fluid saturated in silica. Si is dissolved during cataclasis and precipitate in strain shadow and fractures. The deformation mechanism is suggested to be similar to that of the Cameroon Central Shear Zone (CCSZ) [7, 10] and Wyangala shear zone, Australia [3]. The metamorphic conditions are similar as indicated in Tombel Graben [7]: green-schist facies with epidote, sericite, neocrystalized quartz and chlorite assemblage, low temperature grain boundaries ($\sim$300 °C), but the albitization of K-feldspar by the formation of perthite suggest a low-medium (400–500 °C) conditions metamorphism. The coexistence of such microstructures at different grades suggests that the deformation started in the presence of a residual melt and ended after the full crystallization of the rock at high temperature. The sinistral strike-slip sense of shear has recorded in the CCSZ follow by dextral shear sense [7, 11]. The N010E to N040E trend of mylonitic corridor in ESZ confirms how anastomosing is the CCSZ. Similar age (neoproterozoic) has been recorded in Panafrican fold belt in Cameroon and in the environment of the HPQ deposit is Brazil [12]. In the optical microscope, the amount of inclusions in Etam quartz is very small. Preliminary ICP-MS data shows very low amount of all elements, and high SiO_2 contain. These suggest an optimistic result of HPQ source. The only problem is probably the brittle nature of this quartz which can enhance the formation of fluid inclusions that causes the formation of bubbles during fusion processes and negatively affect the purity of the quartz [12].

5 Conclusions

We show in this study that quartz in veins are milky to transparent, with no significant minerals or fluid inclusions observed in optical microscope. This minor amount of impurities in this quartz is an indicator of their purity, which allows assessing the quartz vein as potential HPQ source in the further studies.

References

1. Ferry, J.M., Gerdes, M.L.: Chemically reactive fluid flow during metamorphism. Ann. Rev. Earth Planet. Sci. **26**, 255–287 (1998)
2. Streit, J.E., Cox, S.F.: Fluid infiltration and volume change during mid-crustal mylonitization of Proterozoic granite, King Island, Tasmania. J. Metamorph. Geol. **16**, 197–212 (1998)
3. Spruzeniece, L., Piazolo, S.: Strain localization in brittle–ductile shear zones: fluid-abundant versus fluid-limited conditions (an example from Wyangala area, Australia). Solid Earth **6**, 881–901 (2015)
4. Suh, C.E., Dada, S.S.: Fault rocks and differential reactivity of minerals in the kanawaViolaine uraniferous vein, N.E. Nigeria. J. Struct. Geol. (1997)
5. Widmer, T., Thompson, A.B.: Local origin of high pressure vein material in eclogitefacies rocks of the Zermatt-Saas zone, Switzerland. Am. J. Sci. **301**, 627–656 (2001)
6. Bons, P.D.: Development of crystal morphology during unitaxial growth in a progressively widening vein: I. The numerical model. J. Struct. Geol. **23**, 865–872 (2001)
7. Njome, M.S., Suh, C.E., Ghogomu, R.T.: A microstructural approach to interpreting the structural setting of the Tombel graben, south western Cameroon. Geo. Acta **2**, 181–200 (2003)
8. Mosoh Bambi, C.K., Frimmel, H.E., Zeh, A., Suh, C.E.: Age and origin of Pan-African granites and associated U-Mo mineralization at Ekomedion, southwestern Cameroon. J. Afr. Earth Sci. **88**, 15–37 (2013)
9. Njome, M.S., Suh, C.E.: Tectonic evolution of the Tombelgraben basement. Southwestern Cameroon Episodes, **28**, 37–41 (2005)
10. Dawaï, D., Tchameni, R., Bascou, J., Wangmene, S.A., Tchunte, P.M.F., Bouchez, J.L.: Microstructures and magnetic fabrics of the Ngaoundere granite pluton (Cameroon): Implications to the late-Pan-African evolution of Central Cameroon Shear Zone. J. Afr. Earth Sci. **129**, 887–897 (2017)
11. Ngako, V., Affaton, P., Nnange, J.M., Njanko, T.H.: Pan-African tectonic evolution in central and Southern Cameroon: transpression and transtension during sinistral shear movements. J. Afr. Earth Sc. **36**, 207–214 (2003)
12. Santos, M.F.M., Fujiwara, E., Schenkel, E.A., Enzweiler, J., Suzuki, C.K.: Quartz sand resources in the Santa Maria Eterna formation, Bahia, Brazil: a geochemical and morphological study. J. South Am. Earth Sci. **53**(62), 176–185 (2015)